

High precision spectroscopy of helium-like heavy ions  
with resonant coherent excitation

Yuichi Takabayashi



# Abstract

Dynamics of resonant coherent excitation (RCE) have been investigated extensively. Recently, we have observed the RCE of hydrogen-like and helium-like systems, *i.e.*,  $\text{Ar}^{17+}$ ,  $\text{Ar}^{16+}$ ,  $\text{Fe}^{25+}$ , and  $\text{Fe}^{24+}$  ions through measurements of the charge state distribution of the ions transmitted through Si crystals and projectile deexcitation X-rays. We found that the resonance peak position (angle) can be determined with a high precision. This means that the transition energy of the ion can be determined precisely. By using the RCE phenomena, we performed high-precision spectroscopy of helium-like ions. For  $\text{Fe}^{24+}$  ion, the obtained transition energy is in reasonable agreement with theory. We have demonstrated that the RCE observation can be used as a new method for spectroscopy of heavy ions.

# Contents

<b>1</b>	<b>Introduction</b>	<b>1</b>
1.1	Channeling . . . . .	1
1.2	Resonant coherent excitation (RCE) . . . . .	5
1.2.1	RCE condition . . . . .	5
1.2.2	Methods to observe RCE . . . . .	6
1.2.3	Historical background . . . . .	8
1.2.4	Energy levels and wave functions . . . . .	13
1.2.5	Excitation process . . . . .	22
1.3	Convoy electron . . . . .	28
1.4	Spectroscopy of hydrogen-like and helium-like ions . . . . .	29
1.5	Purpose . . . . .	34
<b>2</b>	<b>Experimental</b>	<b>35</b>
2.1	HIMAC . . . . .	35
2.2	Observation of RCE . . . . .	35
2.2.1	Beam transport . . . . .	35
2.2.2	Goniometer . . . . .	36
2.2.3	Si crystal . . . . .	37
2.2.4	Detection system . . . . .	37
2.2.5	Data acquisition system . . . . .	43
2.2.6	Determination of crystal orientation . . . . .	44
<b>3</b>	<b>Observation of resonant coherent excitation</b>	<b>50</b>
3.1	Hydrogen-like Ar <sup>17+</sup> ions . . . . .	53
3.1.1	RCE from 1s to $n = 2$ states . . . . .	55
3.1.2	RCE from 1s to $n = 3$ states . . . . .	62
3.1.3	RCE from 1s to $n = 4$ and $n = 5$ states . . . . .	66
3.2	Helium-like Ar <sup>16+</sup> ions . . . . .	66
3.3	Hydrogen-like Fe <sup>25+</sup> ions . . . . .	73
3.3.1	RCE from 1s to $n = 2$ states . . . . .	73
3.3.2	RCE from 1s to $n = 3$ states . . . . .	75
3.4	Helium-like Fe <sup>24+</sup> ions . . . . .	79
3.5	Lithium-like Fe <sup>23+</sup> ions . . . . .	83

3.6	Discussion . . . . .	83
<b>4</b>	<b>High precision spectroscopy of helium-like ions</b>	<b>94</b>
4.1	Energy shift due to the Stark effect . . . . .	96
4.2	Exit angle dependence of RCE . . . . .	98
4.3	Spectroscopy of helium-like $\text{Ar}^{16+}$ ions . . . . .	99
4.4	Spectroscopy of helium-like $\text{Fe}^{24+}$ ions . . . . .	107
4.5	Discussion . . . . .	112
<b>5</b>	<b>Summary</b>	<b>115</b>
<b>A</b>	<b>Energy levels and transition amplitudes</b>	<b>117</b>
A.1	RCE for planar channeling . . . . .	117
A.2	Energy levels . . . . .	118
A.3	Transition amplitudes . . . . .	119
<b>B</b>	<b>Measurements of convoy electron spectra</b>	<b>121</b>
B.1	Introduction . . . . .	121
B.2	Experimental . . . . .	123
B.3	Target thickness dependence (390 MeV/u $\text{Ar}^{17+}$ ) . . . . .	123
B.4	Initial state dependence (460 MeV/u $\text{Fe}^{23+,24+,25+}$ ) . . . . .	130



# Chapter 1

## Introduction

### 1.1 Channeling

Crystals consist of periodically ordered atoms, and therefore the open space where the electron density is low exists along the axis or plane [1]. This open space is called a channel. If energetic ions are incident on a crystal in the direction parallel to the axis or plane, the ions pass through the channel without suffering large angle scattering. This phenomenon is called channeling.

The motion of the channeling ion can be treated classically, and is determined by the atomic potential averaged along the axis or plane. For planar channeling, the planar potential formed by the single atomic plane is written as

$$U_p^{(s)}(x) = 2\pi N d_p \int_0^\infty V(r) \rho d\rho, \quad (1.1)$$

where  $N$  is the target atomic density,  $d_p$  is the distance between the planes,  $V(r)$  is the target atomic potential,  $\rho^2 = r^2 - x^2$ , and  $x$  is the distance from the plane. Using this potential, the planar potential consisting of all the planes is written as

$$U_p(x) = \sum_n U_p^{(s)}(x - n d_p). \quad (1.2)$$

As an atomic potential, the Molière potential and the Ziegler-Biersack-Littmark (ZBL) potential are often used. The Molière potential is given by,

$$V(r) = \frac{Z_p Z_t e^2}{r} \sum_{n=1}^3 \alpha_n \exp(-\beta_n r / a_{TF}), \quad (1.3)$$

$$\alpha_n = (0.35, 0.55, 0.1), \quad (1.4)$$

$$\beta_n = (0.3, 1.2, 6.0), \quad (1.5)$$

where  $Z_p$  is the atomic number of the projectile ion,  $Z_t$  is the atomic number of the target atom, and  $a_{TF}$  is the Thomas-Fermi radius. This radius  $a_{TF}$  is written as

$$a_{TF} = 0.8853 a_B Z_t^{-1/3}, \quad (1.6)$$

where  $a_B$  is the Bohr radius. The ZBL potential is given by

$$V(r) = \frac{Z_p Z_t e^2}{r} \sum_{n=1}^4 \alpha_n \exp(-\beta_n r/a_s), \quad (1.7)$$

$$\alpha_n = (0.1818, 0.5099, 0.2802, 0.02817), \quad (1.8)$$

$$\beta_n = (3.2, 0.9423, 0.4029, 0.2016), \quad (1.9)$$

$$a_s = 0.8853 a_B Z_t^{-0.23}. \quad (1.10)$$

Using the Molière potential, the planar potential is given by

$$U_p(x) = 2\pi Z_p Z_t e^2 N d_p a_{TF} \sum_{n=1}^3 \frac{\alpha_n \cosh(\beta_n x/a_{TF})}{\beta_n \sinh(\beta_n d_p/2a_{TF})}, \quad (1.11)$$

$x$  being the distance from the channel center. Taking into account the thermal vibration of the crystal atom, the planar potential can be modified to

$$U_p^{(vib)}(x) = \frac{1}{\sqrt{2\pi}u_1} \int_{-\infty}^{\infty} \exp\left(-\frac{u^2}{2u_1^2}\right) U_p(x+u) du, \quad (1.12)$$

where  $u_1$  is the amplitude of the thermal vibration, which is 0.075 Å for Si at room temperature [1]. The planar potential calculated for a proton channeled in the (220) plane of a Si crystal is shown in Fig. 1.1. In this case,  $d_p$  is 1.92 Å, *i.e.*, the distance between the atomic plane and the channel center,  $d_p/2$ , is 0.96 Å. We also calculated the electric field of the planar potential, which is shown in Fig. 1.2. From the Poisson equation, the electron density in the (220) planar channel is calculated from the planar potential as

$$\begin{aligned} n_e(x) &= \frac{1}{4\pi} \frac{1}{Z_p e^2} \frac{d^2 U_p(x)}{dx^2} \\ &= \frac{Z_t N d_p}{2a_{TF}} \sum_{n=1}^3 \frac{\alpha_n \beta_n \cosh(\beta_n x/a_{TF})}{\sinh(\beta_n d_p/2a_{TF})}. \end{aligned} \quad (1.13)$$

The obtained electron density is shown in Fig. 1.3, where the arrow shows the average electron density.

If the incident angle of the projectile ion is smaller than the critical angle, the ion will be channeled. The critical angle  $\Psi_a$  for axial channeling is given by

$$\Psi_a = \sqrt{\frac{4Z_p Z_t e^2}{pvd}}, \quad (1.14)$$

$p$  is the momentum of the projectile ion,  $v$  is the projectile velocity, and  $d$  is the distance between the atoms. The critical angle  $\Psi_p$  for planar channeling is given by

$$\Psi_p = \sqrt{\frac{4\pi Z_p Z_t e^2 N a_{TF} d_p}{pv}}. \quad (1.15)$$

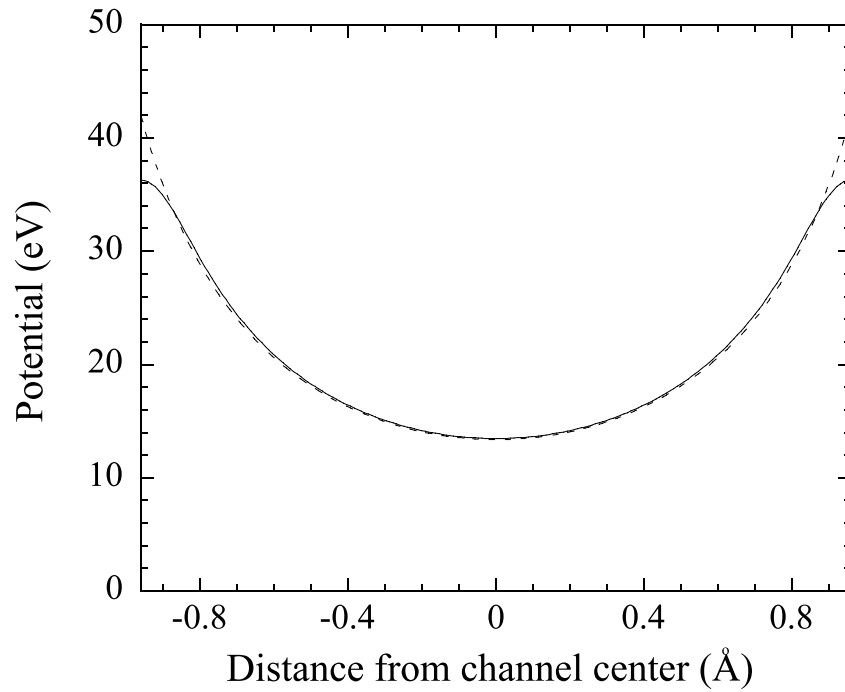


Figure 1.1: Planar potential for the proton channeled in the (220) plane. solid line: with thermal vibration, dashed line: without thermal vibration.

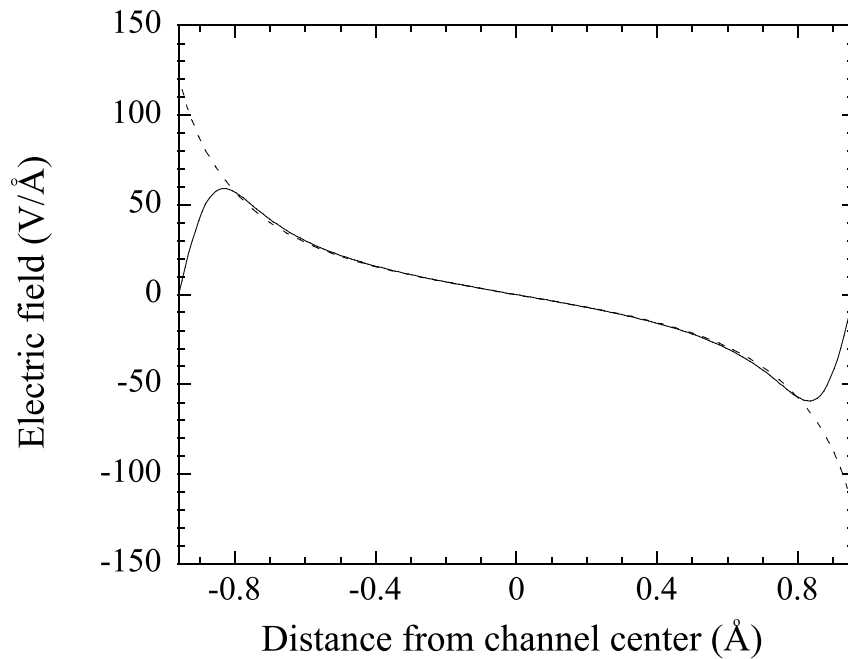


Figure 1.2: Electric field for the (220) planar channel. solid line: with thermal vibration, dashed line: without thermal vibration.

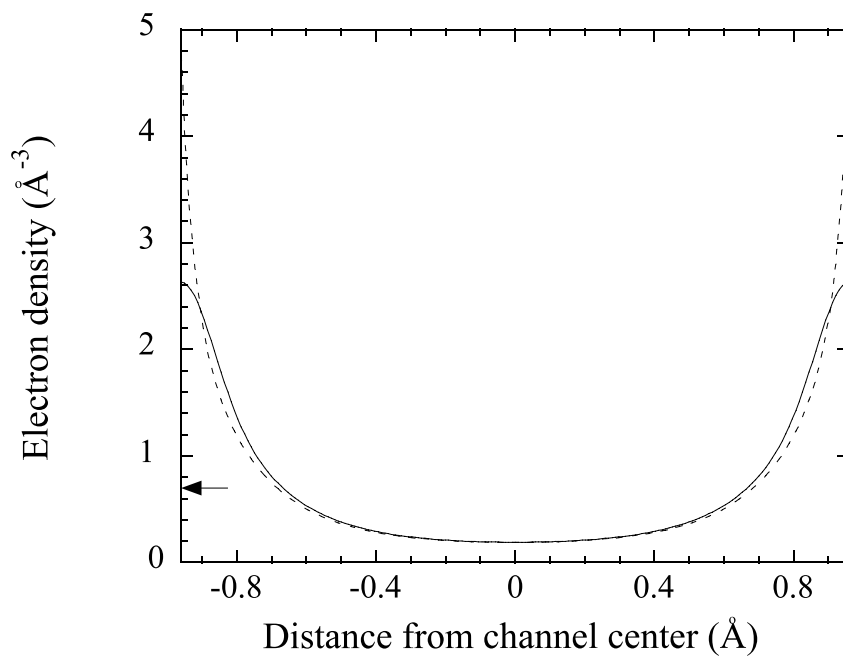


Figure 1.3: Electron density for the (220) planar channel. solid line: with thermal vibration, dashed line: without thermal vibration. The arrow shows the average electron density.

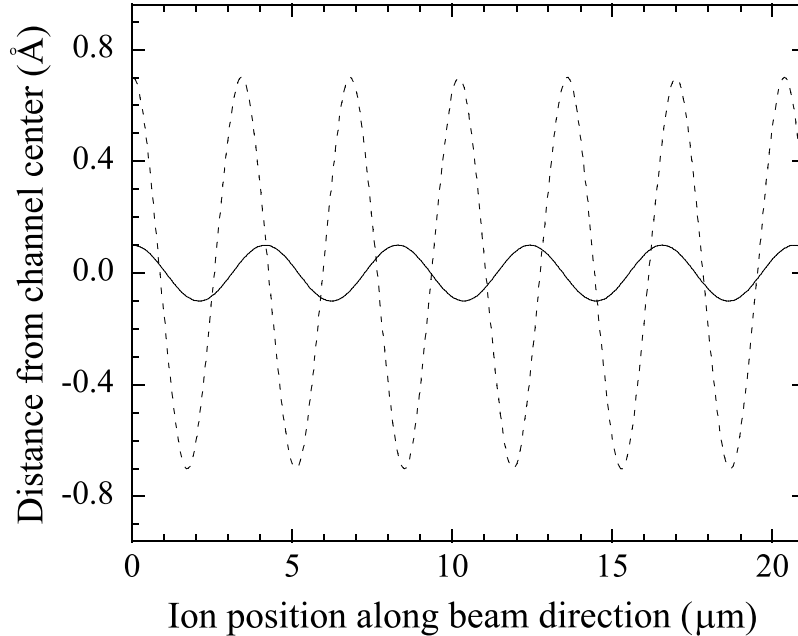


Figure 1.4: Trajectories of 390 MeV/u  $\text{Ar}^{18+}$  ions channeled in the (220) plane. The ions are incident in the direction parallel to the (220) plane. solid line: amplitude=0.1 Å, dashed line: amplitude=0.7 Å

For example, in the case of 390 MeV/u  $\text{Ar}^{18+}$  ions channeled in a Si crystal,  $\Psi_a$  for the  $\langle 110 \rangle$  axis and  $\Psi_p$  for the (220) plane are estimated to be 0.38 mrad and 0.15 mrad, respectively.

We simulated the motion of 390 MeV/u  $\text{Ar}^{18+}$  ions channeled in the (220) plane of a 21  $\mu\text{m}$  Si crystal. Figure 1.4 shows the calculated trajectories of the planar channeled ions. The ions are incident in the direction parallel to the (220) plane. The solid and dashed lines show the trajectories with the oscillation amplitudes of 0.1 and 0.7 Å, respectively. As shown in Fig. 1.4, the path length per oscillation depends on the oscillation amplitude.

## 1.2 Resonant coherent excitation (RCE)

### 1.2.1 RCE condition

Ions channeled along a crystal axis feel a periodic potential of the crystal, as shown in Fig. 1.5. The frequency  $\nu$  which the ions feel is given by

$$\nu = \frac{v}{d}, \quad (1.16)$$

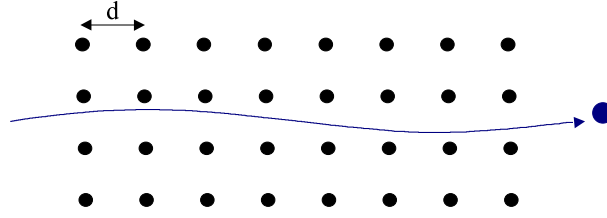


Figure 1.5: Schematic drawing of the axial channeling.

where  $v$  is the ion velocity and  $d$  is the distance between the atoms. If the following condition is fulfilled,

$$E_{trans} = h\nu = h\frac{v}{d}, \quad (1.17)$$

where  $E_{trans}$  is the transition energy of the ion, the ion will be excited. This phenomenon is called resonant coherent excitation (RCE). Taking into account the higher order Fourier potentials, the resonance condition is modified to

$$E_{trans} = h\nu = h\frac{kv}{d}, \quad (1.18)$$

where  $k$  is an integer. In the relativistic energy region, the resonance condition is written as

$$E_{trans} = h\nu = h\frac{kv}{(d/\gamma)} = h\frac{\gamma kv}{d}, \quad (1.19)$$

which is due to the Lorentz contraction of the distance between the atoms.

Figure 1.6 shows the arrangement of the atoms on the (220) plane of a Si crystal. This can be regarded as a two-dimensional (2D) crystal. In this case, the 2D base vectors are  $\mathbf{A} = [110]a/2$  and  $\mathbf{B} = [001]a$ , where  $a$  is the lattice constant of Si. For the (220) planar channeling, the RCE condition is given by

$$E_{trans} = \frac{h\gamma v}{a}(\sqrt{2}k \cos \theta + l \sin \theta), \quad (1.20)$$

where  $(k, l)$  are the Miller indices to identify atomic strings parallel to  $\mathbf{A}/k - \mathbf{B}/l$  (see Appendix A).

### 1.2.2 Methods to observe RCE

The schematic drawing of the atomic processes of the projectile ion inside a Si crystal is shown in Fig. 1.7. When the RCE occurs, the ionization process is enhanced, because the ionization cross section for the excited state is larger than for the ground state. Moreover, the intensity of the deexcitation X-rays from the projectile ions is expected to increase due to the increase of the population of the excited states. Accordingly, RCE can be observed through measurements of the charge state of the projectile ion transmitted through the crystal and the projectile deexcitation X-rays.

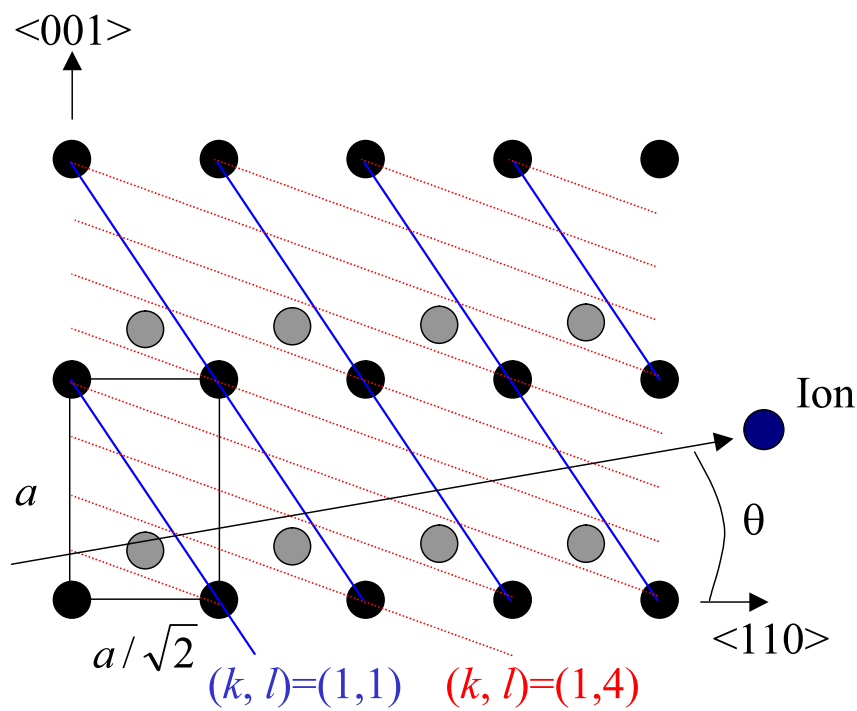


Figure 1.6: Arrangement of the atoms on the (220) plane.

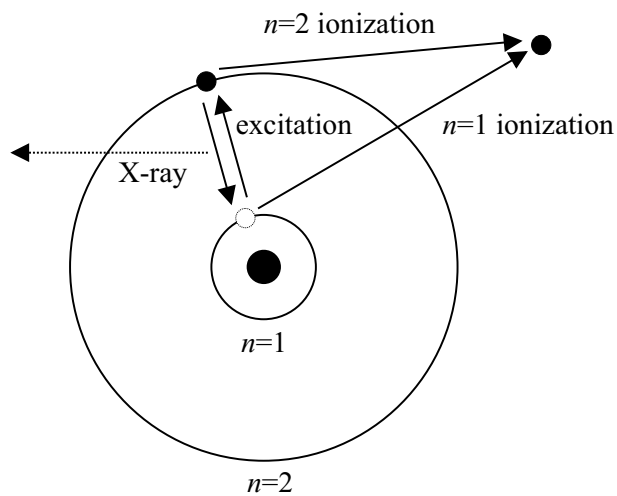


Figure 1.7: Schematic drawing of the atomic processes of the projectile ion inside a Si crystal.

Table 1.1: Ions that have ever been used in the RCE experiments.

Ion	Crystal	Order	Ref.
$C^{5+}, N^{6+}, O^{7+}, F^{8+}$	Au $\langle 100 \rangle, \langle 110 \rangle, \langle 111 \rangle$	$k=2,3,4,5,6$	[3, 13, 14]
$C^{5+}, O^{7+}, F^{8+}$	Au $\langle 100 \rangle$	$k=1,2$	[15]
Ne $^{9+}$	Au $\langle 111 \rangle$	$k=6$	[4]
F $^{8+}$	Au $\langle 110 \rangle$	$k=3$	[16]
C $^{5+}$	Au $\langle 100 \rangle$	$k=2$	[5]
Mg $^{11+}$	Au $\langle 100 \rangle$	$k=4$	[17]
$C^{5+}, N^{6+}$	Si $\langle 111 \rangle$	$k=4,5,7,8$	[18]
N $^{6+}, Mg^{11+}$	Au(100), Ni(100)	$(k, l) = (2, 0)$	[19]
Si $^{13+}$	Si $\langle 111 \rangle$	$k=7,8$	[20, 21]
B $^{4+}$	SnTe(100)	$k = 2$	[6, 22]
H	LiF(100)	$(k, l) = (1, 1)$	[7, 23, 24]
N $^{6+}$	Pt(110)	$k=2$	[25]

### 1.2.3 Historical background

In 1965, Okorokov predicted that the channeled ions will be excited when the frequency  $\nu$  which the ions feel coincides with  $E_{trans}/h$  [2].

In 1978, Datz *et al.* observed the RCE for the first time by observing the charge states of the ions transmitted through crystals [3].

In 1988, Fujimoto *et al.* confirmed the RCE by observing the deexcitation X-rays from the ions. [4].

In 1991, Kimura *et al.* measured convoy electrons emitted from the resonant coherently excited ions [5].

In 1996, the RCE of the surface channeled ions were observed [6, 7].

The ions that have ever been used in the RCE experiments are summarized in table 1.1.

Theoretical investigations on RCE have also been performed extensively [8, 9, 10]. By solving the time-dependent Schrödinger equation, the RCE process is discussed [11, 12].

Recently, we observed the RCE of 390 MeV/u Ar $^{17+}$  ions channeled in the (220) plane of a Si crystal. We observed the RCE from  $1s$  to  $n = 2$  states. In the relativistic energy region, RCE has been observed for the first time. To fulfill the resonance condition, we tilted the crystal under the (220) planar channeling condition. This corresponds to scanning of the frequency  $\nu$  which the ions feel in the crystal. In this measurement, we adopted a Si detector of 94.7  $\mu\text{m}$  in thickness as a target crystal in order to measure the energy deposition (loss) of the channeled ion. The energy deposition is related to the oscillation amplitude of the channeled ion [26, 27], so that the information on the impact parameter dependence of the RCE can be obtained. We measured the charge state distribution of the ions transmitted through the crystal in coincidence with the energy depositions of the ions channeled in the Si crystal. Since the ionization cross section of

$n = 2$  states is larger than that of  $1s$  state inside the crystal, the fraction of the ionized ions ( $\text{Ar}^{18+}$  ions) is expected to increase when the RCE from  $1s$  to  $n = 2$  states occurs. The fraction of  $\text{Ar}^{17+}$  ions transmitted through the Si crystal is shown in Fig. 1.8. The resonance in the higher energy side was assigned to the transition  $1s \rightarrow n = 2(j = 3/2)$ , and one in the lower energy side was assigned to the transition  $1s \rightarrow n = 2(j = 1/2)$ . Due to the Stark effect originating from the crystal potential, the  $j = 3/2$  and  $j = 1/2$  peaks were skewed toward higher and lower energies, respectively. In addition, the  $j = 1/2$  peak was split into two peaks. Figure 1.9 shows the ionized fraction via the RCE process as a function of tilt angle and energy deposition together with the sliced sections. The tilt angle and the energy deposition correspond to the transition energy and the oscillation amplitude of the channeled ions, respectively. The transition energies of  $1s \rightarrow n = 2$  states were found to vary depending on the impact parameter. This reflects the Stark effect originating from the electric field of the Si crystal. The probability of the RCE was large near the atomic plane.

Figure 1.10 shows the calculated transition energies as a function of distance from the channel center, where we assume that the RCE occurs at the maximum distance from the channel center. The calculation method for the transition energies will be discussed later (section 1.2.4). The profile of the ionized fraction shown in Fig. 1.9 is in good agreement with the calculated transition energies.

Figure 1.11 shows the resonance peak for  $2p_{3/2}$ , which is a sliced section of the ionized fraction with the energy deposition from 8.25 MeV to 8.85 MeV in Fig. 1.9. The solid line shows the gaussian fitting of the resonance peak. The ions forming this peak are considered to pass through the channel center, where the contribution of the Stark effect is small. As shown in Fig. 1.11, the relative energy width  $\Delta E_{trans}/E_{trans}$  (full width at half maximum) was  $6 \times 10^{-4}$ . The resonance peak observed in the present experiment was narrow compared to those observed by other groups. As an example, the resonance profile observed by Datz *et al.* in the case of  $\text{Mg}^{11+}$  ions planar channeled in Ni is shown in Fig. 1.12 [19]. The energy width  $\Delta E_{trans}/E_{trans}$  was  $2 \times 10^{-2}$ , which is about two orders of magnitude broader than that observed in the present work. This difference of the energy widths is due to the difference of the coherence. We used the high energy projectile ions, so that the cross section for the incoherent electron impact was small, which leads to the sharp resonance.

The narrow peak enables us to determine the peak position precisely, *i.e.*, perform a high precision spectroscopy. The peak position (angle) was determined with a precision of  $\sim 0.001^\circ$ , which corresponds to the transition energy precision of  $\sim 10$  ppm. As can be seen in equation 1.20, the frequency  $\nu$  which the ion feels also depends on the velocity of the ion. If we can determine the precise value of the beam velocity, the peak position can be determined with an accuracy of 0.04 eV (transition energy = 3323 eV). This means that the Lamb shift for  $1s$  electron in  $\text{Ar}^{17+}$  ions is determined with a precision of 3.5% (the value of its Lamb shift is 1.14 eV). This precision is comparable to the most precise value (1.5%) that has ever been obtained for  $\text{Ar}^{17+}$  ions [30]. However, due to the inaccuracy of the absolute value of the beam velocity, we have not obtained the  $1s$  Lamb shift with a high precision. A method to measure the beam velocity with a high precision is needed.

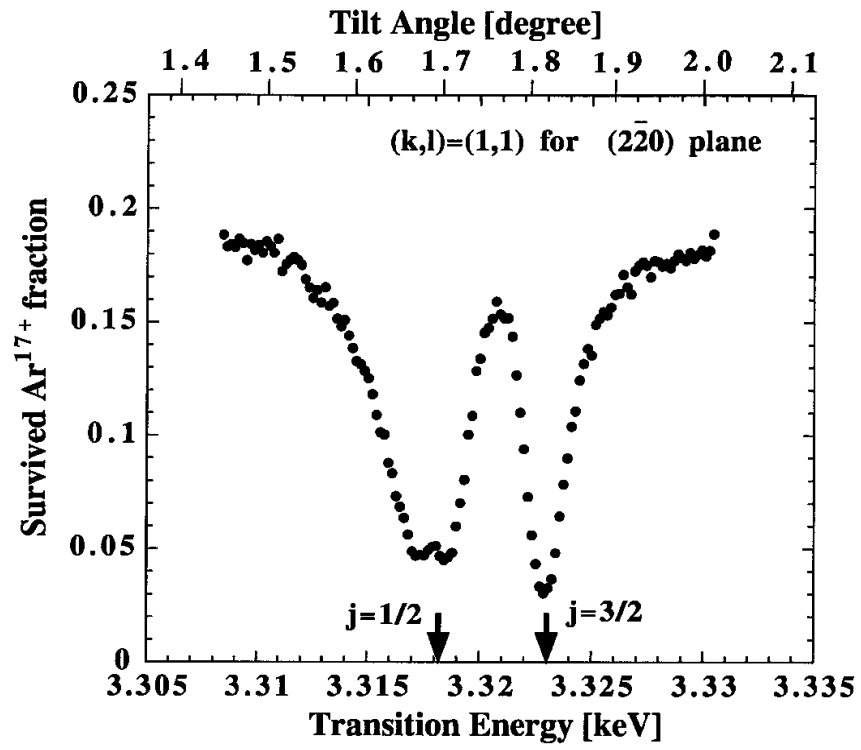


Figure 1.8: Fraction of Ar<sup>17+</sup> ions transmitted through the Si crystal for 390 MeV/u Ar<sup>17+</sup> incidence [28].

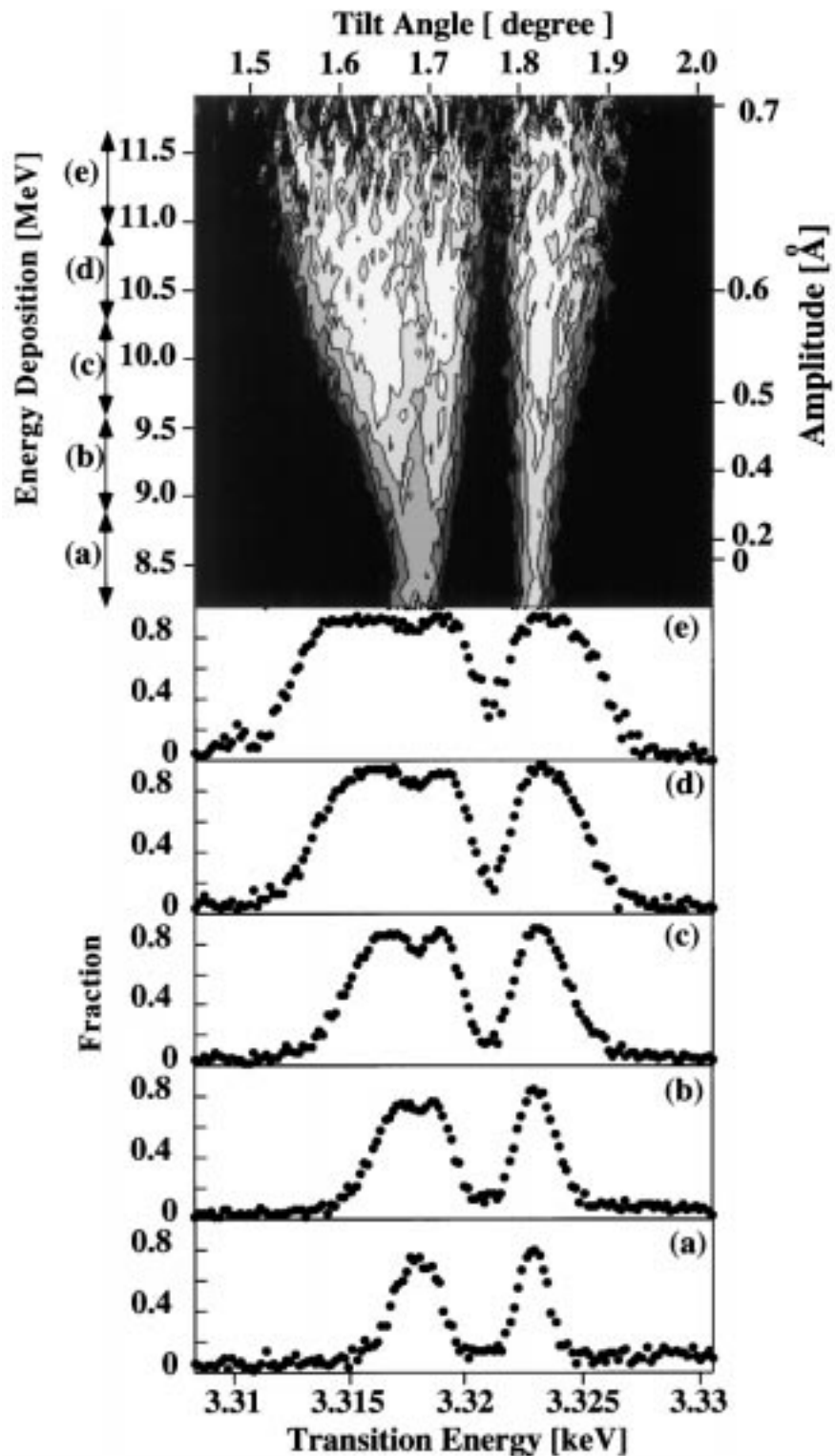


Figure 1.9: Ionized fraction via the RCE process as a function of the tilt angle and the energy deposition [28]. The sliced sections at the region of (a)  $\Delta E = 8.21 - 8.78$  MeV, (b)  $8.78 - 9.36$  MeV, (c)  $9.36 - 9.93$  MeV, (d)  $9.93 - 10.51$  MeV, and (e)  $10.51 - 11.09$  MeV are also shown.

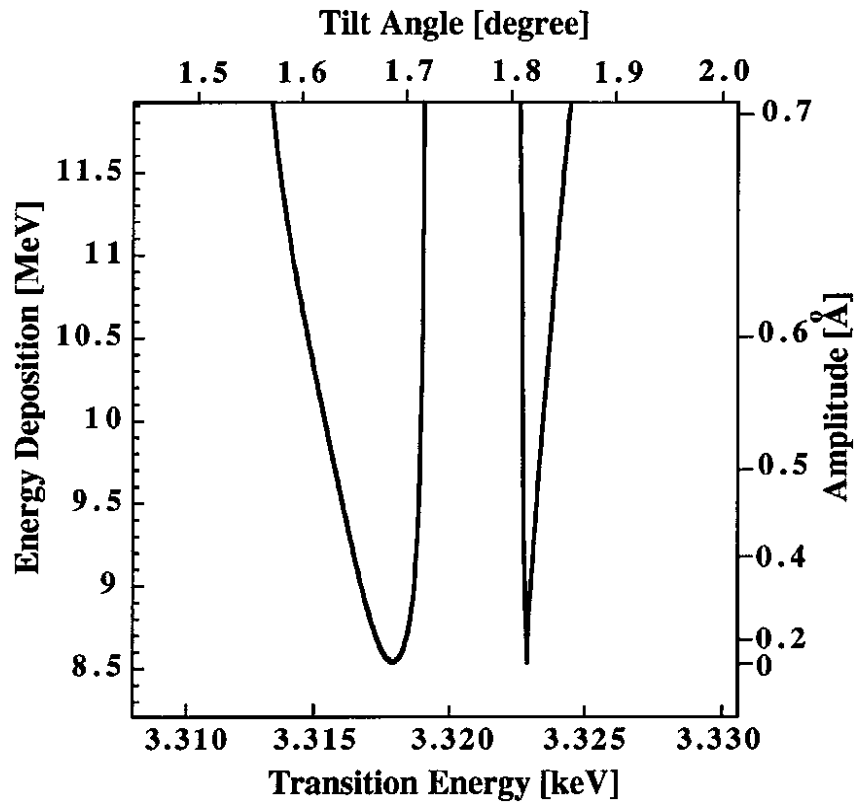


Figure 1.10: Calculated transition energies as a function of distance from channel center [28]. Same as 1.13 except for the scale.

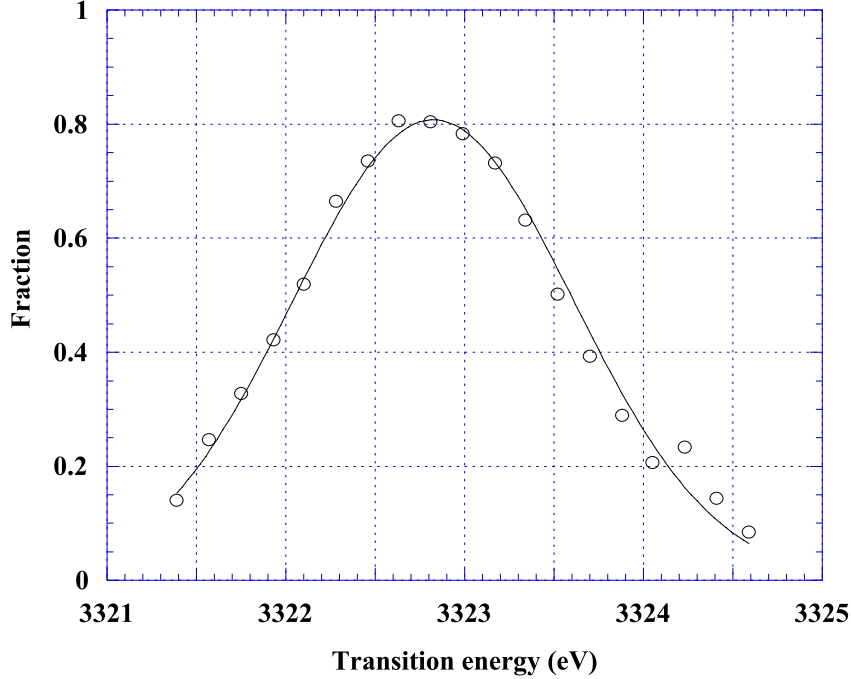


Figure 1.11: Ionized fraction via the RCE process for the  $j = 3/2$  peak (energy deposition = 8.25-8.85 MeV) [29]. The solid line shows the gaussian fitting of the experimental data.

#### 1.2.4 Energy levels and wave functions

Ions channeled in crystals feel a static crystal potential and a wake potential. These lead to the energy shift of the electron bound to the channeled ion due to the Stark effect. The static crystal potential is identical to the planar potential. The energy levels and wave functions of the electrons can be calculated by using the perturbation theory. For  $n = 2$  states in hydrogen-like ions, the energy levels and wave functions are obtained by solving the following secular equation [31] (see Appendix A),

$$\det \langle 2LJ\mu | H_0(\mathbf{r}) + H_1(\mathbf{r}) + H_2(x) - E | 2L'J'\mu' \rangle = 0, \quad (1.21)$$

$$H_0(r) = -c\boldsymbol{\alpha} \cdot \mathbf{p} - \beta mc^2 - \frac{Z_1 e^2}{r}, \quad (1.22)$$

$$H_1(\mathbf{r}) = -e\phi_w(\mathbf{r}), \quad (1.23)$$

$$\begin{aligned} H_2(x) &\simeq -e\gamma\phi_{00}(X+x) \\ &= -e\gamma \frac{U_p(X+x)}{Z_p e}, \end{aligned} \quad (1.24)$$

where  $|2LJ\mu\rangle$  denotes the  $n = 2$  states with the orbital angular momentum  $L$ , total angular momentum  $J$ , its projection  $\mu$  to the quantum axis, and  $X$  is the position of the nucleus of the projectile ion. In this calculation, the mixing between the different  $n$  states

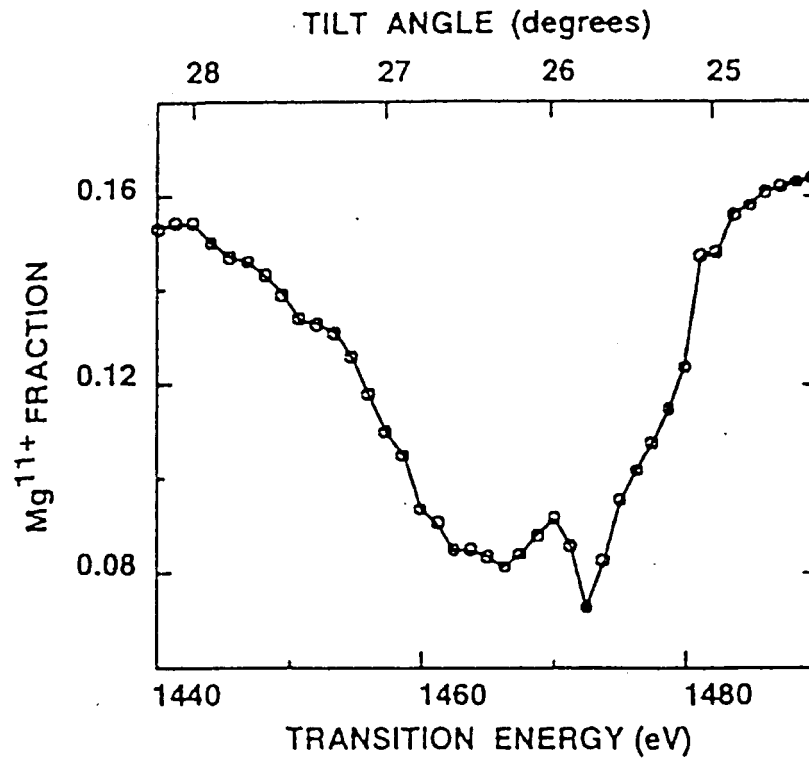


Figure 1.12: Fraction of transmitted  $\text{Mg}^{11+}$  ions as a function of tilt angle (transition energy) for (100) planar channeling in Ni [19]. The projectile energy was 25 MeV/u.

is neglected. The Hamiltonian  $H_0(\mathbf{r})$  is the non-perturbative one for the hydrogen-like ions. On the other hand,  $H_1(\mathbf{r})$  and  $H_2(x)$  are the perturbation potentials, which are due to the wake potential  $\phi_w(\mathbf{r})$  and the static crystal potential  $\phi_{00}(x)$ , respectively. Here,  $x$  axis is perpendicular to the channel plane, and the  $z$  axis is parallel to the beam direction. Although the wake potential  $H_1(\mathbf{r})$  is small compared to the crystal potential  $H_2(x)$  in the high energy region, we took into account the wake potential. The energy of the  $1s$  electron is also shifted due to the Stark effect. The  $1s$  electron energy is given by

$$E_0 = E(1s) + \langle 1s(1/2)\mu | H_1(\mathbf{r}) + H_2(x) | 1s(1/2)\mu \rangle, \quad (1.25)$$

where  $E(1s)$  is the unperturbed energy of the  $1s$  state. The details of the calculation method are described in Appendix A. Figure 1.13 and 1.14 show the calculated transition energies of  $1s \rightarrow n = 2$  and compositions of the wave functions of the  $n = 2$  states as a function of distance from the channel center in the case of 390 MeV/u Ar<sup>17+</sup> ions channeled in the (220) plane of a Si crystal. The  $n = 2$  states are split into four levels due to the  $l \cdot s$  interaction and the Stark effect. As shown in Fig. 1.13 and 1.14, the transition energy and the composition of the wave function vary depending on the distance from the channel center. The transition matrix element of  $1s \rightarrow n = 2$  can also be calculated from the obtained wave functions. Figure 1.15 shows the squared transition matrix elements for Ar<sup>17+</sup> ions ( $(k, l) = (1, 1)$ ).

In the case of 460 MeV/u Fe<sup>25+</sup> ions, the calculated transition energies, compositions of the wave functions, and squared transition matrix elements for  $(k, l) = (2, 1)$  are shown in Fig. 1.16, 1.17, and 1.18. The energy shift due to the Stark effect is small compared to the case of Ar<sup>17+</sup> ions, as shown in Fig. 1.16. This is because the electron orbital radius of Fe<sup>25+</sup> ion is smaller than that of Ar<sup>17+</sup> ion, and the energy difference between  $j = 3/2$  and  $j = 1/2$  for Fe<sup>25+</sup> ions is larger than for Ar<sup>17+</sup> ions. The electron orbital radius scales as

$$\langle r \rangle = \frac{a_B}{Z} n^2, \quad (1.26)$$

where  $a_B$  is the Bohr radius,  $n$  is the principal quantum number, and  $Z$  is the nuclear charge of the ion. The energy difference between the state with  $n, l$ , and  $j = l + 1/2$  and one with  $n, l$ , and  $j = l - 1/2$  is given by

$$\delta E = \frac{1}{l(l+1)} \frac{\alpha^2 Z^4}{n^3} Ry, \quad (1.27)$$

where  $l$  is the orbital angular momentum,  $\alpha$  is the fine structure constant, and  $Ry$  is the Rydberg energy (13.6056981 eV).

We also calculated the absolute values of the transition matrix elements for  $1s \rightarrow 2s, 2p_x, 2p_y$ , and  $2p_z$ , which are shown in Fig. 1.19(1.20) and 1.21(1.22) for Ar ( $(k, l) = (1, 1)$ ) and Fe ( $(k, l) = (2, 1)$ ) ions, respectively. In the case of  $(k, l) = (1, 1)$ , the absolute value of the transition matrix element for  $2p_x$  is 0 at the channel center. In the case of  $(k, l) = (2, 1)$ , on the other hand, the absolute values of the transition matrix elements for  $2p_y$  and  $2p_z$  are 0. This difference is understood by the arrangement of the atomic strings inducing the RCE. Figure 1.23 and 1.24 show the sliced sections ( $x - z$  plane) of the

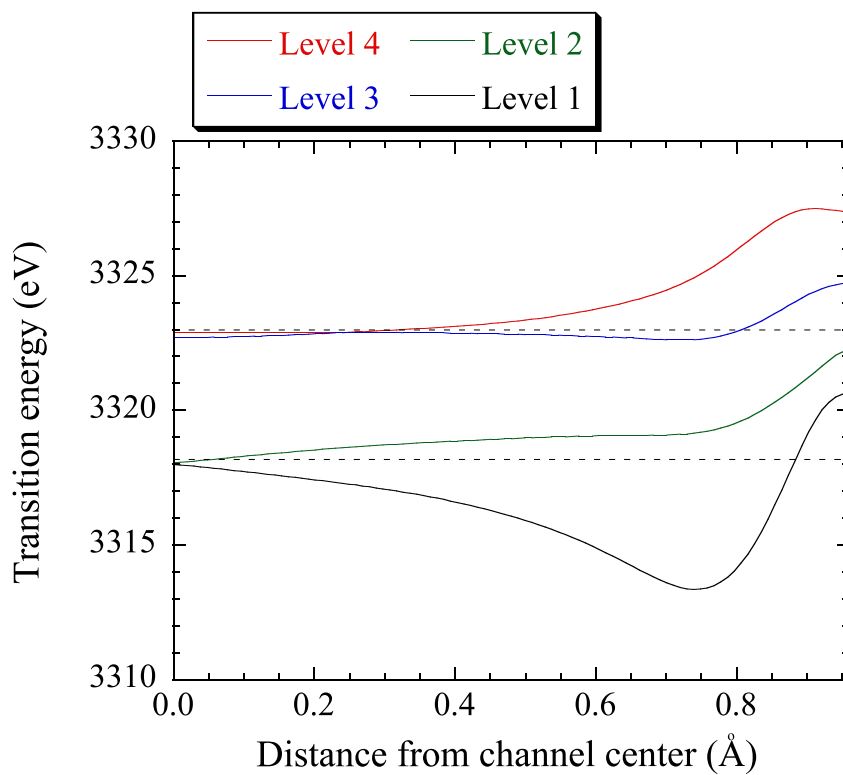


Figure 1.13: Transition energies of  $1s \rightarrow n = 2$  in  $\text{Ar}^{17+}$  ions. The dashed lines show the transition energies in vacuum for  $j = 3/2$  and  $j = 1/2$ .

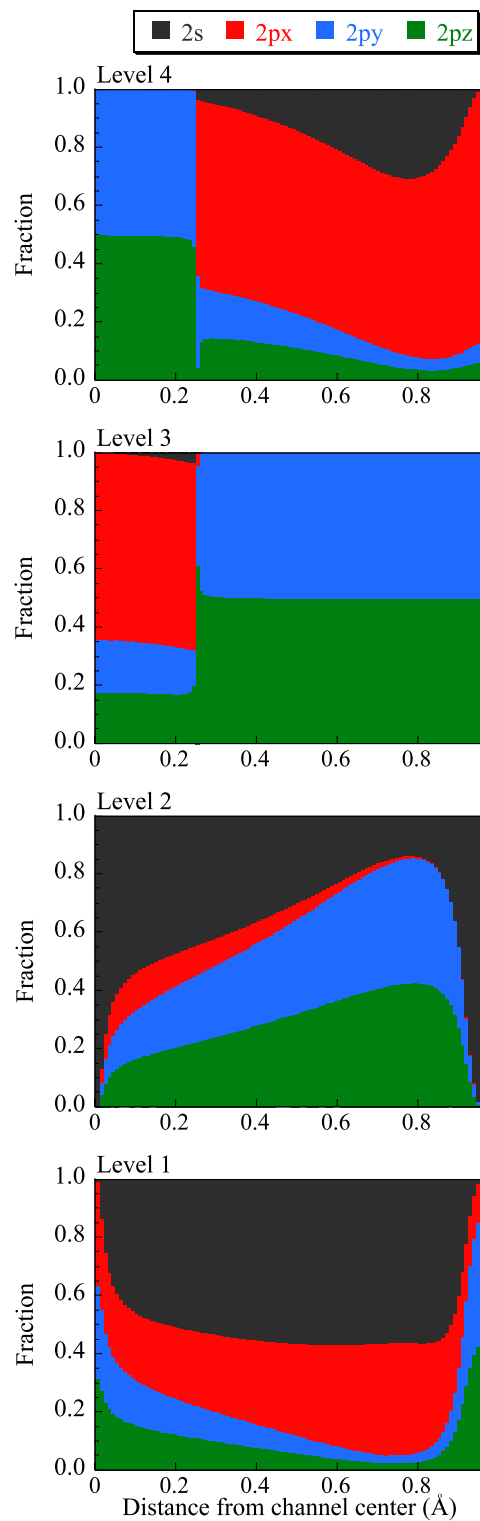


Figure 1.14: Compositions of the wave functions of the  $n = 2$  states in  $\text{Ar}^{17+}$  ions as a function of distance from the channel center, which reflects the electric field of the crystal.

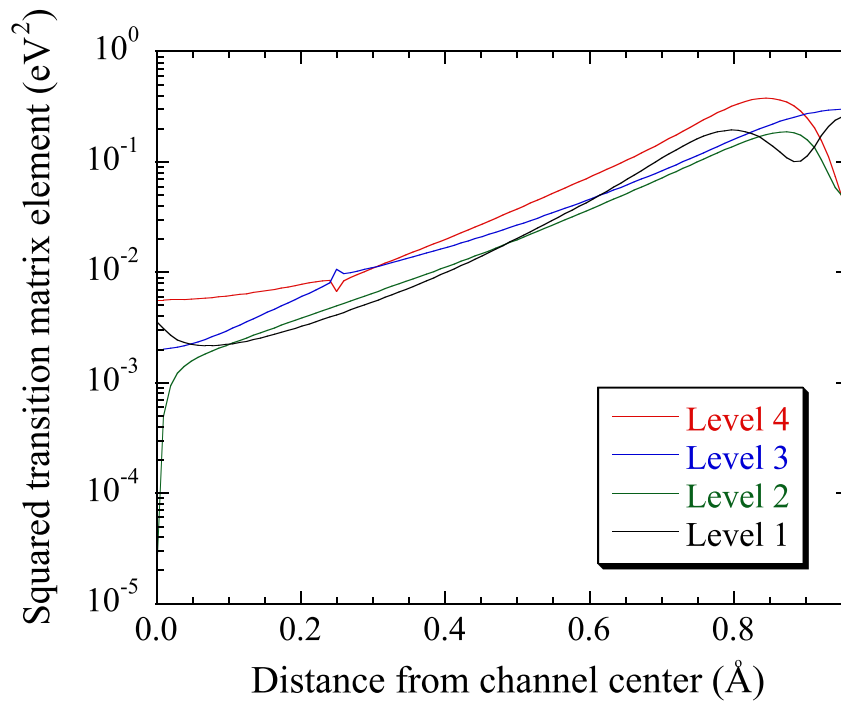


Figure 1.15: Squared transition matrix elements of  $1s \rightarrow n = 2$  in  $\text{Ar}^{17+}$  ions.  $(k, l) = (1, 1)$ .

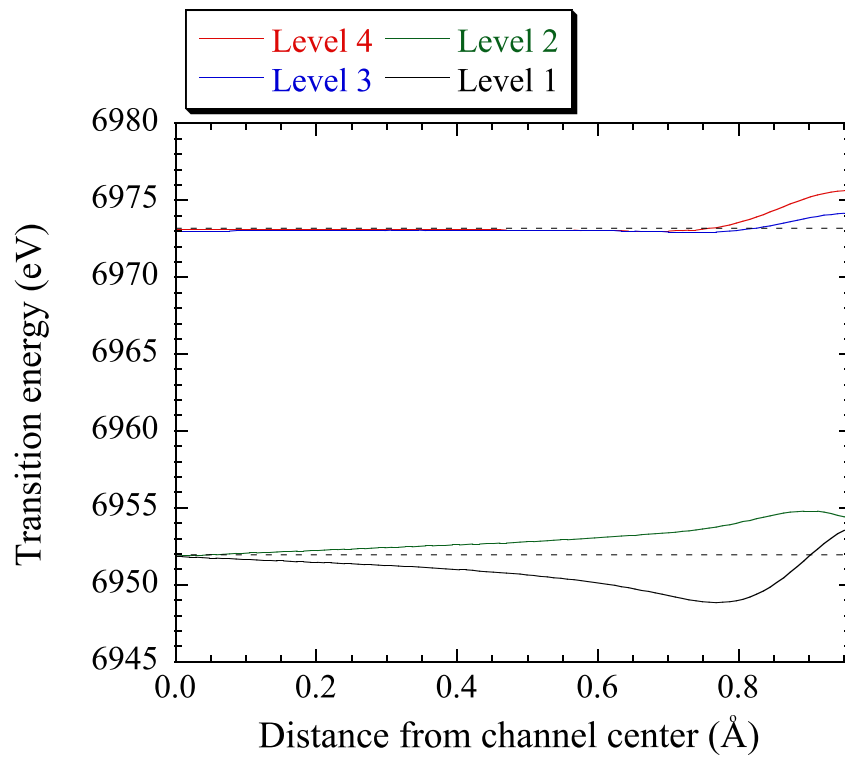


Figure 1.16: Transition energies of  $1s \rightarrow n = 2$  in  $\text{Fe}^{25+}$  ions. The dashed lines show the transition energies in vacuum for  $2p_{3/2}$  and  $2p_{1/2}$ .

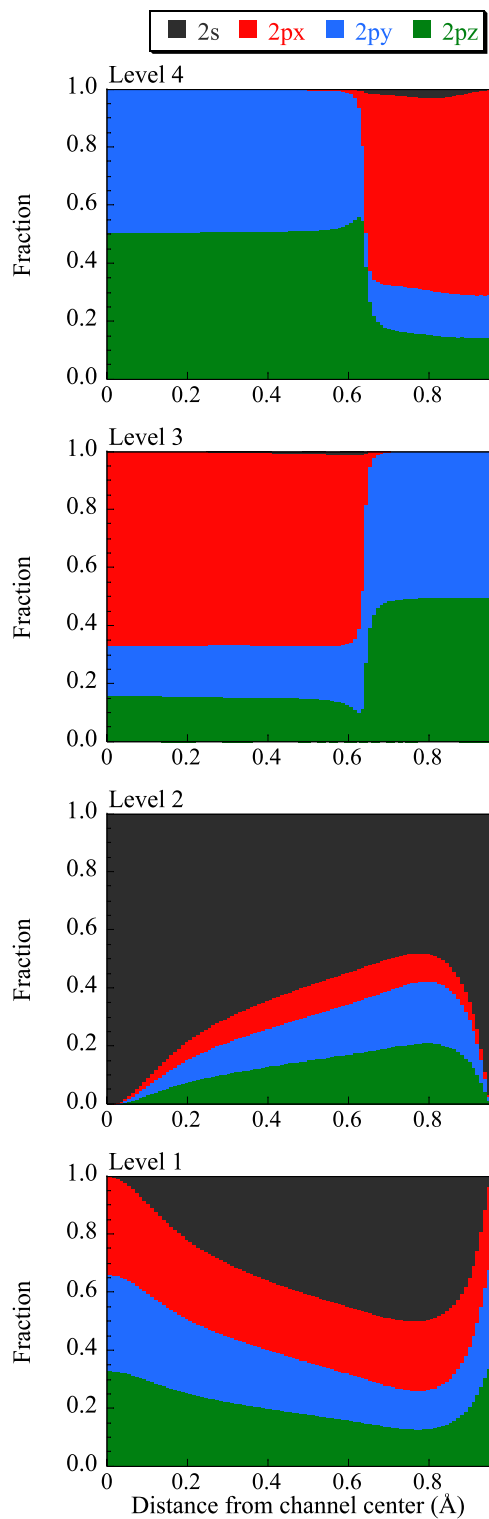


Figure 1.17: Compositions of the wave functions of the  $n = 2$  states in  $\text{Fe}^{25+}$  ions as a function of distance from the channel center, which reflects the electric field of the crystal.

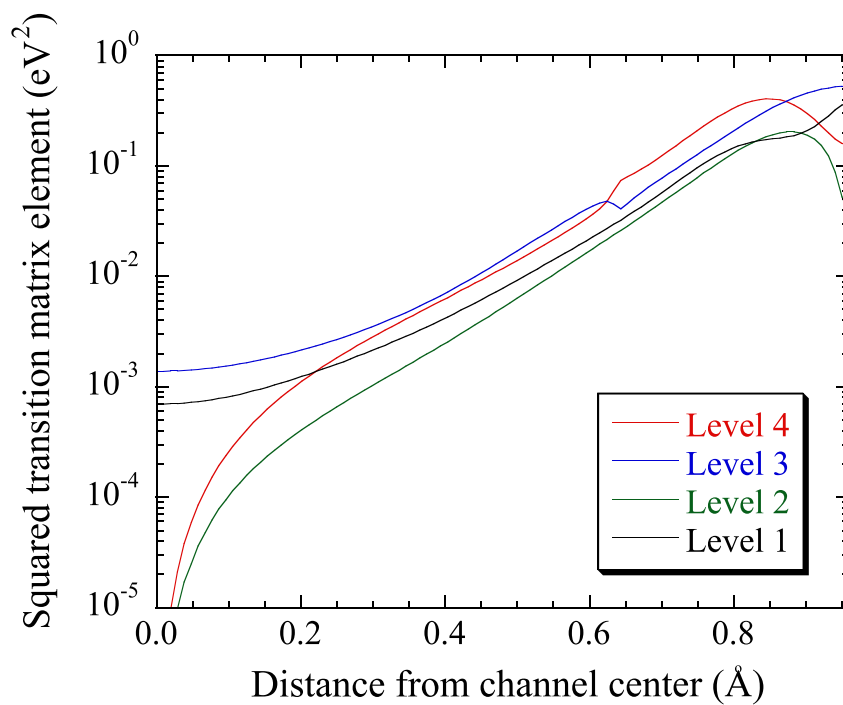


Figure 1.18: Squared transition matrix elements of  $1s \rightarrow n = 2$  in  $\text{Fe}^{25+}$  ions.  $(k, l) = (2, 1)$ .

strings of  $(k, l) = (1, 1)$  and  $(2, 1)$ , respectively. For  $(k, l) = (1, 1)$ , the strings on the (220) atomic planes are symmetric with respect to the channel center, so that the excitation to  $2p_x$  does not occur at the channel center. For  $(k, l) = (2, 1)$ , due to the destructive interference between the perturbations of the upper and lower strings, the excitations to  $2p_y$  and  $2p_z$  do not occur. In the case of the (220) plane of a face-centered cubic, when  $k+l$ =even number, the excitation to  $2p_x$  does not take place at the channel center. When  $k+l$ =odd number, on the other hand, the excitations to  $2p_y$  and  $2p_z$  do not take place.

As will be discussed in Appendix B, the transition matrix element is related to the Fourier potential of the crystal. Figure 1.25(1.26) and 1.27(1.28) show the calculated absolute values of the Fourier potentials for  $k = 1$  and  $2$ , respectively. The absolute values of the Fourier potentials tend to decrease with increasing  $k$  and  $l$ .

### 1.2.5 Excitation process

As shown in Appendix A, the time evolution of the wave function  $\Psi(\mathbf{r}, t)$  is written as

$$i\hbar \frac{\partial \Psi(\mathbf{r}, t)}{\partial t} = [H_{st}(\mathbf{r}) + H_3(\mathbf{r}, t)]\Psi(\mathbf{r}, t), \quad (1.28)$$

where  $H_{st} = H_0 + H_1 + H_2$  and  $H_3$  is the time-dependent potential. The wave function  $\Psi(\mathbf{r}, t)$  is expanded as

$$\Psi(\mathbf{r}, t) = \sum_j C_j(t) \Psi_j(\mathbf{r}) \exp\left(\frac{-iE_j t}{\hbar}\right). \quad (1.29)$$

Here, we consider the transition from  $1s$  to the  $n=2$  state. We define the wave functions of the  $1s$  and  $n = 2$  states as  $\Psi_0(\mathbf{r})$  and  $\Psi_j(\mathbf{r})$  ( $1 \leq j \leq 4$ ), respectively. Substituting  $\Psi(\mathbf{r}, t)$  into equation 1.28, we obtain

$$\begin{aligned} i\hbar \frac{dC_j(t)}{dt} &= \langle j | H_3(\mathbf{r}, t) | 0 \rangle C_0(t) \exp\left[\frac{i(E_j - E_0)t}{\hbar}\right] \\ &= M_{j0}(X) C_0(t) \exp(i\Delta_{j0}t), \end{aligned} \quad (1.30)$$

where  $M_{j0}(X)$  is the transition matrix element (see Appendix A) and  $\Delta_{j0} = (E_j - E_0)/\hbar - 2\pi\nu$ . In this case, the population of the excited state oscillates with the angular frequency  $\Omega$ , which is given by

$$\Omega = \sqrt{\Delta_{j0}^2 + \frac{4|M_{j0}(X)|^2}{\hbar^2}}. \quad (1.31)$$

This phenomenon is known as Rabi oscillation. Figure 1.29 shows the schematic diagram of the atomic processes of the projectile ion. In the above calculation, the ionization and radiative deexcitation processes are neglected. The inverse process of the RCE is called resonant coherent deexcitation (RCD).

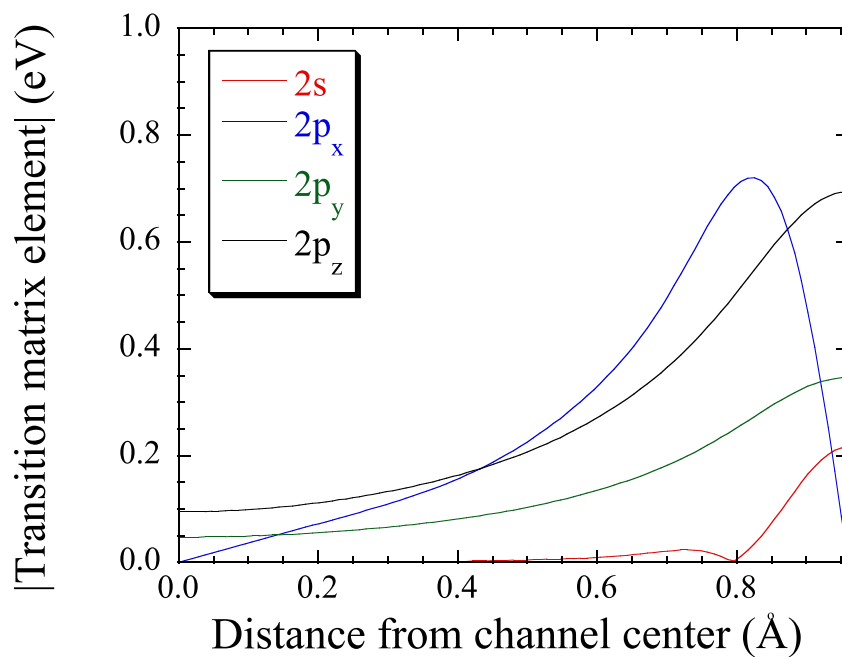


Figure 1.19: Absolute values of the transition matrix elements for Ar ions.  $(k, l) = (1, 1)$ .

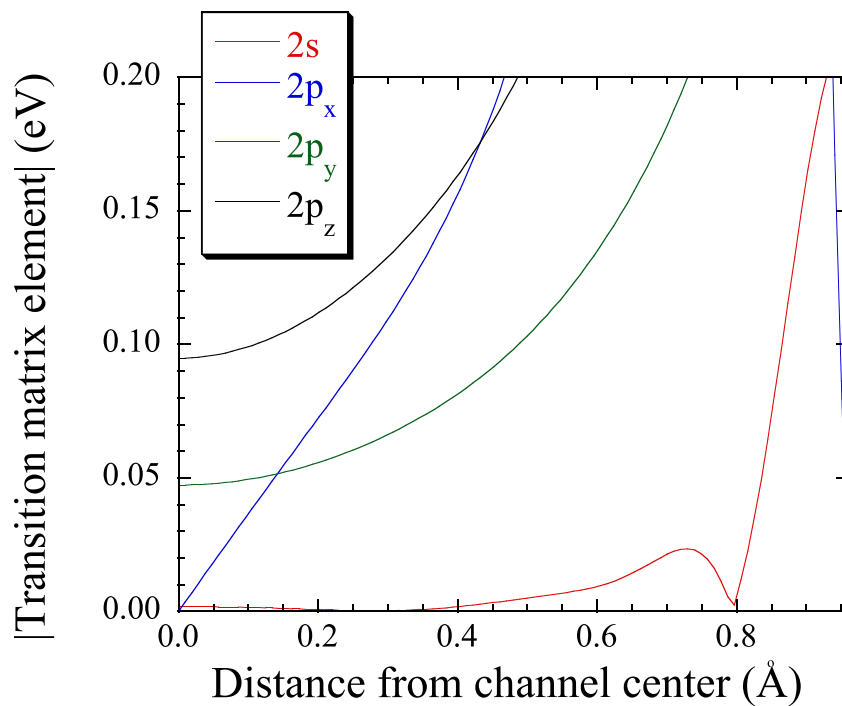


Figure 1.20: Same as Fig. 1.19 except for the vertical scale.

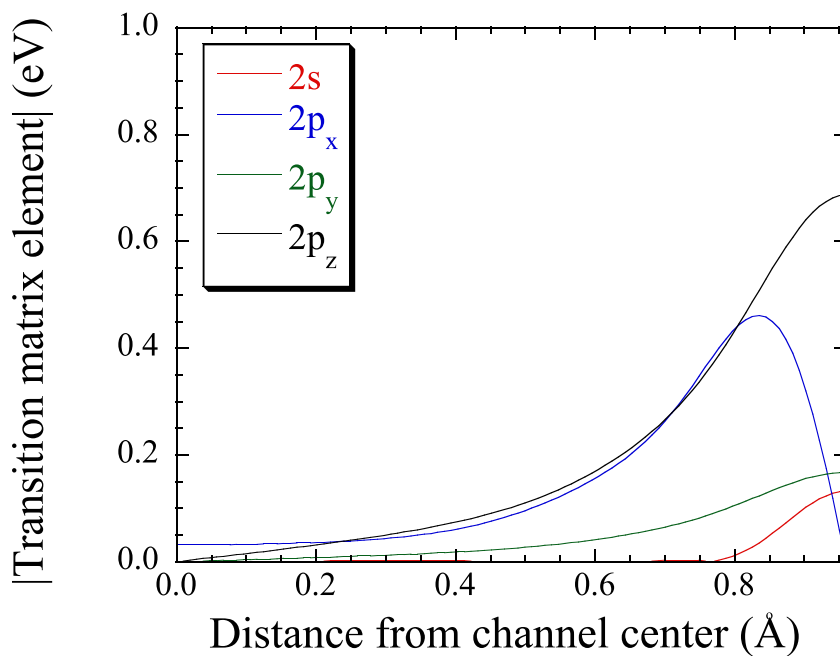


Figure 1.21: Absolute values of the transition matrix elements for Fe ions.  $(k, l) = (2, 1)$ .

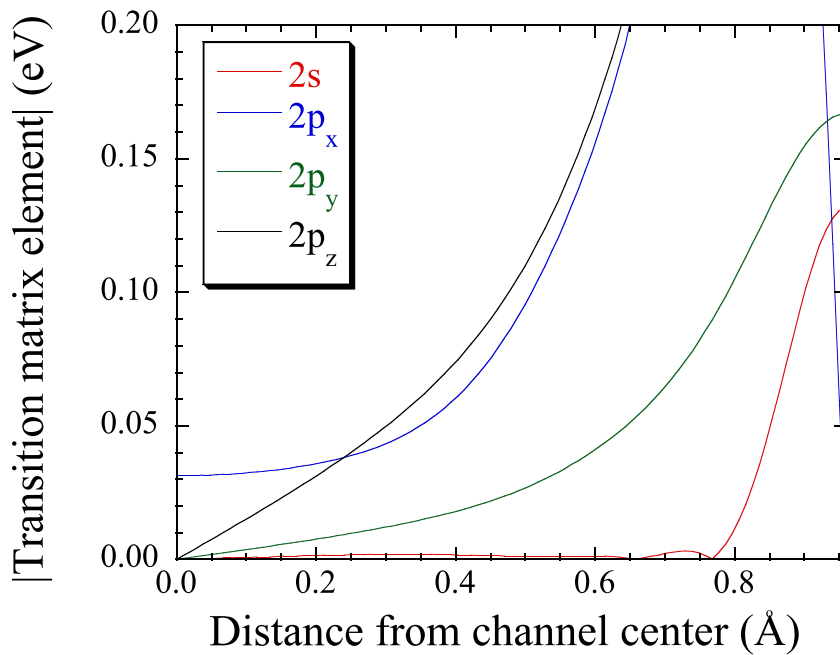
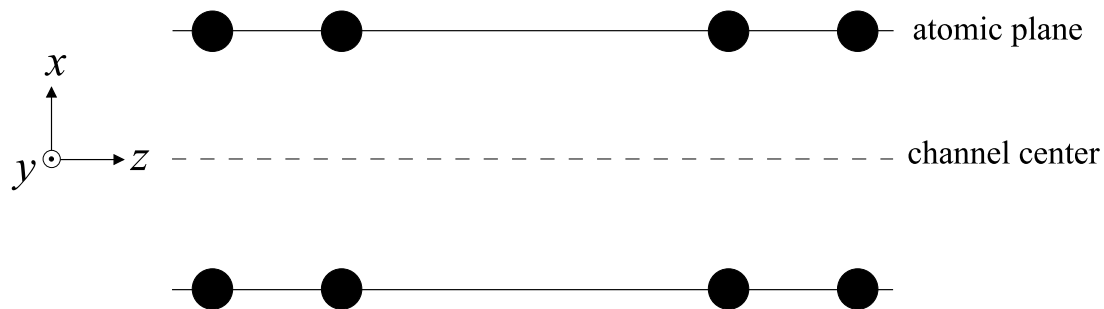
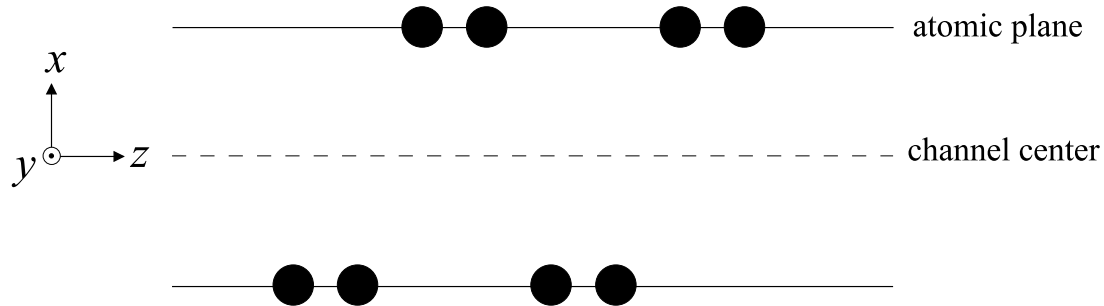


Figure 1.22: Same as Fig. 1.21 except for the vertical scale.

Figure 1.23: Schematic drawing of the strings of  $(k, l) = (1, 1)$ .Figure 1.24: Schematic drawing of the strings of  $(k, l) = (2, 1)$ .

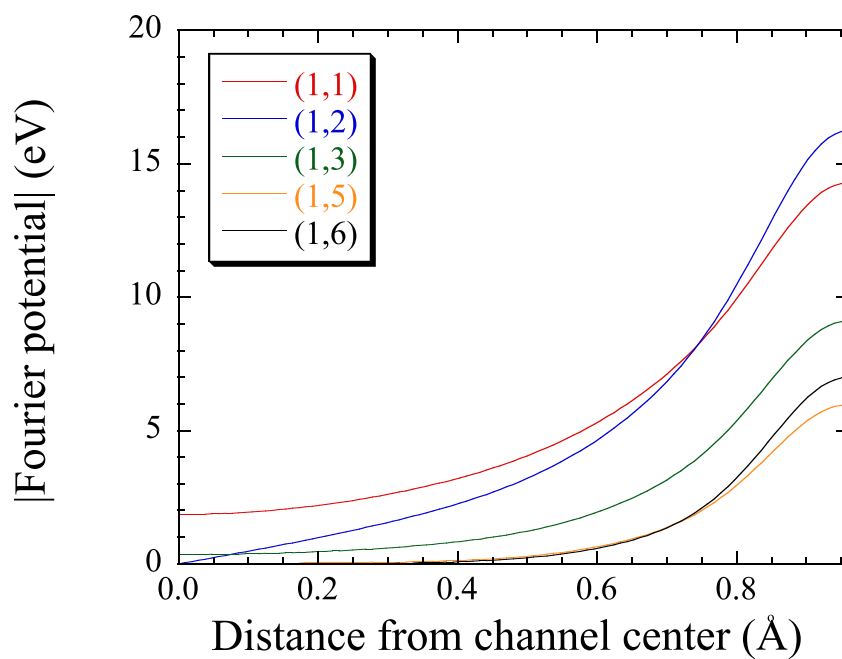


Figure 1.25: Absolute values of the Fourier potentials for  $(k, l) = (1, 1), (1, 2), (1, 3), (1, 5)$  and  $(1, 6)$ .

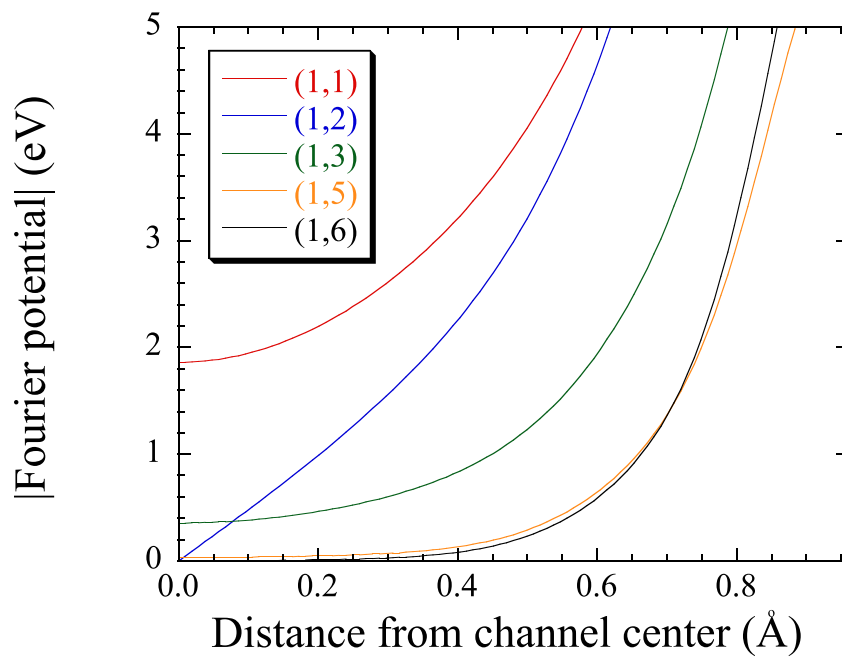


Figure 1.26: Same as Fig. 1.25 except for the vertical scale.

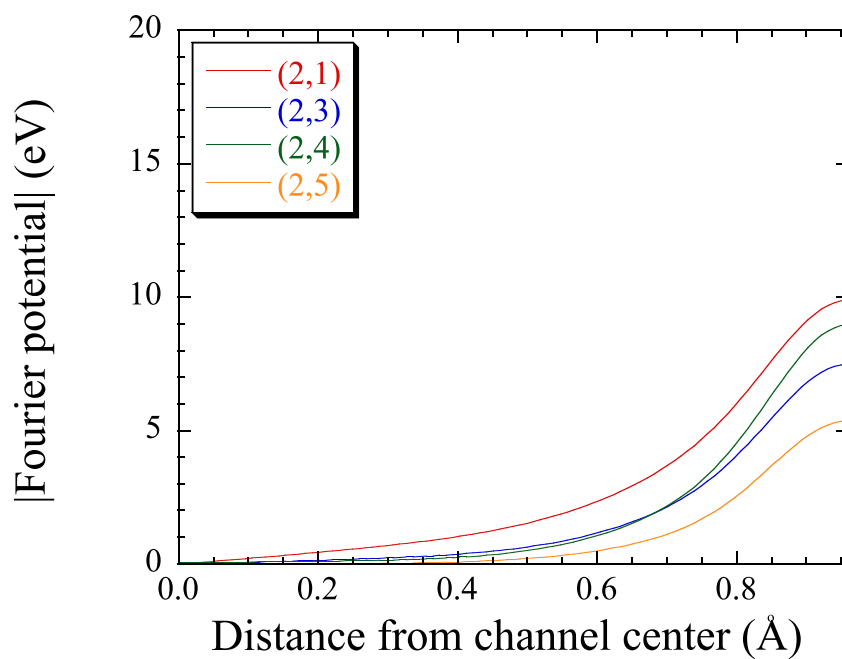


Figure 1.27: Absolute values of the Fourier potentials for  $(k, l) = (2, 1), (2, 3), (2, 4)$  and  $(2, 5)$ .

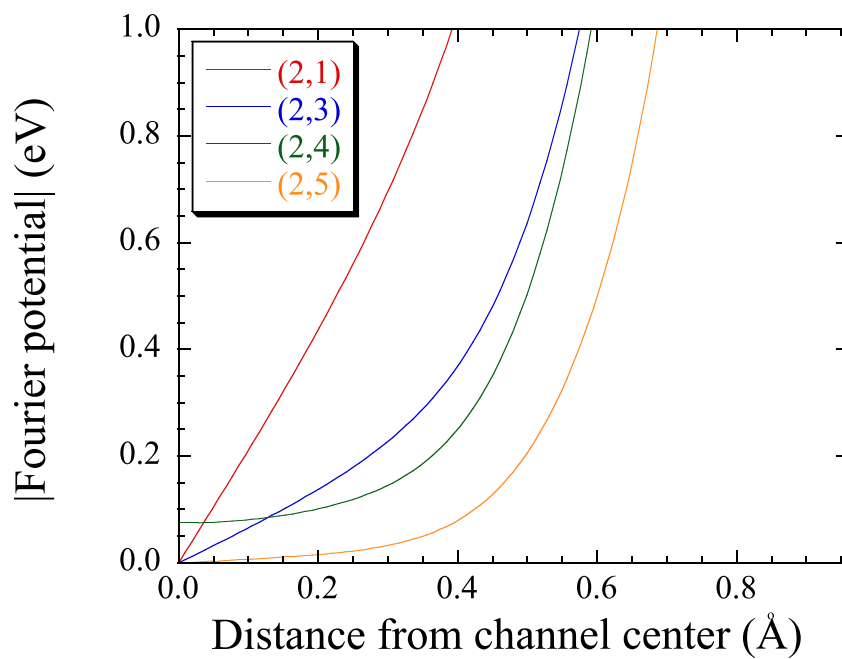


Figure 1.28: Same as Fig. 1.27 except for the vertical scale.

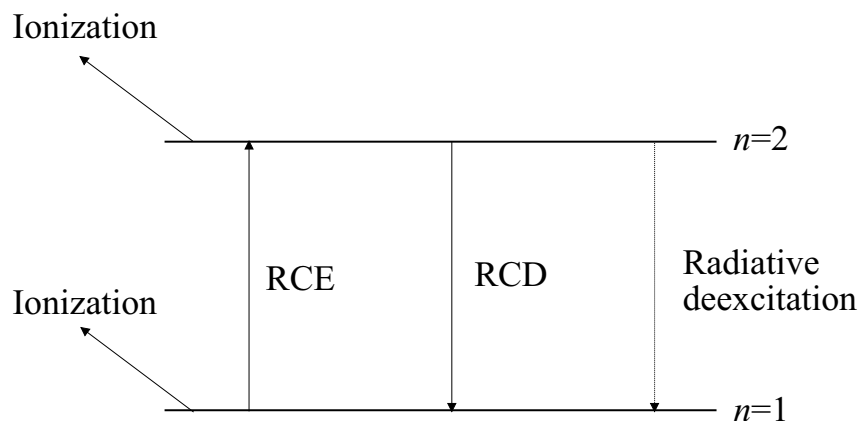


Figure 1.29: Schematic diagram of the atomic processes of the projectile ion inside a crystal.

### 1.3 Convoy electron

The energy and angular distributions of electrons ejected in energetic ion-atom and ion-solid collisions have been studied extensively [32, 33]. The energy spectrum of the electrons ejected in the forward direction is known to have a cusp-shaped peak at the energy corresponding to the same velocity as the projectile ion. In ion-atom collisions, this cusp-shaped peak originates from Electron Capture to the Continuum (ECC) and Electron Loss to the Continuum (ELC) processes. In the former case, the electron comes from the target atom, and in the latter case, the electron comes from the projectile ion. In the high energy region, the ELC process is dominant. Similar peaks have also been observed in the case of ion-solid collisions, and these electrons are often called convoy electrons.

Under the RCE condition, the yields of convoy electrons are expected to increase due the enhancement of the ionization process. Theoretically, the spectrum shape of the electrons produced in the ELC process is known to depend on the initial states of the electrons lost to the continuum states [34]. For example, the width of the cusp peak in the spectrum of the electrons emitted from  $1s$  states is broader than those from  $2s$ ,  $2p_x$ , and  $2p_y$  states. The peak width for  $2p_x$  is the same as that for  $2p_y$ , and broader than for  $2s$ . For  $2p_z$ , on the other hand, the inverted cusp-shaped peak is formed in the energy spectrum. These spectrum shapes reflect the momentum distributions of the initial states. Accordingly, the spectrum shape of convoy electrons is expected to vary depending on the RCE condition, because the compositions of the wave functions of the excited states vary depending on the RCE condition, as shown in section 1.2.4.

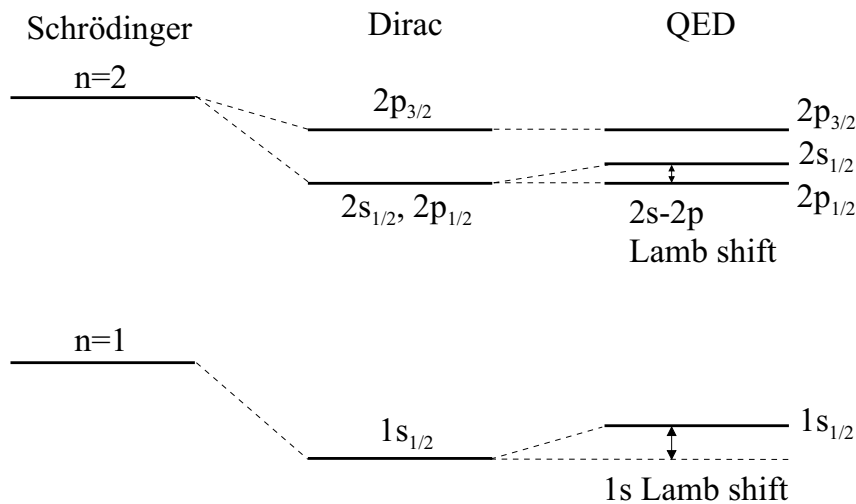


Figure 1.30: Schematic diagram of the energy levels of a hydrogen-like ion.

## 1.4 Spectroscopy of hydrogen-like and helium-like ions

The schematic diagram of the energy levels of a hydrogen-like ion is shown in Fig. 1.30. According to the Schrödinger equation, the electron energy for a one-electron atom is given by

$$E = -\frac{Z^2}{n^2}Ry, \quad (1.32)$$

where  $Z$  is the atomic number of the ion,  $n$  is the principal quantum number, and  $Ry$  is the Rydberg energy (13.6056981 eV). In this theory, the electron energy depends only on  $n$ .

According to the relativistic Dirac equation, the electron energy is given by

$$E = mc^2 \left[ 1 + \left( \frac{\alpha Z}{n - \kappa + \sqrt{\kappa^2 - \alpha^2 Z^2}} \right)^2 \right]^{-1/2}, \quad (1.33)$$

$$\kappa = j + 1/2, \quad (1.34)$$

where  $j$  is the total angular momentum and  $\alpha$  is the fine structure constant. It is noted that this energy includes the rest mass energy ( $mc^2$ ) of the electron. In this theory, the electron energy depends on  $n$  and  $j$ .

In the quantum electrodynamics (QED) theory,  $2s_{1/2}$  and  $2p_{1/2}$  are not degenerate. For a one-electron atom, the difference between the electron energy and the eigenvalue of the Dirac equation is defined as Lamb shift. The Lamb shift can be written as

$$\Delta S = \frac{\alpha (\alpha Z)^4}{\pi n^3} F(\alpha Z) mc^2, \quad (1.35)$$

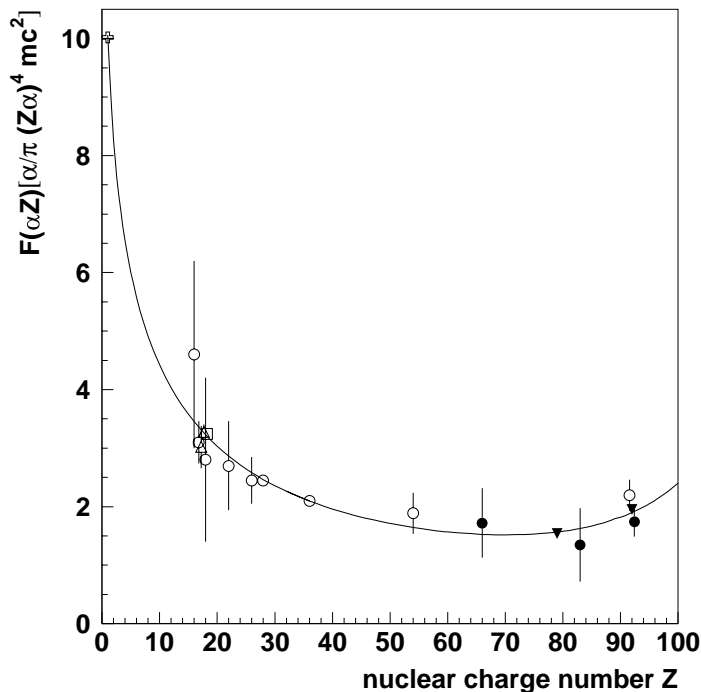


Figure 1.31: Comparison of  $F(\alpha Z)$  for  $1s$  between experiment and theory [36].

where  $F(\alpha Z)$  is the dimensionless function. Figure 1.31 shows the comparison of  $F(\alpha Z)$  for  $1s$  between experiment and theory. The experiment is in good agreement with theory. Table 1.2 shows the experimental and theoretical data on  $1s$  Lamb shift in hydrogen-like ions [35].

The contributions to the Lamb shift are divided into the QED correction and non-QED correction. The main QED corrections are the self-energy (SE) and vacuum-polarization (VP). The main non-QED correction is the nuclear finite-size effect.

Figure 1.32 shows the level diagram of a helium-like ion. Table 1.3 and 1.4 show the experimental and theoretical transition energies for  $1s^2 - 1s2p\ ^1P_1$  and  $1s^2 - 1s2p\ ^3P_1$  in helium-like ions.

For Ar and Fe ions, the transition energies were obtained by measuring the X-ray spectra with crystal spectrometers. There are three methods for producing the excited ions, *i.e.*, X-ray sources, which are beam-foil, recoil ion, and plasma. For beam-foil method, the excited ions are produced by injecting the ions into foils. For recoil-ion method, the ions are incident on the neutral gas, and then the X-rays emitted from the ion ionized by the incident ion are detected. In these methods, the Doppler broadening limits the resolution. For recoil-ion method, the contribution of the Doppler effect is relatively small. In addition, in these methods, the charge states of the ions are not measured, so that the spectator electron in the high  $n$  state shifts the X-ray energy. The methods used for Ar and Fe ions are shown in table 1.5. The X-ray sources used for wavelength calibration of the crystal spectrometer are also shown.

Table 1.2: Lamb shift for  $1s$  in hydrogen-like ions (in eV) [35].

	Z	Experiment	Ref.	Theory [37]	[38]	[39]	[40]
Ar	18	$1.0 \pm 0.5$	[41]	1.14140			
		$1.145 \pm 0.016$	[30]				
Fe	26	$4.13 \pm 0.7$	[42]	3.97246			
		$3.4 \pm 0.6$	[42]				
		$4.07 \pm 0.7$	[43]				
		$4.29 \pm 0.6$	[43]				
Kr	36	$11.95 \pm 0.50$	[44]	11.8579			
Xe	54	$54.0 \pm 10.0$	[45]	47.1016			
U	92	$520 \pm 130$	[46]	458.490	463.4	464.6	465.5
		$470 \pm 16$	[47]				
		$429 \pm 63$	[48]				
		$508 \pm 98$	[49]				

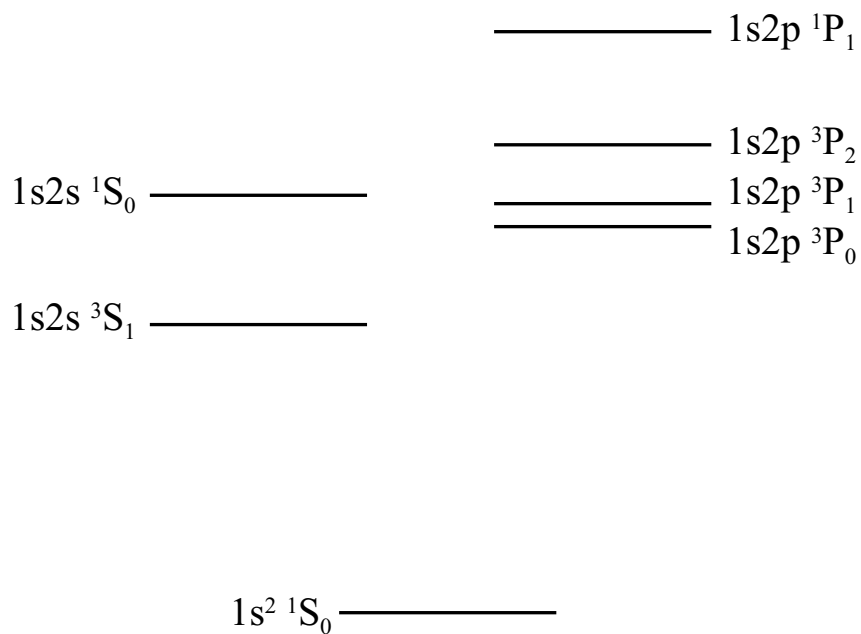


Figure 1.32: Level diagram for a helium-like ion.

Table 1.3: Transition energies of  $1s^2 - 1s2p \ ^1P_1$  in helium-like ions (in eV) [35].

	Z	theory				Experiment	Ref.
		[50]	[51]	[52]	[53]		
Ar	18	3139.617	3139.577	3139.582	3139.649	3139.55±0.04	[54]
						3139.57±0.25	[41]
Fe	26	6700.539	6700.404	6700.427	6700.603	6700.73±0.20	[55]
						6700.90±0.25	[56]
Kr	36	13114.70	13114.34	13114.42	13114.80	13115.31±0.30	[57]
						13114.78±0.71	[58]
Xe	54	30630.64	30629.28	30629.68	30630.76	30629.1±3.5	[45]
U	92	100615.7	100607.3	100614.0		100626±35	[46]
						100649±65	[59]

Table 1.4: Transition energies of  $1s^2 - 1s2p \ ^3P_1$  in helium-like ions (in eV) [35].

	Z	theory				Experiment	Ref.
		[50]	[51]	[52]	[53]		
Ar	18	3123.574	3123.530	3123.534	3123.567	3123.52±0.04	[54]
						3123.60±0.25	[41]
Fe	26	6667.692	6667.552	6667.567	6667.669	6667.50±0.25	[56]
Kr	36	13026.36	13026.00	13026.05	13026.31	13026.8±0.3	[57]
						13026.30±0.71	[58]
Xe	54	30206.91	30205.58	30205.87	30206.53	30209.6±3.5	[45]
U	92	96174.5	96167.2	96172.5		96171±52	[46]

Table 1.5: Methods of spectroscopy used for Ar and Fe ions.

Ref.	transition	method	calibration
Briand <i>et al.</i> [41]	Ar <sup>17+</sup> $1s - 2p_{3/2}$ $1s - 2p_{1/2}$	beam-foil	K $K\alpha$
Beyer <i>et al.</i> [30]	Ar <sup>17+</sup> $1s - 2p_{3/2}$ $1s - 2p_{1/2}$	recoil ion	K $K\alpha$
Marmar <i>et al.</i> [60]	Ar <sup>17+</sup> $1s - 2p_{3/2}$ $1s - 2p_{1/2}$	plasma	K $K\alpha$
Briand <i>et al.</i> [41]	Ar <sup>16+</sup> $1^1S_0 - 2^1P_1$ $1^1S_0 - 2^3P_1$ $1^1S_0 - 2^3P_2$	beam-foil	K $K\alpha$
Deslattes <i>et al.</i> [54]	Ar <sup>16+</sup> $1^1S_0 - 2^1P_1$ $1^1S_0 - 2^3P_1$ $1^1S_0 - 2^3P_2$	recoil ion	Cd $L\alpha$
Briand <i>et al.</i> [42]	Fe <sup>25+</sup> $1s - 2p_{3/2}$ $1s - 2p_{1/2}$	beam-foil	Co $K\alpha$
Silver <i>et al.</i> [43]	Fe <sup>25+</sup> $1s - 2p_{3/2}$ $1s - 2p_{1/2}$	beam-foil	Fe <sup>25+</sup> Balmer- $\beta$
Briand <i>et al.</i> [56]	Fe <sup>24+</sup> $1^1S_0 - 2^1P_1$ $1^1S_0 - 2^3P_1$ $1^1S_0 - 2^3P_2$	beam-foil	Fe <sup>25+</sup> Lyman- $\alpha$
Beiersdorfer <i>et al.</i> [55]	Fe <sup>24+</sup> $1^1S_0 - 2^1P_1$	plasma	X-ray from H-like ion

## 1.5 Purpose

In most of the RCE experiments, the excitations from  $1s$  to the  $n = 2$  states in hydrogen-like light ions have been observed. To investigate the contribution of the  $l \cdot s$  interaction and the QED effect, which increase with increasing  $Z$ , it is important to observe the RCE of heavier ions. As shown in the equation of the RCE condition (equation 1.20), high energy ions are needed to fulfill the low-order RCE condition for heavy ions. Using the projectile ions with relativistic energies, we observed the RCE of hydrogen-like  $\text{Ar}^{17+}$  and  $\text{Fe}^{25+}$  ions through measurements of the charge state distribution of the ions transmitted through crystals and projectile deexcitation X-rays. We also attempted to observe the RCE of helium-like  $\text{Ar}^{16+}$  and  $\text{Fe}^{24+}$  ions. The structure of the resonance profile of the helium-like ion was clearly observed for the first time.

In the recent experiment, we found that the resonance peak position (angle) can be determined precisely. This means that the RCE observation can be applied to the high precision spectroscopy of the ions, if we can determine the beam velocity precisely. The purpose of the present work is to perform spectroscopy of helium-like ions using the RCE phenomena. We determined the beam velocity by observing the RCE of the hydrogen-like ions. In this spectroscopy method, we detect the ions transmitted through the crystal instead of the projectile deexcitation X-rays. Accordingly, the detection efficiency is high, and the Doppler broadening does not matter. Using the RCE, we performed spectroscopy of  $\text{Ar}^{16+}$  and  $\text{Fe}^{24+}$  ions.

# Chapter 2

## Experimental

### 2.1 HIMAC

We used Ar and Fe ions with relativistic energies as projectile ions. Beams of these ions were provided from Heavy Ion Medical Accelerator in Chiba (HIMAC) at National Institute of Radiological Sciences (NIRS), which is mainly used for cancer therapy. This accelerator consists of two ion sources, radio frequency quadrupole (RFQ) linac, Alvarez linac, and two heavy-ion synchrotrons. As ion sources, penning ionization gauge (PIG) and electron cyclotron resonance (ECR) ion sources are used. At HIMAC, various ions such as C, Ne, Si, Ar, Fe, Kr, and Xe ions are available, and can be accelerated up to 800 MeV/u. The present experiment was performed at the PH2 line dedicated for physics experiments. The beam was supplied as a pulse, whose repetition time was 3.3 s and width was 1.5 s. The maximum intensity of the beam was about  $1 \times 10^8$  particles per second (pps).

### 2.2 Observation of RCE

#### 2.2.1 Beam transport

Figure 2.1 shows the schematic drawing of the experimental setup used for observation of RCE. As projectile ions, we used 390 MeV/u hydrogen-like  $\text{Ar}^{17+}$ , 383 MeV/u helium-like  $\text{Ar}^{16+}$ , 460 MeV/u hydrogen-like  $\text{Fe}^{25+}$ , 423 MeV/u helium-like  $\text{Fe}^{24+}$ , and 423 MeV/u lithium-like  $\text{Fe}^{23+}$  ions supplied from HIMAC. The energies of these ions are in the relativistic region. For example,  $\beta = v/c$  and  $\gamma = 1/\sqrt{1 - \beta^2}$  of 390 MeV/u ion are calculated to be 0.71 and 1.42, respectively. We placed a 50-mm thick Fe collimator with an inner diameter of 1 mm at 6.5 m upstream from a target. For 390 MeV/u  $\text{Ar}^{18+}$  and 460 MeV/u  $\text{Fe}^{26+}$  ions in Fe, the ranges are 1.8 and 1.6 cm, respectively. The beams of Ar and Fe ions are stopped in the collimator, but light particles produced via nuclear reaction in collisions of the beam with the collimator escape from it. For example, the range for 390 MeV/u proton in Fe is 15 cm. In order to eliminate such fragments, a 15-cm thick Pb baffle with an inner diameter of 10 mm was placed at 0.35 m upstream from the target.

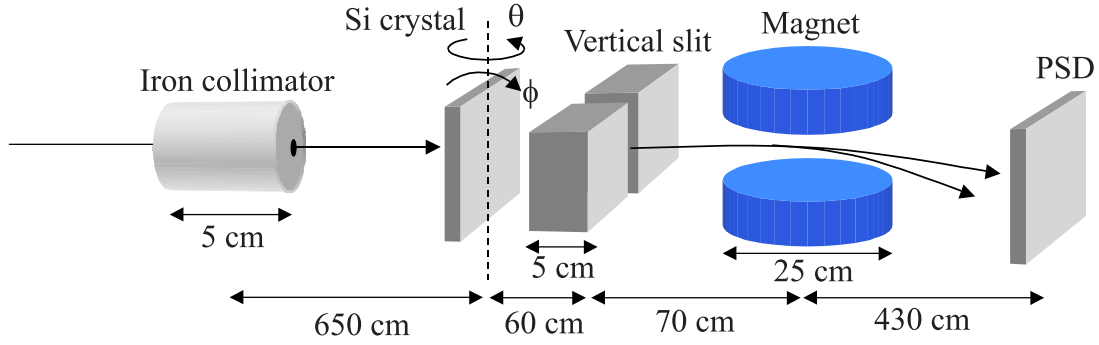


Figure 2.1: Schematic drawing of the experimental setup.

The range for 390 MeV/u proton in Pb is 14 cm.

In front of the collimator, we placed Al foils, which were removable with a linear feedthrough. These foils were used for stripping the electrons from the projectile ions, *i.e.*, used as stripper foils. As will be shown in chapter 4, these foils were used for producing hydrogen-like ions from helium-like ions. For  $\text{Ar}^{16+}$  and  $\text{Fe}^{24+}$  ions, we used  $5\ \mu\text{m}$  and  $13\ \mu\text{m}$  Al-foils, respectively.

As discussed in section 1.1, parallel beams are needed for channeling experiments. We checked the parallelity of the beam in the following method. Before we placed the crystal at the target position, we placed the phosphor screen there. The diameter of the beam spot was  $\sim 2\ \text{mm}$ . After that, we removed the phosphor screen, and then we measured the beam profile with a two-dimensional position-sensitive Si detector (PSD), which was located at 5.6 m downstream from the target. As an example, the beam profile of 423 MeV/u  $\text{Fe}^{24+}$  ions is shown in Fig. 2.2. The diameter of the beam measured with the PSD was  $\sim 2\ \text{mm}$ . This value is almost the same as that measured with the screen, indicating that the angular spread of the beam is small enough. From the beam diameter and the distance between the collimator and the PSD, the angular spread is estimated to be  $\sim 0.1\ \text{mrad}$ , which is of the order of the critical angle for the (220) planar channeling (0.15 mrad). Also, from the beam diameter, the energy width of the beam,  $\Delta E/E$ , was estimated to be  $\leq 2 \times 10^{-4}$  [29].

## 2.2.2 Goniometer

As a target, we used a  $21\ \mu\text{m}$ -thick Si crystal. The Si crystal was mounted on a three-axis  $(\theta, \phi, \omega)$  goniometer. The schematic drawing of the goniometer is shown in Fig. 2.3. We mounted the crystal so that the (220) plane is horizontal. Using the electronic autocollimator (ELCOMAT (MÖLLER-WEDEL)), the precision of the rotating angle,  $|\delta(\Delta\theta)/\Delta\theta|$ , was estimated to be  $\sim 0.01$ , where  $\Delta\theta$  is the rotating angle. We measured the precision for  $\Delta\theta = 0.04^\circ$  and  $0.004^\circ$ .

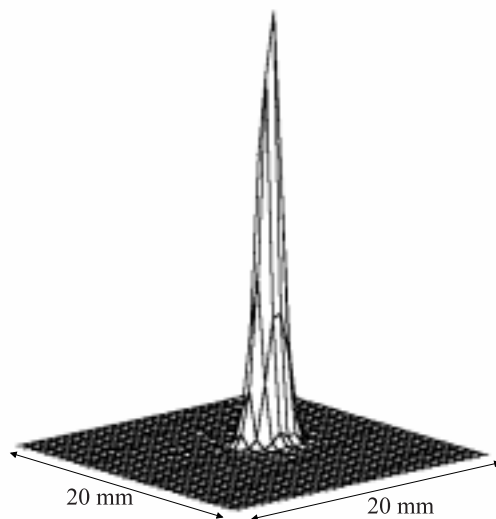


Figure 2.2: Beam profile of 423 MeV/u  $\text{Fe}^{24+}$  ions.

### 2.2.3 Si crystal

We used a 21  $\mu\text{m}$ -thick Si crystal (supplied from Virginia Semiconductor), whose surface is perpendicular to the  $\langle 110 \rangle$  axis. We checked the orientation of the axis and plane of the crystal by X-ray diffraction in advance. Figure 2.4 shows the schematic drawing of the target holder. The hatched area is higher than the neighboring area by 0.1 mm. We attached the crystal to the hatched area of the holder at one point so that the crystal is not bent.

We examined the crystal qualities of the Si detectors (SSD) of 10, 20, and 30  $\mu\text{m}$  in thickness by X-ray topography. It was found that the thinner SSD tends to be bent. Accordingly, we did not use the SSD as a target crystal in the present work.

### 2.2.4 Detection system

#### *Charge state distribution*

The ions transmitted through the target were charge-separated with a magnet of 0.5 T located at 1.3 m downstream from the target. The diameter and the gap of the pole piece of the magnet were 25 cm and 7.8 cm, respectively. In this magnet, the ions were bent by  $\sim 0.02$  rad with respect to the incident beam direction. The charge-separated ions were detected with the PSD located at 5.6 m downstream from the target. The active area of the PSD was 20 mm  $\times$  20 mm, and the thickness of its depletion layer was 200  $\mu\text{m}$ . In the case that we measured the charge state distribution, the beam intensity was reduced

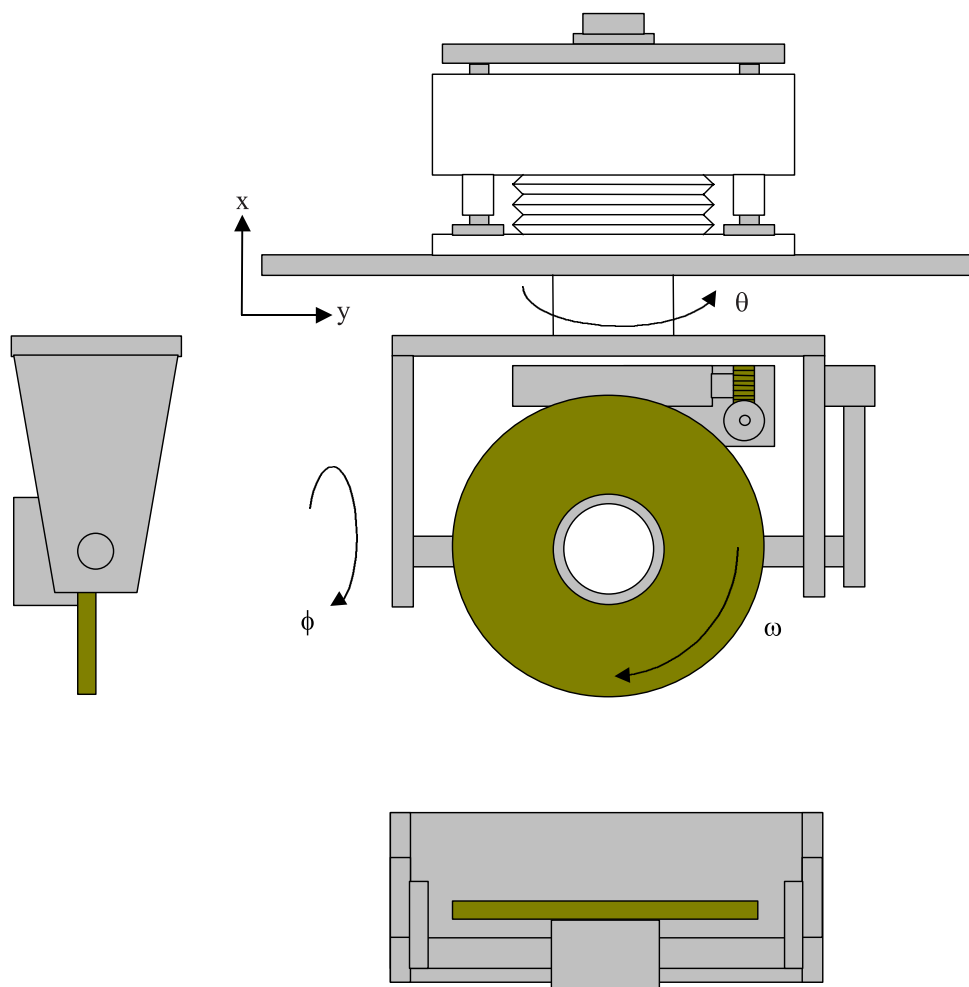


Figure 2.3: Schematic drawing of the goniometer. The side and bottom views are also shown.

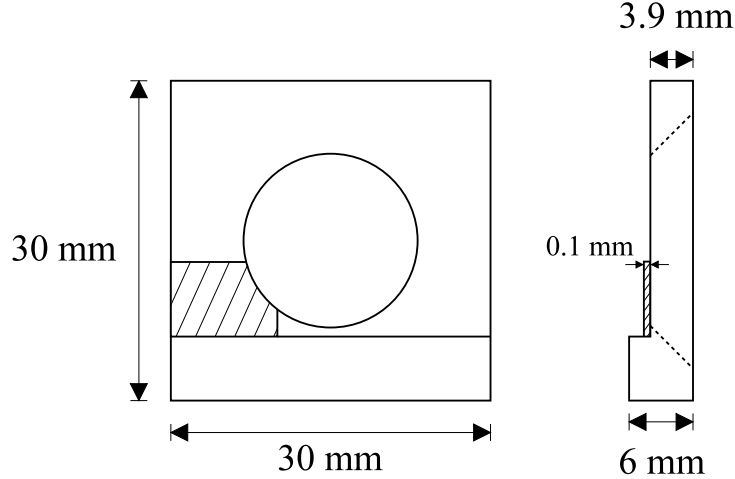


Figure 2.4: Schematic drawing of the target holder. The side view is also shown.

to  $\sim 1000$  pps to avoid pile-up.

Figure 2.5 shows the beam profiles of  $\text{Fe}^{24+}$ ,  $\text{Fe}^{25+}$ , and  $\text{Fe}^{26+}$  ions transmitted through the Si crystal under the (220) planar channeling condition. The profiles of these ions were partly overlapped with each other. To separate these profiles, we placed a vertical slit at 0.6 m downstream from the target. The width of the slit was 1 mm, and its thickness was 5 cm. The profiles of the ions after passing through the slit are shown in Fig. 2.6, where the profiles were clearly separated.

### *Deexcitation X-rays*

Figure 2.7 shows the schematic drawing of the experimental setup used for the X-ray measurements. To measure the deexcitation X-rays from the projectile ions, we placed two Si(Li) detectors at an angle of  $41^\circ$  with respect to the beam direction. One was placed on the horizontal plane, and the other was placed on the vertical plane. The angular distribution of the deexcitation X-rays provides the information on the polarization of the excited states from which the X-rays are emitted. For the electric dipole (E1) transition, the angular distribution of the deexcitation X-rays for  $2p_x \rightarrow 1s$  is written as

$$I(\theta) \propto \sin^2 \theta, \quad (2.1)$$

where  $I(\theta)$  is the intensity of the deexcitation X-rays and  $\theta$  is the emission angle of the X-rays with respect to the  $x$  direction in the projectile frame. According to this equation, when  $2p_x$  decays to  $1s$ , it tends to emit deexcitation X-rays strongly in the direction perpendicular to the  $x$  axis.

The emission angle of the X-ray,  $\theta_p$ , in the projectile frame is expressed as

$$\tan \theta_p = \frac{\sin \theta_l}{\gamma(\cos \theta_l - \beta)}, \quad (2.2)$$

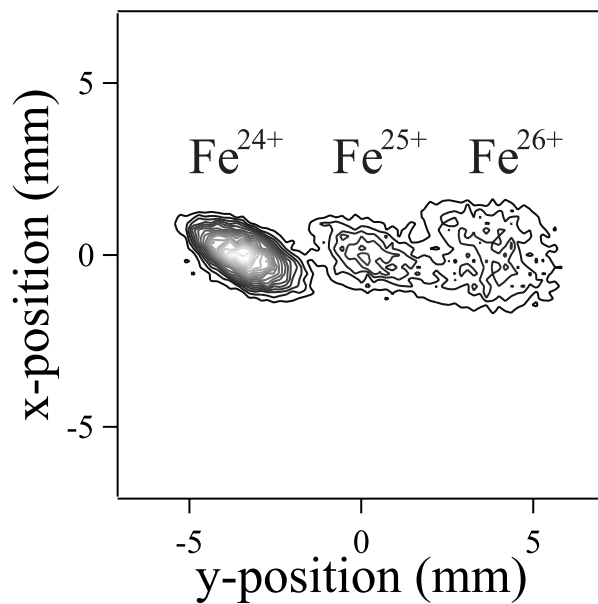


Figure 2.5: Contour plot of the beam profiles of Fe ions channeled in the (220) plane of the Si crystal (without the vertical slit).

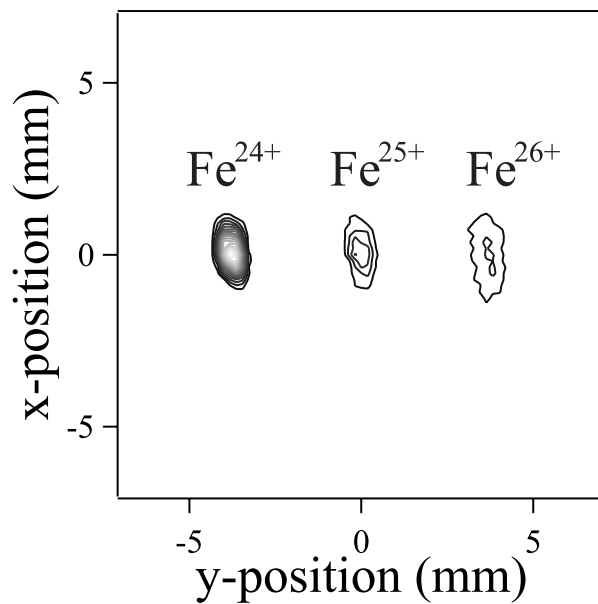


Figure 2.6: Contour plot of the beam profiles of Fe ions channeled in the (220) plane of the Si crystal (with the vertical slit).

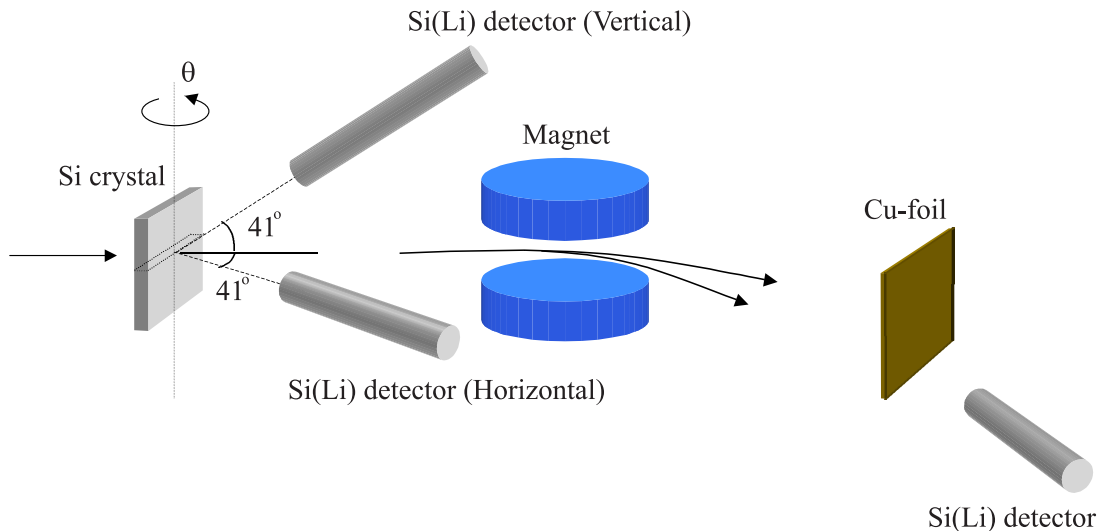


Figure 2.7: Schematic drawing of the experimental setup used for the X-ray measurements.

where  $\theta_l$  is the angle in the laboratory frame. In the present experiment, we placed the Si(Li) detectors at  $\theta_l = 41^\circ$  with respect to the beam direction, so that  $\theta_p$  is calculated to be  $\sim 90^\circ$ . This means that the detected X-rays were emitted in the direction nearly perpendicular to the beam direction in the projectile frame. In other words, the Si(Li) detector placed on the horizontal plane was parallel to the (220) plane, and one placed on the vertical plane was perpendicular to the (220) plane.

We evaluated the detection efficiencies of the Si(Li) detectors by using 5.9 keV and 22.1 keV X-rays which are emitted from  $^{55}\text{Fe}$  and  $^{109}\text{Cd}$  X-ray sources, respectively. To evaluate the detection efficiencies at other energies, we measured the K X-rays emitted from various solids which were irradiated with the 22.1 keV X-rays ( $^{109}\text{Cd}$ ). As the solid targets, we used Ti, V, Cr, Fe, Ni, Cu, Zn, GaAs, Ge, Zr, and Mo. The  $K\alpha$  X-ray energies of these elements are 4.51, 4.95, 5.41, 6.40, 7.48, 8.05, 8.64, 9.25, 9.89, 10.54, 15.77, and 17.48 keV for Ti, V, Cr, Fe, Ni, Cu, Zn, Ga, Ge, As, Zr, and Mo, respectively.

During the measurements of the deexcitation X-rays, the beam intensity was more than  $\sim 10^5$  pps. For such a high intensity beam, the PSD can not be used to measure the beam intensity. To monitor the beam intensity, we placed a Cu-foil of  $50 \mu\text{m}$  in thickness at the end of the beam line, and measured Cu K X-rays emitted in collisions of the projectile ions with the Cu-foil using another Si(Li) detector. To examine the relation between the intensities of the beam and the Cu X-rays, reducing the beam intensity to  $\sim 10^3$  pps, we measured the beam intensity with the PSD, and the Cu X-rays with the Si(Li) detector at the same time. This calibration measurement takes too much time, which was thus performed once before or after the measurements of the projectile deexcitation X-rays.

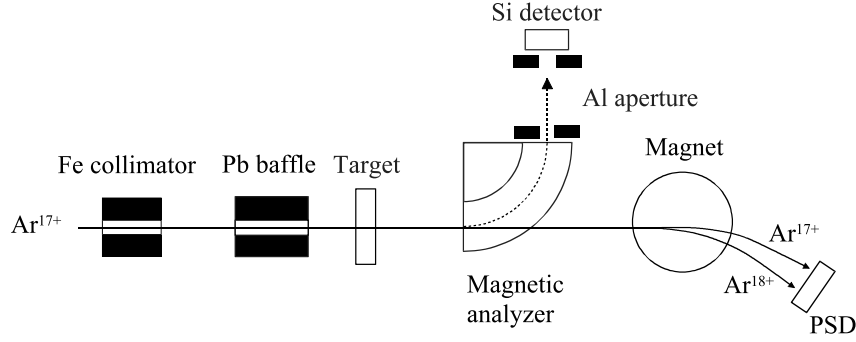


Figure 2.8: Schematic drawing of the experimental setup used for measurements of convoy electron spectra.

### *Convoy electrons*

We also measured the energy spectra of convoy electrons. Before using the Si crystal as a target, we used carbon foils of various thicknesses as a target in order to extract the feature characteristic for the crystal target. The experiments on carbon foil targets will be described in Appendix B. Figure 2.8 shows the schematic diagram of the experimental setup used for measurements of convoy electron spectra. In this measurement, we used 390 MeV/u  $\text{Ar}^{17+}$  ions as projectile ions. As stated in section 1.3, convoy electrons have velocities of  $v \simeq v_p$  ( $v_p$  is the projectile velocity). In the present experiment, the energy of the detected convoy electron is  $\sim 200$  keV. In the lower energy region, an electrostatic electron analyzer is often used for measuring convoy electron spectra. However, it is not suited for measuring spectra of such high energy electrons. We used a magnetic analyzer with a 105 mm central orbit radius and a  $90^\circ$  deflection angle. As an electron detector, a silicon surface barrier detector (SSD) with a depletion layer of 5 mm was used. Figure 2.9 shows the typical energy spectra measured with the SSD. The dashed line shows the fitting to the background. As can be seen in Fig. 2.9, the use of the SSD is essential to discriminate the convoy electrons from the background signals such as other electrons and  $\gamma$ -rays. Two 5-mm thick Al apertures with an inner diameter of 5 mm were placed at the exit of the magnet and also in front of the electron detector. These apertures determine the momentum resolution ( $\Delta p/p \sim \pm 0.02$ ) and the acceptance angle ( $\Delta\theta \sim \pm 1^\circ$ ). The experimental setup used in the case of the Si crystal target was the same as that used in the case of the carbon foil target except for the position of the magnetic analyzer. For the crystal target, the distance between the target and the entrance of the magnet was 155 mm, and the distance between the exit of the magnet and the Si detector was 71 mm. For the carbon foil targets, both of the distances were 105 mm. By scanning the strength of the magnetic field of the analyzer, we obtained the momentum spectra of electrons. In the present work, the electron spectra are plotted as a function of electron energy, which is written as

$$\frac{d\sigma}{dE} = \frac{1}{v} \frac{d\sigma}{dp}, \quad (2.3)$$

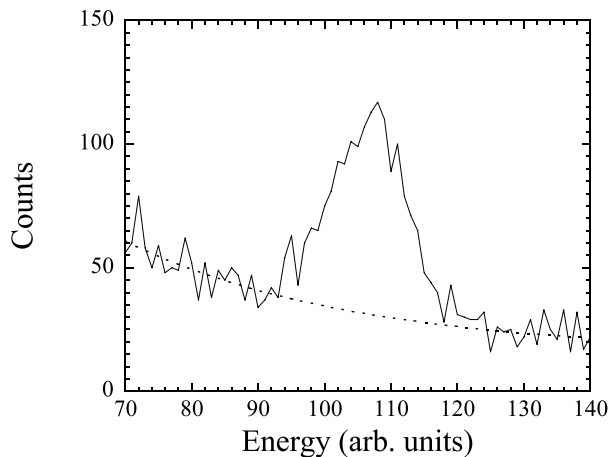


Figure 2.9: Typical energy spectra measured with the SSD. The dashed line shows the fitting to the background.

where  $v$  is the electron velocity and  $d\sigma/dp$  is the obtained momentum spectrum. The absolute electron energy was obtained assuming that the peak energy of convoy electrons is equal to the energy of the electron with the same velocity as the projectile ion for thin carbon foil targets.

During the measurement, the beam intensity was more than  $\sim 10^4$  pps. Similarly to the measurements of the deexcitation X-rays, we placed a  $50 \mu\text{m}$ -thick Cu foil at the end of the beam line (or at 0.6 m downstream from the target), and measured the Cu K X-rays emitted from the Cu-foil using a Si(Li) detector in order to monitor the beam intensity.

## 2.2.5 Data acquisition system

### *Charge state distribution*

The schematic diagram of the electric circuit used for the PSD is shown in Fig. 2.10. The charge signals collected from the four corners of the PSD were converted into voltages with the charge-sensitive pre-amplifiers, and then amplified with the spectroscopy amplifiers. The sum of the output signals of the spectroscopy amplifiers was used as an input signal for the timing-SCA (single channel analyzer). This sum signal corresponds to the total energy which the ion lost in the PSD. The data were taken with the personal computer through the analog to digital converter (ADC) board. The position  $(x, y)$  of the ion was obtained as

$$x = \frac{(Q_1 + Q_4) - (Q_2 + Q_3)}{Q_1 + Q_2 + Q_3 + Q_4}, \quad (2.4)$$

$$y = \frac{(Q_3 + Q_4) - (Q_1 + Q_2)}{Q_1 + Q_2 + Q_3 + Q_4}, \quad (2.5)$$

where  $Q_1, Q_2, Q_3$ , and  $Q_4$  are the digitized pulse heights of the signals collected from the four corners of the PSD. This calculation was performed with the personal computer.

Scanning the angle of the crystal, we measured the charge state distribution of the ions transmitted through the crystal. In this case, we took the data until certain counts are accumulated at each measuring point, and then varied the angle.

### *Deexcitation X-rays*

Figure 2.11 shows the schematic diagram of the electric circuit used for the Si(Li) detectors. We used the OR signal of the three timing signals for the Si(Li) detectors as an input signal for the trigger of the peak holder so that we can take the data through one ADC board (one computer). We used the linear gate and stretcher circuit as a delay circuit.

### *Convoy electrons*

Figure 2.12 shows the schematic diagram of the electric circuit used for measuring convoy electron spectra. Again, we used the OR signal of the timing signals for the SSD and the Si(Li) detector as an input signal for the trigger of the peak holder.

## 2.2.6 Determination of crystal orientation

To determine the crystal orientation, scanning the angles ( $\theta$  and  $\phi$ ), we measured the charge state distribution of the ions transmitted through the crystal. Figure 2.13 shows the survived fraction of  $\text{Fe}^{25+}$  ions after passing through the crystal as a function of  $\phi$  for 460 MeV/u  $\text{Fe}^{25+}$  incidence. At the angle where the channeling occurs, the fraction of  $\text{Fe}^{25+}$  ions increased. The closed circles in Fig. 2.14 show ( $\theta, \phi$ ) where the channeling phenomena were observed. The dashed line shows the scanned path, and the solid lines represent ( $\theta, \phi$ ) fulfilling the channeling conditions. After we performed the wide range scan to determine the orientation of the plane, we performed the detailed scan around the (220) and (004) planar channeling conditions. The orientation ( $\theta, \phi$ ) of the  $\langle 110 \rangle$  axis was determined from the orientation of the (220) and (004) planes, since the  $\langle 110 \rangle$  axis lies in both of the (220) and (004) planes. In the present work, we placed the crystal so that the (220) plane is horizontal, and observed the RCE by scanning  $\theta$  under the (220) planar channeling condition, as discussed later. After the RCE scan, we checked the orientation ( $\theta, \phi$ ) of the  $\langle 110 \rangle$  axis. The shift of the angle of the  $\langle 110 \rangle$  axis from that measured before the RCE scan was  $\leq \pm 0.002^\circ$ . Accordingly, the systematic error of the rotating angle of the goniometer was estimated to be  $\sim \pm 0.002^\circ$ .

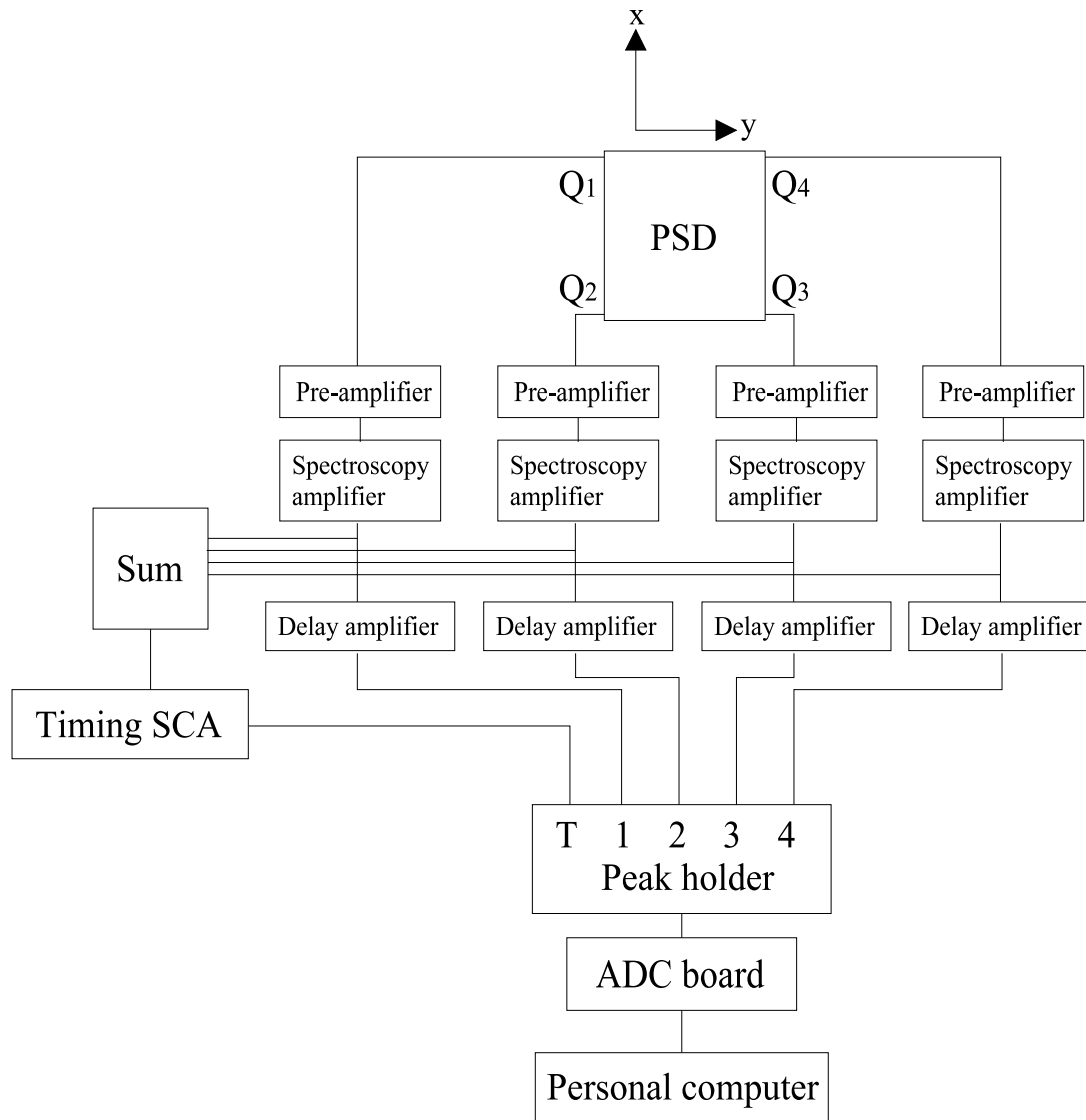


Figure 2.10: Schematic diagram of the electric circuit used for the PSD. In the peak holder, "T" represents the trigger for the peak hold circuit.

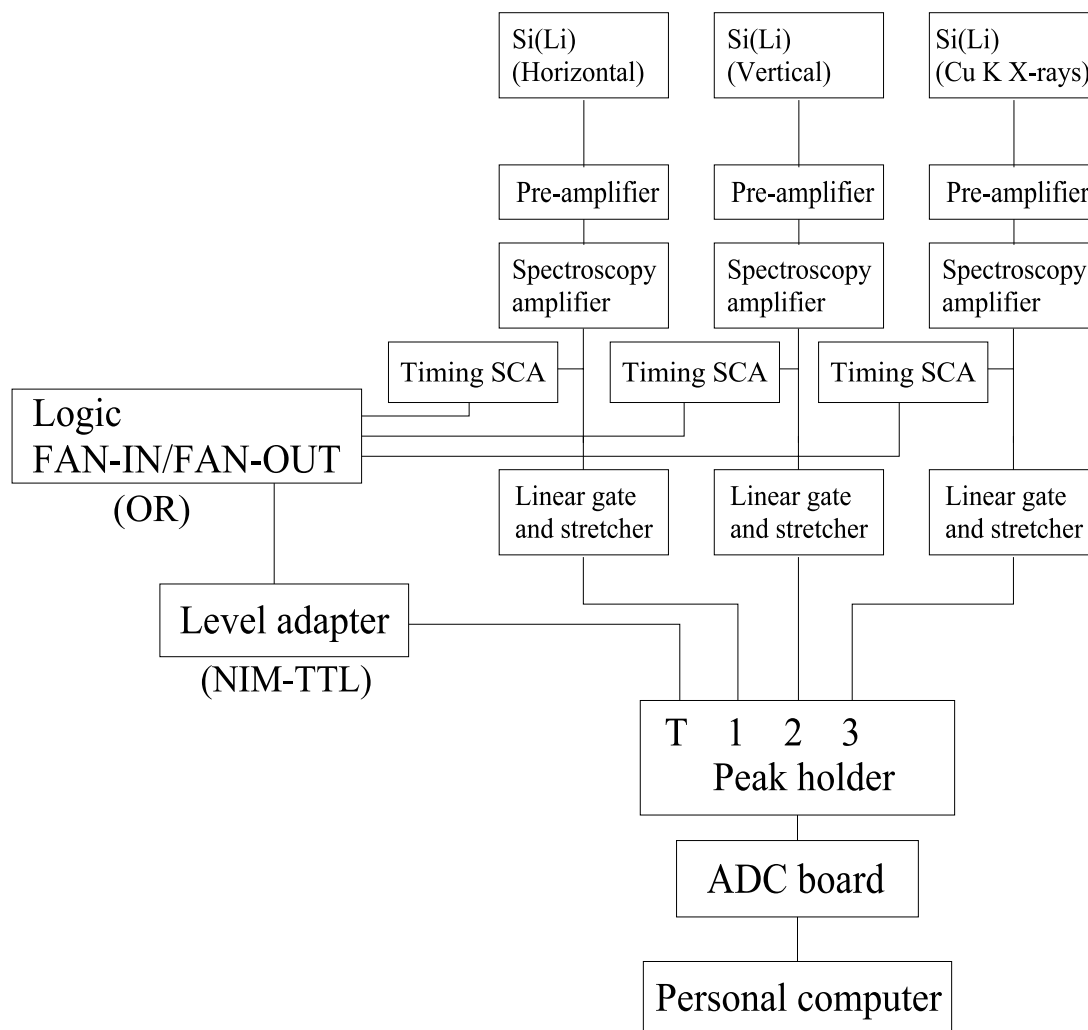


Figure 2.11: Schematic diagram of the electric circuit used for measurements of the de-excitation X-rays.

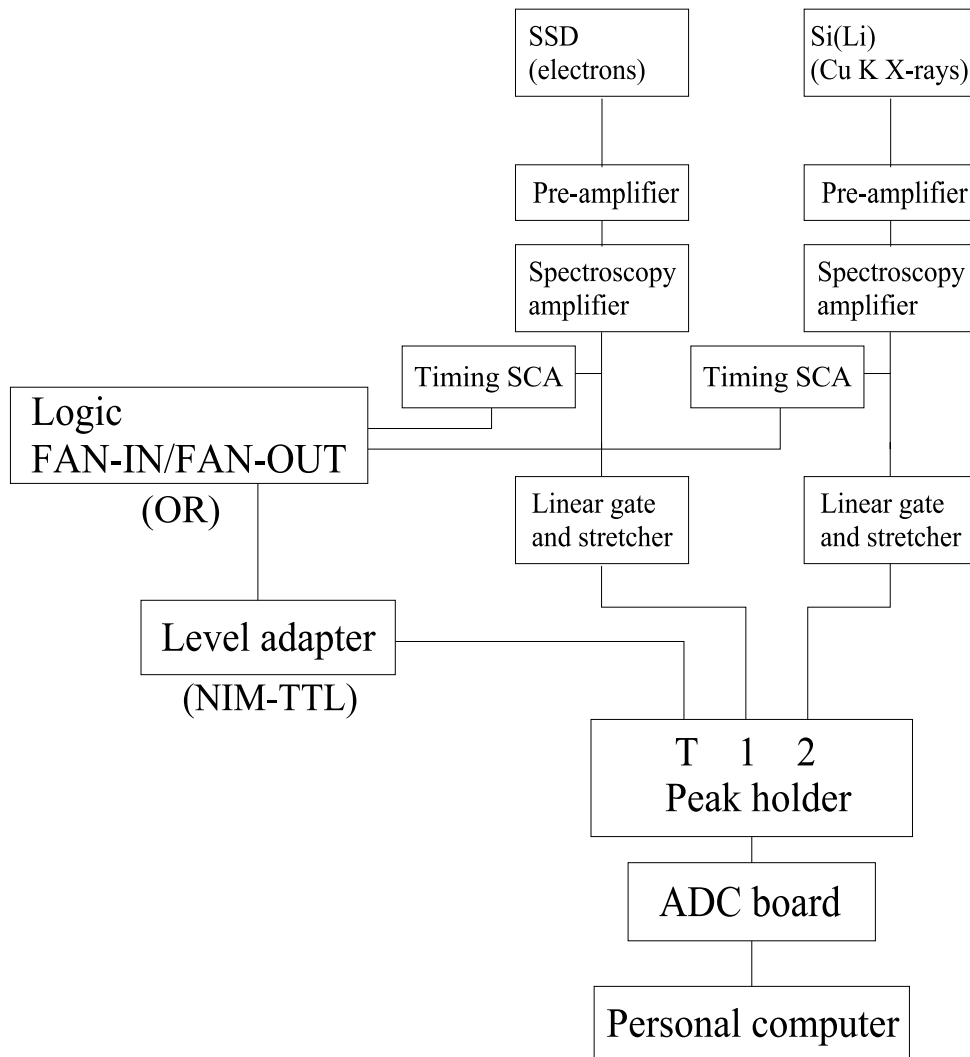


Figure 2.12: Schematic diagram of the electric circuit used for measurements of convoy electron spectra.

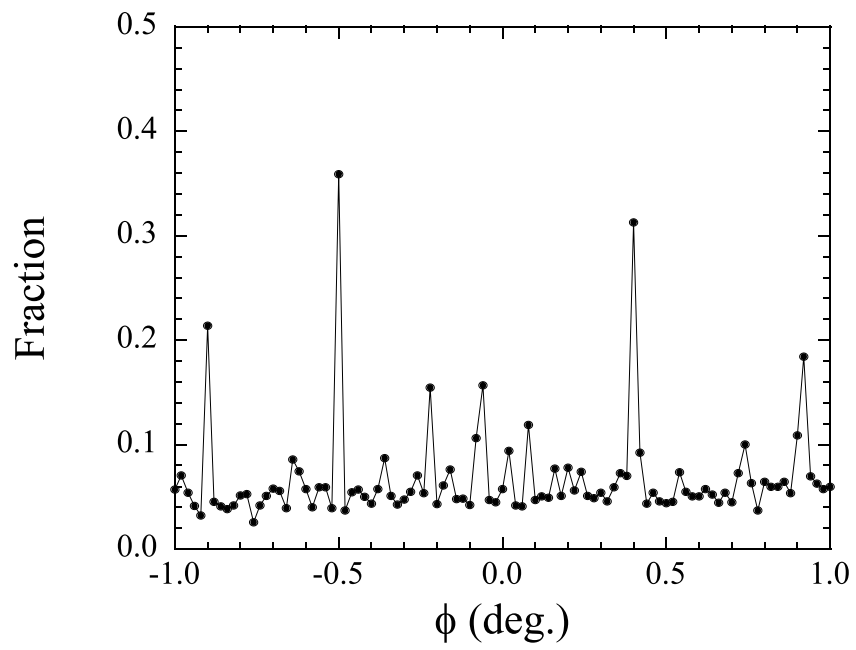


Figure 2.13: Fraction of  $\text{Fe}^{25+}$  ions transmitted through the crystal as a function of  $\phi$  for 460 MeV/u  $\text{Fe}^{25+}$  incidence.

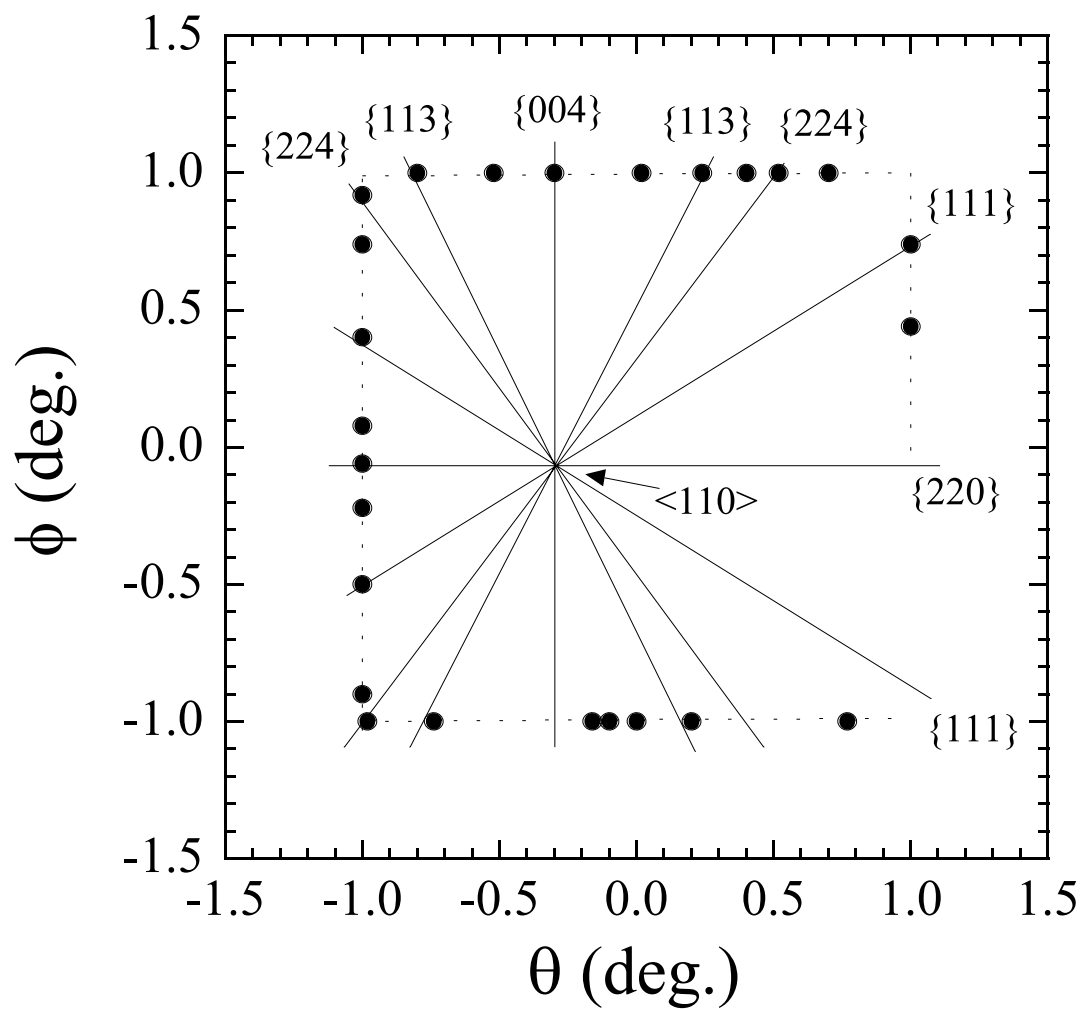


Figure 2.14:  $(\theta, \phi)$  map representing the orientation of the axis and plane of the crystal. The dashed line shows the scanned path. The closed circles show  $(\theta, \phi)$  where the channeling phenomena were observed.

# Chapter 3

## Observation of resonant coherent excitation

We have observed the RCE of 390 MeV/u Ar<sup>17+</sup>, 383 MeV/u Ar<sup>16+</sup>, 460 MeV/u Fe<sup>25+</sup>, 423 MeV/u Fe<sup>24+</sup>, and 423 MeV/u Fe<sup>23+</sup> ions, which are summarized in table 3.1. To observe the RCE, we measured the charge state distribution of the ions transmitted through the crystal and deexcitation X-rays emitted from the projectile ions.

The E1 decay rates for  $n = 2 \rightarrow 1s$  in Ar and Fe ions are summarized in table 3.2. The mean traveling distance for the radiative decay is also shown, which is calculated as  $\gamma v\tau = \gamma\beta c\tau$ , where  $\tau$  is  $1/A$  ( $A$  is the decay rate), and  $\gamma$  is due to the relativistic effect.

According to the empirical Lotz formula [61, 62], the electron impact ionization cross section,  $\sigma_i$ , is given by

$$\sigma_i = 4.5 \times 10^{-14} (cm^2 eV^2) \times \frac{\ln(E/P_i)}{EP_i}, \quad (3.1)$$

where  $E$  is the impact electron energy and  $P_i$  is the binding energy of the electron. For the  $n = 1$  and  $n = 2$  states of 390 MeV/u Ar<sup>17+</sup> ions,  $\sigma_i$  are calculated to be  $1.9 \times 10^{-22}$  and  $1.0 \times 10^{-21}$  cm<sup>2</sup>, respectively. This formula is often used for the rough estimation of  $\sigma_i$ . For the  $n = 1$  and  $n = 2$  states of 460 MeV/u Fe<sup>25+</sup> ions,  $\sigma_i$  are calculated to be  $6.4 \times 10^{-23}$  and  $3.7 \times 10^{-22}$  cm<sup>2</sup>, respectively. The mean free path (MFP)  $\lambda_i$  for electron

Table 3.1: RCE observed in this experiment.

ion	energy (MeV/u)	$\beta = v/c$	$\gamma = 1/\sqrt{1 - \beta^2}$	RCE
Ar <sup>17+</sup>	390	0.709	1.419	$n = 1 \rightarrow n = 2, 3, 4, 5$
Ar <sup>16+</sup>	383	0.706	1.411	$1s^2 \rightarrow 1s2p$
Fe <sup>25+</sup>	460	0.743	1.494	$n = 1 \rightarrow n = 2, 3$
Fe <sup>24+</sup>	423	0.726	1.454	$1s^2 \rightarrow 1s2p$
Fe <sup>23+</sup>	423	0.726	1.454	$1s^2(n = 2) \rightarrow 1s(n = 2)^2$

Table 3.2: Radiative decay rates for Ar and Fe ions.

ion	transition	decay rate ( $s^{-1}$ )	mean traveling distance ( $\mu\text{m}$ )
Ar <sup>17+</sup>	$1s - 2p$	$6.6 \times 10^{13}$	4.6
Ar <sup>16+</sup>	$1s^2 - 1s2p \ ^1P_1$	$1.1 \times 10^{14}$	2.8
Ar <sup>16+</sup>	$1s^2 - 1s2p \ ^3P_1$	$1.8 \times 10^{12}$	170
Fe <sup>25+</sup>	$1s - 2p$	$2.9 \times 10^{14}$	1.2
Fe <sup>24+</sup>	$1s^2 - 1s2p \ ^1P_1$	$4.6 \times 10^{14}$	0.69
Fe <sup>24+</sup>	$1s^2 - 1s2p \ ^3P_1$	$4.4 \times 10^{13}$	7.2

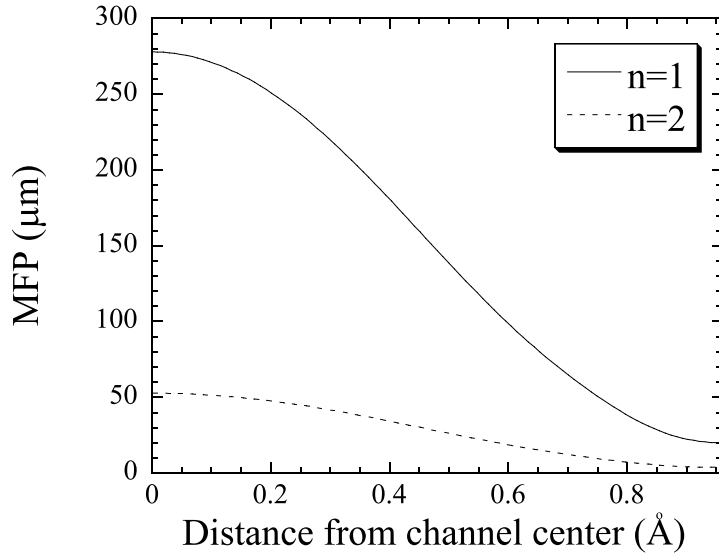


Figure 3.1: MFP for electron impact ionization for 390 MeV/u Ar<sup>17+</sup> ions. The solid and dashed lines show the MFPs for the  $n=1$  and  $n=2$  states, respectively.

impact ionization is written as  $\lambda_i = 1/(n_e \sigma_i)$ , where  $n_e$  is the electron density, which is shown in Fig. 1.3. Figure 3.1 and 3.2 show the calculated  $\lambda_i$  as a function of distance from the channel center for 390 MeV/u Ar<sup>17+</sup> and 460 MeV/u Fe<sup>25+</sup> ions. The MFP  $\lambda_i$  decreases with increasing the distance from the channel center, reflecting the electron density. It is noted that the ionization cross section due to the target nuclear impact is not included here, which is dominant near the atomic plane. For random orientation, the ionization cross sections including the nuclear and electron impacts are shown in table 3.3 [63]. Most of the ions are ionized for random orientation, because the target thickness (21  $\mu\text{m}$ ) is larger than  $\lambda_i$ .

In the present high energy region, electron capture processes such as non-radiative and radiative electron captures are negligible. The cross section for the non-radiative electron

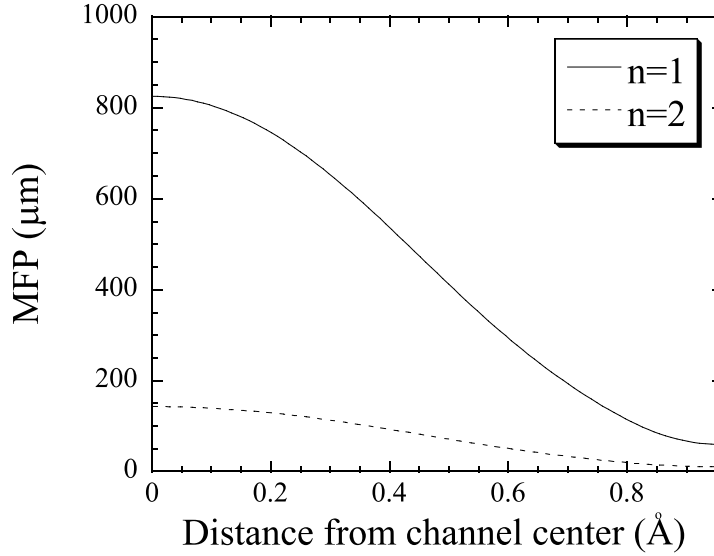


Figure 3.2: MFP for electron impact ionization for 460 MeV/u  $\text{Fe}^{25+}$  ions. The solid and dashed lines show the MFPs for the  $n=1$  and  $n=2$  states, respectively.

Table 3.3: Ionization cross sections and MFPs for 390 MeV/u  $\text{Ar}^{17+}$  and 460 MeV/u  $\text{Fe}^{25+}$  ions incident on Si [63].

	$\sigma_i(1s)$	$\lambda_i(1s)$	$\sigma_i(2p)$	$\lambda_i(2p)$
390 MeV/u $\text{Ar}^{17+}$	$4.6 \times 10^{-20} \text{ cm}^2$	$4.3 \text{ } \mu\text{m}$	$1.9 \times 10^{-19} \text{ cm}^2$	$1.0 \text{ } \mu\text{m}$
460 MeV/u $\text{Fe}^{25+}$	$2.1 \times 10^{-20} \text{ cm}^2$	$9.4 \text{ } \mu\text{m}$	$1.1 \times 10^{-19} \text{ cm}^2$	$1.9 \text{ } \mu\text{m}$

Table 3.4: Half of the path length per Rabi oscillation,  $\lambda_R/2$ .

distance from channel center	0 Å	0.72 Å
$\text{Ar}^{17+}$	6.7 $\mu\text{m}$	0.9 $\mu\text{m}$
$\text{Fe}^{25+}$	15 $\mu\text{m}$	1.1 $\mu\text{m}$

capture (NRC) scales as

$$\sigma_{NRC} \propto \frac{Z_p^5 Z_t^5}{v^{11}}, \quad (3.2)$$

where  $Z_p$  is the projectile atomic number,  $Z_t$  is the target atomic number, and  $v$  is the projectile velocity [64]. For radiative electron capture (REC), the cross section scales as

$$\sigma_{REC} \propto \frac{Z_p^5 Z_t}{v^5}. \quad (3.3)$$

Both cross sections decrease with increasing  $v$ . The electron capture cross sections including the non-radiative and radiative captures to the  $1s$  are estimated to be  $1 \times 10^{-24}$  and  $3 \times 10^{-24}$   $\text{cm}^2$  for 390 MeV/u  $\text{Ar}^{17+}$  and 460 MeV/u  $\text{Fe}^{25+}$  ions incident on Si, respectively [63].

From the squared transition matrix element shown in Fig. 1.15 and 1.18, we estimated the path length per Rabi oscillation  $\lambda_R$  for the RCE from  $1s$  to  $n = 2$ . Table 3.4 shows  $\lambda_R/2$  at the distances of 0 and 0.72 Å, which is  $(3/4)(d_p/2)$  ( $d_p$  is the distance between the (220) atomic planes of Si, 1.92 Å). In this calculation, as the absolute value of the transition matrix element, we used one averaged over the  $n = 2$  states (Level 1 – 4).

### 3.1 Hydrogen-like $\text{Ar}^{17+}$ ions

First, we attempted to observe the RCE of 390 MeV/u  $\text{Ar}^{17+}$  ions. The experimental setup used for this measurement is described in section 2.2. A beam of 390 MeV/u  $\text{Ar}^{17+}$  ions was injected into a 21  $\mu\text{m}$ -thick Si crystal. In this case, the dwell time of the ion in the Si crystal is 99 fs. The crystal thickness is larger than  $\lambda_R/2$  as shown in table 3.4, indicating that the crystal is thick enough to lead to the RCE. As shown in table 3.2, the mean traveling distances for the radiative decays are shorter than the crystal thickness (except for  $^3P_1$  in  $\text{Ar}^{16+}$  ions), so that most of the deexcitation X-rays are emitted inside the Si crystal. Moreover, around the channel center,  $\lambda_i$  for  $n=2$  is longer than the mean traveling distances for the radiative decays, which means that the deexcitation process is dominant around the channel center. On the other hand, near the atomic plane, the ionization process is dominant due to the electron and nuclear impacts.

The Si crystal was mounted on the three-axis goniometer so that the (220) plane of the crystal is horizontal. The projectile ions were channeled in the (220) plane. To fulfill the resonance condition, we scanned the angle  $\theta$  by tilting the crystal under the (220) planar

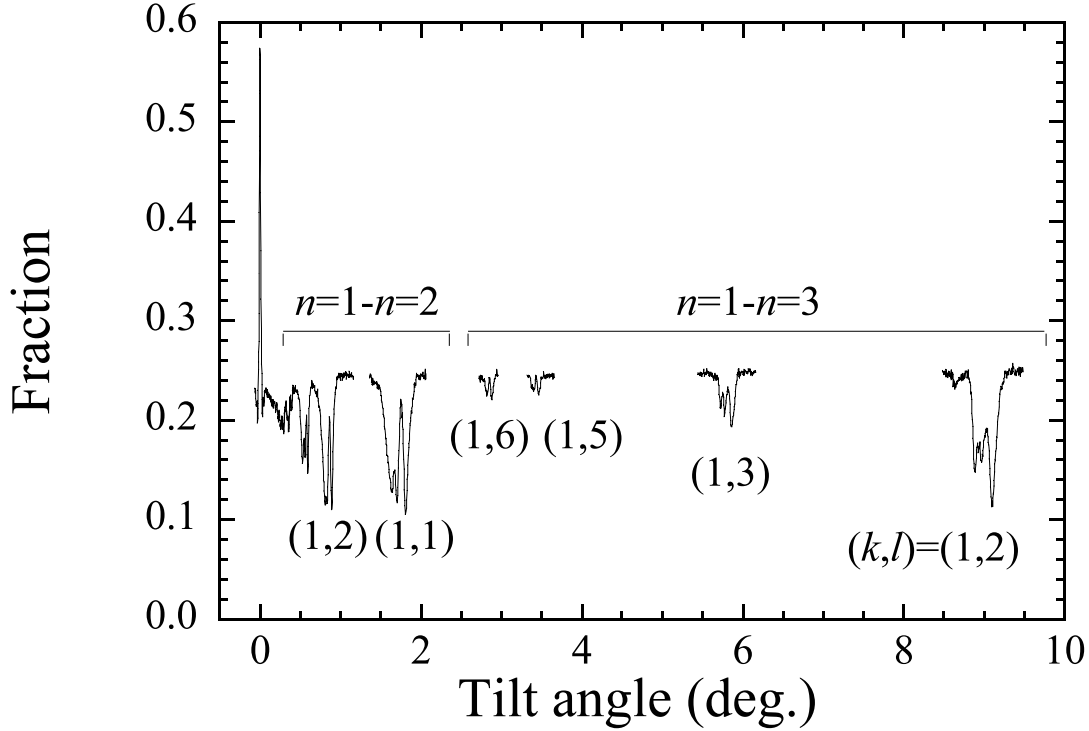


Figure 3.3: Fraction of  $\text{Ar}^{17+}$  ions transmitted through the Si crystal for 390 MeV/u  $\text{Ar}^{17+}$  incidence.

channeling condition, *i.e.*, keeping the (220) plane horizontal. In this case,  $\theta$  is the angle of the  $\langle 110 \rangle$  axis with respect to the beam direction. If the RCE occurs, the fraction of ionized  $\text{Ar}^{18+}$  ions is expected to be enhanced, because the electron orbital radius of the excited ion is large, and therefore the electron is easily stripped off inside the crystal due to the electron or nuclear impact. Moreover, the deexcitation X-rays from the projectile ions are also expected to be enhanced due to the increase of the population of the excited states. Accordingly, to observe the RCE, we measured the charge state distribution of the ions transmitted through the crystal and deexcitation X-rays from the projectile ions.

Figure 3.3 shows the charge state distribution of the transmitted ions as a function of the tilt angle  $\theta$  from the  $\langle 110 \rangle$  axis. The fractions of  $\text{Ar}^{17+}$  and  $\text{Ar}^{18+}$  ions were obtained as

$$F(\text{Ar}^{17+}) = \frac{N(\text{Ar}^{17+})}{N(\text{Ar}^{17+}) + N(\text{Ar}^{18+})}, \quad (3.4)$$

$$F(\text{Ar}^{18+}) = \frac{N(\text{Ar}^{18+})}{N(\text{Ar}^{17+}) + N(\text{Ar}^{18+})}, \quad (3.5)$$

where  $N(\text{Ar}^{17+})$  and  $N(\text{Ar}^{18+})$  are the yields of  $\text{Ar}^{17+}$  and  $\text{Ar}^{18+}$  ions after transmitting through the crystal, respectively. In such a high energy region, the electron capture process is negligible. Indeed,  $\text{Ar}^{q+}$  ( $q \leq 16$ ) ions were not observed. As shown in Fig.

3.3, the fraction of Ar<sup>17+</sup> ions decreased at the resonance conditions. The resonances of  $1s \rightarrow n = 2$  ( $(k, l) = (1, 1), (1, 2), \dots$ ) and  $1s \rightarrow n = 3$  ( $(k, l) = (1, 2), (1, 3), (1, 5)$ , and  $(1, 6)$ ) are seen in Fig. 3.3. Due to the destructive interference originating from the crystal structure (diamond structure), the RCE for  $(k, l) = (1, 4)$  does not occur [29, 18]. Under the off-resonance (planar channeling) condition, the fraction of Ar<sup>17+</sup> was  $\sim 25\%$ . Under the  $\langle 110 \rangle$  axial channeling condition ( $\theta = 0^\circ$ ), on the other hand, its fraction was  $\sim 57\%$ . In the present work, we observed the RCE from  $1s$  to  $n = 2, n = 3, n = 4$ , and  $n = 5$  states, which will be discussed later.

### 3.1.1 RCE from $1s$ to $n = 2$ states

#### *Charge state distribution*

Figure 3.4 shows the charge state distribution for the RCE ( $(k, l) = (1, 1)$ ) from  $1s$  to  $n = 2$  states as a function of transition energy, which is given by

$$E_{trans} = \frac{h\gamma v}{a}(\sqrt{2}k \cos \theta + l \sin \theta). \quad (3.6)$$

Under the off-resonance condition, the fraction of Ar<sup>17+</sup> was  $\sim 45\%$ . This fraction is larger than that observed in Fig. 3.3. This charge state distribution was measured using a Si crystal different from that used in Fig. 3.3. This indicates that the fraction of Ar<sup>17+</sup> ions under the planar channeling condition depends on the crystal quality. The angular spread of the beam also affects the fraction.

We observed two peaks corresponding to the excitations  $1s \rightarrow n = 2(j = 3/2)$  and  $1s \rightarrow n = 2(j = 1/2)$ , which had tails toward the higher energy side and the lower energy side, respectively. Moreover, the  $j = 1/2$  peak was split into two peaks. These structures originate from the Stark effect due to the static crystal field, and are consistent with the calculated transition energies shown in Fig. 1.13.

#### *Deexcitation X-rays*

We also measured deexcitation X-rays from the projectile ions using two Si(Li) detectors [65]. As stated in section 2.2, one detector was placed on the horizontal plane and the other was placed on the vertical plane. The X-ray spectra measured with the horizontal Si(Li) for the resonance condition ( $E_{trans} = 3323$  eV) and the off-resonance condition are shown in Fig. 3.5. The intensities of the X-rays are normalized to that of the projectile ions. The peak seen in  $\sim 1.7$  keV is attributed to Si K X-rays, which was emitted from the target crystal. The peak seen in  $\sim 5$  keV is due to the deexcitation X-rays of  $n = 2 \rightarrow 1s$  in Ar<sup>17+</sup> ions. In the projectile frame, its energy is 3.3 keV. Due to the Doppler effect, its energy was shifted to 5 keV in the laboratory frame. The X-ray energy in the laboratory frame,  $E_l$ , is given by

$$E_l = \frac{E_p}{\gamma(1 - \beta \cos \theta_l)}, \quad (3.7)$$

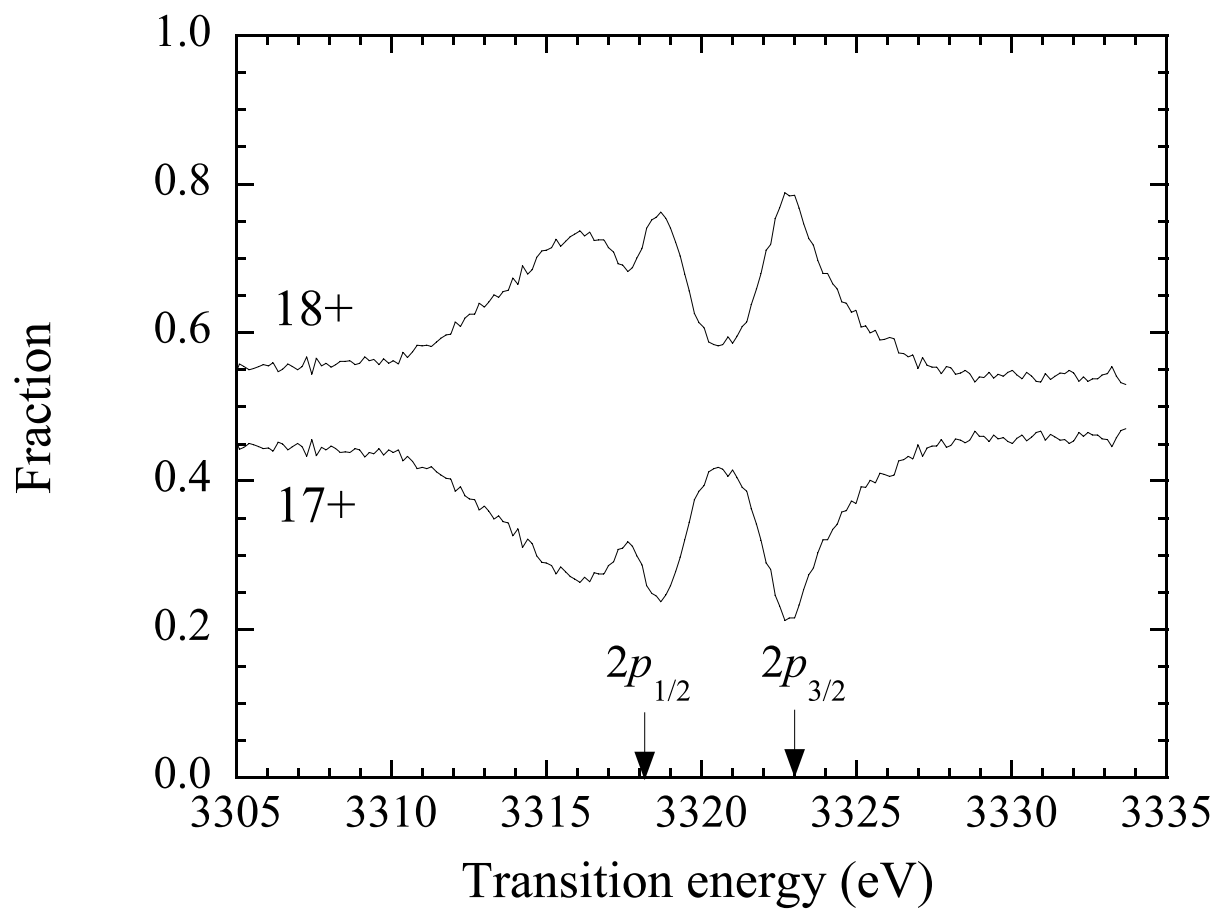


Figure 3.4: Charge state distribution of the ions transmitted through the Si crystal for  $1s \rightarrow n = 2$  in  $\text{Ar}^{17+}$  ions. The arrows show the theoretical transition energies in vacuum.

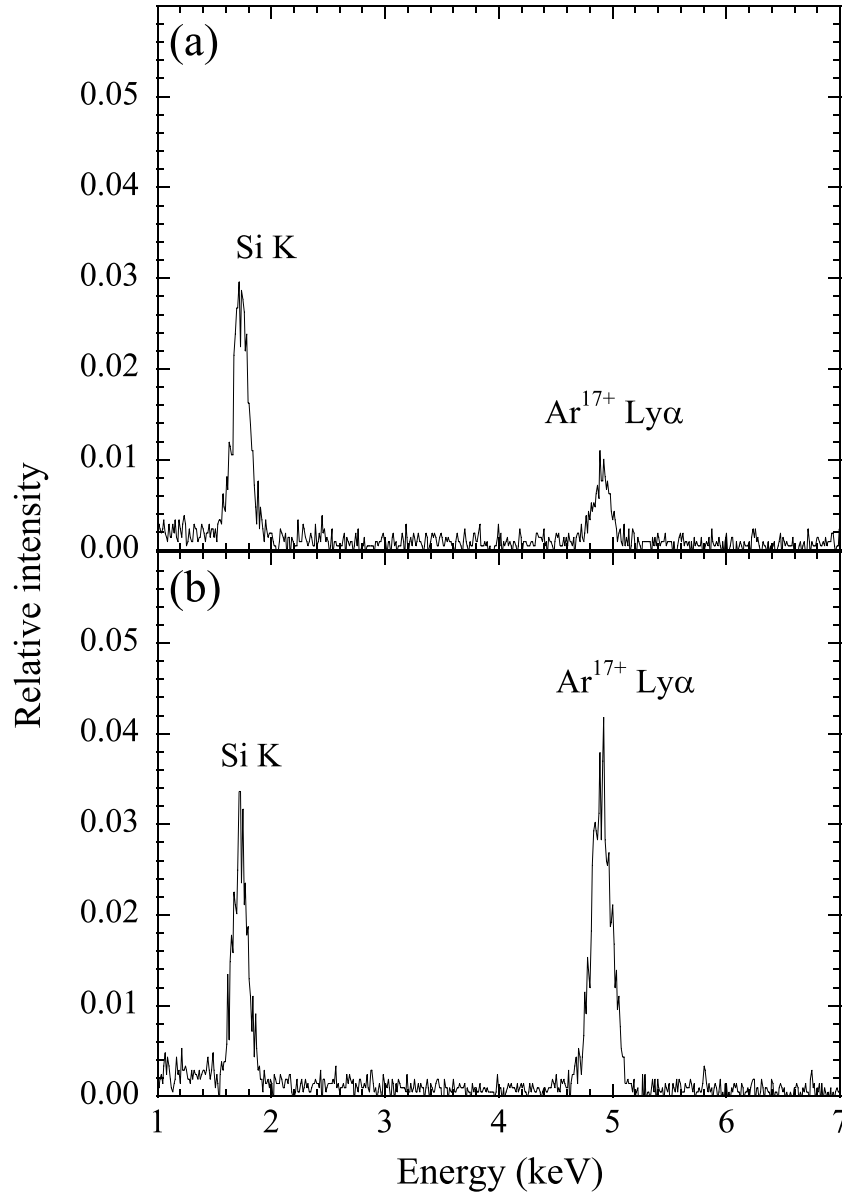


Figure 3.5: X-ray spectra for the (a) off-resonance and (b) resonance ( $E_{trans}=3323$  eV) conditions for  $1s \rightarrow n = 2$  in  $Ar^{17+}$  ions.

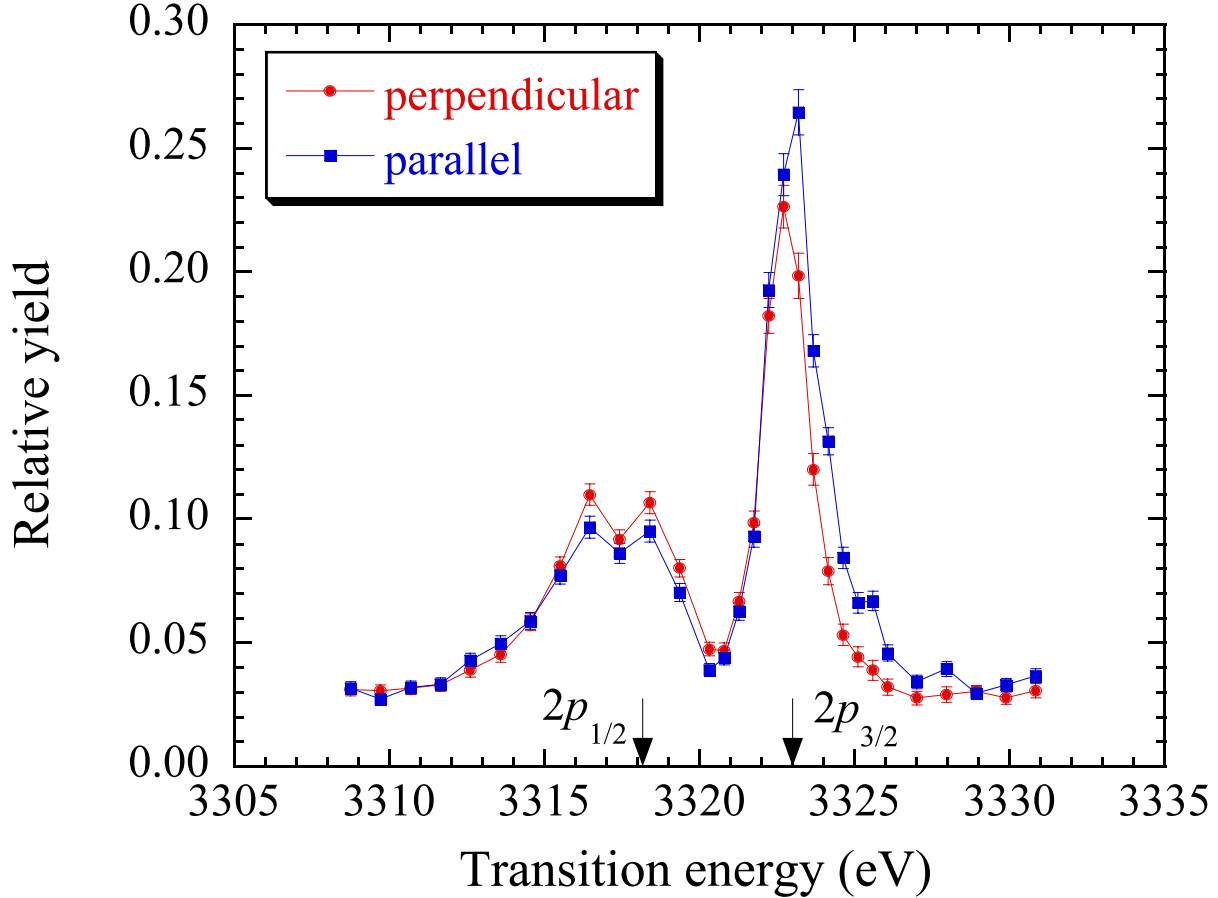


Figure 3.6: Yields of the deexcitation X-rays for  $n = 2 \rightarrow 1s$  in  $\text{Ar}^{17+}$  ions. The closed circle and square show the yields measured with the Si(Li) detectors placed on the vertical and horizontal planes, respectively. The arrows show the theoretical transition energies in vacuum.

where  $E_p$  is the X-ray energy in the projectile frame and  $\theta_l$  is the emission angle of the X-ray with respect to the beam direction in the laboratory frame.

From the measured X-ray spectra, we obtained the yields of the deexcitation X-rays as a function of tilt angle, which corresponds to the transition energy. The obtained yields are shown in Fig. 3.6. The X-ray intensity is plotted as the number of the X-rays emitted from the ions assuming that the angular distribution of the X-rays is isotropic in the projectile frame. Here, the attenuation of the X-ray in the Si crystal is not taken into account. The attenuation length for 5 keV X-ray in Si is  $16 \mu\text{m}$ , so that the yields of the X-rays emitted at the crystal entrance decreases to 18% when they reach the detector. As shown in Fig. 3.6, the peak height for the  $j = 1/2$  was smaller than for the  $j = 3/2$ . This is due to the fact that the fraction of the  $2s$  state included in the  $n = 2$  states at  $j = 1/2$  peak is large compared to that at  $j = 3/2$  peak as shown in Fig. 1.14, and

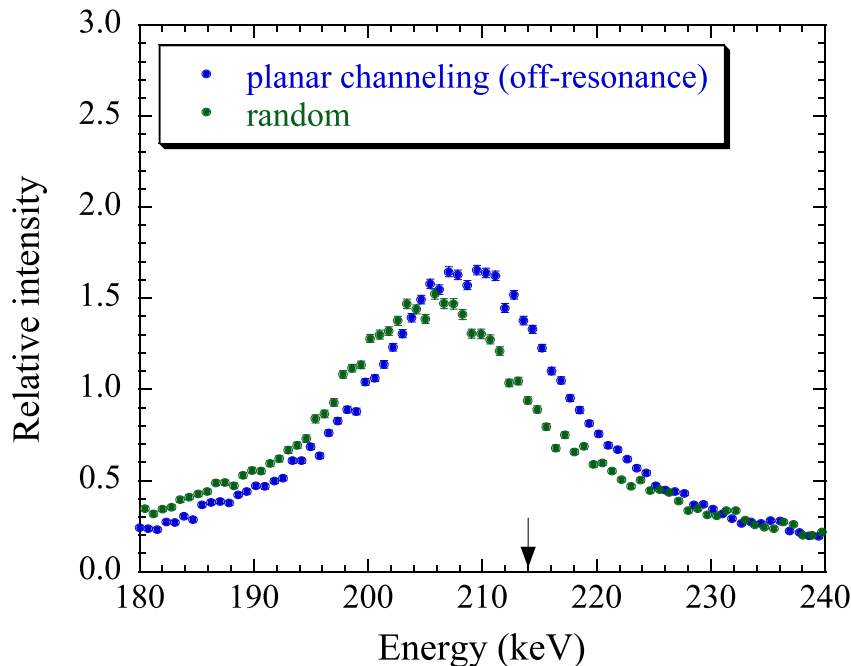


Figure 3.7: Energy spectra of convoy electrons for the random orientation and (220) planar channeling (off-resonance). The arrow shows the energy of the electron with the same velocity as the incident ion.

that the lifetime of  $2s$  is longer than that of  $2p$ . Around  $E_{trans} = 3325$  eV, anisotropy of the deexcitation X-rays were observed. The peak position for the X-rays emitted in the direction parallel to the (220) plane was shifted to the higher energy side compared to that for the X-rays emitted in the direction perpendicular to the (220) plane. This is explained by the wave functions of the Stark-mixed  $n = 2$  states. As shown in Fig. 1.13 and 1.14, Level 4 is excited around  $E_{trans} = 3325$  eV, and the main composition of Level 4 is  $2p_x$ , which tends to emit deexcitation X-rays strongly in the direction perpendicular to the  $x$  axis.

### *Convoy electrons*

We also measured the energy spectra of convoy electrons for 390 MeV/u  $Ar^{17+}$  ions incident on a 21  $\mu\text{m}$ -thick Si crystal. Figure 3.7 shows the energy spectra for the random orientation and (220) planar channeling (off-resonance). The stopping power for 214 keV electrons in Si is 0.51 keV/ $\mu\text{m}$  [66], and the ionization MFP for the  $1s$  electron is 4  $\mu\text{m}$ . Accordingly, in the case of the random orientation, the electron energy loss is estimated to be  $\sim 9$  keV, which is in good agreement with the observed value. We observed the following features in the electron spectra. (i) The peak energy (205 keV) for the random orientation was lower than that (208 keV) for the planar channeling. (ii) The peak width (23 keV) for the random orientation was larger than that (22 keV) for the planar channeling. (iii) The

yields for the random orientation were smaller than for the planar channeling. These observed features ((i)-(iii)) indicate that the energy loss, energy straggling, and angular straggling of the convoy electrons for the random orientation are more significant than for the planar channeling. For the random orientation, the convoy electrons are considered to suffer more collisions than for the planar channeling, since the ionization MFP for the random orientation is shorter than for the planar channeling, *i.e.*, the convoy electrons are created in the shallower region of the crystal.

Figure 3.8 shows the energy spectra of convoy electrons for the off-resonance (planar channeling) condition and RCE condition ( $E_{trans} = 3323$  eV). The spectrum for the off-resonance condition is the same as that shown in Fig. 3.7. The following features were observed in the electron spectra. (i)The peak energy (208 keV) for the off-resonance condition was slightly higher than that (207 keV) for the RCE condition. (ii)The peak width (22 keV) for the off-resonance condition was larger than that (16 keV) for the RCE condition. (iii)The yields for the off-resonance condition were smaller than for the RCE condition. The feature (i) may be due to the fact that the ionization MFP for the RCE condition is shorter than for the off-resonance condition, *i.e.*, the mean path length of the electron lost from the ion inside the crystal for the RCE condition is longer than for the off-resonance condition. The feature (ii) is explained by the contribution of the projectile excited states to the convoy electron production. Similar feature was observed in the case of the carbon foil targets (see Appendix B). The feature (iii) results from the enhancement of the ionization process due to the RCE.

We measured the energy spectra of convoy electrons at various RCE conditions (see Fig. 3.9). To extract the information on the energy spectra of the electrons emitted from the excited states, we subtracted the spectrum for the off-resonance (planar channeling) from those for the RCE conditions. The obtained spectra are shown in Fig. 3.10. The intensities are normalized to unity at the peak positions.

The peak energy was  $\sim 208$  keV, and its width (FWHM) was  $\sim 14$  keV. The spectrum shapes were slightly asymmetric. The reason is not clear. This feature may be due to the transport process of the electron inside the crystal. The significant differences between the obtained convoy electron spectra were not observed. This indicates that there are not large differences between the  $n = 2$  states from which the electrons are emitted at various RCE conditions.

The peak height of the convoy electron spectrum is plotted as a function of transition energy in Fig. 3.11. This profile was expected to be similar to that for the fraction of  $\text{Ar}^{18+}$  ions, because the yields of the electrons lost from the projectile ions are proportional to that of  $\text{Ar}^{18+}$  ions. However, the observed profile was slightly different from that for the fraction of  $\text{Ar}^{18+}$  ions. The reason of this difference is not understood. The transport process of the convoy electrons inside the crystal may lead to this feature.

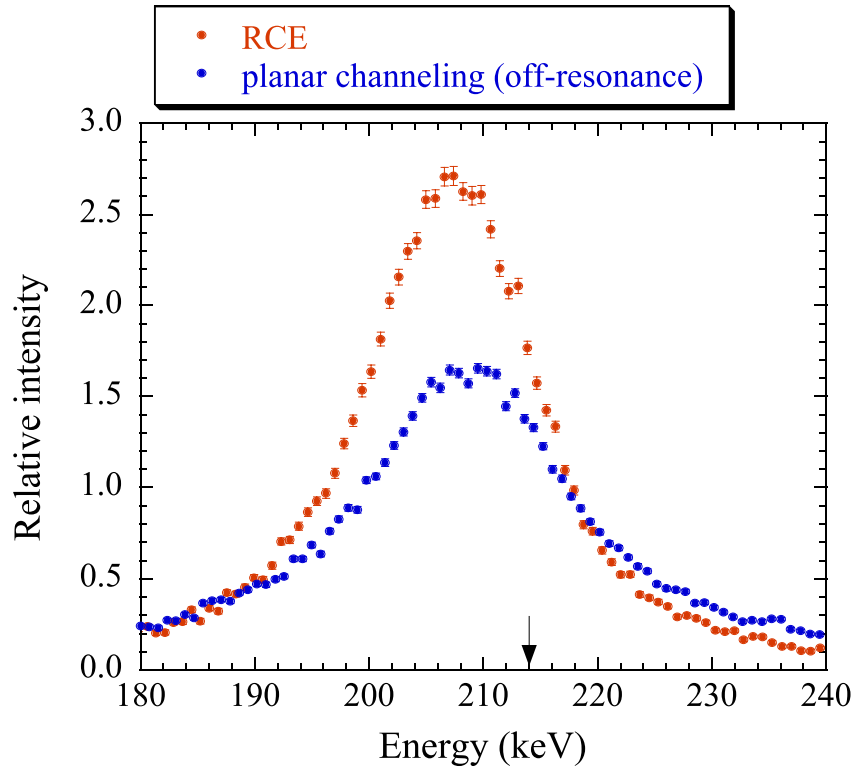


Figure 3.8: Energy spectra of convoy electrons for the (220) planar channeling (off-resonance) and RCE condition. The arrow shows the energy of the electron with the same velocity as the incident ion. The spectrum for the off-resonance condition is the same as that shown in Fig. 3.7.

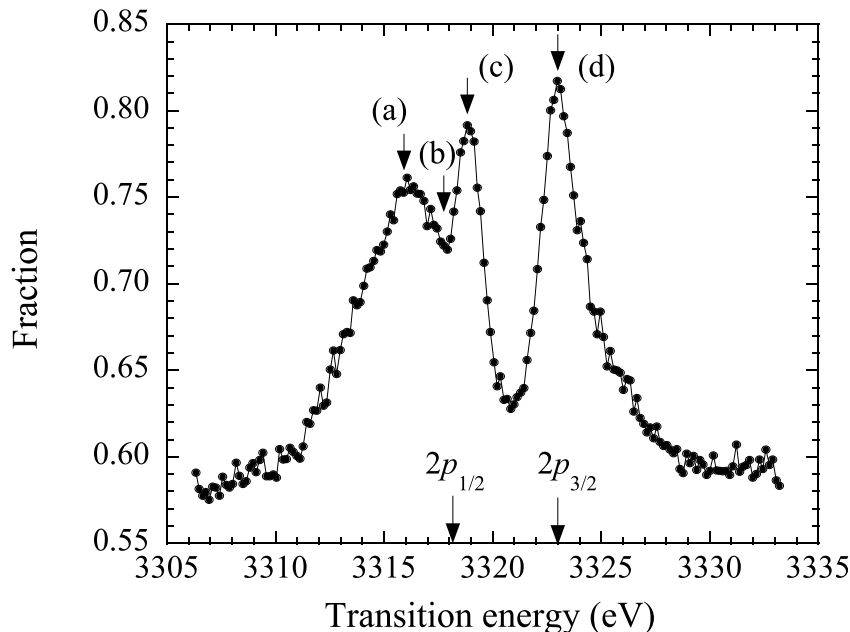


Figure 3.9: Fraction of  $\text{Ar}^{18+}$  ions transmitted through the crystal. The arrows ((a)-(d)) show the resonance conditions in which the convoy electron spectra were measured.

### 3.1.2 RCE from $1s$ to $n = 3$ states

#### *Charge state distribution*

Figure 3.13 shows the survived fraction of  $\text{Ar}^{17+}$  ions for the RCE from  $1s$  to  $n = 3$  states in  $\text{Ar}^{17+}$  ions. The RCE for  $(k, l) = (1, 4)$  was not observed, which is due to the destructive interference originating from the crystal structure [28, 18]. For the (220) plane of a Si crystal, the RCE for  $(k, l)$  satisfying  $2k + l = 4n + 2$  ( $n$  is an integer) does not occur. In Fig. 3.13, the dashed lines show the theoretical transition energies of  $1s \rightarrow 3p_{3/2}$  and  $1s \rightarrow 3p_{1/2}$  in vacuum. In contrast to the case of the  $n = 2$  states, the observed peak positions are not in agreement with these theoretical values. This may be due to the Stark effect. The Stark effect on the  $n = 3$  states is large compared to that of the  $n = 2$  states. We estimated the energy shifts of the  $n = 3$  states due to the Stark effect using the perturbation theory [67]. The observed peak shift was found to be large compared to the calculated energy shift.

In 1996, Forster *et al.* observed the RCE from  $1s$  to the  $n = 3$  states in hydrogen-like  $\text{Si}^{13+}$  ions [20]. However, the structure of the resonance profile was not obtained clearly. In the present measurement, the resonance profile for the  $n = 3$  states was clearly observed for the first time.

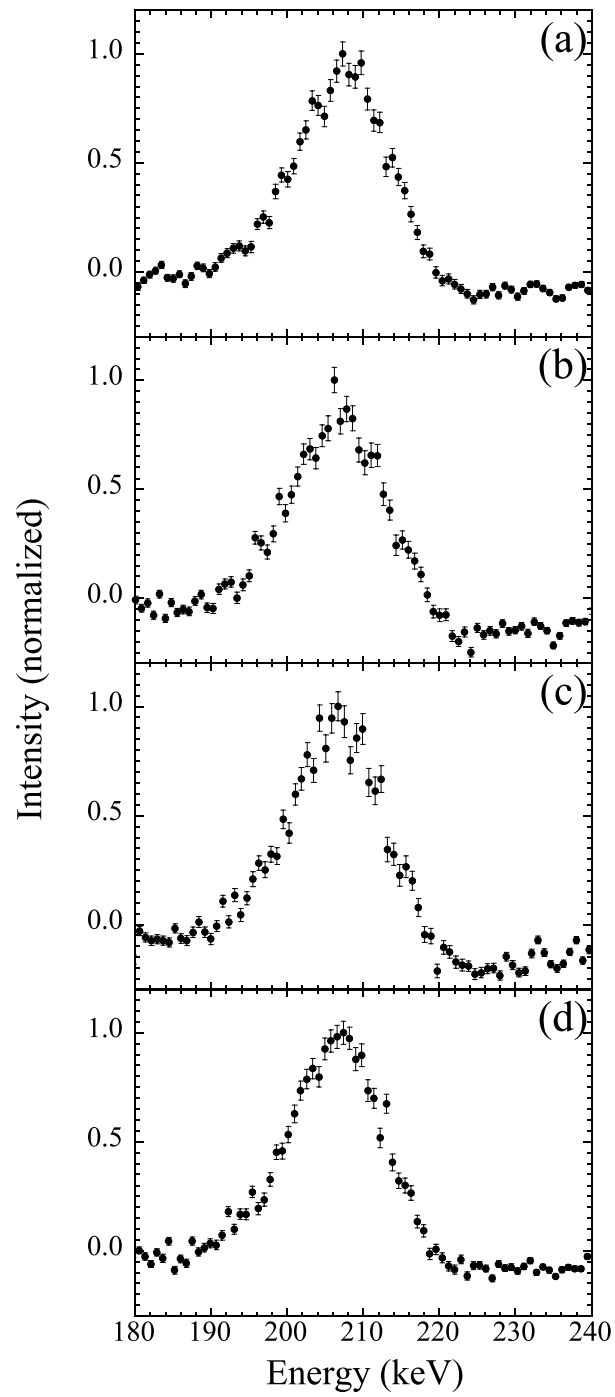


Figure 3.10: Energy spectra of convoy electrons under the RCE conditions. The spectrum for the off-resonance was subtracted.

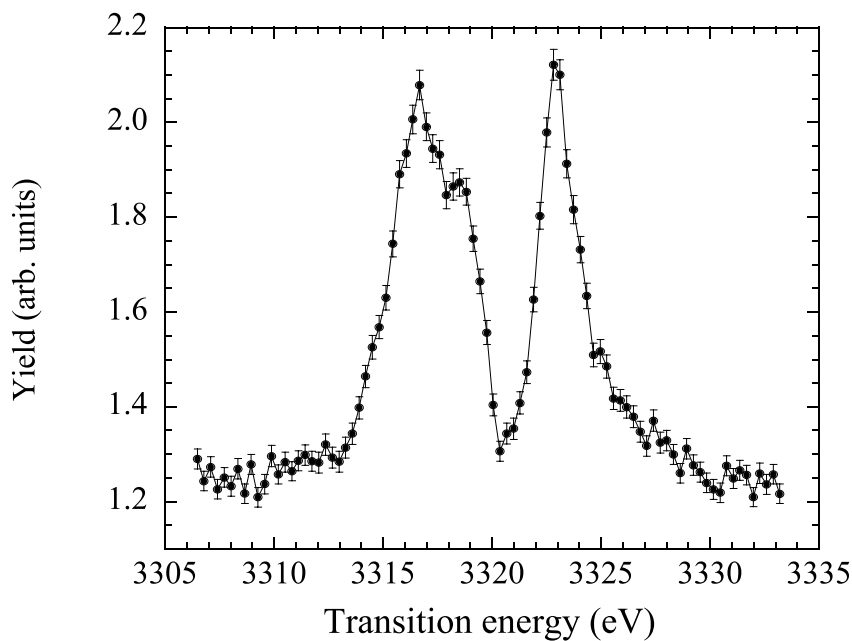


Figure 3.11: Peak height of the energy spectra of convoy electrons.

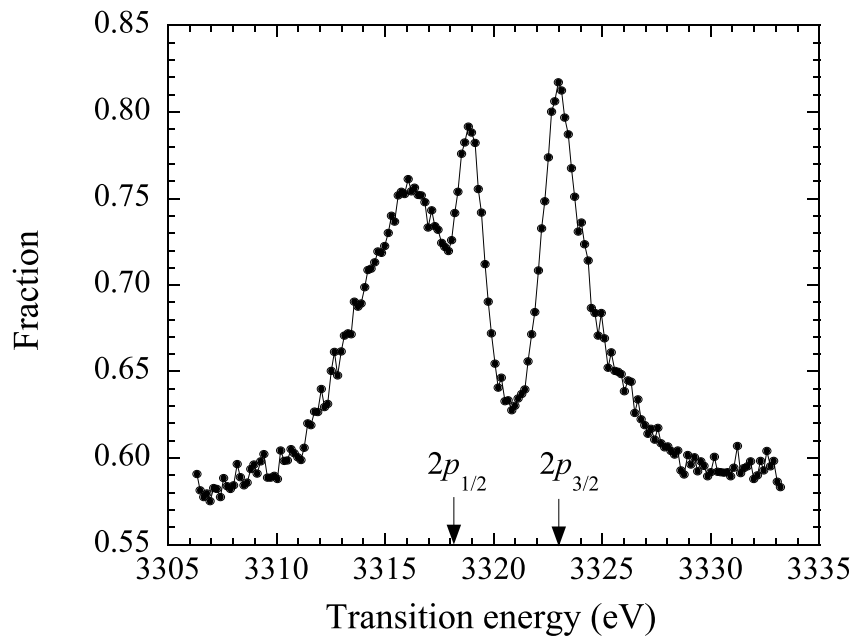


Figure 3.12: Fraction of  $\text{Ar}^{18+}$  ions transmitted through the Si crystal (Same as Fig. 3.9). The arrows show the theoretical transition energies in vacuum.

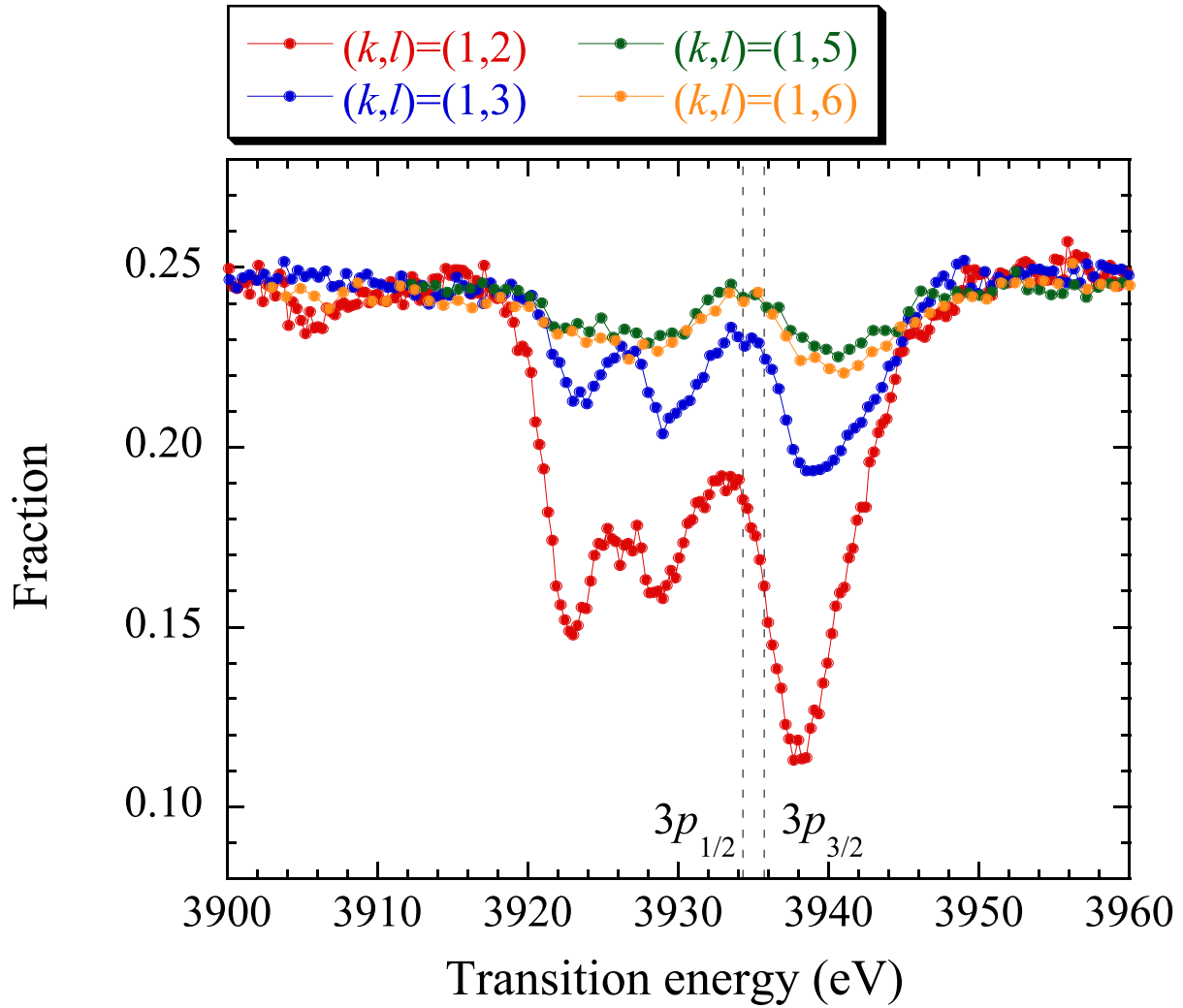


Figure 3.13: Fraction of  $Ar^{17+}$  ions transmitted through the Si crystal for  $1s \rightarrow n = 3$  in  $Ar^{17+}$  ions. The vertical dashed lines show the transition energies in vacuum for  $3p_{3/2}$  and  $3p_{1/2}$ .

### ***Deexcitation X-rays***

We also measured the X-ray spectra under the resonance ( $E_{trans}=3938$  eV,  $(k, l)=(1,2)$ ) and the off-resonance conditions, which is shown in Fig. 3.14. The peak seen in  $\sim 6$  keV is due to  $\text{Ly}\beta$  ( $n = 3 \rightarrow 1s$ ) X-rays from  $\text{Ar}^{17+}$  ions, whose energies were Doppler-shifted from 3.9 keV to  $\sim 6$  keV. Under the resonance condition, as expected, the yields of the deexcitation X-rays increased.

### **3.1.3 RCE from $1s$ to $n = 4$ and $n = 5$ states**

We also observed the RCE from  $1s$  to the  $n = 4$  and  $n = 5$  states. The obtained resonance curves for the survived charge fractions are shown in Fig. 3.15 and Fig. 3.16. The dashed lines show the transition energies for  $1s \rightarrow 4p$  and  $5p$  in vacuum [68]. The widths of the resonance peaks were large compared to the case of the  $n = 2$  and  $n = 3$  states. These structures are affected by the Stark effect. To understand these structures quantitatively, the calculation on the energy levels of such highly excited states inside the crystal is needed.

## **3.2 Helium-like $\text{Ar}^{16+}$ ions**

The excitation (RCE) energy,

$$E_{RCE} = \frac{h\gamma v}{a}(\sqrt{2}k \cos \theta + l \sin \theta), \quad (3.8)$$

is shown in Fig. 3.17 as a function of tilt angle  $\theta$  for 383 MeV/u ions. The black lines show the excitation energies for  $(k, l) = (1, -1), (1, 0), (1, 1), (1, 2), (1, 3), (1, 5),$  and  $(1, 6)$ . The horizontal lines show the transition energies of  $\text{Ar}^{17+}$  ( $1s \rightarrow n = 2$  and  $n = 3$ ) and  $\text{Ar}^{16+}$  ( $1s^2 \rightarrow 1s2p$  and  $1s3p$ ) ions. The RCE condition is fulfilled when the excitation energy coincides with the transition energy of the ion. We chose the beam energy (383 MeV/u) so that the RCE conditions are not overlapped with each other, as shown in Fig. 3.17.

### ***Charge state distribution***

Figure 3.18 shows the charge state distribution of the transmitted ions as a function of tilt angle for 383 MeV/u  $\text{Ar}^{16+}$  incidence. Around  $1.85^\circ$  and  $2.25^\circ$ , the fraction of  $\text{Ar}^{16+}$  ions decreased, and, on the other hand, the fractions of  $\text{Ar}^{17+}$  and  $\text{Ar}^{18+}$  ions increased. These two peaks correspond to the RCE of  $\text{Ar}^{16+}$  ions. At the angles from  $2.5^\circ$  to  $3.0^\circ$ , the fraction of  $\text{Ar}^{17+}$  ( $\text{Ar}^{18+}$ ) ions decreased (increased) while that for  $\text{Ar}^{16+}$  ions did not change. As observed in section 3.1, these peaks are due to the RCE ( $(k, l) = (1, 1)$ ) of  $1s \rightarrow n = 2$  in  $\text{Ar}^{17+}$  ions.

The resonance profile for the RCE of  $\text{Ar}^{16+}$  ions as a function of transition energy is shown in Fig. 3.19. For the first time, we observed the resonance profile for helium-like

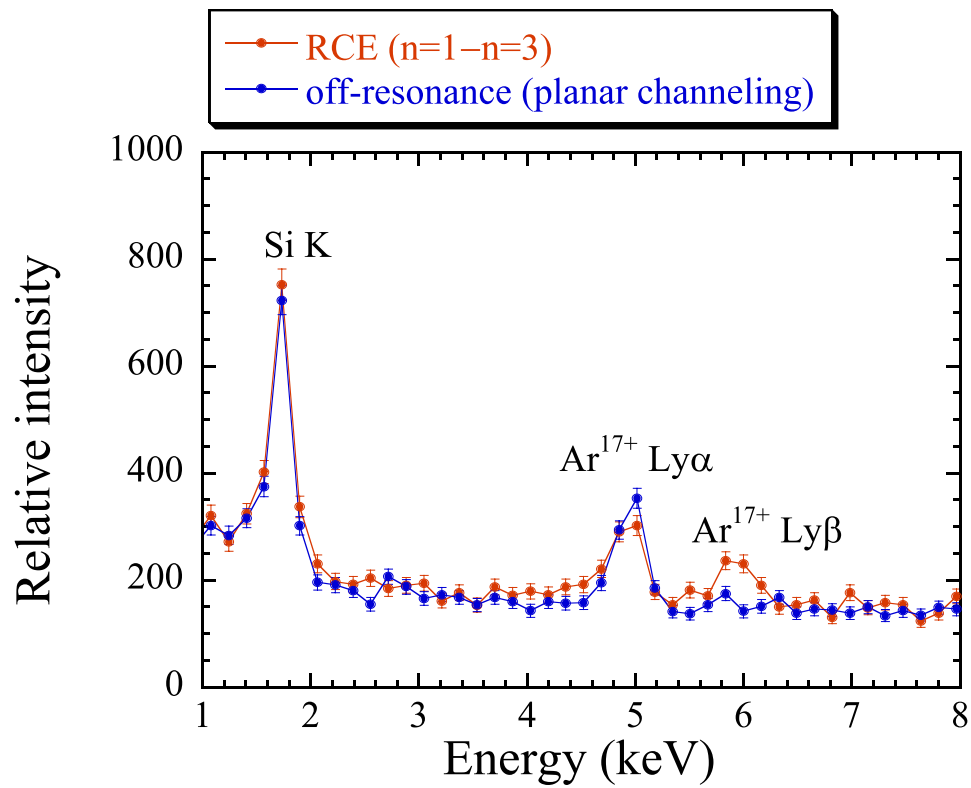


Figure 3.14: X-ray spectra under the resonance ( $E_{trans}=3938$  eV,  $(k, l)=(1, 2)$ ) and off-resonance conditions for  $1s \rightarrow n = 3$  in  $Ar^{17+}$  ions.

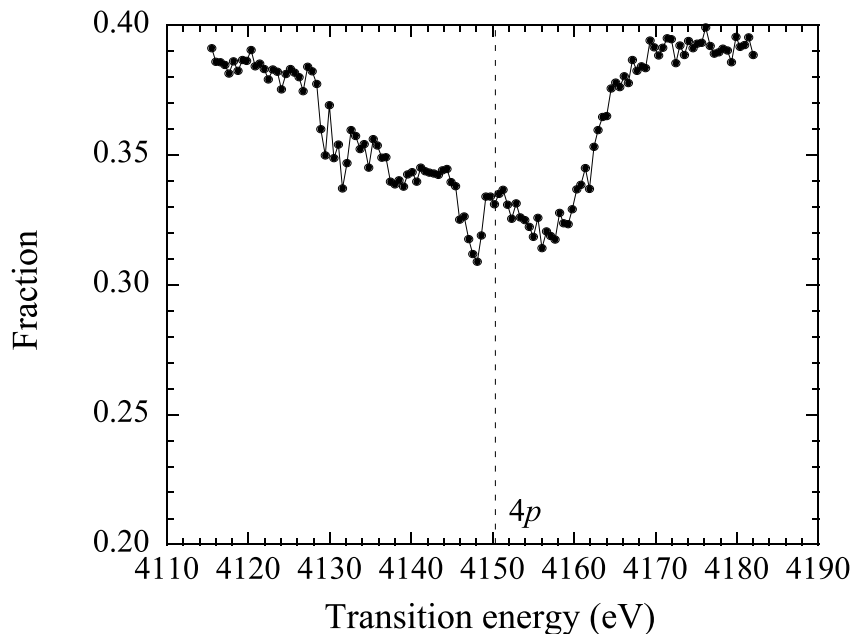


Figure 3.15: Fraction of  $\text{Ar}^{17+}$  ions transmitted through the Si crystal for  $1s \rightarrow n = 4$  in  $\text{Ar}^{17+}$  ions.  $(k, l) = (1, 2)$ . The dashed line shows the transition energy for  $1s \rightarrow 4p$  in vacuum.

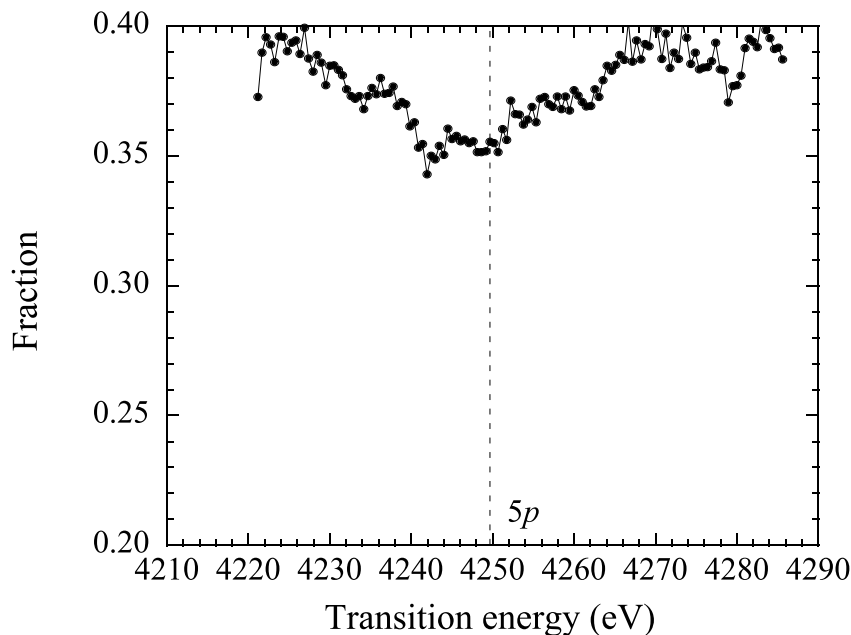


Figure 3.16: Fraction of  $\text{Ar}^{17+}$  ions transmitted through the Si crystal for  $1s \rightarrow n = 5$  in  $\text{Ar}^{17+}$  ions.  $(k, l) = (1, 2)$ . The dashed line shows the transition energy for  $1s \rightarrow 5p$  in vacuum.

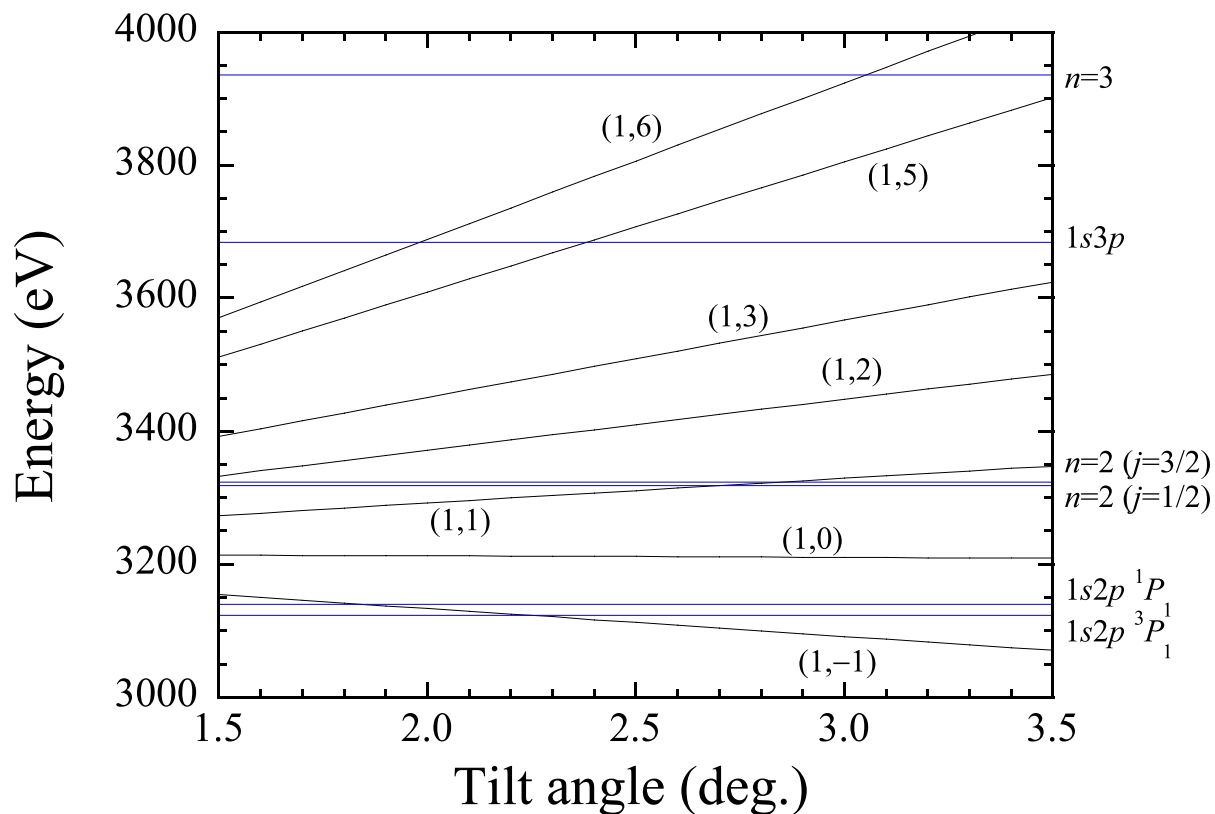


Figure 3.17: Excitation (RCE) energy as a function of tilt angle for 383 MeV/u ions. The black lines show the excitation energies for  $(k, l) = (1, -1), (1, 0), (1, 1), (1, 2), (1, 3), (1, 5),$  and  $(1, 6)$ . The horizontal lines show the transition energies of  $Ar^{17+}$  ( $1s \rightarrow n = 2$  and  $n = 3$ ) and  $Ar^{16+}$  ( $1s^2 \rightarrow 1s2p$  and  $1s3p$ ) ions.

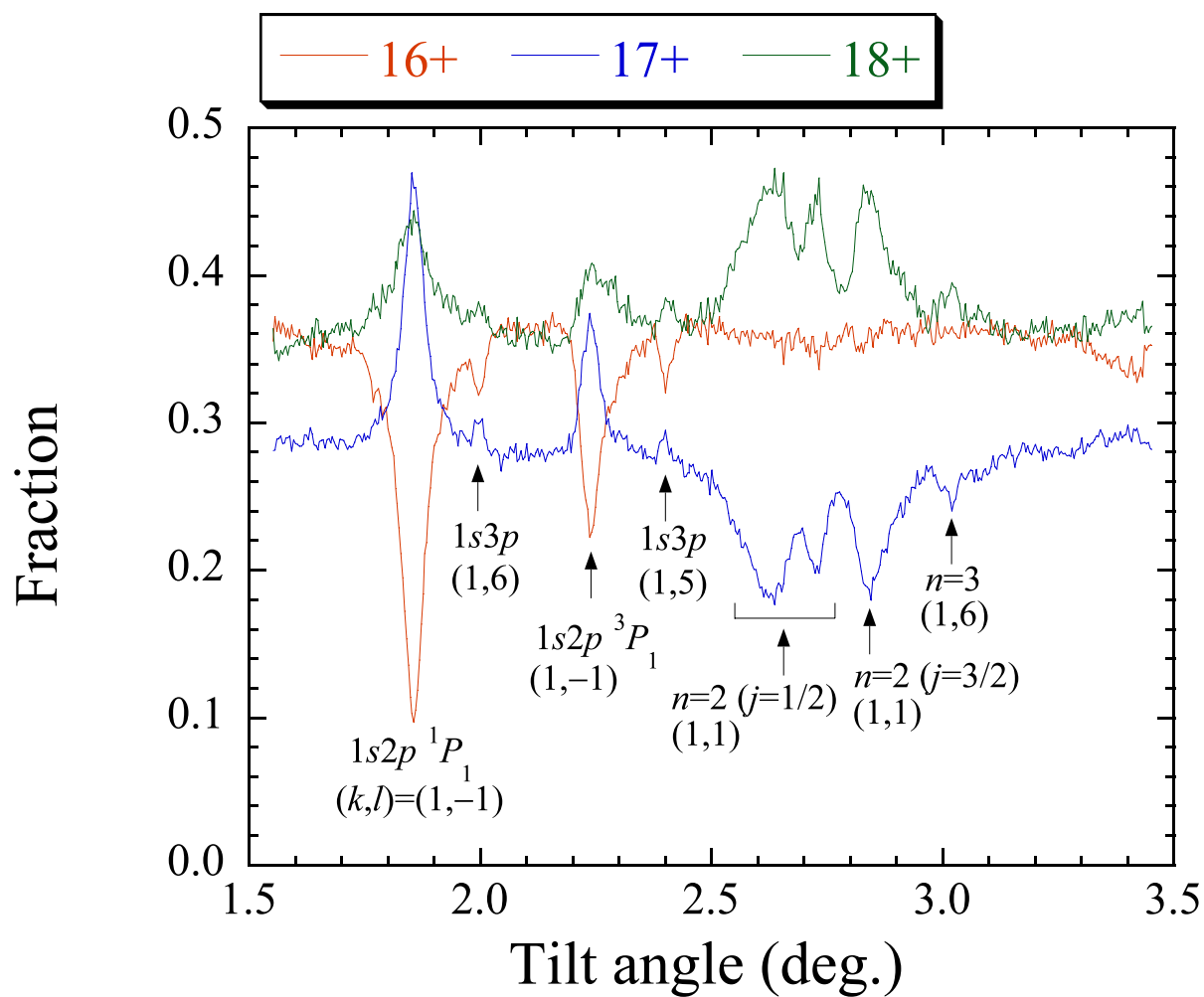


Figure 3.18: Charge state distribution of the ions transmitted through the Si crystal for 383 MeV/u  $\text{Ar}^{16+}$  incidence.

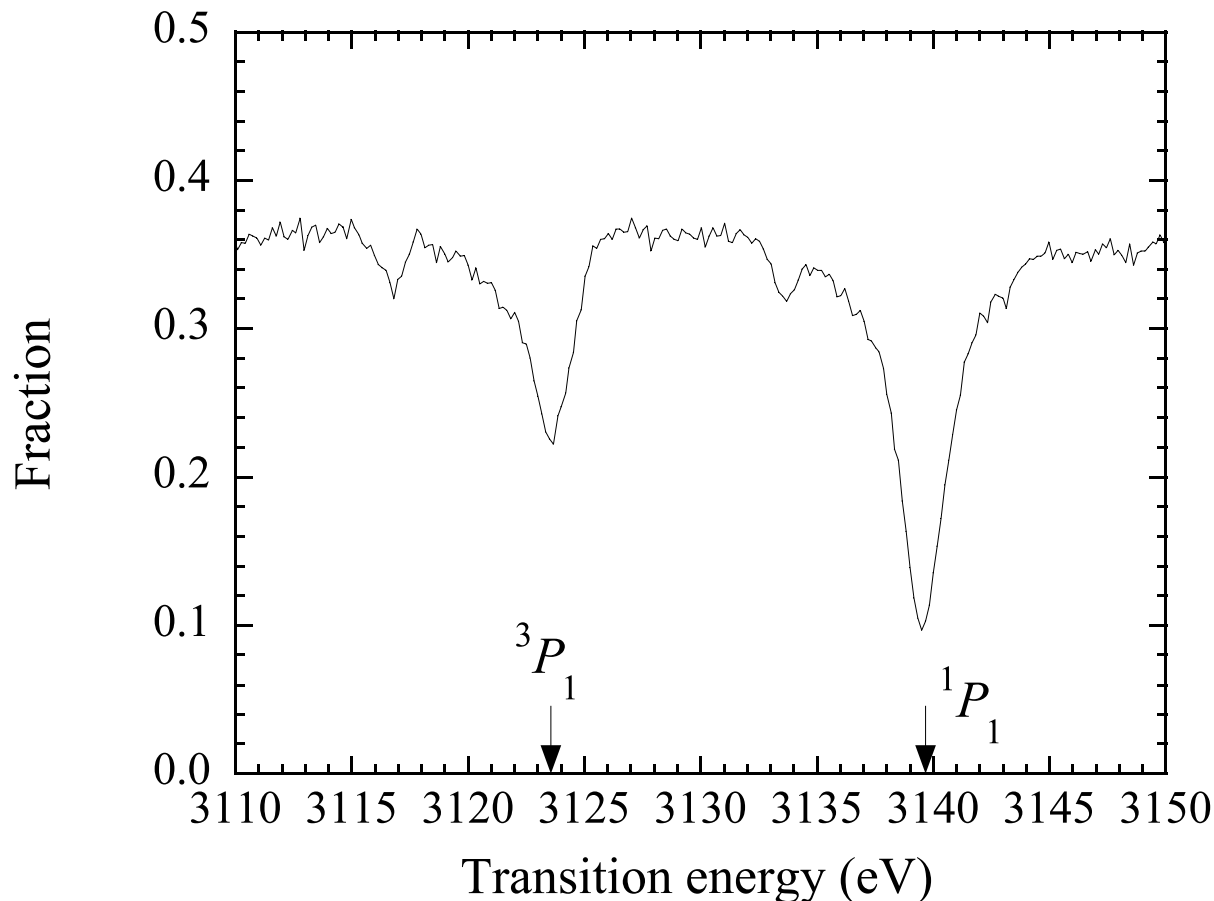


Figure 3.19: Fraction of  $\text{Ar}^{16+}$  ions transmitted through the Si crystal for  $1s^2 \rightarrow 1s2p\ ^1P_1$  and  $^3P_1$  in  $\text{Ar}^{16+}$  ions. The arrows show the theoretical transition energies in vacuum.

ions clearly. From the transition energy at the observed resonance peak position, the right peak was assigned to the excitation  $1s^2 \rightarrow 1s2p\ ^1P_1$ , and the left peak was assigned to the excitation  $1s^2 \rightarrow 1s2p\ ^3P_1$ .

### ***Deexcitation X-rays***

Figure 3.20 shows the yields of the projectile deexcitation X-rays. In this case, we used the Si(Li) detector placed on the vertical plane. This yield is the sum of the yields of the deexcitation X-rays emitted from  $\text{Ar}^{16+}$  and  $\text{Ar}^{17+}$  ions. In the X-ray spectra, these X-rays were not separated due to the poor energy resolution of the Si(Li) detector. Similarly to the case of the charge state distribution, two resonance peaks were observed. The ratio of the peak height for  $^3P_1$  resonance to that for  $^1P_1$  resonance was small compared to the case of the charge state distribution. This is due to the fact that the radiative lifetime of  $^3P_1$  is longer than that of  $^1P_1$ , as shown in table 3.2.

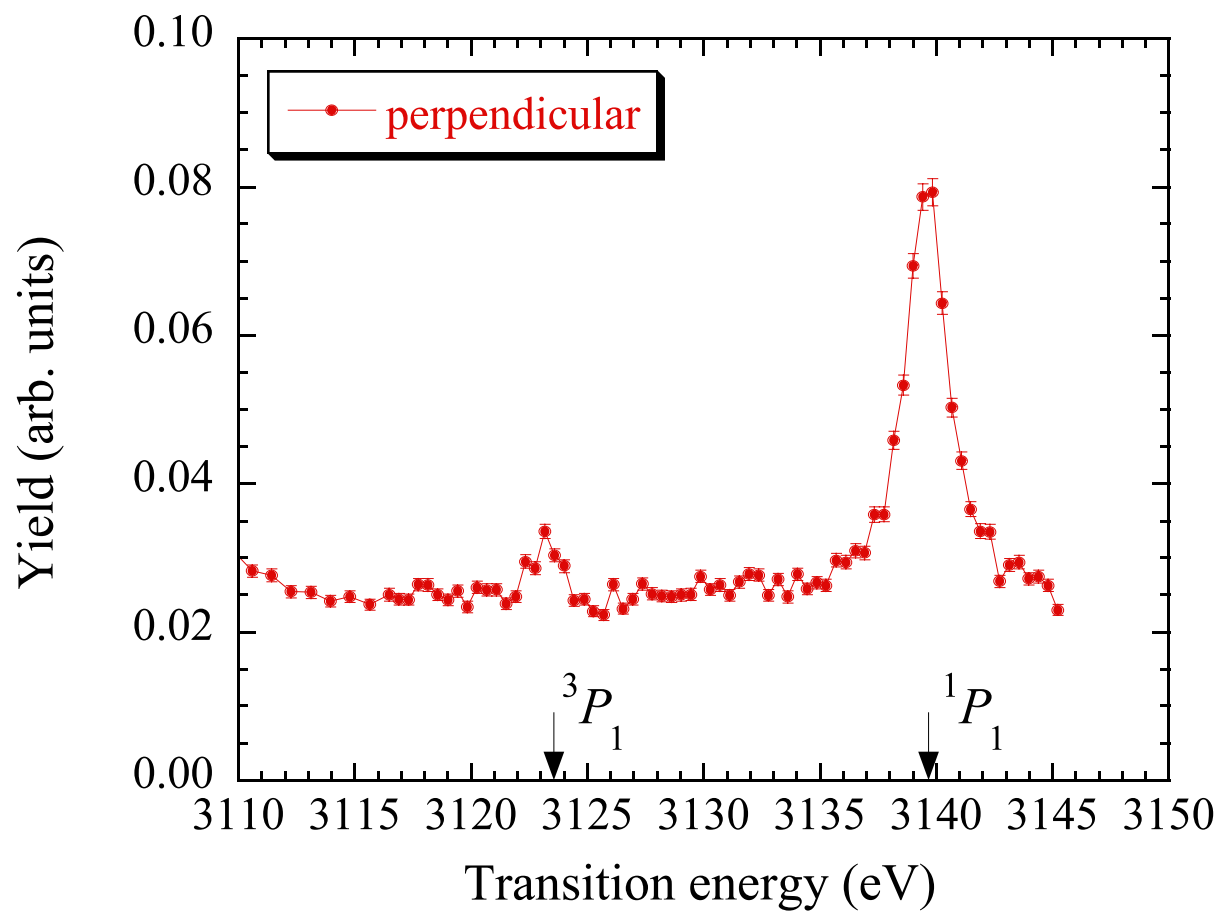


Figure 3.20: Yields of the deexcitation X-rays emitted from  $\text{Ar}^{16+}$  and  $\text{Ar}^{17+}$  ions. The arrows show the theoretical transition energies in vacuum.

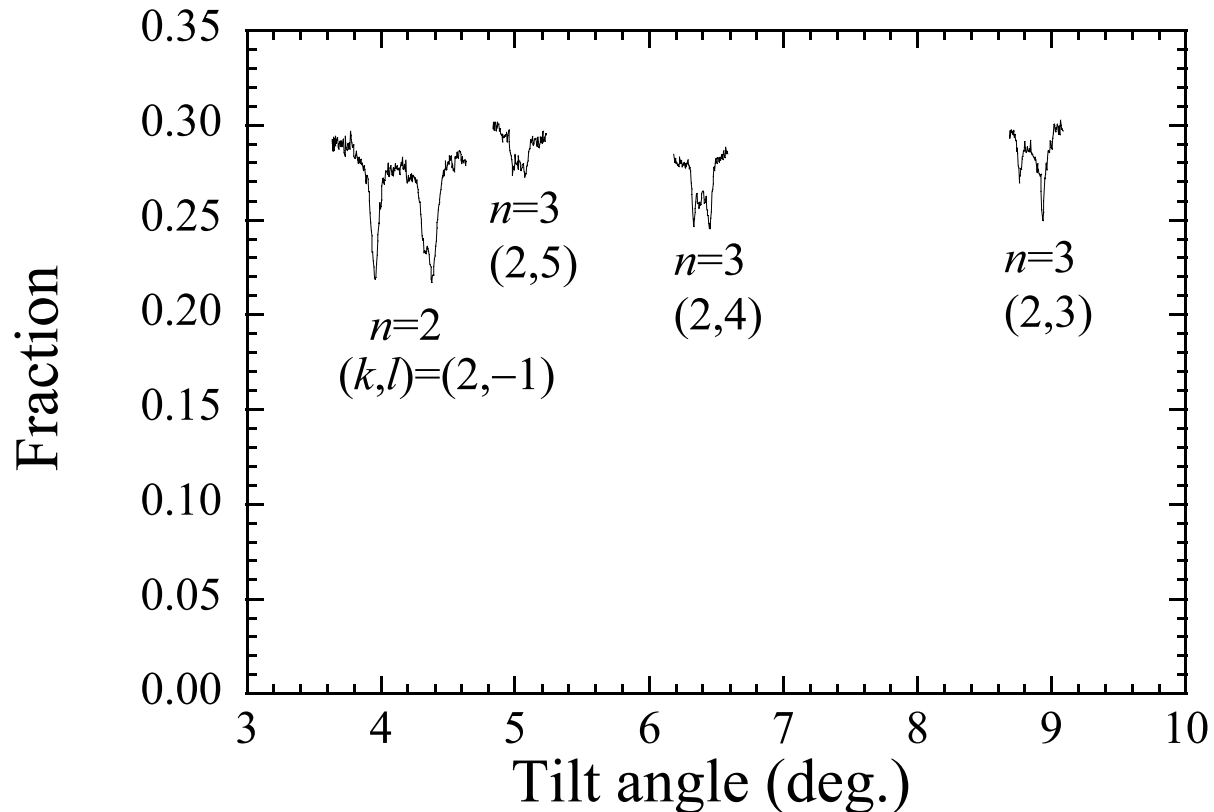


Figure 3.21: Fraction of  $Fe^{25+}$  ions transmitted through the Si crystal for 460 MeV/u  $Fe^{25+}$  incidence.

### 3.3 Hydrogen-like $Fe^{25+}$ ions

We also attempted to observe the RCE of  $Fe^{25+}$  ions, which is the heaviest ion that has ever been investigated of RCE. Figure 3.21 shows the measured charge state distribution of the ions transmitted through the Si crystal for 460 MeV/u  $Fe^{25+}$  incidence. In the case of Fe ions, we observed the second order ( $k = 2$ ) RCE. The resonances for the RCE  $((k, l) = (2, -1))$  of  $1s \rightarrow n = 2$ , and the RCE  $((k, l) = (2, 3), (2, 4), \text{ and } (2, 5))$  of  $1s \rightarrow n = 3$  are seen in Fig. 3.21.

#### 3.3.1 RCE from $1s$ to $n = 2$ states

##### *Charge state distribution*

Figure 3.22 shows the resonance profile for the RCE  $((k, l) = (2, -1))$  from  $1s$  to the  $n = 2$  states. Similarly to the case of  $Ar^{17+}$  ions, two resonance peaks were observed. The right and left peaks are assigned to the transitions  $1s \rightarrow n = 2(j = 3/2)$  and  $1s \rightarrow n = 2(j = 1/2)$ , respectively. As shown in Fig. 3.22, the skewness of the resonance

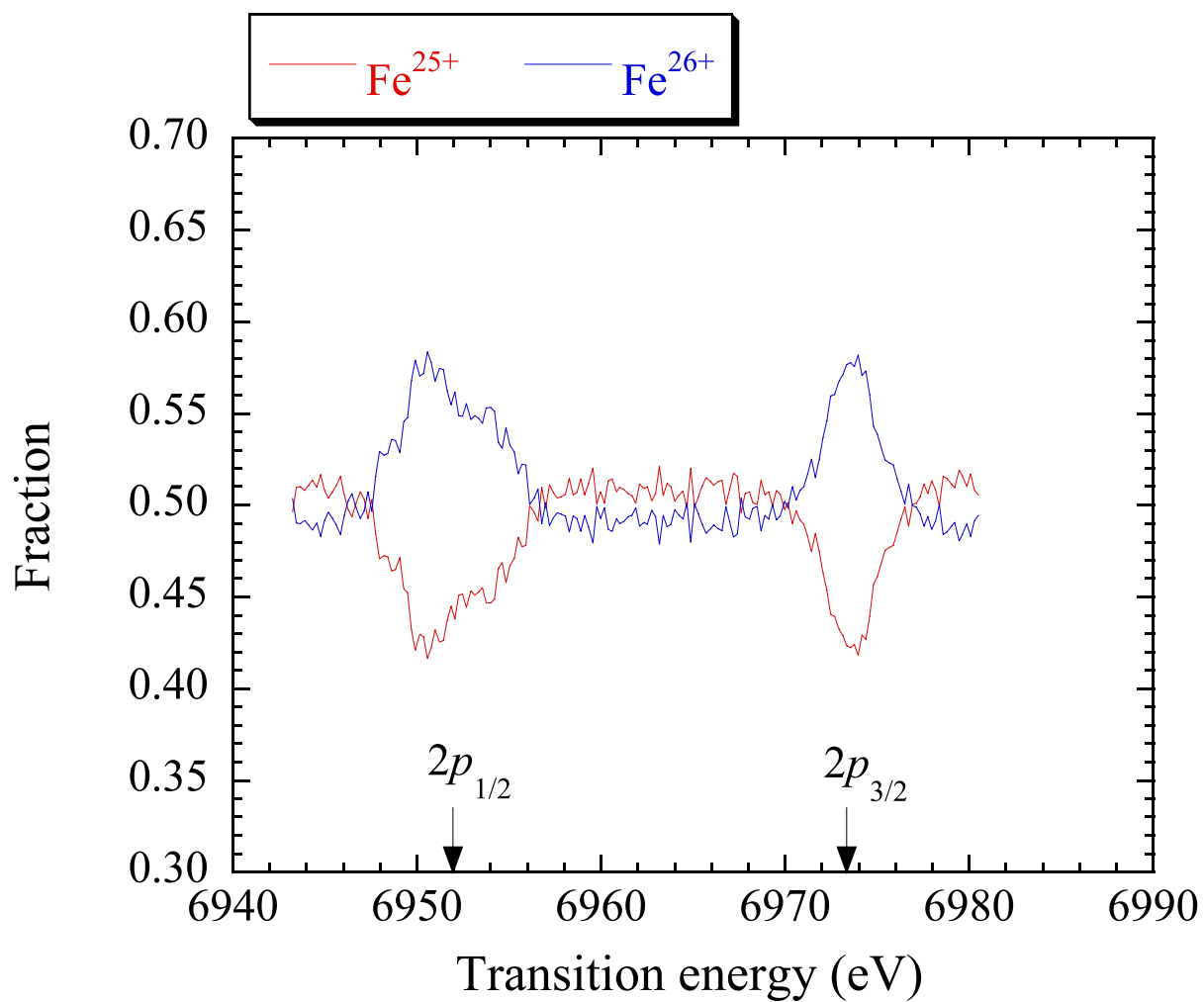


Figure 3.22: Charge state distribution of the ions transmitted through the Si crystal for  $1s \rightarrow n = 2$  in  $\text{Fe}^{25+}$  ions. The arrows show the theoretical transition energies in vacuum.

peak was smaller than that for  $Ar^{17+}$  ions, indicating that the contribution of the Stark effect for  $Fe^{25+}$  ions is smaller than for  $Ar^{17+}$  ions. In contrast to the case of  $Ar^{17+}$  ions, the  $j = 1/2$  peak was not split clearly, which is explained by the excitation probability. As shown in Fig. 1.18, the excitation probability for the Level 2 is smaller than for the Level 1, and the difference of the excitation probability between the Level 1 and Level 2 is large compared to the case of  $Ar^{17+}$  ions.

### ***Deexcitation X-rays***

We also measured X-ray spectra for the resonance ( $E_{trans}=6973$  eV) and off-resonance (planar channeling) conditions, which are shown in Fig. 3.23. The energies of the deexcitation X-rays were shifted from  $\sim 7$  keV to  $\sim 10$  keV due to the Doppler effect. Under the resonance condition, we observed the enhancement of the yields of the deexcitation X-rays.

Figure 3.24 shows the yields of the deexcitation X-rays as a function of transition energy (tilt angle). The attenuation length for 10 keV X-ray in Si is  $140 \mu\text{m}$ . If the X-ray is emitted at the crystal entrance, the intensity of the X-ray decreases to 82% when it reaches the Si(Li) detectors. The  $j = 1/2$  peak was split clearly, which is in contrast to the case of the charge state distribution, in which the resonance for the Level 2 was small. This implies that the contribution of the deexcitation process for the Level 2 is large compared to that for the Level 1. The peak height for the  $j = 1/2$  was smaller than for the  $j = 3/2$ . This is explained by the fact that the sum of fractions of  $2s$  included in the Level 1 and Level 2 is large, similarly to the case of  $Ar^{17+}$  ions. The number of the deexcitation X-rays per incident ion was  $\sim 1.0$  at the  $j = 3/2$  peak, indicating that the incident ion is excited at least once. As shown in Fig. 3.24, anisotropy of the X-ray emission was observed. For the  $j = 3/2$  peak, the yields of the X-rays emitted in the direction parallel to the (220) plane were larger than those in the direction perpendicular to the (220) plane in the projectile frame. For the  $j = 1/2$  peak, on the other hand, the formers were smaller than the latters. This indicates that the fraction of  $2p_x$  included in the Level 3 and Level 4 is large, and that the fraction of  $2p_y$  included in the Level 3 and Level 4 is large. However, this can not be explained easily by the calculated wave functions shown in Fig. 1.17.

### **3.3.2 RCE from $1s$ to $n = 3$ states**

#### ***Charge state distribution***

Figure 3.25 shows the resonance profiles for the RCE from  $1s$  to  $n = 3$  states. The dashed lines show the transition energies of  $1s \rightarrow 3p_{3/2}$  and  $1s \rightarrow 3p_{1/2}$  in vacuum, *i.e.*, without the Stark effect [68]. As observed in the case of  $Ar^{17+}$  ions, the peak width was broad due to the large Stark effect.

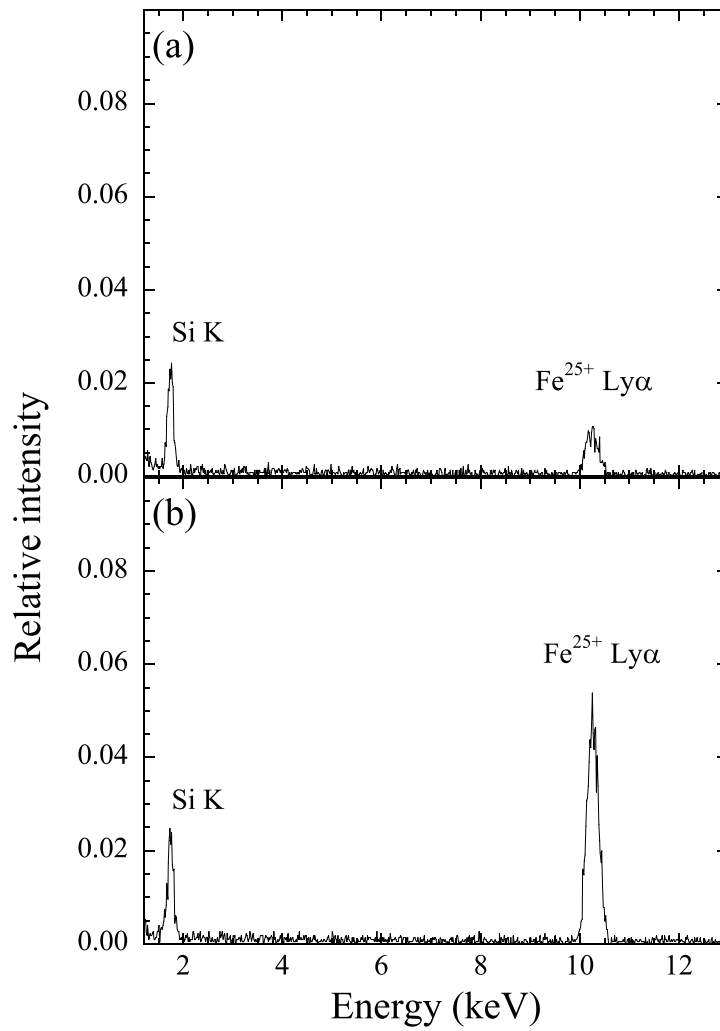


Figure 3.23: X-ray spectra under the (a) off-resonance (planar channeling) and (b) resonance ( $E_{trans}=6973$  eV) conditions for  $1s \rightarrow n = 2$  in  $\text{Fe}^{25+}$  ions.

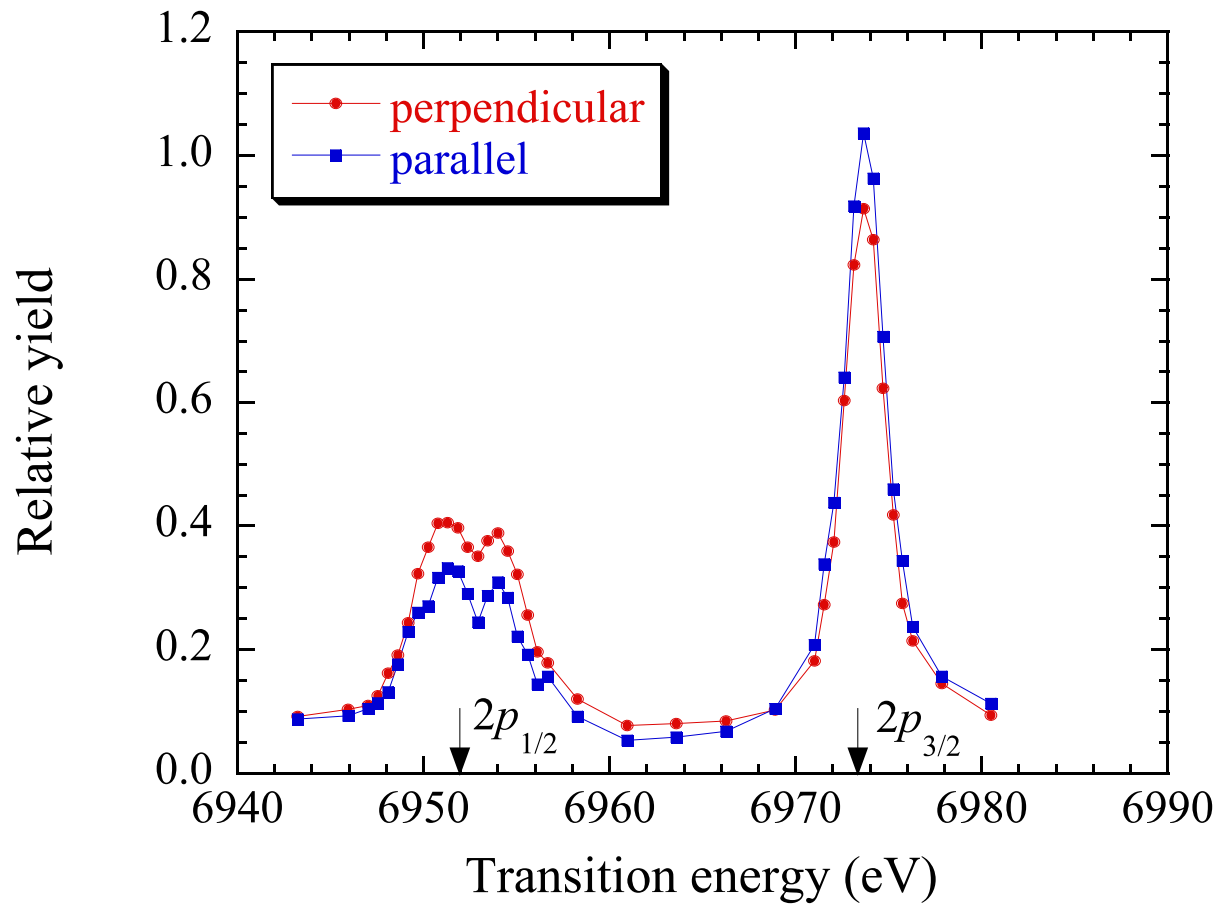


Figure 3.24: Yields of the deexcitation X-rays for  $n = 2 \rightarrow 1s$  in  $Fe^{25+}$  ions. The closed circle and square show the yields measured with the Si(Li) detectors placed on the vertical and horizontal planes, respectively. The arrows show the theoretical transition energies in vacuum.

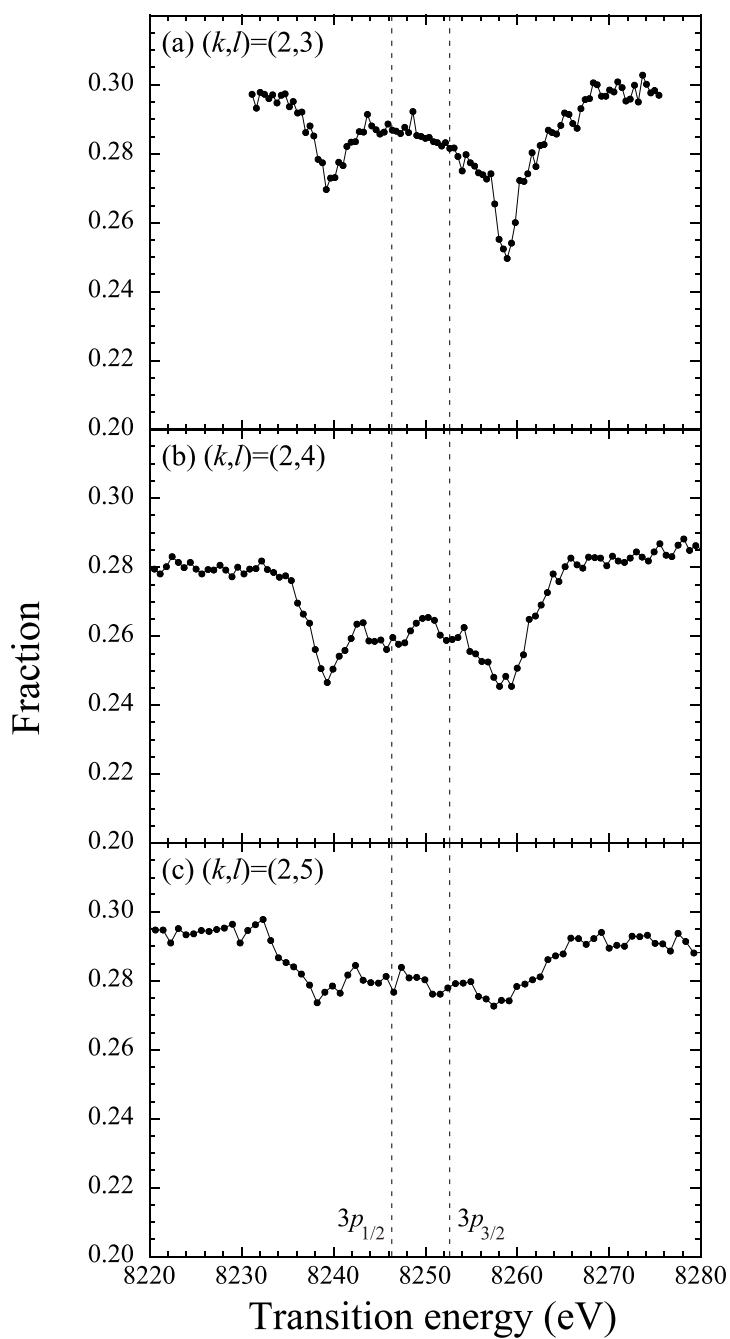


Figure 3.25: Fraction of  $\text{Fe}^{25+}$  ions transmitted through the Si crystal for  $1s \rightarrow n = 3$  in  $\text{Fe}^{25+}$  ions. The dashed lines show the transition energies of  $1s \rightarrow 3p_{3/2}$  and  $3p_{1/2}$  in vacuum. (a)  $(k, l) = (2, 3)$ , (b)  $(k, l) = (2, 4)$ , and (c)  $(k, l) = (2, 5)$ .

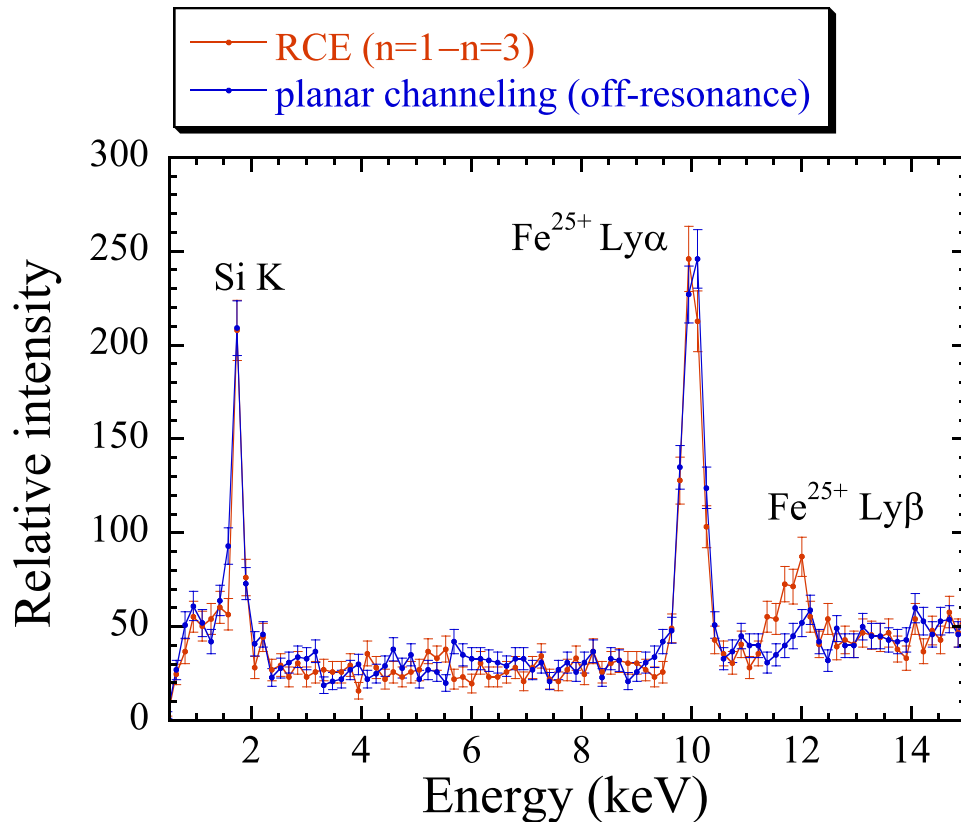


Figure 3.26: X-ray spectra under the resonance ( $E_{trans}=8259$  eV,  $(k, l) = (2, 3)$ ) and off-resonance conditions for  $1s \rightarrow n = 3$  in  $Fe^{25+}$  ions.

### *Deexcitation X-rays*

We also measured the X-ray spectra with the horizontal Si(Li), which is shown in Fig. 3.26. Under the resonance condition ( $E_{trans}=8259$  eV,  $(k, l) = (2, 3)$ ), the enhancement of the yields of the deexcitation X-rays for  $n = 3 \rightarrow 1s$  in  $Fe^{25+}$  ions is seen at  $\sim 12$  keV.

## 3.4 Helium-like $Fe^{24+}$ ions

The excitation (RCE) energy,

$$E_{RCE} = \frac{h\gamma v}{a}(\sqrt{2}k \cos \theta + l \sin \theta), \quad (3.9)$$

is shown in Fig. 3.27 as a function of tilt angle  $\theta$  for 423 MeV/u ions. The black lines show the excitation energies for  $(k, l) = (2, -3), (2, -1), (2, 0), (2, 1), (2, 3), (2, 4), (2, 5)$  and  $(2, 7)$ . The horizontal lines show the transition energies of  $Fe^{25+}$  ( $1s \rightarrow n = 2$  and  $n = 3$ ) and  $Fe^{24+}$  ( $1s^2 \rightarrow 1s2p$  and  $1s3p$ ) ions. We chose the beam energy (423 MeV/u) so that the RCE conditions are not overlapped with each other.

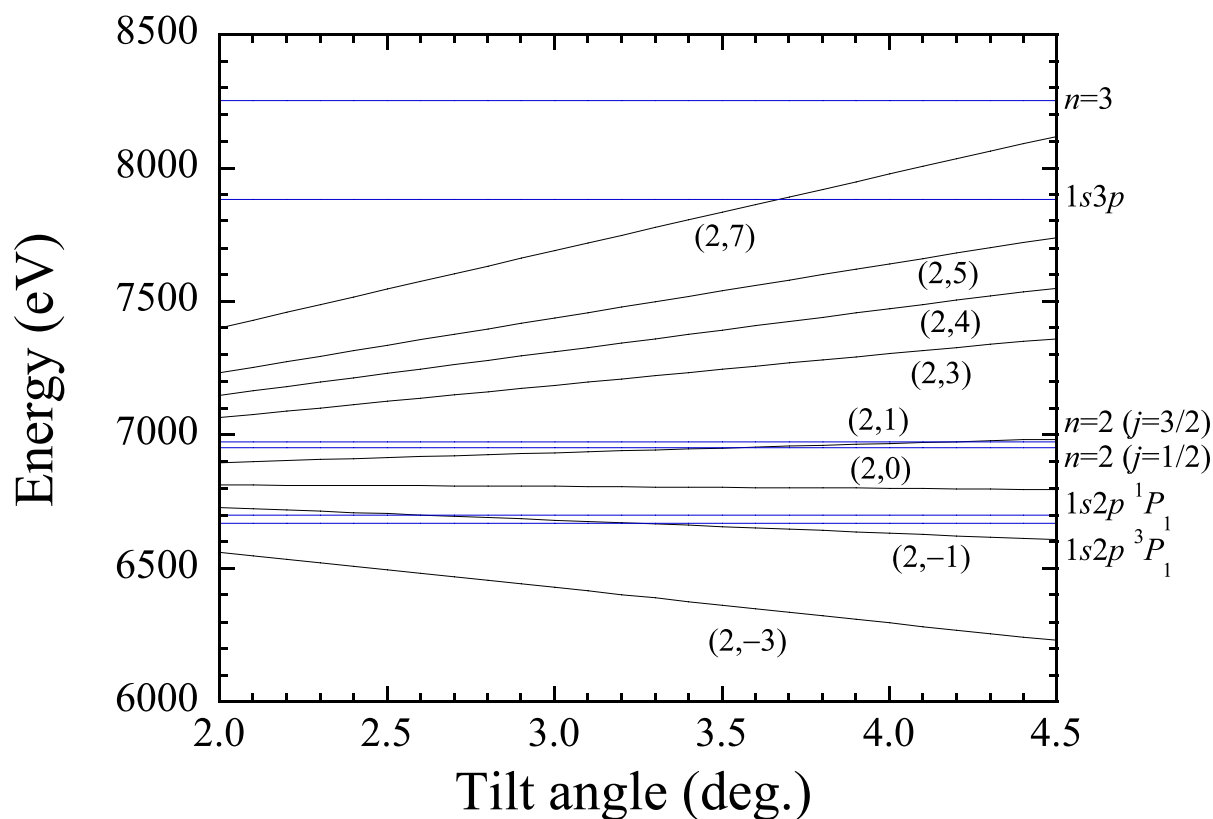


Figure 3.27: Excitation (RCE) energy as a function of tilt angle for 423 MeV/u ions. The black lines show the excitation energies for  $(k, l) = (2, -3), (2, -1), (2, 0), (2, 1), (2, 3), (2, 4), (2, 5)$  and  $(2, 7)$ . The horizontal lines show the transition energies of  $\text{Fe}^{25+}$  ( $1s \rightarrow n = 2$  and  $n = 3$ ) and  $\text{Fe}^{24+}$  ( $1s^2 \rightarrow 1s2p$  and  $1s3p$ ) ions.

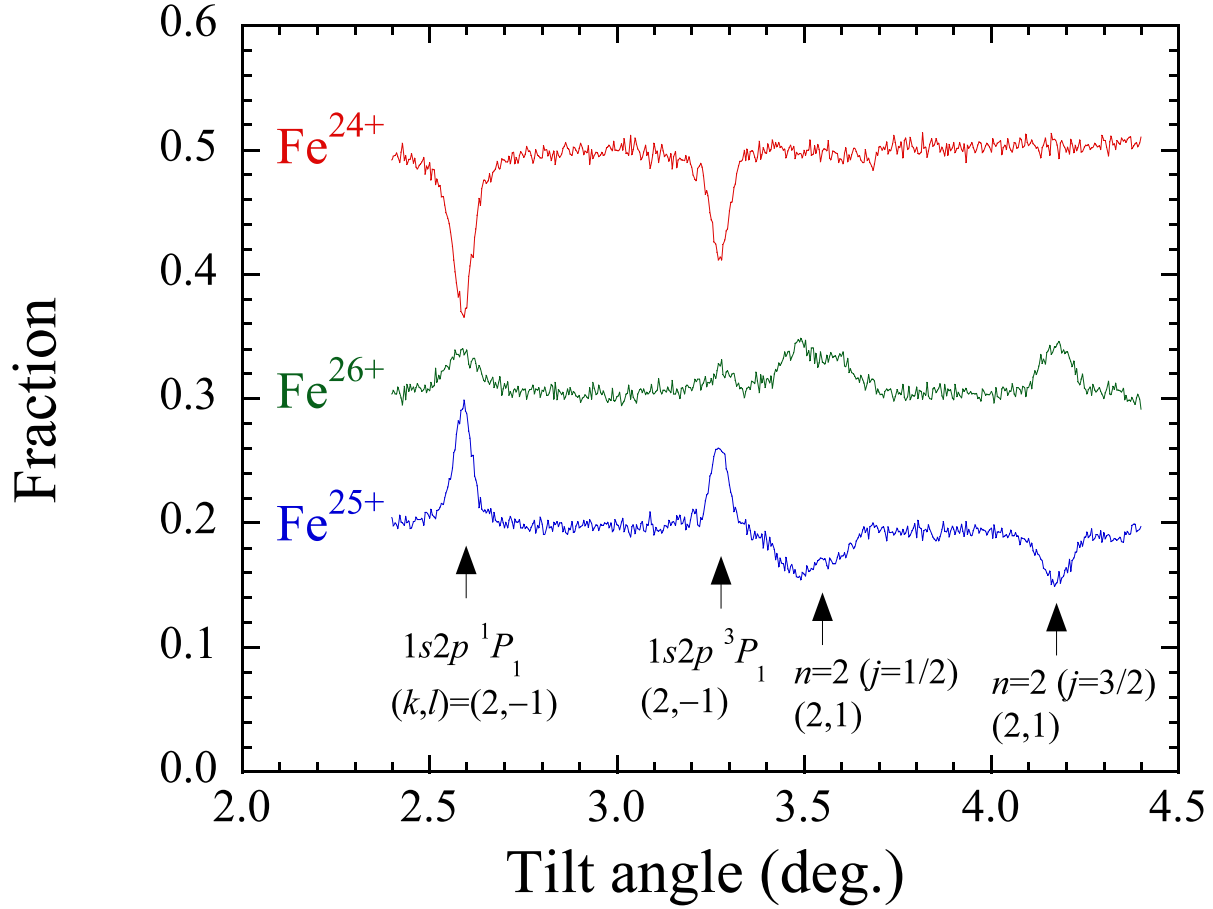


Figure 3.28: Charge state distribution of the ions transmitted through the Si crystal for 423 MeV/u  $Fe^{24+}$  incidence.

### *Charge state distribution*

Figure 3.28 shows the charge state distribution for 423 MeV/u  $Fe^{24+}$  incidence. Around  $2.6^\circ$  and  $3.3^\circ$ , the fraction of  $Fe^{24+}$  ions decreased. These peaks correspond to the RCE of  $Fe^{24+}$  ions. On the other hand, around  $3.5^\circ$  and  $4.2^\circ$ , the fraction of  $Fe^{25+}$  ions decreased. These peaks are attributed to the RCE ( $(k, l) = (2, 1)$ ) of  $1s \rightarrow n = 2$  in  $Fe^{25+}$  ions.

The resonance profile for the RCE of  $Fe^{24+}$  ions is shown in Fig. 3.29. Similarly to the case of  $Ar^{16+}$  ions, two resonance peaks corresponding to the excitations  $1s^2 \rightarrow 1s2p \ ^1P_1$  and  $1s^2 \rightarrow 1s2p \ ^3P_1$  were observed.

### *Deexcitation X-rays*

The X-ray spectra measured with two Si(Li) detectors are shown in Fig. 3.30. In the X-ray spectra, the deexcitation X-rays emitted from  $Fe^{24+}$  and  $Fe^{25+}$  ions were observed. For the random orientation, the yields of the deexcitation X-rays emitted from  $Fe^{25+}$  ions

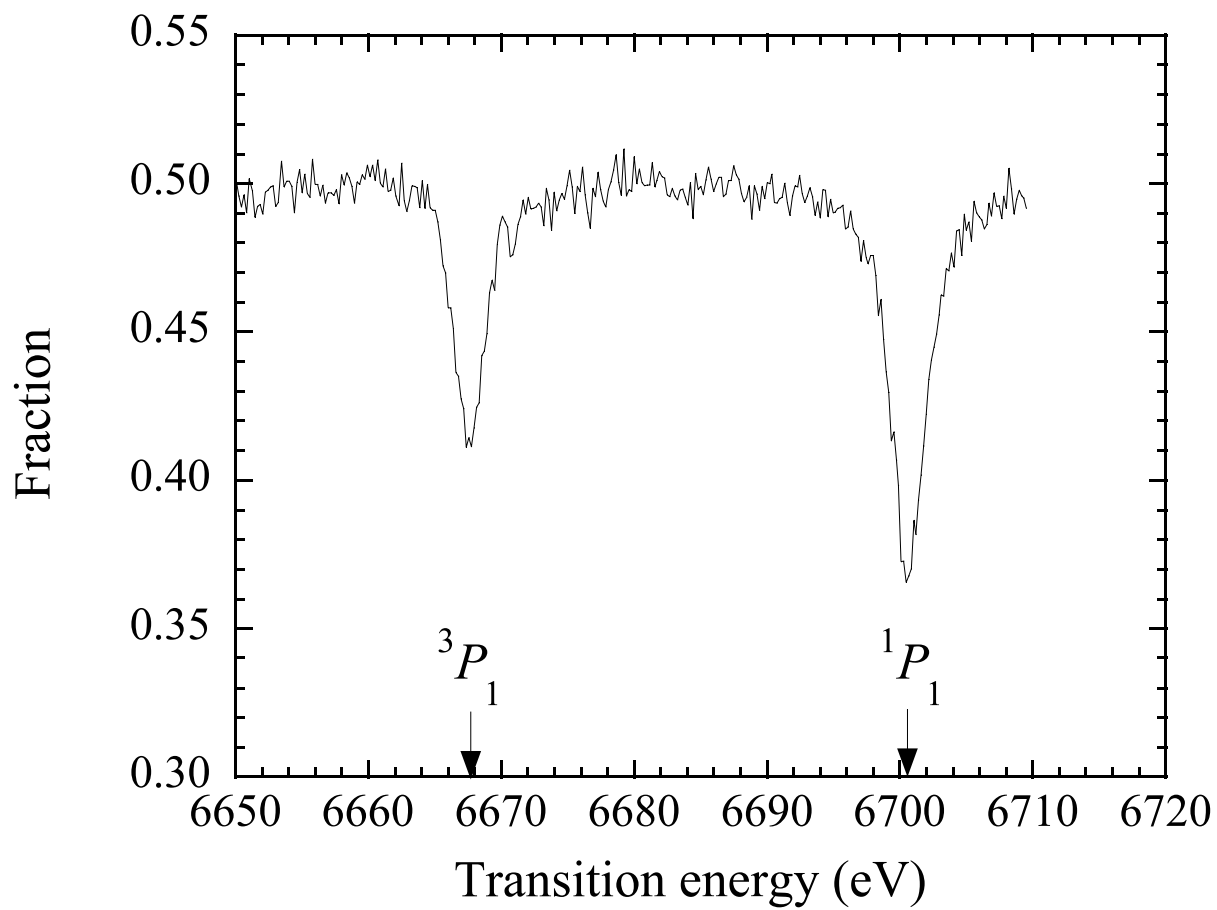


Figure 3.29: Fraction of  $\text{Fe}^{24+}$  ions transmitted through the Si crystal for  $1s^2 \rightarrow 1s2p {}^1P_1$  and  ${}^3P_1$  in  $\text{Fe}^{24+}$  ions. The arrows show the theoretical transition energies in vacuum.

were larger than that from  $Fe^{24+}$  ions. For the planar channeling, on the other hand, the yields of the deexcitation X-rays emitted from  $Fe^{24+}$  ions were larger than that from  $Fe^{25+}$  ions. These reflect the charge state distribution of the ions inside the crystal. As can be seen in Fig. 3.30, for the resonance condition for  $^1P_1$  ( $E_{trans}=6700$  eV), the deexcitation X-rays emitted from  $Fe^{24+}$  ions increased.

Figure 3.31 shows the yields of the deexcitation X-rays detected with the Si(Li) detectors as a function of transition energy (tilt angle). The observed yield is the sum of the yields of the X-rays emitted from  $Fe^{24+}$  and  $Fe^{25+}$  ions. For  $^1P_1$ , large anisotropy of the X-ray emission was observed. As shown in Fig.1.21, the transition probability of  $1s \rightarrow 2p_x$  is large at the channel center, which is consistent with the observed anisotropy.

### 3.5 Lithium-like $Fe^{23+}$ ions

Figure 3.32 shows the charge state distribution for 423 MeV/u  $Fe^{23+}$  ion incidence. The RCE of lithium-like ions was observed for the first time. The resonances of  $Fe^{24+}$  and  $Fe^{25+}$  ions are also seen in Fig. 3.32.

The resonance profile concerning  $Fe^{23+}$  ions is shown in Fig. 3.33. The red and black lines represent the transition energies of  $1s^22s \rightarrow 1s2s2p$  and  $1s^22p \rightarrow 1s2p^2$  in  $Fe^{23+}$  ions in vacuum, respectively [68], which are shown in table 3.5. In this case, many resonance peaks were observed. The Stark effect may play an important role in this structure. For understanding of this structure, theoretical calculations on the Stark effect for three-electron ions are needed.

## 3.6 Discussion

### $Ar^{17+}$ ions

#### *RCE from $1s$ to $n = 2$ states (Charge state distribution)*

As shown in Fig. 3.3, many resonances were observed. In the present experiment, Ar ions were excited with the first order ( $k = 1$ ) RCE. The RCE for  $(k, l) = (1, 4)$  was not observed, which is due to the destructive interference originating from the crystal structure [29]. In the case of (220) planar channeling in Si, the RCE for  $(k, l)$  satisfying  $2k + l = 4n + 2$  ( $n$  is an integer) does not take place. The resonance peak height was found to decrease with increasing  $l$ . This reflects the absolute magnitude of the Fourier potential, which tends to decrease with increasing  $l$ .

As shown in Fig. 3.4, two main peaks ( $j = 3/2$  and  $j = 1/2$ ) were observed for the RCE from  $1s$  to the  $n = 2$  states. This structure results from the  $l \cdot s$  interaction for the bound electron. For  $Ar^{17+}$  ions in vacuum, the energy difference between the  $j = 3/2$  and  $j = 1/2$  states is  $\sim 5$  eV. The  $j = 1/2$  peak was split into two peaks, and the  $j = 3/2$  and  $j = 1/2$  peaks were skewed to the higher and lower energy sides, respectively, which is due to the Stark effect originating from the static crystal potential and the wake potential. In

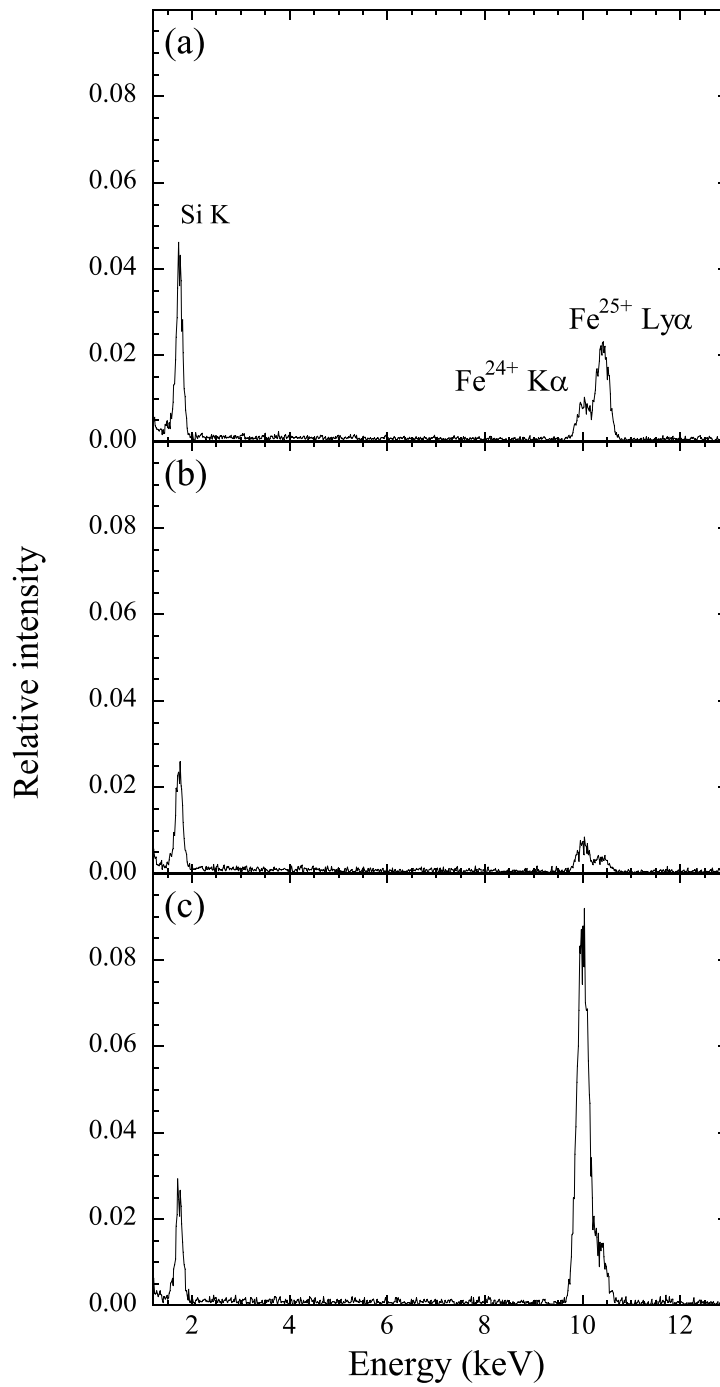


Figure 3.30: X-ray spectra for the (a) random orientation, (b) (220) planar channeling (off-resonance), and (c) RCE condition for  ${}^1P_1$  ( $E_{trans}=6700$  eV) .

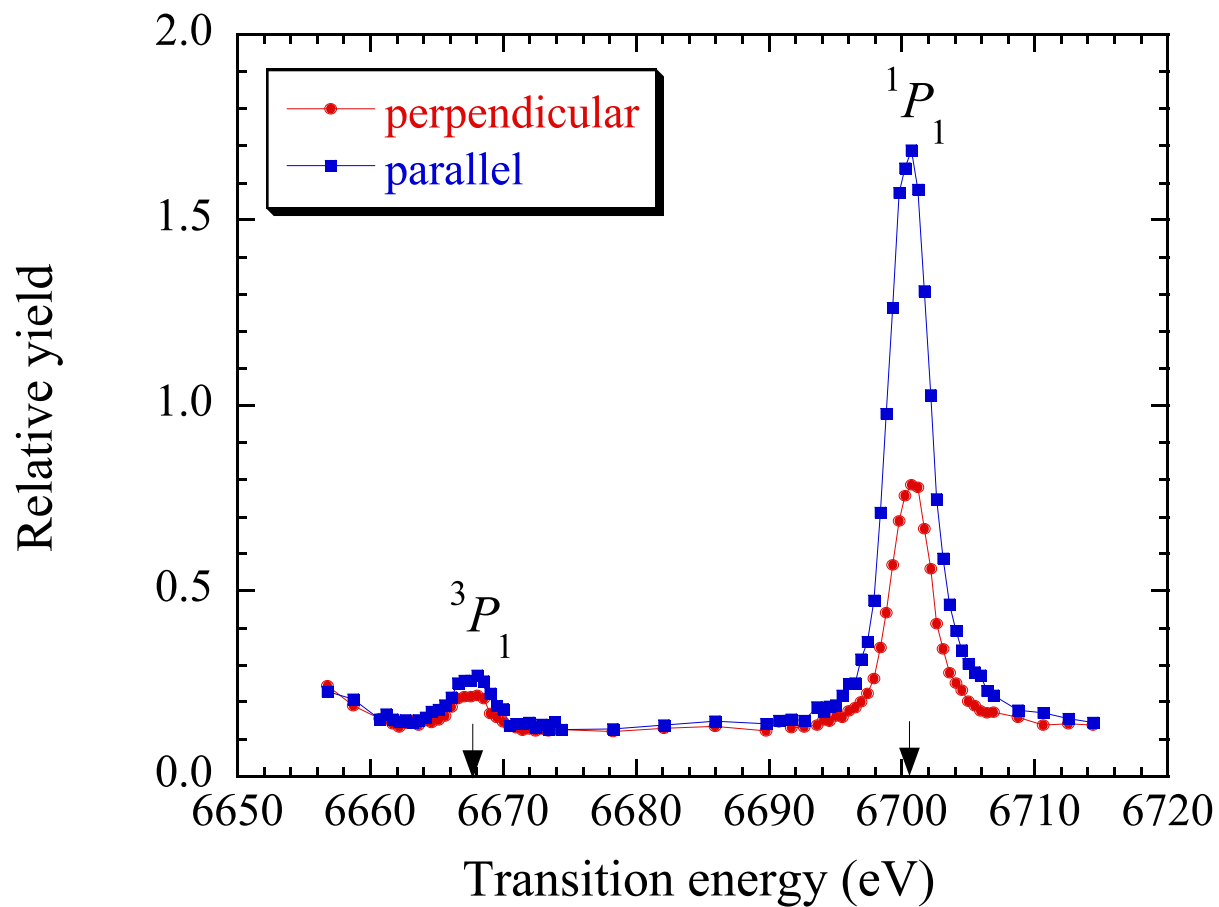


Figure 3.31: Yields of the deexcitation X-rays emitted from  $\text{Fe}^{24+}$  and  $\text{Fe}^{25+}$  ions. The closed circle and square show the yields measured with the Si(Li) detectors placed on the vertical and horizontal planes, respectively. The arrows show the theoretical transition energies in vacuum.

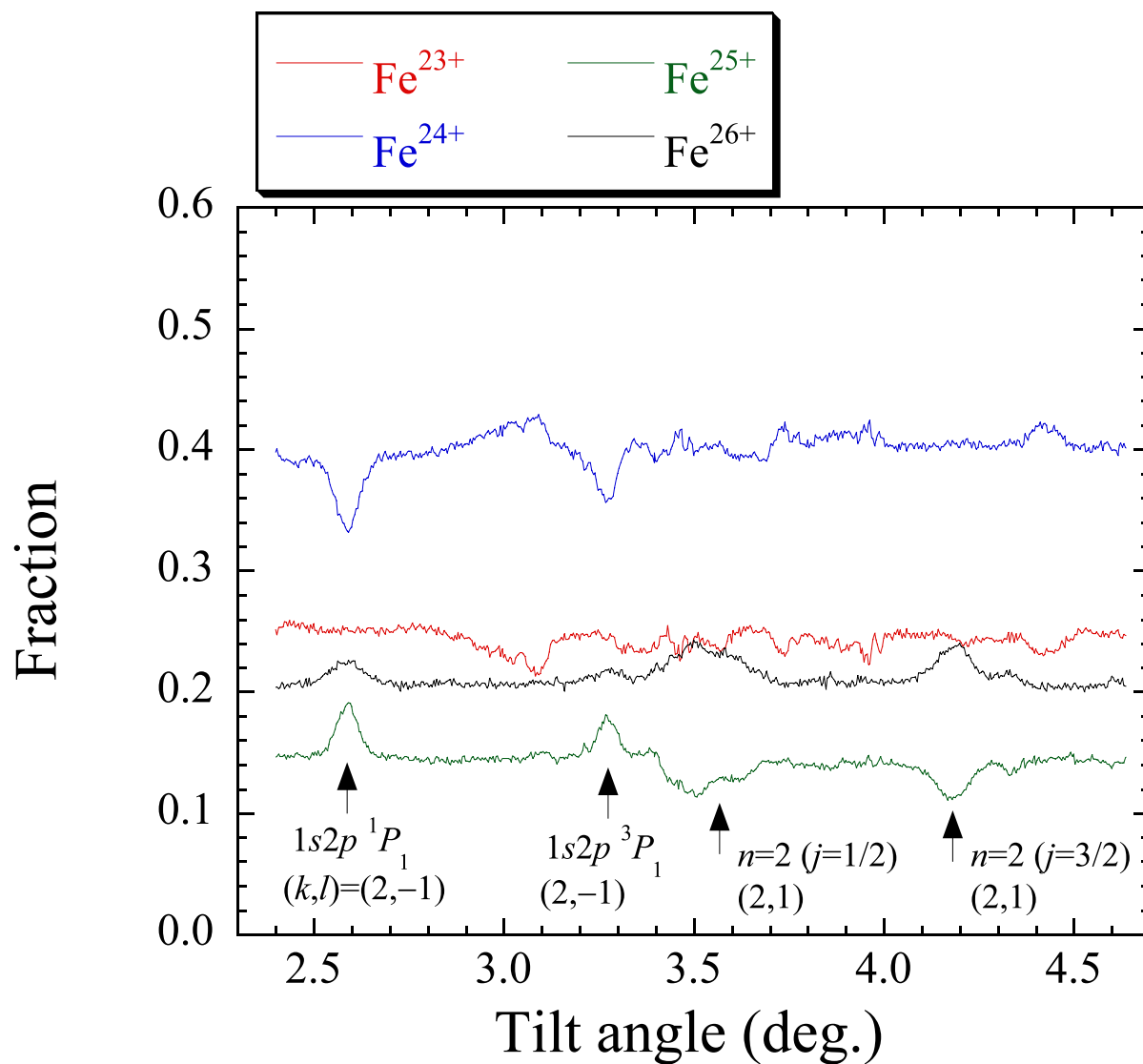


Figure 3.32: Charge state distribution of the ions transmitted through the Si crystal for 423 MeV/u  $\text{Fe}^{23+}$  incidence.

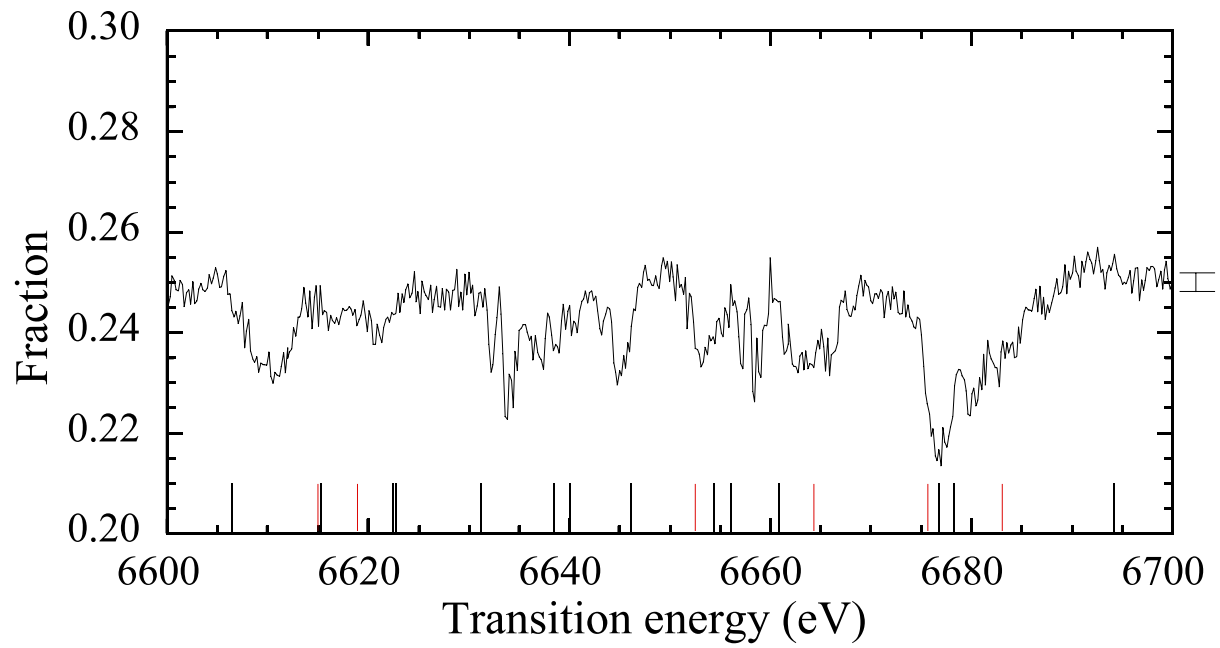


Figure 3.33: Fraction of  $\text{Fe}^{23+}$  ions transmitted through the Si crystal for 423 MeV/u  $\text{Fe}^{23+}$  incidence. The red and black lines show the transition energies of  $1s^22s \rightarrow 1s2s2p$  and  $1s^22p \rightarrow 1s2p^2$  in vacuum, respectively. The typical error bar is shown in the right side of the figure.

Table 3.5: Transition energies of  $1s^2 2s \rightarrow 1s 2s 2p$ ,  $1s^2 2p \rightarrow 1s 2p^2$ , and  $1s^2 2p \rightarrow 1s 2s^2$  in  $\text{Fe}^{23+}$  ions in vacuum [68].

transition	energy (eV)	decay rate ( $10^8 \text{ s}^{-1}$ )
$1s^2 2p \ ^2P_{1/2}^\circ - 1s 2p^2 \ ^2S_{1/2}$	6694.2	$1.0 \times 10^5$
$1s^2 2s \ ^2S_{1/2} - 1s(^2S) 2s 2p(^1P^\circ) \ ^2P_{3/2}^\circ$	6683.1	$4.82 \times 10^6$
$1s^2 2p \ ^2P_{1/2}^\circ - 1s 2p^2 \ ^2P_{3/2}$	6676.8	$1.2 \times 10^5$
$1s^2 2p \ ^2P_{3/2}^\circ - 1s 2p^2 \ ^2S_{1/2}$	6678.2	$2.43 \times 10^6$
$1s^2 2s \ ^2S_{1/2} - 1s(^2S) 2s 2p(^1P^\circ) \ ^2P_{1/2}^\circ$	6675.8	$3.06 \times 10^6$
$1s^2 2s \ ^2S_{1/2} - 1s(^2S) 2s 2p(^3P^\circ) \ ^2P_{3/2}^\circ$	6664.4	$4.4 \times 10^4$
$1s^2 2p \ ^2P_{3/2}^\circ - 1s 2p^2 \ ^2P_{3/2}$	6660.8	$6.24 \times 10^6$
$1s^2 2p \ ^2P_{1/2}^\circ - 1s 2p^2 \ ^2P_{1/2}$	6656.0	$5.47 \times 10^6$
$1s^2 2p \ ^2P_{1/2}^\circ - 1s 2p^2 \ ^2D_{3/2}$	6654.4	$3.16 \times 10^6$
$1s^2 2s \ ^2S_{1/2} - 1s(^2S) 2s 2p(^3P^\circ) \ ^2P_{1/2}^\circ$	6652.6	$1.91 \times 10^6$
$1s^2 2p \ ^2P_{3/2}^\circ - 1s 2p^2 \ ^2D_{5/2}$	6646.1	$2.14 \times 10^6$
$1s^2 2p \ ^2P_{3/2}^\circ - 1s 2p^2 \ ^2P_{1/2}$	6640.0	$1.63 \times 10^6$
$1s^2 2p \ ^2P_{3/2}^\circ - 1s 2p^2 \ ^2D_{3/2}$	6638.4	$3.5 \times 10^5$
$1s^2 2p \ ^2P_{1/2}^\circ - 1s 2p^2 \ ^4P_{3/2}$	6631.2	$1.0 \times 10^3$
$1s^2 2p \ ^2P_{3/2}^\circ - 1s 2p^2 \ ^4P_{5/2}$	6622.7	$3.2 \times 10^5$
$1s^2 2p \ ^2P_{1/2}^\circ - 1s 2p^2 \ ^4P_{1/2}$	6622.4	$2.0 \times 10^5$
$1s^2 2s \ ^2S_{1/2} - 1s(^2S) 2s 2p(^3P^\circ) \ ^4P_{3/2}^\circ$	6619	$1.5 \times 10^5$
$1s^2 2s \ ^2S_{1/2} - 1s(^2S) 2s 2p(^3P^\circ) \ ^4P_{1/2}^\circ$	6615	$4.2 \times 10^4$
$1s^2 2p \ ^2P_{3/2}^\circ - 1s 2p^2 \ ^4P_{3/2}$	6615.2	$8.3 \times 10^4$
$1s^2 2p \ ^2P_{3/2}^\circ - 1s 2p^2 \ ^4P_{1/2}$	6606.4	$2.5 \times 10^3$
$1s^2 2p \ ^2P_{1/2}^\circ - 1s 2s^2 \ ^2S_{1/2}$	6553.4	$9.7 \times 10^4$
$1s^2 2p \ ^2P_{3/2}^\circ - 1s 2s^2 \ ^2S_{1/2}$	6537.4	$9.8 \times 10^4$

the present high energy region, the wake potential is negligible (except for at the channel center). The electric field for the wake potential is  $\sim 0.5 \text{ V/\AA}$ . On the other hand, the electric field for the crystal potential is  $\sim 20 \text{ V/\AA}$  at the distance of  $0.5 \text{ \AA}$  from the channel center. The energy width  $\Delta E$  due to the linear Stark effect is given by

$$\Delta E = \frac{3F}{Z}n(n-1), \quad (3.10)$$

where  $F$  is the strength of the electric field,  $Z$  is the projectile atomic number, and  $n$  is the principal quantum number [69]. For  $F = 20 \text{ V/\AA}$ , the energy width  $\Delta E$  is calculated to be  $\sim 4 \text{ eV}$ . As shown in Fig. 1.13, the energy difference between the Level 1 and Level 2 at the distance of  $0.5 \text{ \AA}$  is  $\sim 3 \text{ eV}$ , which is consistent with the value predicted by the linear Stark effect. In the case of  $\text{Ar}^{17+}$  ions, the contribution of the Stark effect is comparable to that of the  $l \cdot s$  interaction under the present experimental condition.

### ***RCE from $1s$ to $n = 2$ states (Deexcitation X-rays)***

We also observed the resonance profile by measuring the projectile deexcitation X-rays. The enhancement of the deexcitation X-rays was observed at the resonance condition. As shown in Fig. 3.6, the peak height for the  $j = 1/2$  was smaller than that for the  $j = 3/2$ . This is explained by the fact that the fraction of the  $2s$  state which the Level 1 and Level 2 include is large as shown in Fig. 1.14, and that the radiative lifetime for  $2s$  is longer than for  $2p$ . The anisotropy observed around  $E_{trans} = 3325 \text{ eV}$  is also explained by the compositions of the wave functions of the  $n = 2$  states. As can be seen in Fig. 1.13 and Fig. 1.14, the Level 4 is excited around  $E_{trans} = 3325 \text{ eV}$ , and the fraction of  $2p_x$  which the Level 4 includes is large. In the deexcitation process for  $2p_x \rightarrow 1s$ , the deexcitation X-rays are emitted strongly in the direction perpendicular to the  $x$  axis, *i.e.*, parallel to the  $(220)$  plane.

### ***RCE from $1s$ to $n = 2$ states (Convoy electrons)***

The spectra measured for the random orientation and the planar channeling (off-resonance) are shown in Fig. 3.7, where the following features were observed. (i) The peak energy (205 keV) for the random orientation was lower than that (208 keV) for the planar channeling. (ii) The peak width (23 keV) for the random orientation was larger than that (22 keV) for the planar channeling. (iii) The yields for the random orientation was smaller than for the planar channeling. These observed features indicate that the energy loss, energy straggling, and angular straggling of the emitted electron for the random orientation are more significant than for the planar channeling. This may be attributed to the fact that the ionization MFP for the random orientation is shorter than for the planar channeling, *i.e.*, the path length of the electron lost from the ion inside the crystal is longer than for the planar channeling. The transport process of the electron emitted under the planar channeling condition is considered to be complex. In this case, the electrons are emitted from the ion in the planar channel, where the electron density is low. After that, however, the emitted electrons tend to approach the atomic plane where the electron

density is high. In addition, the diffraction effect may contribute to the transport process of the electron. To clarify its contribution, the measurement of the angular distribution of the electrons is needed as well as that of the energy distribution.

Figure 3.8 shows the energy spectra of convoy electrons for the off-resonance (planar channeling) condition and RCE condition ( $E_{trans} = 3323$  eV). We observed the following features in the electron spectra. (i) The peak energy (208 keV) for the off-resonance condition was slightly higher than that (207 keV) for the RCE condition. (ii) The peak width (22 keV) for the off-resonance condition was larger than that (16 keV) for the RCE condition. (iii) The yield for the off-resonance condition was smaller than for the RCE condition. The feature (i) may be due to the fact that the ionization MFP for the off-resonance condition is longer than for the RCE condition, *i.e.*, the mean path length of the electron lost from the projectile ion for the off-resonance condition is short compared to the case of the RCE condition. The feature (ii) is explained by the contribution of the projectile excited states to the convoy electron production, as observed in the case of the carbon foil targets (see Appendix B). The spectrum shape of the electron produced in the Electron Loss to the Continuum (ELC) process is known to depend on the initial state of the electron lost from the projectile ion. As discussed in Appendix B, the peak width of the convoy electrons was found to decrease due to the enhancement of the contribution of the excited states. The feature (iii) is due to the enhancement of the ionization process due to the RCE.

The spectra measured at the various RCE conditions are shown in Fig. 3.10. Since the shape of convoy electron spectrum depends on the initial state of the electron lost to the continuum state, we expected that the spectrum shape varies depending on the RCE condition. As stated in section 1.3, the peak formed by the electrons emitted from  $2s$  is narrower than those from  $2p_x(2p_y)$ . For  $2p_z$ , on the other hand, the inverted cusp-shaped peak is formed, and thereby the peak becomes broad if the contribution of the  $2p_z$  is large. However, the significant differences between the obtained convoy electron spectra were not observed. This indicates that there are not large differences of the momentum distributions between the  $n = 2$  states from which the electrons are emitted at various RCE conditions. Near the atomic plane, the ionization probability is large compared to the channel center. This may lead to the mixing of the  $n = 2$  states, which is in contrast to the case of the deexcitation X-rays.

### ***RCE from $1s$ to $n = 3, 4$ , and $5$ states (Charge state distribution)***

The RCE from  $1s$  to  $n = 3, 4$ , and  $5$  were also observed. The structures of the resonance profiles for such highly excited states were observed for the first time. As shown in Fig. 3.13, for the  $n = 3$  states, the resonance peak height decreased with increasing  $l$ , which reflects the absolute value of the Fourier potential. Also, the resonance peak width was found to increase with increasing  $n$ . Table 3.6 shows the comparison between the energy widths,  $\Delta E$ , predicted by the linear Stark effect and the experimental ones. For  $n=2, 3$ , and  $4$ , the energy widths calculated for  $F=50$  V/Å are in reasonable agreement with the experiment. As shown in Fig. 1.2,  $F=50$  V/Å is approximately the maximum

Table 3.6: Energy width due to the Stark effect for Ar<sup>17+</sup> ions.

$n$	orbital radius (Å)	observed width (eV)	$n(n-1)$	$\Delta E$ ( $F=50$ V/Å)(eV)
2	0.12	$\sim 10$	2	9
3	0.27	$\sim 30$	6	26
4	0.47	$\sim 50$	12	53
5	0.74	$\sim 60$	20	88

value of the electric field. For  $n=5$ , the calculated energy width is not in agreement with the experiment. In this case, the scanned energy range was not enough, which may be the cause of the disagreement. The peak structures of the resonance profiles can not be easily explained by the linear Stark effect. By taking into account the impact parameter dependence of the excitation and ionization probabilities, these structures may be explained.

## Ar<sup>16+</sup> ions

### *Charge state distribution*

The structures of the resonance profiles for helium-like ions were observed for the first time. As shown in Fig. 3.19, the excitations from  $1s^2$  to  $1s2p$   $^1P_1$  and  $^3P_1$  were observed. The skewness of the resonance peak was small compared to the case of hydrogen-like Ar<sup>17+</sup> ions, reflecting that the energy levels are not degenerate with respect to the angular momenta in the case of helium-like ions.

### *Deexcitation X-rays*

As shown in Fig. 3.20, the ratio of the resonance peak height for  $^3P_1$  to that for  $^1P_1$  in the resonance profile for the deexcitation X-rays was small compared to the case of the resonance profile for the charge state distribution. This is because the radiative lifetime of  $1s2p$   $^3P_1 \rightarrow 1s^2$  ( $5.6 \times 10^{-13}$  s) is longer than that of  $1s2p$   $^1P_1 \rightarrow 1s^2$  ( $9.1 \times 10^{-15}$  s). These lifetimes correspond to the mean traveling distances of 170 and 2.8  $\mu\text{m}$  for  $^3P_1$  and  $^1P_1$ , respectively. As shown in Fig. 3.1, the mean free path (MFP) of  $n = 2$  for electron impact ionization is  $\sim 50$   $\mu\text{m}$  at the channel center. This MFP is shorter than the mean traveling distance (170  $\mu\text{m}$ ) for  $^3P_1$ . Accordingly, in the case of  $^3P_1$ , the ionization process is much more probable than the radiative deexcitation process.

## Fe<sup>25+</sup> ions

### *RCE from $1s$ to $n = 2$ states (Charge state distribution)*

As shown in Fig. 3.22, two peaks ( $n = 2(j = 3/2)$  and  $n = 2(j = 1/2)$ ) were observed for the RCE from  $1s$  to  $n = 2$  states in Fe<sup>25+</sup> ions, which are the heaviest ions that have ever

Table 3.7: Energy width due to the Stark effect for Fe<sup>25+</sup> ions.

$n$	orbital radius (Å)	observed width (eV)	$n(n-1)$	$\Delta E$ ( $F=50$ V/Å)(eV)
2	0.08	$\sim 8$	2	6
3	0.18	$\sim 25$	6	18

been used in the RCE experiments. In this case, Fe ions were excited with the second order ( $k = 2$ ) RCE. The skewness of the resonance peak was small compared to the case of Ar<sup>17+</sup> ions, indicating that the contribution of the Stark effect for Fe<sup>25+</sup> ions is smaller than for Ar<sup>17+</sup> ions. This is due to the fact that the electron orbital radius for Fe<sup>25+</sup> ions is smaller than for Ar<sup>17+</sup> ions, and that the energy difference between the  $j = 3/2$  and  $j = 1/2$  states for Fe<sup>25+</sup> ions ( $\sim 21$  eV) is larger than for Ar<sup>17+</sup> ions ( $\sim 5$  eV). For the  $n = 2$  states in Fe<sup>25+</sup> ion, the energy width due to the linear Stark effect is calculated to be  $\sim 3$  eV for  $F = 20$  V/Å. In the case of Fe<sup>25+</sup> ions, the contribution of the Stark effect is small compared to that of the  $l \cdot s$  interaction.

#### ***RCE from 1s to n = 2 states (Deexcitation X-rays)***

As shown in Fig. 3.24, the peak height for  $j = 1/2$  was smaller than for  $j = 3/2$  in the resonance profile for the deexcitation X-rays. Similarly to the case of Ar<sup>17+</sup> ions, this is explained by the fraction of 2s state. At the  $j = 3/2$  and  $j = 1/2$  peaks, anisotropies of the angular distributions of the deexcitation X-rays were observed. The observed features indicate that the deexcitation processes of  $2p_x \rightarrow 1s$  and  $2p_y \rightarrow 1s$  are dominant at the  $j = 3/2$  and  $j = 1/2$  peaks, respectively. The former is explained as follows. At the channel center, the excitation probability for the Level 3 is larger than for the Level 4, and the fraction of  $2p_x$  included in the Level 3 is large, as shown in Fig. 1.17 and 1.18. On the other hand, the latter can not be easily explained by the compositions of the wave functions. There is not significant difference between the fractions of  $2p_x$  and  $2p_y$  included in the Level 1 and Level 2. To understand these features quantitatively, the theoretical study using the time-dependent Schrödinger equation may be needed.

#### ***RCE from 1s to n = 3 states (Charge state distribution)***

The RCE from 1s to the  $n = 3$  states is shown in Fig. 3.25. Similarly to the case of Ar<sup>17+</sup> ions, the resonance peak height decreased with increasing  $l$ , which is also explained by the absolute value of the Fourier potential. The resonance peak for the  $n = 3$  states was wider than for the  $n = 2$  states. Table 3.7 shows the energy widths  $\Delta E$  predicted by the linear Stark effect and the observed widths. A reasonable agreement is obtained between the theory and experiment.

## Fe<sup>24+</sup> ions

### *Charge state distribution*

Similarly to the case of helium-like Ar<sup>16+</sup> ions, two resonance peaks ( $1s^2 \rightarrow 1s2p\ ^1P_1$  and  $\ ^3P_1$ ) were observed, as shown in Fig. 3.29. In this case, the order of the RCE was  $(k, l) = (2, -1)$ . Compared to the case of hydrogen-like Fe<sup>25+</sup> ions, the skewness of the resonance peak was small, which indicates that the contribution of the Stark effect is small. This is due to the fact that the energy levels are not degenerate with respect to the angular momenta for helium-like ions.

### *Deexcitation X-rays*

We also obtained the resonance profile by measuring the projectile deexcitation X-rays. As shown in Fig. 3.31, the ratio of the resonance peak height for  $\ ^3P_1$  to that for  $\ ^1P_1$  was small compared to the case of the charge state distribution. This is due to the fact that the lifetime of  $1s2p\ ^3P_1 \rightarrow 1s^2$  ( $2.3 \times 10^{-14}$  s) is longer than that of  $1s2p\ ^1P_1 \rightarrow 1s^2$  ( $2.2 \times 10^{-15}$  s). The large anisotropy observed at the  $\ ^1P_1$  peak position is qualitatively explained by the excitation probability. As shown in Fig. 1.21(1.22), the absolute value of the transition matrix element for  $1s \rightarrow 2p_x$  is large at the channel center, where the radiative deexcitation process is dominant.

## Fe<sup>23+</sup> ions

The RCE of lithium-like ions was observed for the first time. As shown in Fig. 3.33, many resonance peaks were observed. We compared the observed peak energies with the transition energies in vacuum. However, the assignments of the peaks were difficult. To perform the assignments, we need to calculate the transition energy shift due to the Stark effect for the three-electron ions.

# Chapter 4

## High precision spectroscopy of helium-like ions

As shown in the equation of the RCE condition,

$$E_{trans} = \frac{h\gamma v}{a}(\sqrt{2}k \cos \theta + l \sin \theta), \quad (4.1)$$

the transition energy of the ion is determined from the beam velocity (energy) as well as the resonance peak position (angle), which can be determined with a high precision under the present experimental condition. For determining the transition energy precisely, we need to measure the beam energy precisely. The precision of the transition energy also depends on that of the lattice constant of Si, which was measured with a high precision [70, 71]. By using the following method, we measured the beam energy, and determined the transition energies of helium-like  $\text{Ar}^{16+}$  and  $\text{Fe}^{24+}$  ions. The flow chart of this procedure is shown in Fig. 4.1.

First, we observed the RCE of the hydrogen-like ions. These ions were produced by stripping the helium-like ions using Al foils. As stated in section 2.2, these foils were placed in front of the collimator. As shown in the RCE condition (equation 4.1), the beam velocity (energy) is determined from the resonance angle and the transition energy of the ion. By using the theoretical value as the transition energy, we determined the beam energy. To obtain the beam energy of the helium-like ions before entering the Al foil, we took into account the energy loss of the ion in the Al foil.

Second, we observed the RCE of the helium-like ions. In this case, we removed the Al foil. Using the beam energy obtained from the observation of the RCE of the hydrogen-like ions, we determined the transition energies of the helium-like ions. This procedure corresponds to determining the transition energy of the helium-like ion with respect to that of the hydrogen-like ion. It is to be noted that the precision of the lattice constant does not matter.

Inside the crystal, the transition energy is shifted from one in vacuum due to the Stark effect originating from the crystal potential and the wake potential. Moreover, the transition energy depends on the distance from the channel center. Accordingly, when we

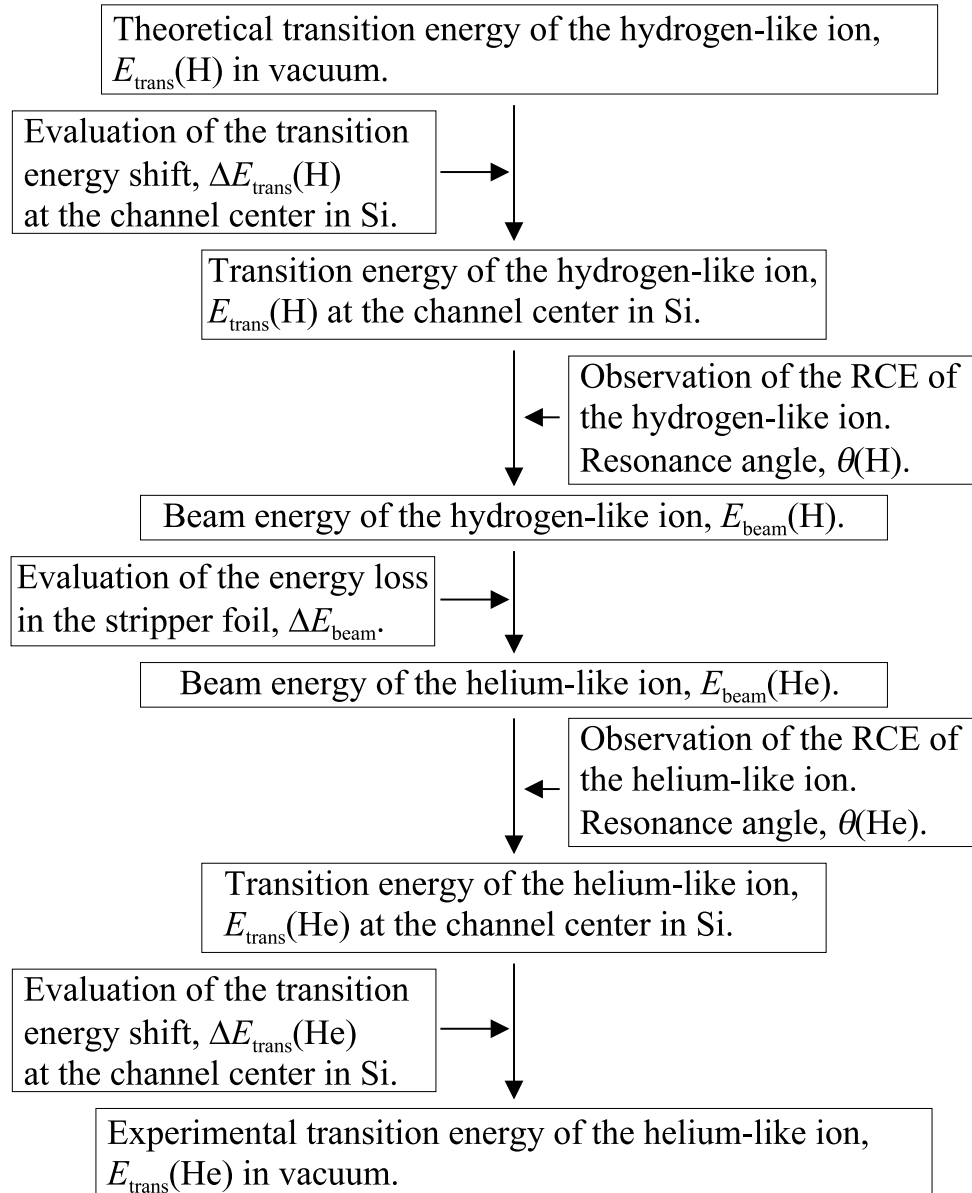


Figure 4.1: Flow chart of the procedure to perform spectroscopy of helium-like ions.

Table 4.1: Theoretical transition energies in vacuum (in eV) [37].

	$1s - 2p_{3/2}$	$1s - 2p_{1/2}$	$1s - 2s_{1/2}$
Ar <sup>17+</sup>	3322.992	3318.176	3318.334
Fe <sup>25+</sup>	6973.175	6951.961	6952.525

perform the above procedure, we need to evaluate the energy shift due to the position-dependent Stark effect. As stated in section 1.2.3, by using the SSD as a target crystal, we measured the energy deposition of the channeled ions, and obtained the information on the impact parameter dependence of the RCE. Here, instead of it, we measured the exit angle dependence of the RCE. The ion with a small oscillation amplitude tends to emerge from the crystal with a small exit angle, and be projected onto the region around  $x = 0$  in the PSD. Here, the peak position of the beam profile at the PSD was defined as  $x = 0$ . The energy shift for this ion is small, because this ion passed near the channel center where the strength of the electric field is small. By selecting the ions projected onto the region around  $x = 0$  in the PSD, we can restrict the amplitudes of the channeled ions.

As shown in chapter 3, for the helium-like ion incidence, we can also observe the RCE of the hydrogen-like ion which is produced inside the Si crystal. In this case, however, we can not determine the velocity of the helium-like ion from the resonance angle for the hydrogen-like ion, because the channeled hydrogen-like ion is likely produced from a helium-like ion with a large oscillation amplitude, which is due to the fact that the ionization probability is high near the atomic plane.

In the present work, we determined the transition energies of  $1s^2 \rightarrow 1s2p \ ^1P_1$  and  $\ ^3P_1$  in Ar<sup>16+</sup> and Fe<sup>24+</sup> ions. By observing the RCE of  $1s \rightarrow 2p_{3/2}$  in the hydrogen-like ions, we obtained the beam energies. In section 4.1, we evaluated the transition energy shift due to the Stark effect. In section 4.2, the exit angle dependence of the RCE is discussed. In section 4.3 and 4.4, the results of the high precision spectroscopy are shown for Ar<sup>16+</sup> and Fe<sup>24+</sup> ions, respectively.

## 4.1 Energy shift due to the Stark effect

Inside the Si crystal, the energy level of the electron bound to the ion is shifted from one in vacuum due to the Stark effect, which originates from the wake potential and the planar potential. As shown in section 1.2.4, we calculated the transition energies of  $1s \rightarrow n = 2$  in hydrogen-like Ar<sup>17+</sup> and Fe<sup>25+</sup> ions using the perturbation theory. The theoretical transition energy in vacuum which we used in the calculation is shown in table 4.1. Table 4.2 shows the obtained shifts of the transition energies of  $1s \rightarrow 2p_{3/2}$  (Level 3 and 4) at the channel center.

We also evaluated the energy shifts for the helium-like ions. At the channel center,

Table 4.2: Shifts of the transition energies of  $1s \rightarrow 2p_{3/2}$  (Level 3 and 4) at the channel center (in eV).

	Level 3	Level 4	average
Ar <sup>17+</sup>	-0.30	-0.12	-0.21 ± 0.09
Fe <sup>25+</sup>	-0.15	-0.06	-0.11 ± 0.05

the perturbation potential due to the static crystal potential  $\phi_{00}(x)$  is approximated as

$$\begin{aligned}
H_2(x) &= -e\gamma \times \phi_{00}(x) \\
&\simeq -e\gamma \times \left( \phi_{00}(0) + \frac{1}{2} \left( \frac{d^2\phi_{00}(x)}{dx^2} \right)_{x=0} x^2 \right) \\
&= -e\gamma \times (\phi_{00}(0) + 2\pi en_e(0)x^2),
\end{aligned} \tag{4.2}$$

where  $n_e(0)$  is the electron density at the channel center. Accordingly, using the perturbation theory, the shift  $\Delta E_{trans}$  of the transition energy is calculated as

$$\Delta E_{trans} = -2\pi\gamma e^2 n_e(0) (\langle 1s2p|x_1^2 + x_2^2|1s2p\rangle - \langle 1s^2|x_1^2 + x_2^2|1s^2\rangle), \tag{4.3}$$

where  $x_1$  and  $x_2$  denote the coordinates of the electrons of the helium-like ions. We used the following wave functions as those of the helium-like ions, and calculated the energy shift.

$$|1s^2\rangle = \phi_{1s}(\mathbf{r}_1)\phi_{1s}(\mathbf{r}_2), \tag{4.4}$$

$$|1s2p(^1P_1)\rangle = \frac{1}{\sqrt{2}} (\phi_{1s}(\mathbf{r}_1)\phi_{2p}(\mathbf{r}_2) + \phi_{1s}(\mathbf{r}_2)\phi_{2p}(\mathbf{r}_1)), \tag{4.5}$$

$$|1s2p(^3P_1)\rangle = \frac{1}{\sqrt{2}} (\phi_{1s}(\mathbf{r}_1)\phi_{2p}(\mathbf{r}_2) - \phi_{1s}(\mathbf{r}_2)\phi_{2p}(\mathbf{r}_1)), \tag{4.6}$$

where  $\phi_{1s}(\mathbf{r})$  and  $\phi_{2p}(\mathbf{r})$  are the hydrogenic wave functions of  $1s$  and  $2p$  states, respectively. For  $1s2p_x$ ,  $\Delta E_{trans}$  is obtained as

$$\Delta E_{trans} = -2\pi\gamma e^2 n_e(0) \frac{17a_B^2}{Z_p^2}, \tag{4.7}$$

where  $a_B$  is the Bohr radius and  $Z_p$  is the effective projectile charge. For  $1s2p_y$  and  $1s2p_z$ ,  $\Delta E_{trans}$  is obtained as

$$\Delta E_{trans} = -2\pi\gamma e^2 n_e(0) \frac{5a_B^2}{Z_p^2}. \tag{4.8}$$

In the case of Ar<sup>16+</sup> ions,  $Z_p$  is considered to be in the range from 17 and 18. The effective charge  $Z_p = 17$  means the full screening by the other electron. The energy shift  $\Delta E_{trans}$  calculated for Ar<sup>16+</sup> and Fe<sup>24+</sup> ions are summarized in table 4.3. Here,  $n_e(0)$  was calculated using the Molière potential as an atomic potential (see equation 1.13). This

Table 4.3: Shifts of the transition energies of  $1s^2 \rightarrow 1s2p$  at the channel center (in eV).

	$Z_p$	$1s2p_x$	$1s2p_y$ and $1s2p_z$	$1s2p(\text{average})$
Ar <sup>16+</sup>	17	-0.39	-0.12	-0.21
Ar <sup>16+</sup>	18	-0.35	-0.11	-0.19
Fe <sup>24+</sup>	25	-0.19	-0.06	-0.10
Fe <sup>24+</sup>	26	-0.18	-0.06	-0.09

Table 4.4: Evaluated shifts of the transition energies of  $1s^2 \rightarrow 1s2p$  in Ar<sup>16+</sup> and Fe<sup>24+</sup> ions at the channel center.

	energy shift, $\Delta E_{trans}$ (eV)
Ar <sup>16+</sup>	$-0.16 \pm 0.05$
Fe <sup>24+</sup>	$-0.14 \pm 0.05$

electron density agrees with one calculated using the ZBL potential within  $\sim 20\%$ , and one calculated using the Doyle-Turner potential within  $\sim 10\%$ .

As shown in Fig. 1.19(1.20) and Fig. 1.21(1.22), we calculated the transition matrix elements for  $1s \rightarrow 2p_x, 2p_y,$  and  $2p_z$  for Ar and Fe ions, respectively. The orders  $(k, l)$  of the RCE are  $(1, 1)$  and  $(2, 1)$  for Ar and Fe ions, respectively. In the case of Ar ions, at the channel center, the absolute value of the transition matrix elements for  $2p_y$  and  $2p_z$  are larger than that for  $2p_x$ , which is 0. This indicates that the transition to  $2p_y$  and  $2p_z$  is dominant at the channel center. Accordingly, the transition energy shift of  $1s^2 \rightarrow 1s2p$  is considered to be in the range from  $-0.21$  eV ( $\Delta E_{trans}(Z_p = 17)$  for  $1s2p(\text{average})$ ) to  $-0.11$  eV ( $\Delta E_{trans}(Z_p = 18)$  for  $1s2p_y$  and  $1s2p_z$ ). In the case of Fe ions, on the other hand, the absolute value of the transition matrix element for  $2p_x$  is larger than those for  $2p_y$  and  $2p_z$  at the channel center, which are 0. Accordingly, the transition energy shift is considered to be in the range from  $-0.19$  eV ( $\Delta E_{trans}(Z_p = 25)$  for  $1s2p_x$ ) to  $-0.09$  eV ( $\Delta E_{trans}(Z_p = 26)$  for  $1s2p(\text{average})$ ). Therefore, we evaluated the transition energy shifts of  $1s^2 \rightarrow 1s2p$  in Ar<sup>16+</sup> and Fe<sup>24+</sup> ions as  $-0.16 \pm 0.05$  eV and  $-0.14 \pm 0.05$  eV, respectively. These values are shown in table 4.4.

## 4.2 Exit angle dependence of RCE

The exit angle of the channeled ion is related to the vertical position ( $x$ ) of the ion detected with the PSD. The position  $x$  of the ion in the PSD is written as  $x = L \tan(\theta_{exit}) + x_i \simeq L\theta_{exit} + x_i$ , where  $L$  is the distance between the Si crystal and the PSD,  $\theta_{exit}$  is the exit angle, and  $x_i$  is the incident position of the ion at the crystal.

To investigate the relation between the exit angle and the oscillation amplitude of the

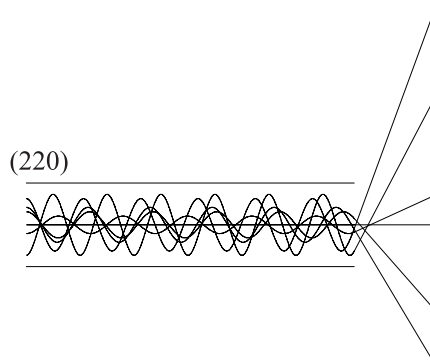


Figure 4.2: Trajectories of 390 MeV/u  $\text{Ar}^{18+}$  ions channeled in the (220) plane of the 21  $\mu\text{m}$  Si crystal.

channeled ion, we simulated the trajectories of the ions. Figure 4.2 shows some examples of the trajectories for 390 MeV/u  $\text{Ar}^{18+}$  ions channeled in the (220) plane of the 21  $\mu\text{m}$  Si crystal. The exit angle depends on the incident angle and incident position.

Figure 4.3 and 4.4 show the simulated exit angle distributions of 390 MeV/u  $\text{Ar}^{17+}$  ions channeled in the (220) plane with the oscillation amplitudes of 0 – 0.1  $\text{\AA}$  and 0.6 – 0.7  $\text{\AA}$ , respectively. As shown in these figures, the ions with small oscillation amplitudes emerge from the crystal with small exit angles. This indicates that we can restrict the amplitudes of the ions by selecting the exit angles, *i.e.*, position  $x$ .

Figure 4.5 shows the ionized fraction of  $\text{Ar}^{17+}$  ions via the RCE process for  $1s \rightarrow n = 2$  in 390 MeV/u  $\text{Ar}^{17+}$  ions as a function of transition energy (tilt angle) and position  $x$ . The position  $x$  reflects the oscillation amplitude of the channeled ion. This figure is similar to the contour plot shown in Fig. 1.9, where the ionized fraction is plotted as a function of the energy deposition. As can be seen in Fig. 4.5, the transition energy varies depending on the position  $x$ . The shift from the transition energy in vacuum increases with increasing  $|x|$ . Figure 4.6 shows the ionized fraction of  $\text{Fe}^{25+}$  ions via the RCE process for  $1s \rightarrow n = 2$  in 460 MeV/u  $\text{Fe}^{25+}$  ions. The energy shift is small compared to that for  $\text{Ar}^{17+}$  ions.

### 4.3 Spectroscopy of helium-like $\text{Ar}^{16+}$ ions

#### *Resonance angle*

We observed the resonance profiles for  $1s \rightarrow 2p_{3/2}$  in  $\text{Ar}^{17+}$  ions, and those for  $1s^2 \rightarrow 1s2p$   $^1P_1$  and  $^3P_1$  in  $\text{Ar}^{16+}$  ions by measuring the charge state distributions of the ions transmitted through the Si crystal. The hydrogen-like  $\text{Ar}^{17+}$  ions were produced by stripping the helium-like  $\text{Ar}^{16+}$  ions using the 5  $\mu\text{m}$  Al foil, which was placed in front of the collimator. When we observed the RCE of  $\text{Ar}^{16+}$  ions, we removed this Al foil. In this case, under the (220) planar channeling condition, the charge state fractions of  $\text{Ar}^{16+}$ ,  $\text{Ar}^{17+}$ , and  $\text{Ar}^{18+}$  ions transmitted through the Si crystal were 33%, 32%, and 35%, respectively. When

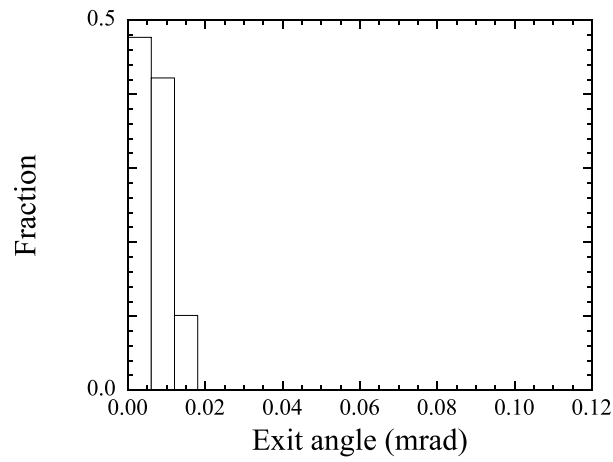


Figure 4.3: Exit angle distribution of 390 MeV/u  $\text{Ar}^{17+}$  ions channeled in the (220) plane with the oscillation amplitudes of 0 – 0.1 Å.

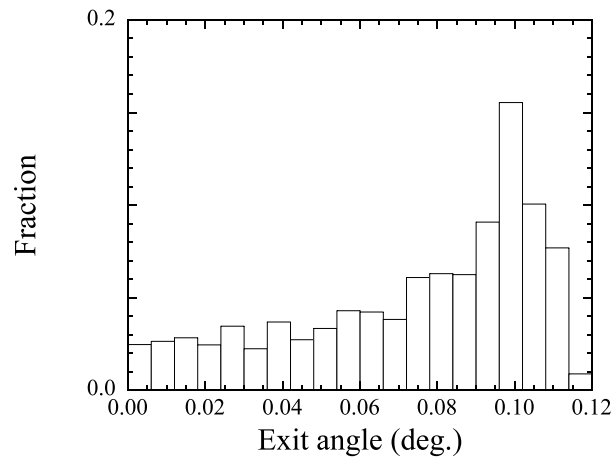


Figure 4.4: Exit angle distribution of 390 MeV/u  $\text{Ar}^{17+}$  ions channeled in the (220) plane with the oscillation amplitudes of 0.6 – 0.7 Å.

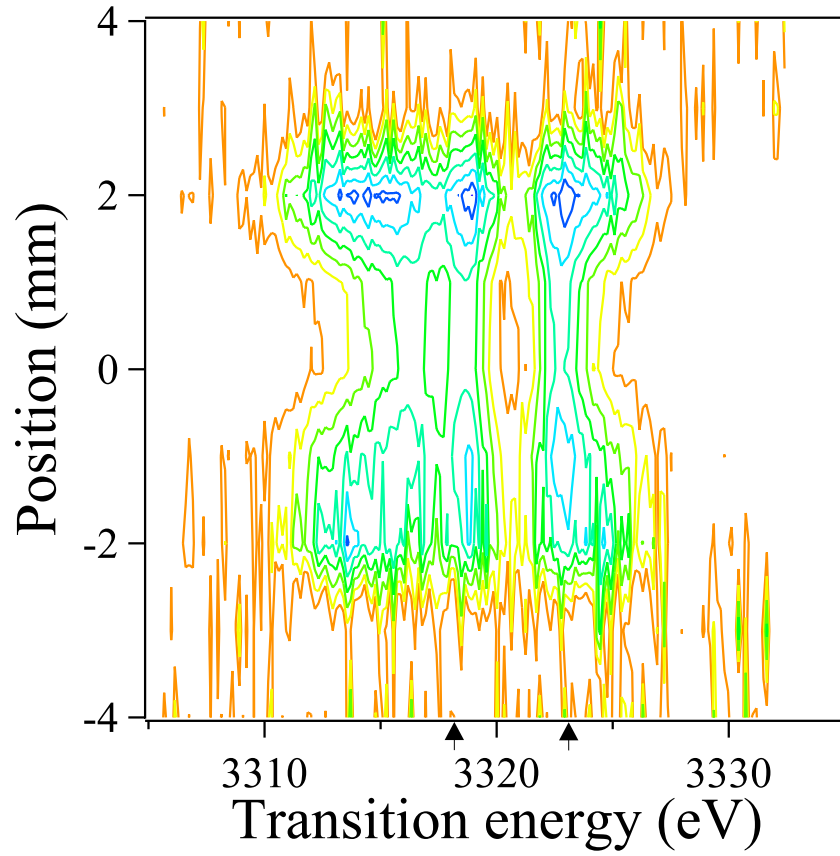


Figure 4.5: Contour plot of the ionized fraction via the RCE process for  $1s \rightarrow n = 2$  in  $\text{Ar}^{17+}$  ions. The arrows show the theoretical transition energies in vacuum.

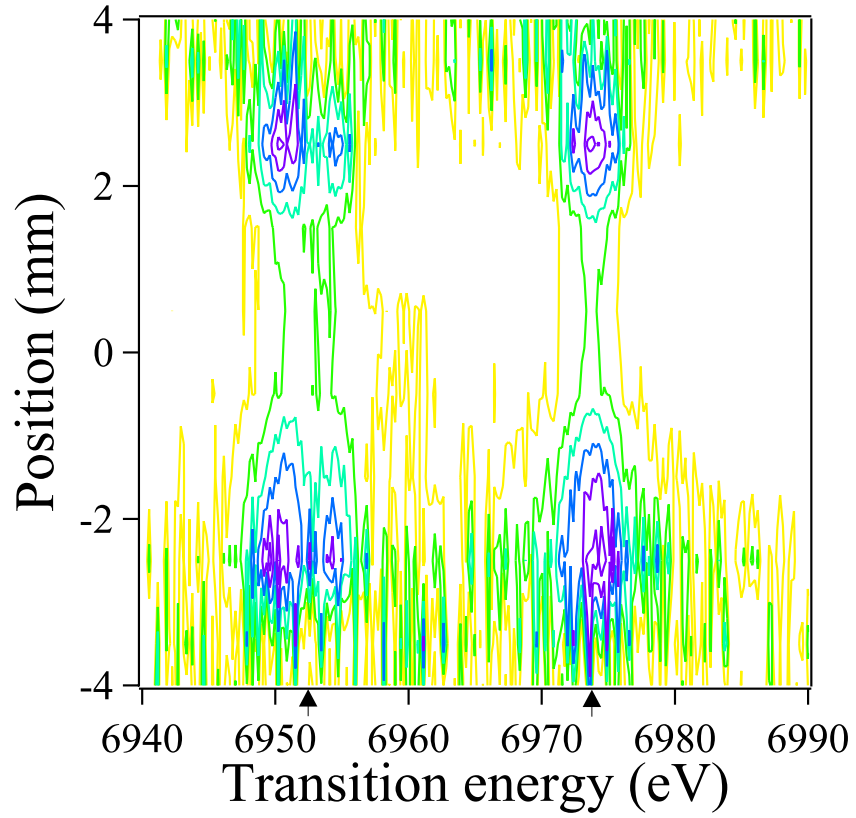


Figure 4.6: Contour plot of the ionized fraction via the RCE process for  $1s \rightarrow n = 2$  in  $\text{Fe}^{25+}$  ions. The arrows show the theoretical transition energies in vacuum.

we placed the 5  $\mu\text{m}$  Al foil, the charge state fractions of Ar<sup>16+</sup>, Ar<sup>17+</sup>, and Ar<sup>18+</sup> ions were 1%, 13%, and 86%, respectively. Figure 4.7, 4.8, and 4.9 show the typical resonance profiles for  $2p_{3/2}$  in Ar<sup>17+</sup>,  $^1P_1$  and  $^3P_1$  in Ar<sup>16+</sup> ions, respectively. These profiles were obtained from the ions projected onto the position of  $-\Delta x \leq x \leq +\Delta x$  in the PSD. By fitting the gaussian profiles to the observed resonance profiles, we determined the peak positions, and examined its  $\Delta x$  dependence. For  $2p_{3/2}$  in Ar<sup>17+</sup> ions, the  $\Delta x$  dependence is shown in Fig. 4.10. The resonance angle varied depending on  $\Delta x$ , which is due to the fact that the contribution of the Stark effect increases with increasing  $\Delta x$ . We determined the peak positions as  $2.8411 \pm 0.0009^\circ$ ,  $1.8510 \pm 0.0002^\circ$ , and  $2.2347 \pm 0.0006^\circ$  for  $2p_{3/2}$ ,  $^1P_1$ , and  $^3P_1$ , respectively. Here, the errors show the statistical ones. The systematic error of the angle was estimated to be  $\pm 0.002^\circ$ , as shown in section 2.2.6.

### **Beam energy**

For Ar<sup>17+</sup> ions, by substituting the observed peak position ( $2.8411^\circ$ ) and the theoretical transition energy into the equation of the RCE condition, the beam energy of Ar<sup>17+</sup> ions is calculated to be 382.908 MeV/u. As the theoretical transition energy of  $1s \rightarrow 2p_{3/2}$ , we used the value of 3322.79 eV. This energy is the average transition energy of  $1s \rightarrow n = 2$  (Level 3) (3322.69 eV) and  $n = 2$  (Level 4) (3322.88 eV) at the channel center.

For obtaining the beam energy before entering the 5  $\mu\text{m}$  Al foil, we need to take into account the energy loss of the ion in the foil. We calculated the energy loss using the Bethe-Bloch formula,

$$S = \frac{4\pi N Z_{eff}^2 Z_t e^4}{mv^2} \left( \ln \frac{2mv^2}{I} - \ln(1 - \beta^2) - \beta^2 \right), \quad (4.9)$$

where  $S$  is the stopping power,  $N$  is the target atomic density,  $Z_{eff}$  is the effective projectile charge,  $Z_t$  is the target atomic number,  $e$  is the electron charge,  $m$  is the electron mass,  $v$  is the projectile velocity,  $\beta = v/c$ , and  $I$  is the mean excitation energy. In this formula, the stopping power is proportional to  $Z_{eff}^2$ . The effective charge  $Z_{eff}$  of Ar<sup>17+</sup> ion passed through the 5  $\mu\text{m}$  Al foil for Ar<sup>16+</sup> incidence is considered to be in the range from 16 to 18, so that the energy loss is estimated to be  $0.023 \pm 0.003$  MeV/u. Accordingly, the beam energy of Ar<sup>16+</sup> ion before entering the Al foil is calculated to be  $382.931 \pm 0.025$  MeV/u. The errors of the beam energy are summarized in table 4.5.

### **Transition energy**

From this beam energy and the observed peak positions, we obtained the transition energies at the channel center as 3139.11 and 3123.14 eV for  $1s^2 \rightarrow 1s2p$   $^1P_1$  and  $1s^2 \rightarrow 1s2p$   $^3P_1$  in Ar<sup>16+</sup> ions, respectively. Taking into account the energy shifts due to the Stark effect ( $-0.16$  eV) at the channel center, which are shown in table 4.4, the transition energies in vacuum were obtained as  $3139.27 \pm 0.15$  and  $3123.30 \pm 0.16$  eV for  $^1P_1$  and  $^3P_1$ , respectively. The errors of the transition energies are shown in table 4.6 and 4.7.

Comparison between the transition energies obtained in the present work and the theoretical values are shown in table 4.8. The transition energies calculated by the relativistic

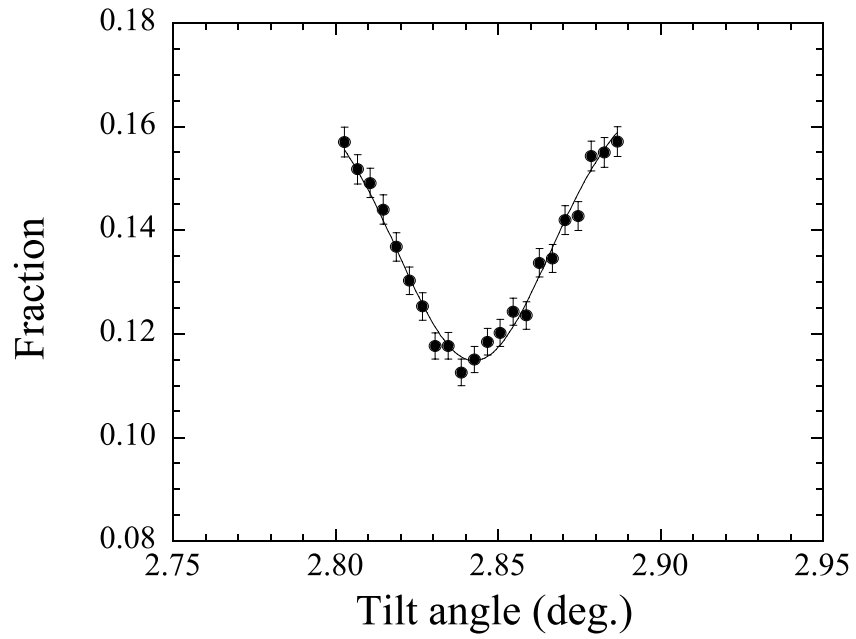


Figure 4.7: Resonance profile for  $1s \rightarrow 2p_{3/2}$  in  $\text{Ar}^{17+}$  ions.  $\Delta x = 0.2$  mm.

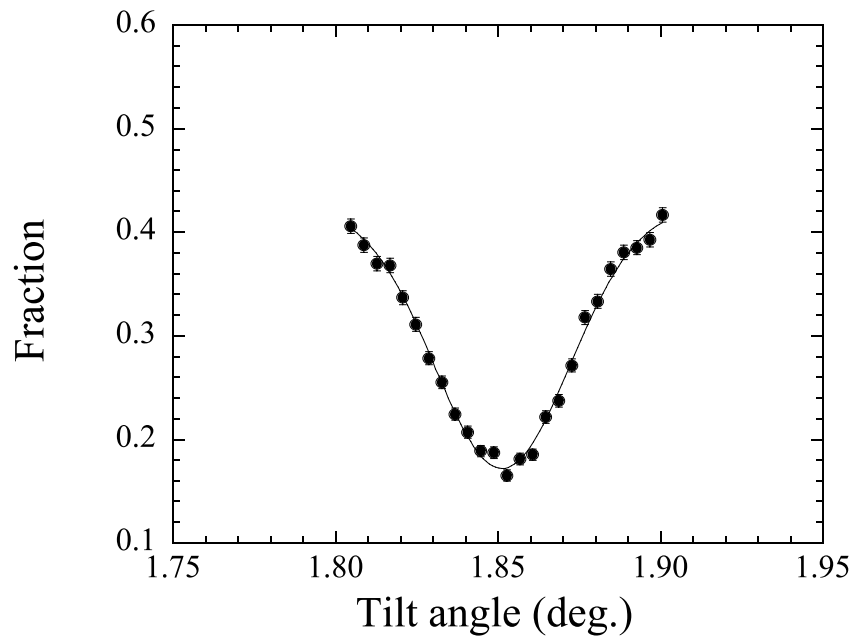


Figure 4.8: Resonance profile for  $1s^2 \rightarrow 1s2p \ ^1P_1$  in  $\text{Ar}^{16+}$  ions.  $\Delta x = 0.2$  mm.

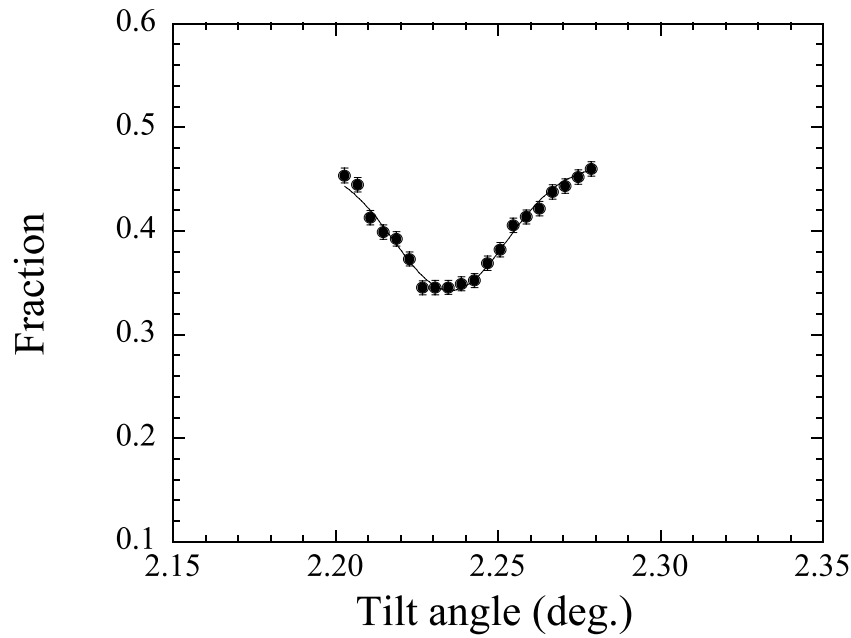


Figure 4.9: Resonance profile for  $1s^2 \rightarrow 1s2p^3P_1$  in  $\text{Ar}^{16+}$  ions.  $\Delta x = 0.2$  mm.

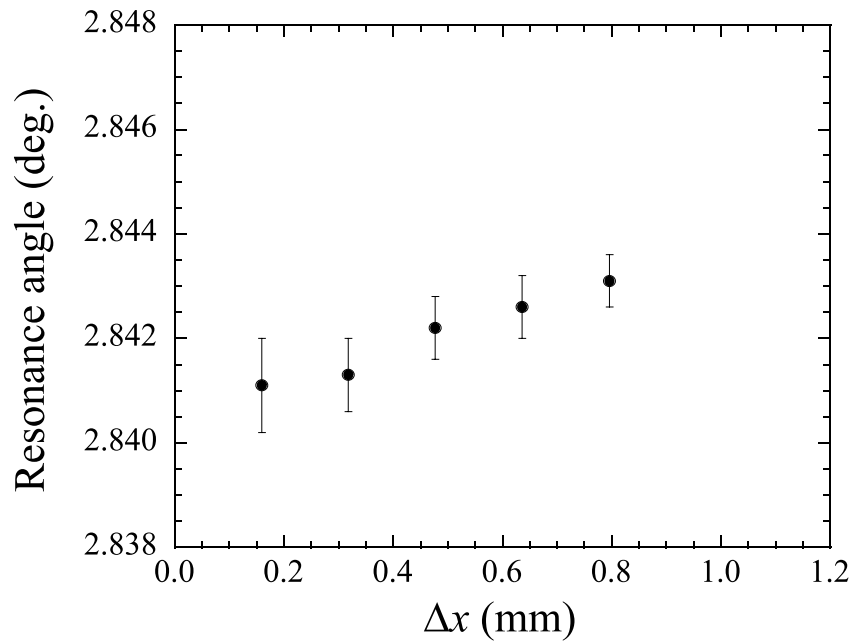


Figure 4.10:  $\Delta x$  dependence of the resonance angle for  $2p_{3/2}$  in  $\text{Ar}^{17+}$  ions.

Table 4.5: Errors of Ar<sup>16+</sup> beam energy.

		(MeV/u)	(ppm)
angle(stat.)	0.0009°	0.007	18
angle(syst.)	0.002°	0.015	39
energy loss (Al)		0.003	8
transition energy at the channel center	0.09 eV	0.018	47
total		0.025	65

Table 4.6: Errors of the transition energy for <sup>1</sup>P<sub>1</sub> in Ar<sup>16+</sup> ions.

		(eV)	(ppm)
angle(stat.)	0.0002°	0.01	3
angle(syst.)	0.002°	0.08	25
beam energy	0.025 MeV/u	0.12	38
transition energy at the channel center		0.05	16
total		0.15	48

Table 4.7: Errors of the transition energy for <sup>3</sup>P<sub>1</sub> in Ar<sup>16+</sup> ions.

		(eV)	(ppm)
angle(stat.)	0.0006°	0.03	10
angle(syst.)	0.002°	0.08	26
beam energy	0.025 MeV/u	0.12	38
transition energy at the channel center		0.05	16
total		0.16	51

Table 4.8: Comparison of the transition energies for  $1s^2 \rightarrow 1s2p$   $^1P_1$  and  $^3P_1$  in  $Ar^{16+}$  ions between theories and the present experiment (in eV).

	Cheng <i>et al.</i> Rel. CI [50]	Drake Unif. theory [51]	Plante <i>et al.</i> All-order [52]	Indelicato <i>et al.</i> MCDF [53]	exp. present work
$^1P_1$	3139.617	3139.577	3139.582	3139.649	$3139.27 \pm 0.15$
$^3P_1$	3123.574	3123.530	3123.534	3123.567	$3123.30 \pm 0.16$

Table 4.9: Experimental transition energies for  $1s^2 \rightarrow 1s2p$   $^1P_1$  and  $^3P_1$  in  $Ar^{16+}$  ions (in eV).

	Deslattes <i>et al.</i> [54]	Briand <i>et al.</i> [41]	present work
$^1P_1$	$3139.55 \pm 0.04$	$3139.57 \pm 0.25$	$3139.27 \pm 0.15$
$^3P_1$	$3123.52 \pm 0.04$	$3123.60 \pm 0.25$	$3123.30 \pm 0.16$

configuration-interaction code [50], unified method [51], all-order many-body calculations [52], and multiconfiguration Dirac-Fock (MCDF) [53] method are shown as the theoretical values. Table 4.9 shows the transition energies measured by other groups and in the present work. The precision of the present work is comparable to those of other groups. They performed spectroscopy using crystal spectrometers. As shown in table 4.8 and 4.9, the present experimental values are smaller than the theories and the experimental values measured by other groups by about 0.3 eV. The reason of this disagreement is not clear. As shown in Fig. 4.5, the energy shift due to the Stark effect for  $2p_{3/2}$  in  $Ar^{17+}$  ion is large. The contribution of the ions with large oscillation amplitudes may be large while we selected the position  $x$ .

## 4.4 Spectroscopy of helium-like $Fe^{24+}$ ions

### *Resonance angle*

We also performed spectroscopy of  $Fe^{24+}$  ions using the same method as that for  $Ar^{16+}$  ions. To produce  $Fe^{25+}$  ions, we used a 13  $\mu\text{m}$  Al foil as a stripper foil. The charge state fractions of  $Fe^{24+}$ ,  $Fe^{25+}$ , and  $Fe^{26+}$  ions transmitted through the Si crystal under the (220) planar channeling condition were 56%, 20%, and 25%, respectively, when the stripper foil was removed. In the case that we used it, the charge state fractions of  $Fe^{24+}$ ,  $Fe^{25+}$ , and  $Fe^{26+}$  ions were 2%, 17%, and 81%, respectively. Figure 4.11, 4.12, and 4.13 show the typical resonance profiles for  $1s \rightarrow 2p_{3/2}$  in  $Fe^{25+}$  ions, and those for  $1s^2 \rightarrow 1s2p$   $^1P_1$  and  $^3P_1$  in  $Fe^{24+}$  ions, respectively. These profiles were obtained from the position-selected

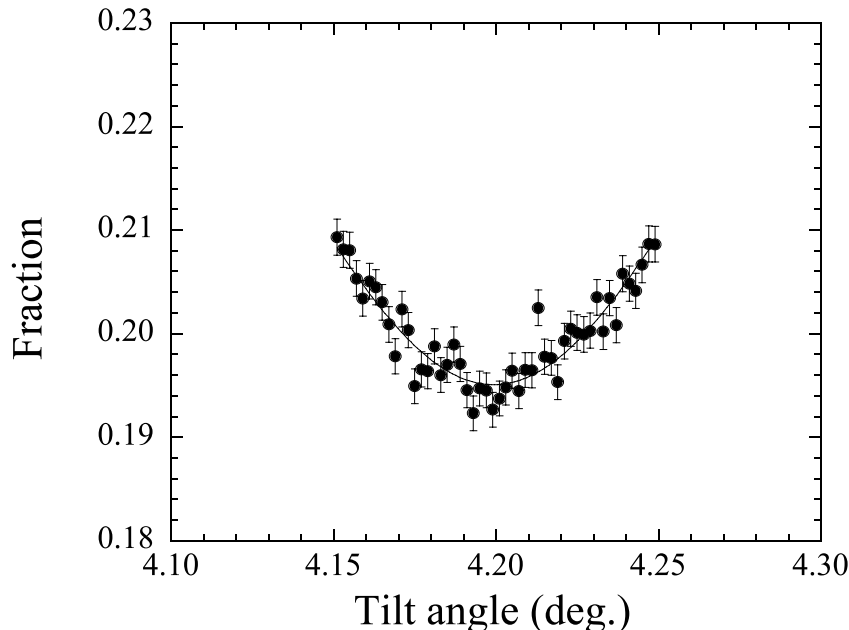


Figure 4.11: Resonance profile for  $1s \rightarrow 2p_{3/2}$  in  $\text{Fe}^{25+}$  ions.  $\Delta x = 1.2$  mm.

ions.

By fitting the gaussian profiles to the observed resonance profiles, we obtained the resonance angles. Figure 4.14 shows the  $\Delta x$  dependence of the resonance angle for  $2p_{3/2}$  in  $\text{Fe}^{25+}$  ions. Similarly to the case of  $\text{Ar}^{17+}$  ions, the resonance angle varied depending on  $\Delta x$  due to the Stark effect. The peak positions were determined as  $4.1970 \pm 0.0020^\circ$ ,  $2.5882 \pm 0.0006^\circ$ , and  $3.2683 \pm 0.0007^\circ$  for  $2p_{3/2}$ ,  $^1P_1$ ,  $^3P_1$ , respectively. Here, these errors show the statistical ones. Similarly to the case of Ar ions, the systematic error of the angle was  $0.002^\circ$ .

### ***Beam energy***

From the observed resonance angle ( $4.1970^\circ$ ) and the theoretical transition energy for  $2p_{3/2}$ , the beam energy is calculated to be 422.857 MeV/u. As the theoretical transition energy, we used the value of 6973.07 eV, which is the average transition energy of  $1s \rightarrow n = 2(\text{Level } 3)$  (6973.02 eV) and  $n = 2(\text{Level } 4)$  (6973.12 eV) at the channel center. The energy loss of  $\text{Fe}^{25+}$  ion passed through the 13  $\mu\text{m}$  Al foil is estimated to be  $0.089 \pm 0.007$  MeV/u, since the effective projectile charge  $Z_{eff}$  is considered to be in the range from 24 to 26. Taking into account this energy loss, the beam energy amounts to  $422.946 \pm 0.013$  MeV/u. The errors of the beam energy are shown in table 4.10.

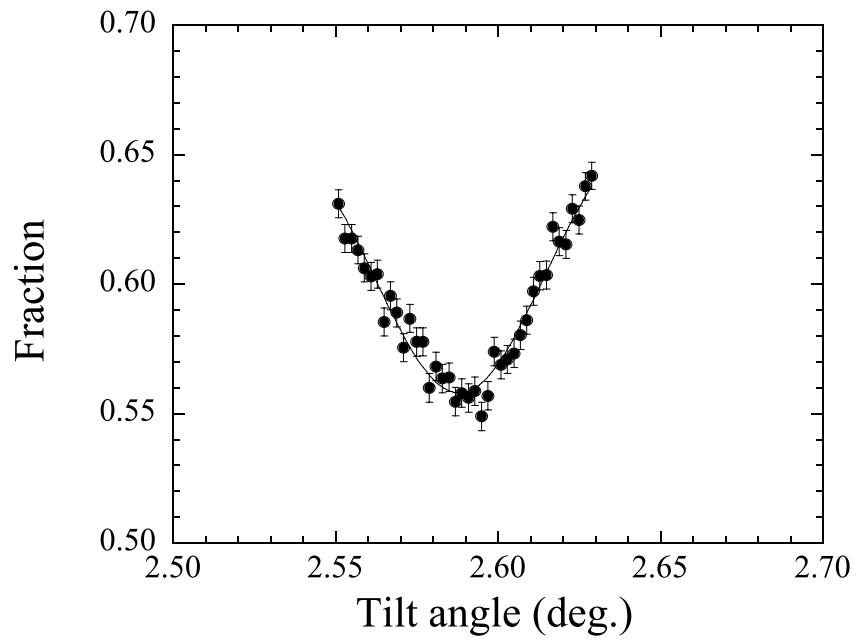


Figure 4.12: Resonance profile for  $1s^2 \rightarrow 1s2p \ ^1P_1$  in  $Fe^{24+}$  ions.  $\Delta x = 0.3$  mm.

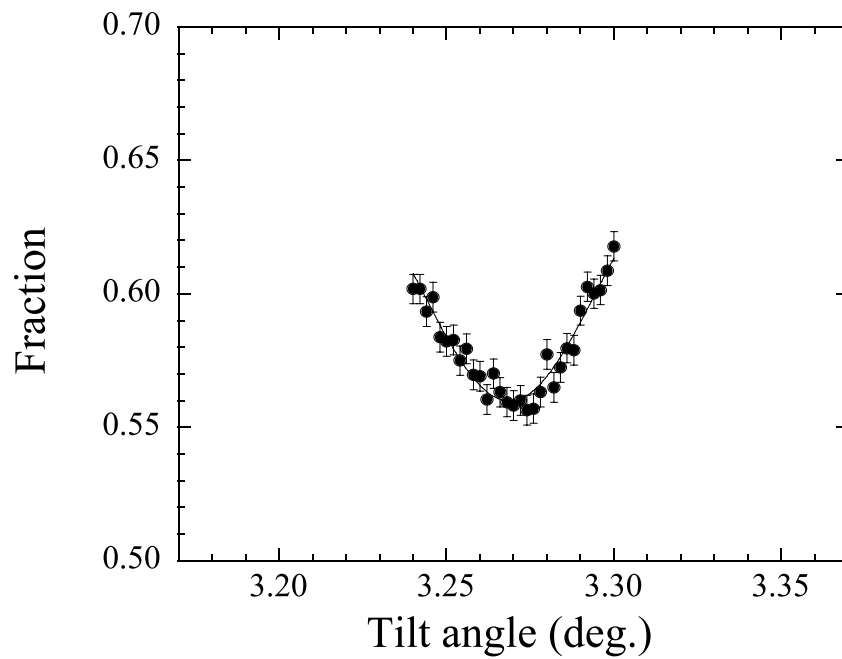
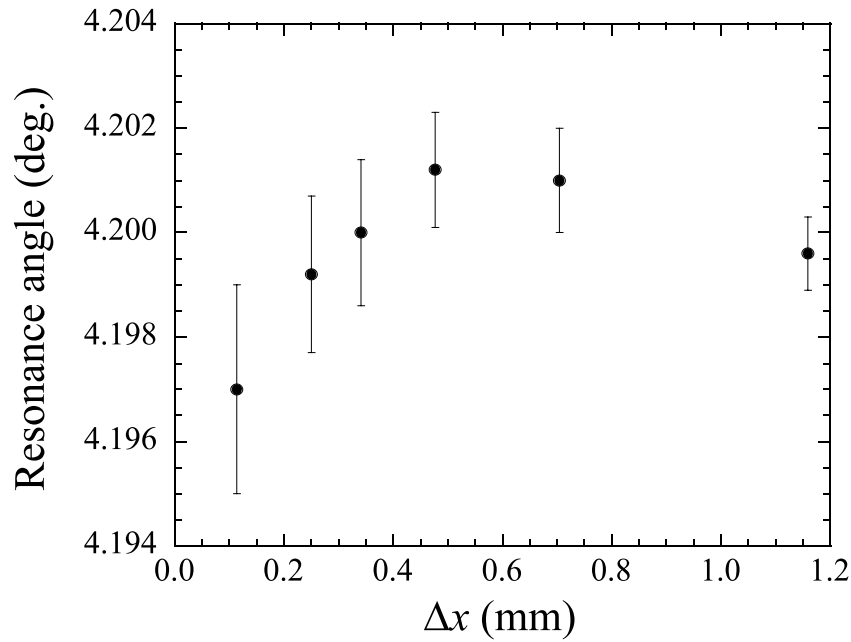


Figure 4.13: Resonance profile for  $1s^2 \rightarrow 1s2p \ ^3P_1$  in  $Fe^{24+}$  ions.  $\Delta x = 0.3$  mm.

Figure 4.14:  $\Delta x$  dependence of the resonance angle for  $2p_{3/2}$  in  $\text{Fe}^{25+}$  ions.Table 4.10: Errors of  $\text{Fe}^{24+}$  beam energy.

		(MeV/u)	(ppm)
angle(stat.)	$0.0020^\circ$	0.007	17
angle(syst.)	$0.002^\circ$	0.007	17
energy loss (Al)		0.007	17
transition energy at the channel center	0.05 eV	0.005	12
total		0.013	31

Table 4.11: Errors of the transition energy for  $^1P_1$  in  $Fe^{24+}$  ions.

		(eV)	(ppm)
angle(stat.)	0.0006°	0.03	4
angle(syst.)	0.002°	0.09	13
beam energy	0.013 MeV/u	0.12	18
transition energy at the channel center		0.05	7
total		0.16	24

Table 4.12: Errors of the transition energy for  $^3P_1$  in  $Fe^{24+}$  ions.

		(eV)	(ppm)
angle(stat.)	0.0007°	0.03	4
angle(syst.)	0.002°	0.10	15
beam energy	0.013 MeV/u	0.12	18
transition energy at the channel center		0.05	7
total		0.17	25

### ***Transition energy***

Using the obtained beam energy, the transition energies at the channel center were obtained as 6700.08 and 6667.38 eV for  $^1P_1$  and  $^3P_1$  in  $Fe^{24+}$  ions, respectively. In section 4.1, the energy shift  $\Delta E_{trans}$  is evaluated to be  $-0.14 \pm 0.05$  eV. As a result, the transition energies in vacuum were obtained as  $6700.22 \pm 0.16$  and  $6667.52 \pm 0.17$  eV for  $^1P_1$  and  $^3P_1$ , respectively. The errors of the transition energies are summarized in table 4.11 and 4.12.

Table 4.13 shows the comparison between the present experiment and theories, and table 4.14 shows the comparison between the present experimental values and those measured by other groups. For  $^3P_1$ , the transition energy obtained in the present work is in good agreement with the theories and the experimental value measured by Briand *et al.* For  $^1P_1$ , the obtained transition energy is in reasonable agreement with the theoretical values calculated by the unified theory and the all-order many-body calculations, however, slightly smaller than the theoretical values calculated by the relativistic CI method and MCDF method. The present experimental value is not in agreement with the experimental ones obtained by Beiersdorfer *et al.* and Briand *et al.* within experimental errors. The values obtained by Beiersdorfer *et al.* and Briand *et al.* are slightly larger than the theories. The cause of the discrepancies is not clear. To clarify it, more precise measurements and analyses are needed.

Table 4.13: Comparison of the transition energies for  $1s^2 \rightarrow 1s2p$   $^1P_1$  and  $^3P_1$  in  $\text{Fe}^{24+}$  ions between theories and the present experiment (in eV).

	Cheng <i>et al.</i> Rel. CI [50]	Drake Unif. theory [51]	Plante <i>et al.</i> All-order [52]	Indelicato <i>et al.</i> MCDF [53]	exp. present work
$^1P_1$	6700.539	6700.404	6700.427	6700.603	$6700.22 \pm 0.16$
$^3P_1$	6667.692	6667.552	6667.567	6667.669	$6667.52 \pm 0.17$

Table 4.14: Experimental transition energies for  $1s^2 \rightarrow 1s2p$   $^1P_1$  and  $^3P_1$  in  $\text{Fe}^{24+}$  ions (in eV).

	Beiersdorfer <i>et al.</i> [55]	Briand <i>et al.</i> [56]	present work
$^1P_1$	$6700.73 \pm 0.20$	$6700.90 \pm 0.25$	$6700.22 \pm 0.16$
$^3P_1$		$6667.50 \pm 0.25$	$6667.52 \pm 0.17$

## 4.5 Discussion

For  $\text{Ar}^{16+}$  ions, the obtained transition energies were slightly smaller than the theories and the experimental values obtained by other groups. There is a possibility that the contribution of the ions channeled with large oscillation amplitudes was large while we restricted the exit angles of the ions by selecting the position  $x$  in the PSD. To select the amplitudes of the channeled ions, we selected the exit angles. However, some ions with large oscillation amplitudes emerge from the crystal with small exit angles. In the case of  $\text{Ar}^{17+}$  ions, the energy shift due to the Stark effect is large, as shown in Fig. 1.13 and 4.5. Figure 4.15 shows the position ( $x$ ) dependence of the resonance angle for  $2p_{3/2}$  in  $\text{Ar}^{17+}$  ions. The maximum shift of the resonance angle from one at  $x=0$  is  $\sim 0.01^\circ$ , which leads to the transition energy shift of about +0.4 eV for  $\text{Ar}^{16+}$  ions. Accordingly, there is a possibility that the disagreement between the theory and the present experiment is explained by the peak shift due to the contribution of the ions with large oscillation amplitudes. On the other hand, for  $2p_{3/2}$  in  $\text{Fe}^{25+}$  ions, the transition energy shift is small compared to the case of  $\text{Ar}^{17+}$  ions, as can be seen in Fig. 1.16 and 4.6. For  $^3P_1$  in  $\text{Fe}^{24+}$  ions, the obtained transition energy is in good agreement with the theories and the experimental value measured by Briand *et al.* For  $^1P_1$  in  $\text{Fe}^{24+}$  ions, on the other hand, the obtained transition energy is in good agreement with the unified theory and the all-order many-body calculations. However, the obtained transition energy is slightly smaller than the theoretical values predicted by the relativistic CI method and the MCDF method and the experimental values measured by Beiersdorfer *et al.* and Briand *et al.* These experimental values are larger than the theories. The reason of the disagreement

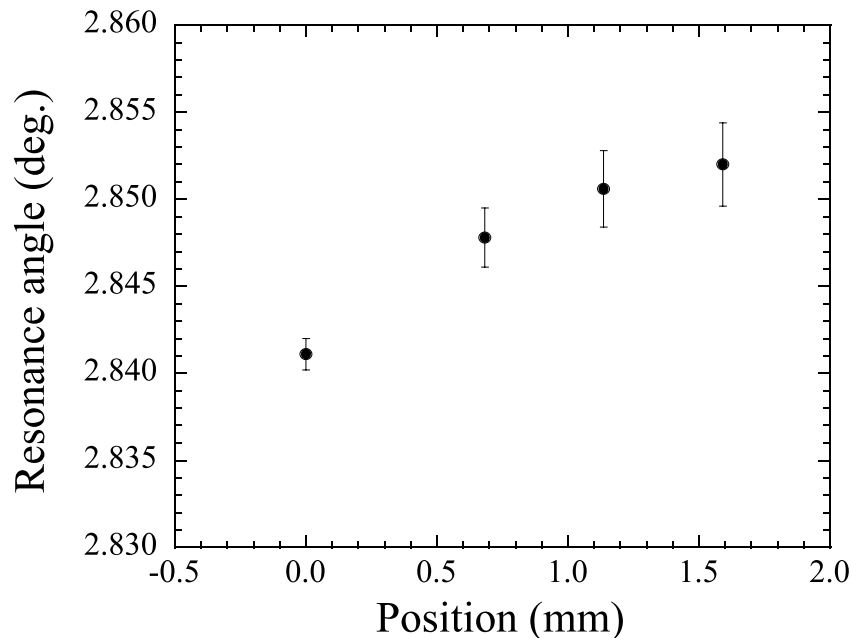


Figure 4.15: Position dependence of the resonance angle for  $2p_{3/2}$  in  $\text{Ar}^{17+}$  ions. The error bar shows the statistical error.

between these values and our data is not clear. The theoretical calculation including the higher-order QED corrections is anticipated.

As stated in section 1.2.3, we can also select the oscillation amplitudes by selecting the energy depositions of the channeled ions in the crystal, if we use the Si detector (SSD) as a target crystal. For example, the energy depositions of the ions channeled in the channel center are smallest. However, the thin SSD tends to be bent, so that it is difficult to perform the channeling experiment using such a thin SSD. If we can obtain the thin SSD which is not bent, we can select the amplitudes more strictly by using it.

As a high precision spectroscopy for Ar and Fe ions, the method using a crystal spectrometer has been used. In this method, the Doppler broadening and the spectator electrons limit the precision. The former originates from the motion of the ion from which the X-rays are emitted. The latter is due to the fact that the charge states of the ions are not checked. In the present method for atomic spectroscopy, we detect the ions transmitted through the crystal, so that the detection efficiency is high compared to the methods detecting the deexcitation X-rays. In addition, the obtained transition energy is not affected by the Doppler effect. Moreover, the spectator electron in the high  $n$  state does not exist, because the electron capture process is negligible in the present high energy region.

### Resolution limiting factors

In the spectroscopy method with RCE, there are some resolution limiting factors such as the energy loss of the projectile ion in the crystal and the angular spread of the projectile ion. The energy loss of the projectile ion broadens the width of the resonance peak. The energy loss of 390 MeV/u Ar<sup>17+</sup> ions channeled in the (220) plane of the 21  $\mu\text{m}$  Si is  $\sim 2$  MeV (0.05 MeV/u). This energy loss corresponds to the transition energy shift of  $\sim 0.2$  eV. The RCE is considered to occur near the crystal entrance, because the half of the path length of the Rabi oscillation is shorter than the crystal thickness. Accordingly, the effective energy loss affecting the resolution is considered to be smaller than the value estimated above.

The angular spread of the projectile ions also affects the resolution. As stated in section 2.2.1, the angular spread was estimated to be 0.1 mrad. This spread corresponds to the transition energy width of 0.2 eV.

In the present work, these factors are canceled out to some extent, since we determined the transition energy of the helium-like ion with respect to that of the hydrogen-like ion which were produced from the helium-like ion using a stripper foil.

### Outlook

This new method for atomic spectroscopy can be applied to other ions, for example, much heavier ions. The spectroscopy of high- $Z$  ions is important for testing the QED in the strong electric field. As stated above, the detection efficiency of this method is high, so that this method can be applied to the spectroscopy of radioisotope (RI) ions.

Similarly to the case of atomic levels, nuclear levels are considered to be excited with RCE, as predicted by Okorokov. However, the nuclear RCE has not been observed so far. We plan to observe the RCE of <sup>57</sup>Fe nucleus, whose excitation energy from the ground state to the first excited state (14.4 keV) is relatively small in the nuclei. One of the methods to observe the nuclear RCE is to measure the deexcitation  $\gamma$ -rays. If the RCE takes place, the yields of the deexcitation  $\gamma$ -rays are expected to increase. In the case that the nucleus has bound electrons, the nuclear RCE is confirmed by observing the phenomena originating from the internal-conversion process, which leads to the increase of the yields of the internal-conversion electrons and the ionized nuclei. This measurement has a possibility to become a new method for nuclear spectroscopy as well as atomic spectroscopy.

# Chapter 5

## Summary

We have observed the resonant coherent excitation (RCE) of hydrogen-like  $\text{Ar}^{17+}$ , helium-like  $\text{Ar}^{16+}$ , hydrogen-like  $\text{Fe}^{25+}$ , helium-like  $\text{Fe}^{24+}$ , and lithium-like  $\text{Fe}^{23+}$  ions. For  $\text{Ar}^{17+}$  ions, the RCE from  $1s$  to  $n = 2, n = 3, n = 4$ , and  $n = 5$  states were observed. In the case of the  $n = 2$  states, we obtained the resonance profiles by measuring the charge states of the ions transmitted through the crystals and deexcitation X-rays from the ions. In these resonance profiles, two peaks were observed. One is assigned to the transition  $1s \rightarrow n = 2(j = 3/2)$ , and the other is assigned to the transition  $1s \rightarrow n = 2(j = 1/2)$ . The observed profiles reflected the nature of the Stark-mixed  $n = 2$  states. The resonance peak width increased with increasing  $n$ , which is also explained by the Stark effect. For  $\text{Fe}^{25+}$  ions, the RCE from  $1s$  to  $n = 2$  and  $n = 3$  states were observed. Similarly to the case of  $\text{Ar}^{17+}$  ions, for  $n = 2$  states, two resonance peaks corresponding to the transitions  $1s \rightarrow n = 2(j = 3/2)$  and  $n = 2(j = 1/2)$  were observed. The contribution of the Stark effect for  $\text{Fe}^{25+}$  ions was found to be small compared to that for  $\text{Ar}^{17+}$  ions. This is due to the fact that the electron orbital radius of  $\text{Fe}^{25+}$  is smaller than that of  $\text{Ar}^{17+}$ , and that the energy difference between  $n = 2(j = 3/2)$  and  $n = 2(j = 1/2)$  for  $\text{Fe}^{25+}$  is larger than for  $\text{Ar}^{17+}$ . For helium-like  $\text{Ar}^{16+}$  and  $\text{Fe}^{24+}$  ions, the RCE from  $1s^2$  to  $1s2p \ ^1P_1$  and  $\ ^3P_1$  were observed. The contribution of the Stark effect was small compared to that for the hydrogen-like ions. This is explained by the fact that the energy levels for helium-like ions are not degenerate with respect to the angular momenta.

We have demonstrated that we can perform a high precision spectroscopy of helium-like heavy ions through observation of RCE. The beam energy was also determined with a high precision using the theoretical value of the transition energy of  $1s \rightarrow 2p_{3/2}$  in the hydrogen-like ion. In the case of  $\text{Ar}^{16+}$  ions, we determined the transition energies as  $3139.27 \pm 0.15$  and  $3123.30 \pm 0.16$  eV for  $1s^2 \rightarrow 1s2p \ ^1P_1$  and  $\ ^3P_1$ , respectively. These values are smaller than the theoretical ones by about 0.3 eV. In the case of  $\text{Fe}^{24+}$  ions, we obtained the transition energies as  $6700.22 \pm 0.16$  and  $6667.52 \pm 0.17$  eV for  $1s^2 \rightarrow 1s2p \ ^1P_1$  and  $\ ^3P_1$ , respectively. For  $\ ^3P_1$ , the obtained transition energy is in good agreement with the theories. For  $\ ^1P_1$ , the obtained transition energy is in reasonable agreement with the unified theory and the all-order many-body calculations. This new method for atomic spectroscopy has advantages such as high detection efficiency and Doppler-free, which is

in quite contrast to the method using a crystal spectrometer.

# Appendix A

## Energy levels and transition amplitudes

### A.1 RCE for planar channeling

The arrangement of the atoms on the (220) plane of a Si crystal is shown in Fig. 1.6. [31]. This can be regarded as a two-dimensional (2D) crystal. In this case, the 2D base vectors are  $\mathbf{A} = [110]a/2$  and  $\mathbf{B} = [001]a$ , where  $a$  is the lattice constant of Si. The 3D reciprocal lattice vector is expressed as

$$\mathbf{g} = \mathbf{G}(k, l) + n\mathbf{h} = k\mathbf{A}^* + l\mathbf{B}^* + n\mathbf{h}, \quad (\text{A.1})$$

where  $\mathbf{A}^*$ ,  $\mathbf{B}^*$ , and  $\mathbf{h}$  are the reciprocal lattice vectors. The vector  $\mathbf{h}$  denotes the channeling plane. A 2D Miller index  $(k, l)$  corresponds to atomic strings parallel to  $\mathbf{A}/k - \mathbf{B}/l$ .

The position of a channeled ion in the laboratory frame (L-frame) is written as

$$\mathbf{R}(t') = \mathbf{R}_\perp + \mathbf{v}t' = (X, Y, vt'), \quad (\text{A.2})$$

where  $\mathbf{v}$  is the vector of the ion velocity. Since  $\mathbf{v}$  is parallel to the plane,  $\mathbf{v} \cdot \mathbf{h} = 0$ . The scalar potential at the ion position in the L-frame is given by

$$\begin{aligned} \Phi'(\mathbf{R}_\perp + \mathbf{v}t') &= \sum_{\mathbf{g}} \phi_{\mathbf{g}} \exp[-2\pi i \mathbf{g} \cdot (\mathbf{R}_\perp + \mathbf{v}t')] \\ &= \sum_{k,l} \sum_n \phi_{\mathbf{g}} \exp[-2\pi i (\mathbf{G}(k, l) + n\mathbf{h}) \cdot (\mathbf{R}_\perp + \mathbf{v}t')] \\ &= \sum_{k,l} \phi_{kl}(X) \exp(-2\pi i \mathbf{G}_\perp(k, l) \cdot \mathbf{R}_\perp) \times \exp(-2\pi i \mathbf{G}(k, l) \cdot \mathbf{v}t'), \end{aligned} \quad (\text{A.3})$$

where

$$\phi_{kl}(X) = \sum_n \phi_{\mathbf{g}} \exp(-2\pi i n X/d_p). \quad (\text{A.4})$$

This is the amplitude of the oscillating potential and  $d_p = 1/|\mathbf{h}|$  is the distance between the planes. For  $k = l = 0$ ,

$$\phi_{00}(x) = \sum_n \phi_{nh} \exp(-2\pi inx/d_p), \quad (\text{A.5})$$

which represents the continuum potential.

The frequency  $\nu'$  which the ion feels in the L-frame is given by

$$\nu' = \mathbf{G}(k, l) \cdot \mathbf{v}. \quad (\text{A.6})$$

In the projectile frame (P-frame), this frequency is transformed to

$$\nu = \gamma\nu' = \gamma\mathbf{G}(k, l) \cdot \mathbf{v} = \gamma(k\mathbf{A}^* + l\mathbf{B}^*) \cdot \mathbf{v}. \quad (\text{A.7})$$

Accordingly, the resonance condition is given by

$$E_{trans} = h\nu = \frac{\gamma h v}{a} (\sqrt{2}k \cos \theta + l \sin \theta), \quad (\text{A.8})$$

where  $\theta$  is the angle of the  $\langle 110 \rangle$  axis with respect to the beam direction, *i.e.*, the angle between  $\mathbf{A}$  and  $\mathbf{v}$ .

## A.2 Energy levels

In the P-frame, the Hamiltonian for the electron in hydrogen-like ions is given by

$$H(\mathbf{r}, t) = H_0(\mathbf{r}) + H_1(\mathbf{r}) + H_2(\mathbf{r}) + H_3(\mathbf{r}, t), \quad (\text{A.9})$$

where  $H_0$  is the non-perturbative Hamiltonian for hydrogen-like ions,  $H_1$  and  $H_2$  are the perturbation potentials due to the wake field and the static crystal potential, respectively, and  $H_3$  is the time-dependent potential due to the crystal periodic potential, which leads to the RCE. The Hamiltonian  $H_0$  is written as

$$H_0(r) = -c\boldsymbol{\alpha} \cdot \mathbf{p} - \beta mc^2 - \frac{Z_1 e^2}{r}, \quad (\text{A.10})$$

where  $\boldsymbol{\alpha}$  and  $\beta$  are the Dirac matrices.

The potential  $\phi'(\mathbf{r}')$  of the crystal in the L-frame is transformed to the four potentials in the P-frame as,  $A_x(\mathbf{r}, t) = A_y(\mathbf{r}, t) = 0$ ,  $A_z(\mathbf{r}, t) = -(v/c)\gamma\phi'(\mathbf{r}')$ , and  $\phi(\mathbf{r}, t) = \gamma\phi'(\mathbf{r}')$ . Accordingly, the Hamiltonian in the P-frame is written as

$$\begin{aligned} H(\mathbf{r}, t) &= -\boldsymbol{\alpha} \cdot [c\mathbf{p} + e\mathbf{A}(\mathbf{r}, t)] - \beta mc^2 - \frac{Z_1 e^2}{r} - e[\phi_w(\mathbf{r}) + \phi(\mathbf{r}, t)] \\ &= -c\boldsymbol{\alpha} \cdot \mathbf{p} - \beta mc^2 - \frac{Z_1 e^2}{r} - e\phi_w(\mathbf{r}) - e\gamma \left(1 - \frac{v}{c}\alpha_z\right) \phi'(\mathbf{r}'), \end{aligned} \quad (\text{A.11})$$

where  $\phi_w(\mathbf{r})$  is the wake potential.

The coordinates  $(\mathbf{r}', t')$  of the electron in the L-frame are written as  $\mathbf{r}' = \mathbf{R}_\perp + \mathbf{r}_\perp + \gamma(z\mathbf{e}_z + \mathbf{v}t)$  and  $t' = \gamma(t + vz/c^2)$ , where  $\mathbf{e}_z$  is a unit vector of  $z$ -axis. Substituting these coordinates into equation A.11, the perturbation potentials are expressed as

$$H_1(\mathbf{r}) = -e\phi_w(\mathbf{r}), \quad (\text{A.12})$$

$$H_2(x) = -e\gamma \left(1 - \frac{v}{c}\alpha_z\right) \phi_{00}(x), \quad (\text{A.13})$$

$$\begin{aligned} H_3(\mathbf{r}, t) &= -e\gamma \left(1 - \frac{v}{c}\alpha_z\right) \sum_{kl}^l \phi_{kl}(X + x) \\ &\times \exp[-2\pi i \mathbf{G}(k, l) \cdot (\mathbf{R}_\perp + \mathbf{r}_\perp + \gamma z \mathbf{e}_z)] \\ &\times \exp[-2\pi i \nu t], \end{aligned} \quad (\text{A.14})$$

where  $\sum_{kl}'$  runs over all combinations of  $(k, l)$  except for  $(k, l) = (0, 0)$ .

Here, the wave function with the principal quantum number  $n$ , orbital angular momentum  $L$ , total angular momentum  $J$ , and its projection  $\mu$  to the quantum axis is defined as  $|nLJ\mu\rangle$ . The energy of the  $1s$  state inside the crystal is given by

$$E_0 = E(1s) + \langle 1s(1/2)\mu | H_1(\mathbf{r}) + H_2(x) | 1s(1/2)\mu \rangle, \quad (\text{A.15})$$

where  $E(1s)$  is the unperturbed energy of the  $1s$  state.

The energy levels of  $n = 2$  states are obtained by solving the secular equation,

$$\det \langle 2LJ\mu | H_0(\mathbf{r}) + H_1(\mathbf{r}) + H_2(x) - E | 2L'J'\mu' \rangle = 0. \quad (\text{A.16})$$

As the unperturbed wave functions of the  $n = 2$  states, linear combinations of the non-relativistic wave functions  $R_{nl}(r)Y_{lm}(\theta, \phi)$  with the spin states,  $|\uparrow\rangle$  or  $|\downarrow\rangle$  were used. The wake potential  $\phi_w(\mathbf{r})$  was calculated from a dielectric function in the plasmon pole approximation, and  $H_2(x)$  was approximated as  $H_2(x) = -e\gamma\phi_{00}(x)$ . The obtained transition energies of  $1s \rightarrow n = 2$  are shown in section 1.2.

## A.3 Transition amplitudes

Here, the energies and wave functions are defined as  $E_j$  and  $\Psi_j$ , respectively, where  $j = 0$  denotes the perturbed  $1s$  state and  $j = 1 - 4$  denotes the  $n = 2$  states. The time evolution of the wave function  $\Psi(\mathbf{r}, t)$  is written as

$$i\hbar \frac{\partial \Psi(\mathbf{r}, t)}{\partial t} = [H_{st}(\mathbf{r}) + H_3(\mathbf{r}, t)]\Psi(\mathbf{r}, t), \quad (\text{A.17})$$

where  $H_{st} = H_0 + H_1 + H_2$ . The wave function  $\Psi(\mathbf{r}, t)$  is expanded as

$$\Psi(\mathbf{r}, t) = \sum_j C_j(t) \Psi_j(\mathbf{r}) \exp\left(\frac{-iE_j t}{\hbar}\right). \quad (\text{A.18})$$

Substituting this wave function into equation A.17, we obtain

$$\begin{aligned}
i\hbar \frac{dC_j(t)}{dt} &= \sum_{j'} \langle j | H_3(\mathbf{r}, t) | j' \rangle C_{j'}(t) \exp \left[ \frac{i(E_j - E_{j'})t}{\hbar} \right] \\
&= -e\gamma \sum_{j'} \sum_{kl} \langle j | \phi_{kl}(X + x) \exp[-2\pi i \mathbf{G}(k, l) \cdot (\mathbf{r}_\perp + \gamma z \mathbf{e}_z)] | j' \rangle C_{j'}(t) \quad (\text{A.19}) \\
&\times \exp[-2\pi i \mathbf{G}(k, l) \cdot \mathbf{R}_\perp] \\
&\times \exp \left[ 2\pi i \left( \frac{E_j - E_{j'}}{h} - \nu \right) t \right].
\end{aligned}$$

The strength of the RCE transition is given by the matrix element,

$$M_{j0} = -e\gamma \langle j | \phi_{kl}(X + x) \exp[-2\pi i \mathbf{G}(k, l) \cdot (\mathbf{r}_\perp + \gamma z \mathbf{e}_z)] | 0 \rangle. \quad (\text{A.20})$$

# Appendix B

## Measurements of convoy electron spectra

Before the measurements of the energy spectra of convoy electrons using the Si crystal as a target, we measured those using carbon foils as targets. Comparison between these spectra is important to extract the information on the interaction between convoy electrons and a crystal.

### B.1 Introduction

Most of the experiments on convoy electrons have been performed in the MeV/u energy region so far. Some groups measured the target thickness dependence of convoy electron spectra [72, 73]. In these experiments, a double peak structure was observed in the electron spectrum. One peak was observed at the energy corresponding to the same velocity as the incident ion. Its shape was cusp-like, which is characteristic for the Coulomb interaction between the ion and the electron. The other peak was observed at the energy lower than that of the cusp-shaped peak, and its width was broadened. The electrons associated with this peak suffer multiple collisions and lose their energies. The electrons forming the cusp-shaped peak were referred to as intrinsic convoy electrons, and those forming the broad peak were referred to as electron-loss convoy electrons [72]. The ratio of the intensity of the former peak to that of the latter peak was found to decrease with increasing target thickness, which is due to multiple collisions with the target atoms.

The convoy electron spectra have been investigated by comparing them with the Electron Capture to the Continuum (ECC) and Electron Loss to the Continuum (ELC) electron spectra. These spectrum shapes are related to the angular distribution of the electrons in the projectile frame. The doubly differential cross section of the emitted electron in the projectile frame is expressed in terms of a multipole expansion using Legendre polynomials,  $d\sigma/d\mathbf{v} = (\sigma_0/v) \sum \beta_k P_k(\cos\theta)$ , where  $\mathbf{v}$  is the electron velocity in the projectile frame,  $\theta$  is its polar angle,  $P_k$  is a Legendre polynomial of order  $k$ , and  $\sigma_0$  is a constant. The parameter  $\beta_k$  shows the anisotropy of the electron angular distribution. For ECC process, the electron spectrum is known to be skewed toward lower energy, which

is characterized by negative  $\beta_1$  [74]. On the other hand, for ELC process, the shape of the electron spectrum is symmetric. In the projectile frame, the ELC electrons tend to be emitted transversely, which leads to the narrow cusp peak in the electron spectrum measured in the laboratory frame [34]. In 1985, Elston *et al.* measured the three-dimensional velocity distribution of ELC electrons in ion-atom collisions [75]. They found that the high-order multipoles play an important role in the doubly differential cross section of the ELC electrons. By using the similar experimental method, Berry *et al.* measured the angular distribution of convoy electrons in ion-solid collisions [76]. The observed angular distribution of convoy electrons resembled that of ELC electrons except that the former is more strongly transverse.

In the MeV/u energy region, it is difficult to fulfill a single collision condition, because the mean free paths (MFPs) for capture, excitation, and ionization are short, and the thinness of the foil which we can obtain is limited. For fulfilling a single collision condition, high energy ions and thin foils are needed. In 1991, to observe the electron spectra in the single collision regime, Gibbons *et al.* employed high energy ions (36 MeV/u Ar ions) as projectile ions [77]. They measured the target thickness dependence of the anisotropy parameters  $\beta_k$  of convoy electron distributions for 36 MeV/u Ar<sup>15+,17+,18+</sup> ion collisions with thin carbon foils. In that experiment, the rapid evolutions of the anisotropy parameters with target thickness were observed, which reflects the fact that the bound electrons are excited to the high- $n$  states inside the solid.

We used ions with much higher energies such as 390 MeV/u ( $\beta = v/c = 0.71, \gamma = 1.42$ ) Ar<sup>17+</sup> ions. As targets, we adopted carbon foils with thicknesses from 25 to 8700  $\mu\text{g}/\text{cm}^2$ . We measured the energy spectra of electrons emitted at  $0^\circ$  using carbon foils as targets [78]. In this energy range, (i) the electron capture process is negligible compared to the ionization process. (ii) The MFP for projectile excitation is long. For example, the MFP for projectile 1s electron excitation is  $\sim 3000 \mu\text{g}/\text{cm}^2$  [63]. (iii) The MFPs for the elastic and inelastic collisions of the emitted electrons are also long. Accordingly, for thinner targets, the convoy electron spectra are considered to resemble those for binary ion-atom collisions. In the present measurement, for thicker targets, the width of the convoy electron peak was found to increase with increasing target thickness, which is due to the energy straggling of the electron. On the other hand, we have observed that the width of the convoy electron peak decreases as the target thickness increases for thinner targets. Similar feature was observed in the lower energy region, and attributed to the evolution of the projectile excited state distribution inside solid targets, since the spectra of the electrons produced by the ELC process depend on the initial states of the emitted electrons. Theoretically, Burgdörfer *et al.* had investigated the initial state (Compton profile) dependence of the ELC cusp [34, 79]. For example, they showed that the peak width of the ELC electrons emitted from 2s is narrower than that from 1s. In order to verify this dependence, we have also measured the spectra of convoy electrons produced for 460 MeV/u ( $\beta = v/c = 0.74, \gamma = 1.49$ ) Fe<sup>23+</sup> (1s<sup>2</sup>2s), Fe<sup>24+</sup> (1s<sup>2</sup>), and Fe<sup>25+</sup> (1s) ions incident on carbon foils with thicknesses from 50 to 1900  $\mu\text{g}/\text{cm}^2$ . In the present work, the experimental results are compared with the simulation based on the classical transport theory (CTT) [80], which is in good agreement with the experiment. In this theory, the

electron trajectory is calculated classically taking into account the projectile Coulomb potential and the elastic and inelastic collisions which the electrons suffer inside solids. This CTT simulation has been applied to the various experiments so far, and a good agreement is obtained between simulation and experiment [73, 81, 82]. The simulation code extended to the relativistic energy region is applied to the present experiment [83, 84].

## B.2 Experimental

The schematic drawing of the experimental setup is shown in Fig. 2.8. We used 390 MeV/u Ar<sup>17+</sup>, 460 MeV/u Fe<sup>25+</sup>, Fe<sup>24+</sup>, and Fe<sup>23+</sup> ions as projectile ions. As targets, we used carbon foils with thicknesses from 25 to 8700  $\mu\text{g}/\text{cm}^2$ . For carbon foils thicker than 1000  $\mu\text{g}/\text{cm}^2$ , we evaluated their thicknesses by measuring the energy loss of 6 MeV proton passing through the foil. A beam of 6 MeV protons was provided from the tandem accelerator at University of Tsukuba. We also evaluated the inhomogeneity of the foil thickness from the full width at half maximum of the energy loss peak for protons. For carbon foils thinner than 1000  $\mu\text{g}/\text{cm}^2$ , the accuracy and inhomogeneity of the thickness are both estimated to be  $\pm 10\%$  by a carbon foil supplier (Arizona carbon foil).

## B.3 Target thickness dependence (390 MeV/u Ar<sup>17+</sup>)

### *Charge state distribution*

We used 390 MeV/u hydrogen-like Ar<sup>17+</sup> ions and carbon foils with thicknesses from 25 to 8700  $\mu\text{g}/\text{cm}^2$  as projectile ions and targets, respectively. First, we measured the charge state distribution of the ions passing through the carbon foils. Figure B.1 shows the charge state distribution of the transmitted ions as a function of carbon foil thickness. The fractions are plotted in a semilogarithmic scale. At the present high collision energy, the electron capture process is negligible compared to the ionization process. Indeed, only Ar<sup>17+</sup> and Ar<sup>18+</sup> ions were observed. The fraction of Ar<sup>18+</sup> ions was less than 1% at 25  $\mu\text{g}/\text{cm}^2$ , and increased to more than 99% at 8700  $\mu\text{g}/\text{cm}^2$ . It is noted that the charge state distribution is not equilibrated even at 8700  $\mu\text{g}/\text{cm}^2$ . In Fig. B.1, the solid lines show the simulation based on the CTT. This simulation is in good agreement with the measured charge state distribution, indicating that the CTT is valid for this collision system. The solid line for Ar<sup>17+</sup> fraction is not straight but slightly bent, which means that the fraction of Ar<sup>17+</sup> is not expressed as a single exponential function. This reflects the evolution of the projectile excited state distribution inside the foil, which results from collisions with the target atoms.

### *Energy spectra*

Figure B.2 shows the energy spectra of electrons observed at 0° in collisions of 390 MeV/u Ar<sup>17+</sup> ions with the carbon foils. The intensities are normalized to unity at the peak positions. The vertical dashed line indicates the energy of the electron with the same

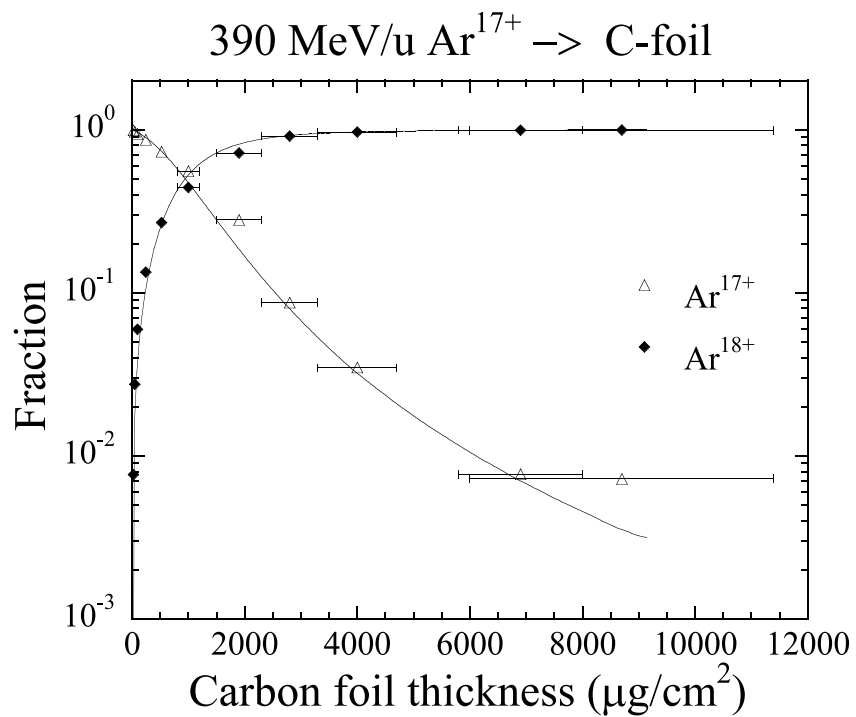


Figure B.1: Charge state distributions of the ions transmitted through the carbon foils for 390 MeV/u Ar<sup>17+</sup> incidence. The solid lines show the simulation.

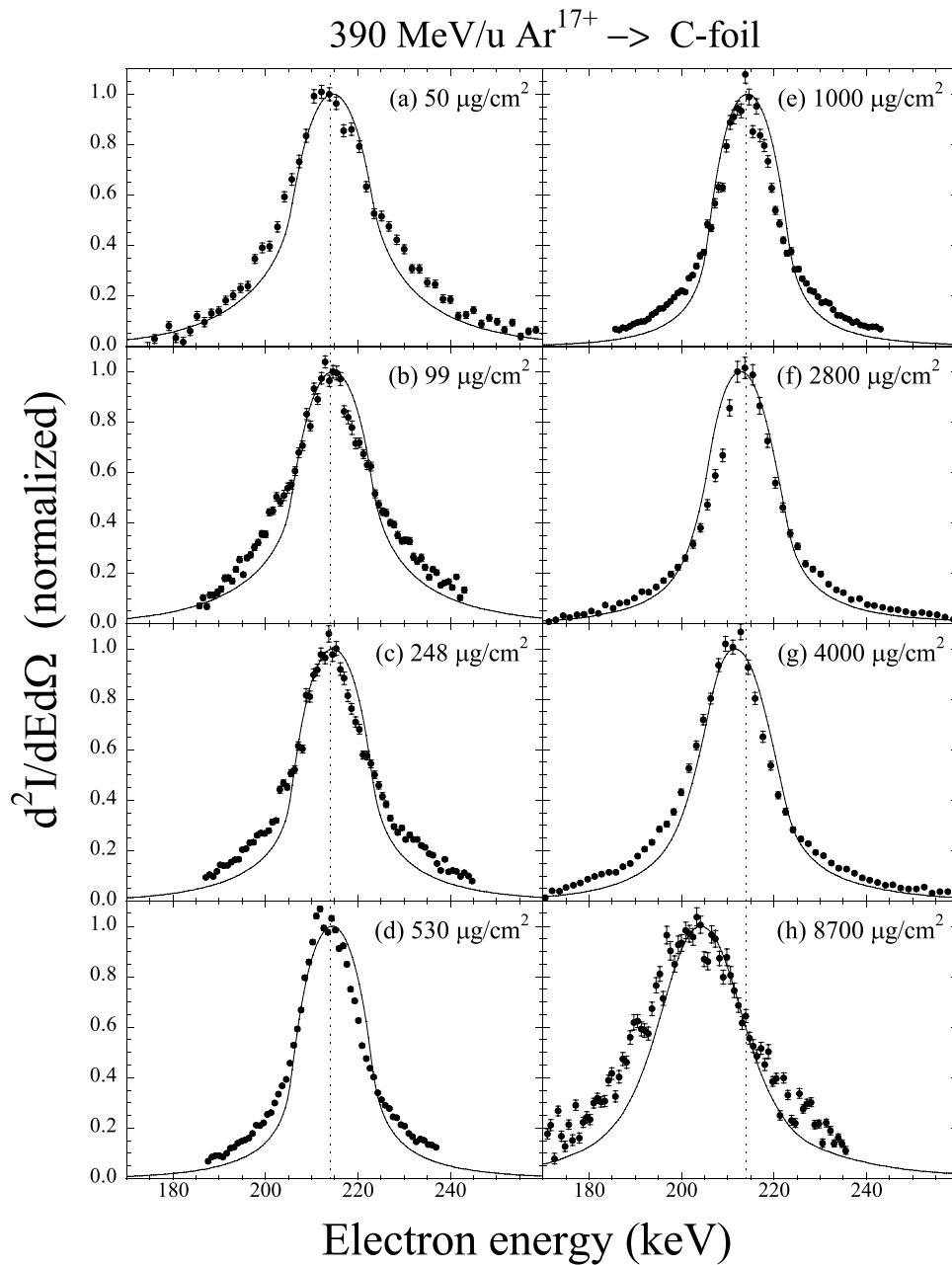


Figure B.2: Energy spectra of electrons ejected at  $0^\circ$  in collisions of 390 MeV/u Ar<sup>17+</sup> ions with (a) 50, (b) 99, (c) 248, (d) 530, (e) 1000, (f) 2800, (g) 4000, and (h) 8700  $\mu\text{g}/\text{cm}^2$  carbon foils. The intensities are normalized to unity at the peak positions. The vertical dashed line indicates the electron energy corresponding to the same velocity as the incident ion. The solid lines show the simulation.

velocity as the incident ion (214 keV). The solid lines show the spectra calculated by the CTT, which are convoluted with the analyzer resolution. It is noted that the observed peaks are not cusp-shaped in the energy spectra. The poor energy resolution of the electron analyzer obscures the cusp-shaped peak. The energy loss of the incident ion is estimated to be 0.2 MeV/u for the thickest target ( $8700 \mu\text{g}/\text{cm}^2$ ), leading to the energy shift of 0.1 keV for convoy electrons. This value is negligible, so that the peak shift toward lower energy seen in Fig. B.2 is attributed to the energy loss of the electron itself. The stopping power for 200 keV electron in carbon is  $2.5 \text{ eV}/(\mu\text{g}/\text{cm}^2)$ , and the MFP for projectile  $1s$  ionization is  $2000 \mu\text{g}/\text{cm}^2$ . Accordingly, the mean energy loss of the electron for the thickest target ( $8700 \mu\text{g}/\text{cm}^2$ ) is estimated to be 17 keV, in reasonable agreement with the observed energy loss. Inside the foil, the electrons are lost to the continuum states at various positions. Since the range of 200 keV electron in carbon is about  $50000 \mu\text{g}/\text{cm}^2$  [66], most of the emitted electrons escape from the thickest target.

### **Peak energy and FWHM**

The energy and full width at half maximum (FWHM) of the convoy electron peak as a function of target thickness are summarized in Fig. B.3. The open circles show the simulated results, which reproduce the peak energy and peak width well. (i) For the targets thinner than  $500 \mu\text{g}/\text{cm}^2$ , the peaks were seen at 214 keV. The peak widths decreased as the target thickness increased from 25 to  $500 \mu\text{g}/\text{cm}^2$ . (ii) For the targets with thicknesses between 500 and  $3000 \mu\text{g}/\text{cm}^2$ , the peaks were observed at about 214 keV, and the peak widths were almost constant. (iii) For the targets thicker than  $3000 \mu\text{g}/\text{cm}^2$ , the peaks were shifted to the lower energy side. The peak widths increased with increasing target thickness. Thus, the electron spectra are divided into three regions depending on the target thickness.

In the region (i) ( $\leq 500 \mu\text{g}/\text{cm}^2$ ), the energy loss and energy straggling of the electron are very small. The energy loss was less than 1% of the peak energy. Inside the foil, the excited state distribution of the projectile ions evolves with target thickness due to collisions with the target atoms. As the target thickness increases, the contribution of the projectile excited states to the convoy electron production is enhanced, and the electrons tend to be emitted transversely in the projectile frame, as observed by Gibbons *et al.* [77]. The electrons in the excited states are lost by the small momentum transfers. In addition, the width of the Compton profile decreases as the binding energy of the electron increases. These lead to the narrow energy distribution of the emitted electrons [34]. In the projectile frame, convoy electrons are low energy electrons produced in the soft collision with the target atom, where the transversal momentum transfer plays an important role compared to the longitudinal momentum transfer. Accordingly, the momentum distribution of the initial state is projected onto that of the continuum state because the initial momentum distribution is not destroyed by the longitudinal momentum transfer. Recently, Moshhammer *et al.* measured the spectra of the low energy electrons ejected from a target atom in ion-atom collisions, and observed the initial-state dependent structure in the electron spectra [85]. These electrons resemble convoy electrons except that the

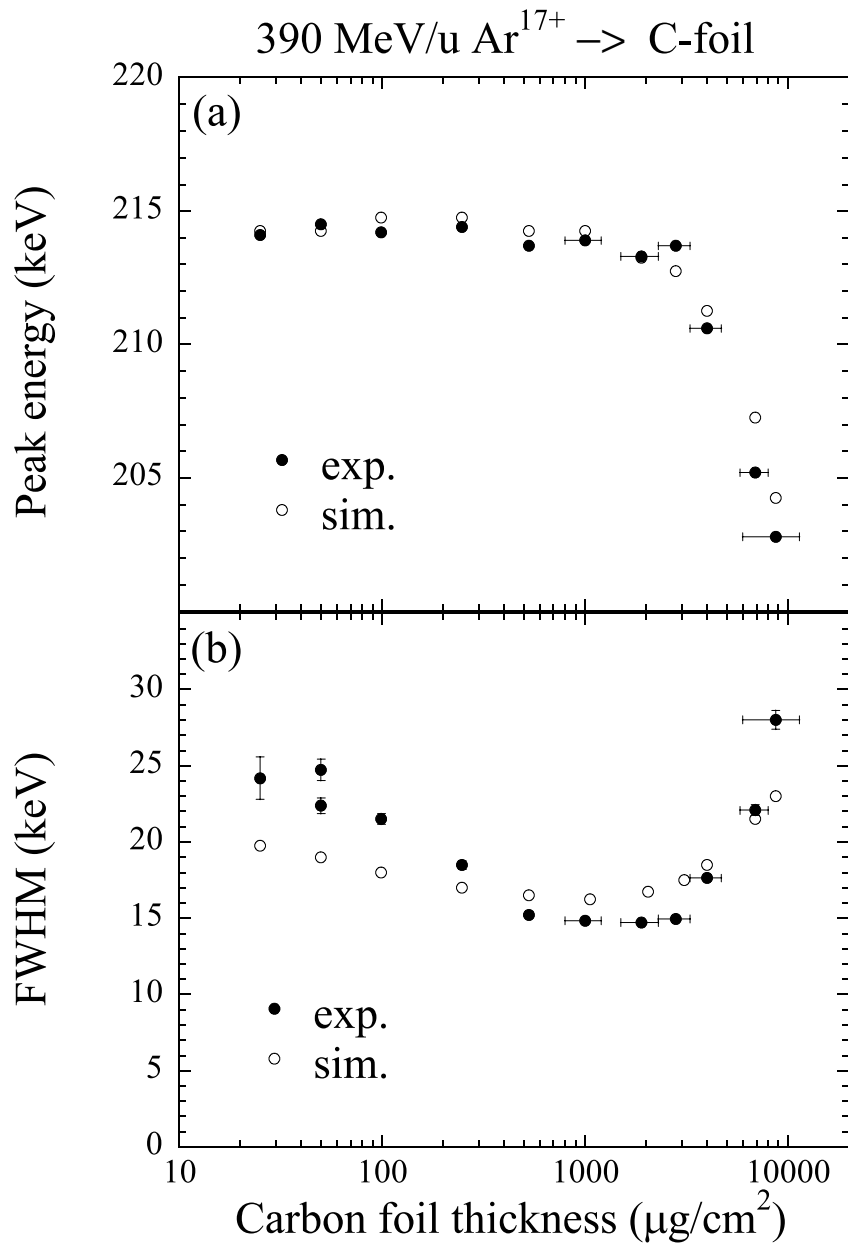


Figure B.3: (a) Energy and (b) full width at half maximum (FWHM) of the convoy electron peak as a function of carbon foil thickness for 390 MeV/u Ar<sup>17+</sup> incidence. The closed and open circles show the experiment and simulation, respectively.

former is emitted from a neutral atom by ion impact.

In the region (ii) ( $500\text{--}3000\ \mu\text{g}/\text{cm}^2$ ), the mean energy loss of the emitted electron is still small. The observed constant peak width is considered to reflect the small variation of the excited state distribution in this thickness region.

In the region (iii) ( $\geq 3000\ \mu\text{g}/\text{cm}^2$ ), multiple collisions leading to energy loss, energy straggling, and angular straggling play an important role. As seen in Fig. B.1, most of the incident ions are ionized in this thickness region, where multiple collisions are dominant after the electrons are lost to the continuum. In the CTT simulation, double peaks are formed in the energy spectrum of convoy electrons when the energy resolution of the electron analyzer is neglected [84]. One is a cusp-shaped peak and located at 214 keV. The other is a broad peak and located at the energy lower than 214 keV. The electrons forming this peak lose their energies due to multiple collisions. These double peaks were observed in the lower energy region [72, 73], while in the present experiment, only one peak was observed due to the poor energy resolution of the electron analyzer.

### ***Yield***

Furthermore, we examined the yields of the detected electrons,  $Y(\text{Ar}^{17+})$ , as a function of target thickness, which is shown in Fig. B.4. These yields were obtained by integrating the singly differential spectra from  $E_p - 20$  to  $E_p + 20$  keV ( $E_p$  is the peak energy). If all the electrons lost from the incident ions are detected,  $Y(\text{Ar}^{17+})$  is proportional to the fraction of  $\text{Ar}^{18+}$  ions after passing through the carbon foil,  $F(\text{Ar}^{17+}; \text{Ar}^{18+})$ . To verify this, we evaluated the ratio of the yield of the detected electrons to that of the total electrons lost from the projectile ions, which is expressed as  $R(\text{Ar}^{17+}) = Y(\text{Ar}^{17+})/F(\text{Ar}^{17+}; \text{Ar}^{18+})$ , which is shown in Fig. B.4. Indeed,  $R(\text{Ar}^{17+})$  was almost constant for the targets thinner than  $500\ \mu\text{g}/\text{cm}^2$ . On the other hand, for thicker targets,  $R(\text{Ar}^{17+})$  decreased with increasing target thickness. For such thick targets, the angular straggling of the electron is large, so that the yields of the electrons detected with the analyzer with a finite acceptance angle decreased. In Fig. B.4, the open circles show the simulated results, which are normalized so that the simulated data at  $530\ \mu\text{g}/\text{cm}^2$  matches with the experimental one. The reasonable agreement is obtained between the simulation and the experiment.

As described above, we have observed that the width of the convoy electron peak decreases with increasing target thickness for the targets thinner than  $500\ \mu\text{g}/\text{cm}^2$ . This interesting feature reflects the evolution of the projectile excited state distribution inside the foil, since the electron spectrum originating from the ELC process depends on the initial state of the electron emitted from the projectile ion. In order to observe the initial state dependence more clearly, we have measured the incident projectile charge state dependence of convoy electron spectra, which is described below.

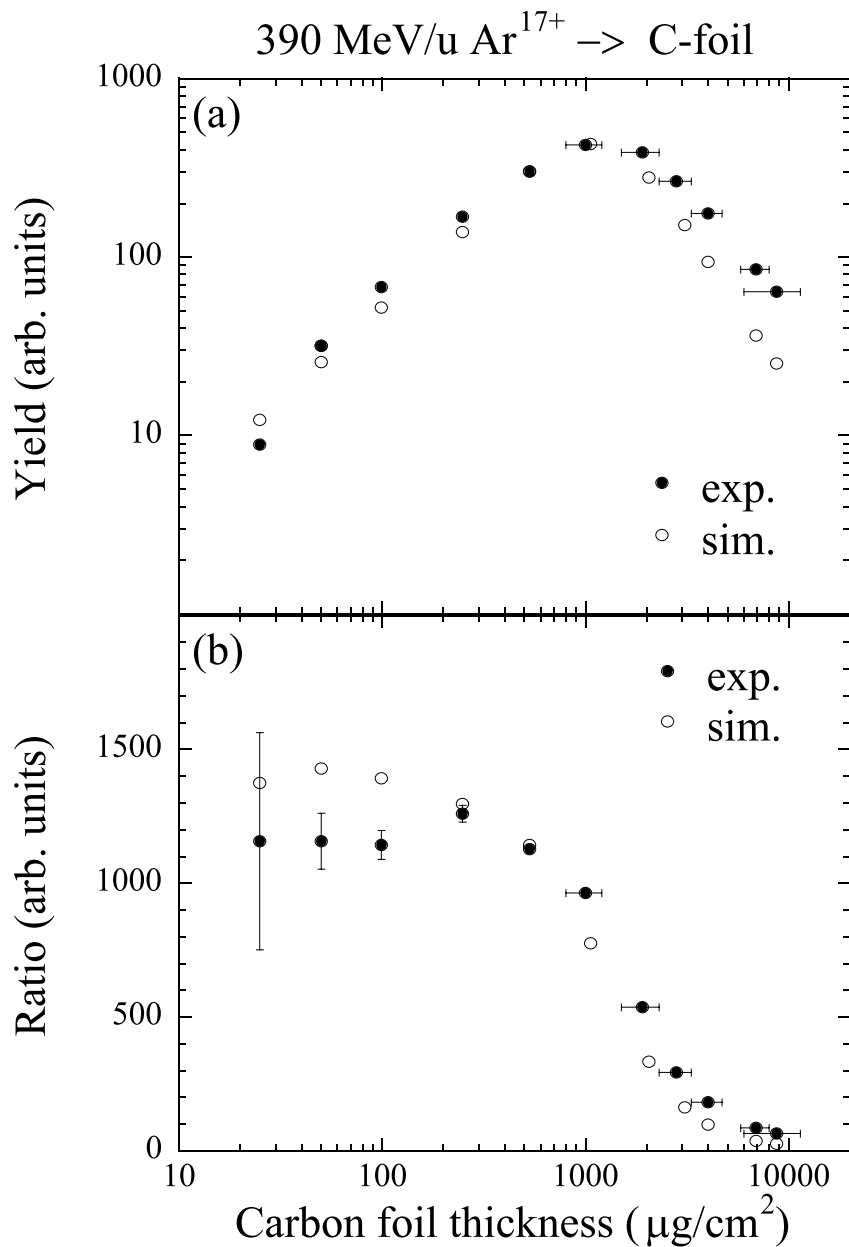


Figure B.4: (a) Yields of the detected electrons,  $Y(\text{Ar}^{17+})$ , as a function of carbon foil thickness for 390 MeV/u  $\text{Ar}^{17+}$  incidence. The simulated yields are normalized so that the simulated data at 530  $\mu\text{g}/\text{cm}^2$  is equal to the experimental one. (b) Ratios of the yields of the detected electrons to those of the total electrons lost from the incident ions,  $R(\text{Ar}^{17+})=Y(\text{Ar}^{17+})/F(\text{Ar}^{17+};\text{Ar}^{18+})$ , for 390 MeV/u  $\text{Ar}^{17+}$  ions incident on carbon foils.  $F(\text{Ar}^{17+};\text{Ar}^{18+})$  represents the fraction of  $\text{Ar}^{18+}$  ions transmitted through the carbon foils for  $\text{Ar}^{17+}$  incidence. The closed and open circles show the experiment and simulation, respectively.

## B.4 Initial state dependence (460 MeV/u Fe<sup>23+,24+,25+</sup>)

### *Charge state distribution*

We used 460 MeV/u Fe<sup>25+</sup> ( $1s$ ), Fe<sup>24+</sup> ( $1s^2$ ), and Fe<sup>23+</sup> ( $1s^22s$ ) ions and carbon foils with thicknesses from 50 to 1900  $\mu\text{g}/\text{cm}^2$  as projectile ions and targets, respectively. Figure B.5 show the charge state distributions as functions of carbon foil thickness for 460 MeV/u Fe<sup>25+</sup> ( $1s$ ), Fe<sup>24+</sup> ( $1s^2$ ), and Fe<sup>23+</sup> ( $1s^22s$ ) ions incident on carbon foils, respectively, where the solid lines show the simulated results. In this simulation, electron-electron correlation is not taken into account for a multi-electron system. The charge state distributions observed for a multi-electron system (Fe<sup>23+</sup> and Fe<sup>24+</sup> ions) as well as a single electron system (Fe<sup>25+</sup> ion) are in good agreement with the simulation.

### *Energy spectra*

We have measured the spectra of electrons ejected at  $0^\circ$  in collisions of 460 MeV/u Fe<sup>23+,24+,25+</sup> ions with carbon foils with thicknesses from 50 to 1900  $\mu\text{g}/\text{cm}^2$ . The measured energy spectra are shown in Fig. B.6. The intensities are normalized to unity at the peak positions. The vertical dashed line indicates the energy of the electron with the same velocity as the incident ion (252 keV). In this thickness region, the electron energy loss is again small, as seen in the case of Ar ions. In Fig. B.6, the solid lines show the simulated spectra, which are convoluted with the analyzer resolution. The simulated results agree with the experimental observations satisfactorily. This indicates that this simulation is effective in calculating the electron spectra for a multi-electron system as well as a single electron system.

### *Peak energy and FWHM*

Figure B.7 show the energy and FWHM of the convoy electron peak as a function of target thickness. The open circles show the simulated results. In the case of Fe<sup>24+</sup> and Fe<sup>25+</sup> incidences, the peak width decreased with increasing target thickness for thinner targets, which is attributed to the evolution of the projectile excited state distribution similarly to the case of Ar ions.

For a thin target (50  $\mu\text{g}/\text{cm}^2$  carbon foil), the width of the convoy electron peak for Fe<sup>23+</sup> incidence was narrower than for Fe<sup>24+</sup> and Fe<sup>25+</sup> incidences. In the case of Fe<sup>23+</sup> incidence, the contribution of the  $2s$  electron to the convoy electron production is dominant for thinner targets, which will be discussed later (Fig. B.8). In addition, as already predicted, the peak width of ELC cusp for  $2s$  is narrower than for  $1s$ , reflecting the momentum distribution, *i.e.*, Compton profile of the initial state of the emitted electron. Accordingly, the observed result is explained by such an initial state dependence. In the present experiment, by the use of the high energy ions and thin foils, the initial-state dependent structure was clearly observed in the convoy electron spectra. However, in the lower energy region, the convoy electron spectra reflecting the initial state were not observed because the single collision condition is not fulfilled. As shown in Fig. B.7, for

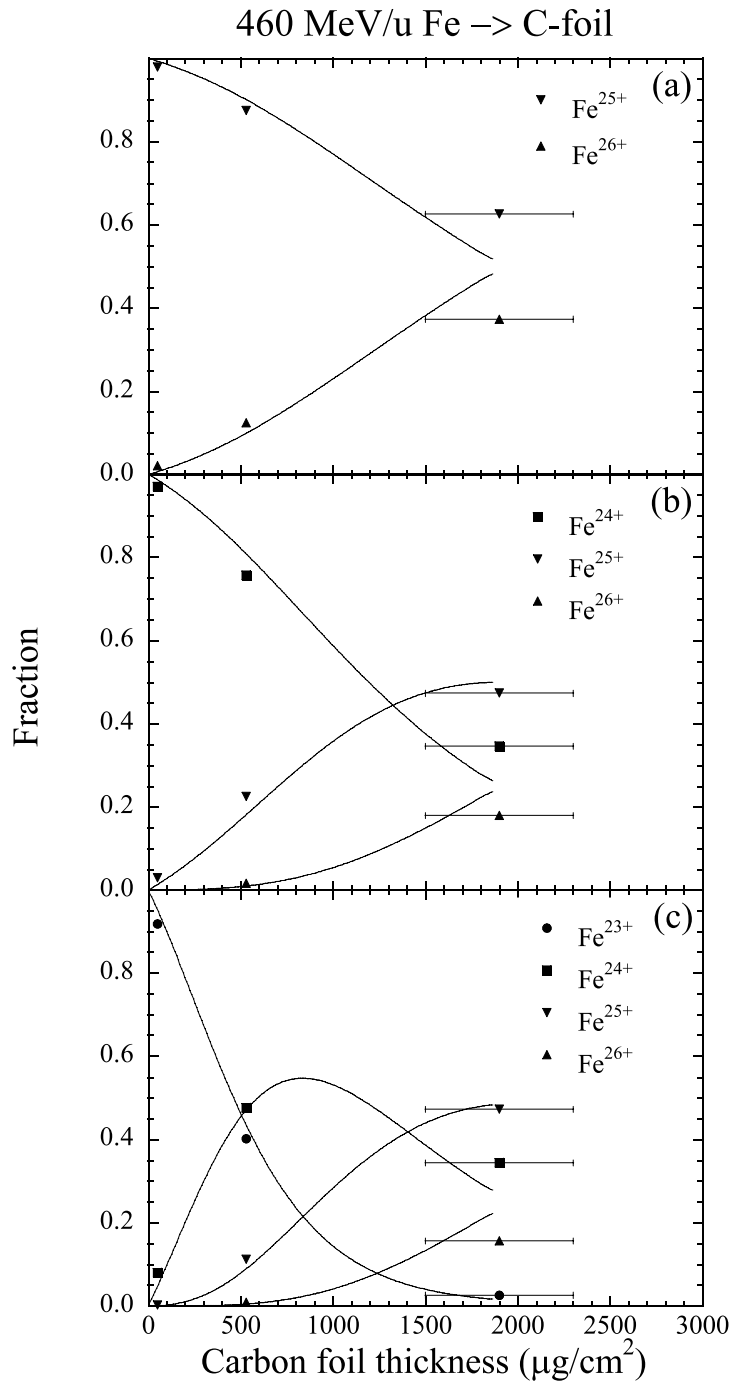


Figure B.5: Charge state distributions of the ions transmitted through the carbon foils for 460 MeV/u (a)  $Fe^{25+}$ , (b)  $Fe^{24+}$ , and (c)  $Fe^{23+}$  ions incident on carbon foils. The solid lines show the simulation.

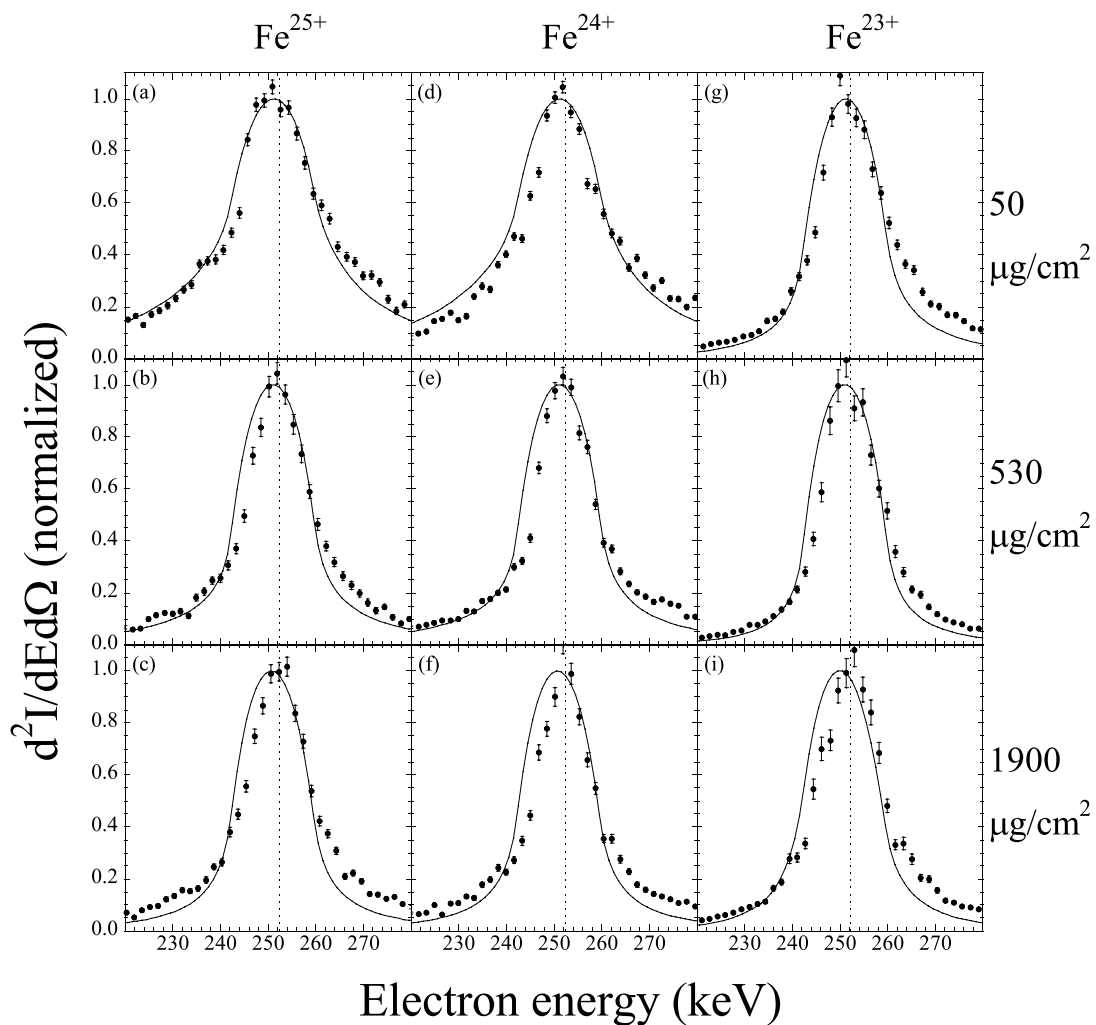


Figure B.6: Energy spectra of the electrons ejected at  $0^\circ$ . 460 MeV/u  $\text{Fe}^{25+}$  ions + (a) 50, (b) 530, and (c)  $1900 \mu\text{g}/\text{cm}^2$  carbon foils. 460 MeV/u  $\text{Fe}^{24+}$  ions + (d) 50, (e) 530, and (f)  $1900 \mu\text{g}/\text{cm}^2$  carbon foils. 460 MeV/u  $\text{Fe}^{23+}$  ions + (g) 50, (h) 530, and (i)  $1900 \mu\text{g}/\text{cm}^2$  carbon foils. The solid lines show the simulation.

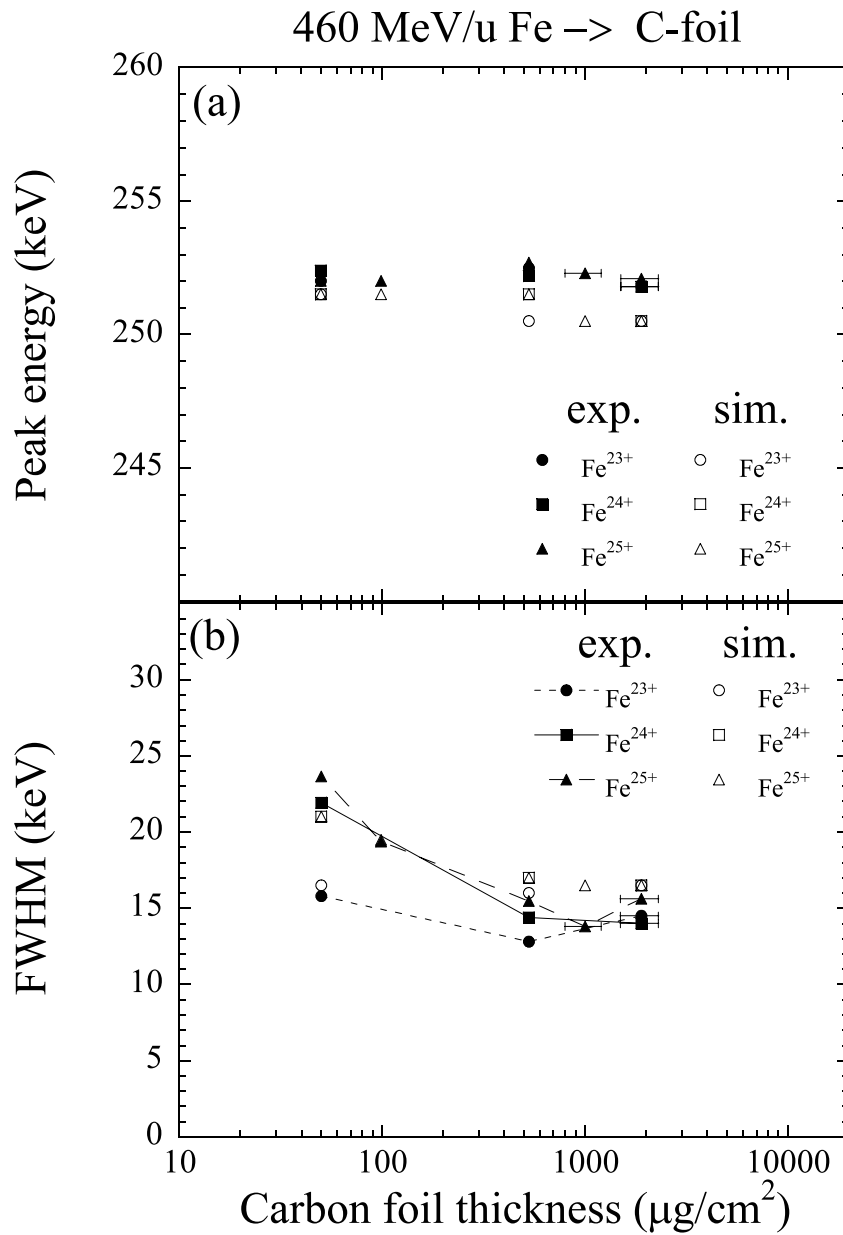


Figure B.7: (a) Energy and (b) FWHM of the convoy electron peak as a function of carbon foil thickness for 460 MeV/u Fe<sup>23+,24+,25+</sup> incidences. The closed and open symbols show the experiment and simulation, respectively.

$\text{Fe}^{23+}$  incidence, the variation of the peak width with target thickness was small compared to  $\text{Fe}^{24+}$  and  $\text{Fe}^{25+}$  incidences. This is due to the fact that the incident  $\text{Fe}^{23+}$  ion in the ground state has the  $2s$  electron.

### ***Yield***

We also measured the yields of the convoy electrons,  $Y(\text{Fe}^{23+})$ ,  $Y(\text{Fe}^{24+})$ , and  $Y(\text{Fe}^{25+})$  for  $\text{Fe}^{23+}$ ,  $\text{Fe}^{24+}$ , and  $\text{Fe}^{25+}$  incidences, which are shown in Fig. B.8. These yields were obtained by integrating the singly differential spectra from  $E_p - 30$  to  $E_p + 30$  keV ( $E_p$  is the peak energy). Again, we evaluated the ratios of the yields of the detected electrons to those of the total electrons lost from the projectile ions,  $R(\text{Fe}^{23+})$ ,  $R(\text{Fe}^{24+})$ , and  $R(\text{Fe}^{25+})$  for  $\text{Fe}^{23+}$ ,  $\text{Fe}^{24+}$ , and  $\text{Fe}^{25+}$  incidences. These values are expressed as

$$R(\text{Fe}^{23+}) = \frac{Y(\text{Fe}^{23+})}{F(\text{Fe}^{23+}; \text{Fe}^{24+}) + 2 \times F(\text{Fe}^{23+}; \text{Fe}^{25+}) + 3 \times F(\text{Fe}^{23+}; \text{Fe}^{26+})}, \quad (\text{B.1})$$

$$R(\text{Fe}^{24+}) = \frac{Y(\text{Fe}^{24+})}{F(\text{Fe}^{24+}; \text{Fe}^{25+}) + 2 \times F(\text{Fe}^{24+}; \text{Fe}^{26+})}, \quad (\text{B.2})$$

$$R(\text{Fe}^{25+}) = \frac{Y(\text{Fe}^{25+})}{F(\text{Fe}^{25+}; \text{Fe}^{26+})}, \quad (\text{B.3})$$

where, for example,  $F(\text{Fe}^{23+}; \text{Fe}^{24+})$  is the fraction of  $\text{Fe}^{24+}$  ions after transmitting through the carbon foils for  $\text{Fe}^{23+}$  incidence. In Fig. B.8, the experimental results are compared with the simulation, which are normalized so that the simulated data at  $530 \mu\text{g}/\text{cm}^2$  for  $\text{Fe}^{25+}$  incidence is equal to the experimental one. For  $50 \mu\text{g}/\text{cm}^2$  carbon foil,  $Y(\text{Fe}^{23+})$  is about one order of magnitude larger than for  $Y(\text{Fe}^{25+})$ . This indicates that the loosely bound  $2s$  electron plays an important role in the convoy electron production for thinner targets. As shown in Fig. B.8,  $R(\text{Fe}^{23+})$  is about twice as large as  $R(\text{Fe}^{24+})$  and  $R(\text{Fe}^{25+})$ , which implies the narrow peak for  $\text{Fe}^{23+}$  incidence.

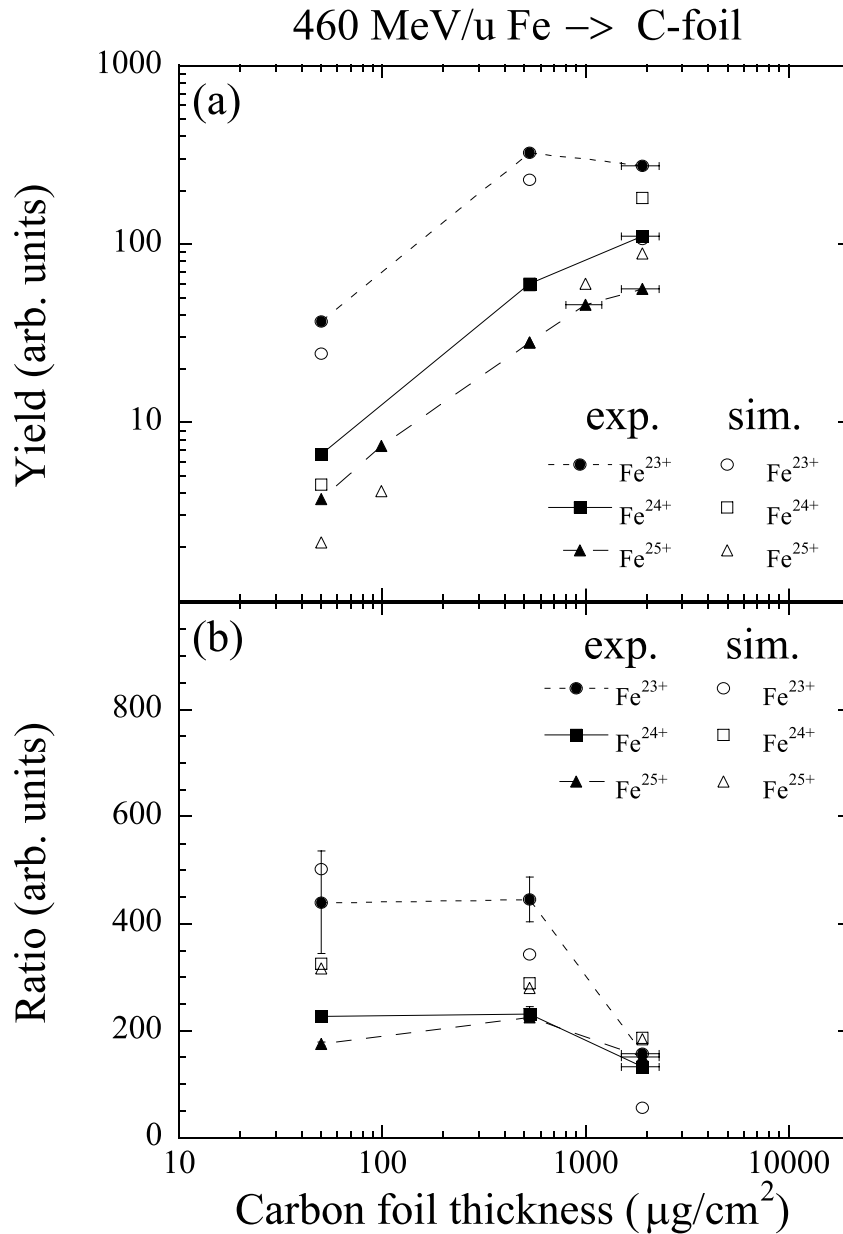


Figure B.8: (a) Yields of the detected electrons,  $Y(Fe^{23+})$ ,  $Y(Fe^{24+})$ , and  $Y(Fe^{25+})$ , as a function of carbon foil thickness for 460 MeV/u  $Fe^{23+}$ ,  $Fe^{24+}$ , and  $Fe^{25+}$  incidences, respectively. The simulated yields are normalized so that the simulated data at 530  $\mu\text{g}/\text{cm}^2$  for  $Fe^{25+}$  incidence is equal to the experimental one. (b) Ratios of the yields of the detected electrons to those of the total electrons lost from the incident ions for 460 MeV/u  $Fe^{23+}$ ,  $Fe^{24+}$ , and  $Fe^{25+}$  ions incident on carbon foils, respectively. For example,  $F(Fe^{23+};Fe^{24+})$  represents the fraction of  $Fe^{24+}$  ions transmitted through the carbon foils for  $Fe^{23+}$  incidence. The closed and open symbols show the experiment and simulation, respectively.

# Acknowledgments

I would like to acknowledge my supervisor, Prof. K. Komaki, who introduced me to this interesting field of physics and gave me this interesting theme. The calculations on the energy levels for the channeled ions were performed by him. I would like to acknowledge Prof. Y. Yamazaki, who gave me valuable advice and encouragement. I would like to acknowledge Prof. T. Azuma, who gave me advice about the experiment and encouraged me.

I would like to acknowledge Dr. T. Ito. I performed most of the present experiments with him. I thank Mr. C. Kondo. I performed the experiments on the RCE of Fe ions with him.

I appreciate Dr. T. Murakami, Dr. E. Takada, Dr. A. Kitagawa, and Dr. M. Torikoshi (National Institute of Radiological Sciences), who supplied me with the parallel beam of good quality at HIMAC. The present experiment was performed as one of research projects with heavy ions at NIRS-HIMAC. I also thank Mr. T. Kato and Mr. T. Kamiya, who assisted me in preparing the experiment.

I acknowledge Prof. S. Datz, who gave me advice about the RCE experiments. I appreciate Prof. H. Tawara, who participated in the experiments on convoy electrons and gave me advice. I thank Prof. K. Shima, who performed the measurements of the carbon foil thicknesses at University of Tsukuba. I acknowledge Prof. J. Burgdörfer, Dr. K. Tókési, and Dr. M. Seliger, who performed the CTT simulation.

In the end, I would like to thank the former and present members of Komaki-Yamazaki laboratory, Dr. H. A. Torii, Mr. K. Kuroki, Dr. S. Ninomiya, Dr. T. Ichioka, Mr. Y. Morishita, Dr. H. Higaki, Dr. N. Oshima, Dr. Z. Wang, Dr. K. Franzén Yoshiki, Mr. Y. Tsuruta, Mr. N. Okabayashi, Mr. Y. Iwai, Mr. H. Matsushima, Mr. N. Kuroda, Ms. A. Endo, Mr. D. Murakoshi, Mr. S. Yoneda, Mr. H. Shimada, Ms. M. Niigaki, and Mr. E. Noguchi.

# Bibliography

- [1] D. S. Gemmell. *Rev. Mod. Phys.* *46*, page 129, 1974.
- [2] V. V. Okorokov. *JETP Lett.* *2*, page 111, 1965.
- [3] S. Datz, C. D. Moak, O. H. Crawford, H. F. Krause, P. F. Dittner, J. Gomez del Campo, J. A. Biggerstaff, P. D. Miller, P. Hvelplund, and H. Knudsen. *Phys. Rev. Lett.* *40*, page 843, 1978.
- [4] F. Fujimoto, K. Komaki, A. Ootuka, E. Vilalta, Y. Iwata, Y. Hirao, T. Hasegawa, M. Sekiguchi, and A. Mizobuchi. *Nucl. Instr. and Meth. B* *33*, page 354, 1988.
- [5] K. Kimura, J. P. Gibbons, S. B. Elston, C. Biedermann, R. DeSerio, N. Keller, J. C. Levin, M. Breinig, J. Burgdörfer, and I. A. Sellin. *Phys. Rev. Lett.* *66*, page 25, 1991.
- [6] K. Kimura, H. Ida, M. Fritz, and M. Mannami. *Phys. Rev. Lett.* *76*, page 3850, 1996.
- [7] C. Auth, A. Mertens, H. Winter, A. G. Borizov, and F. J. García de Abajo. *Phys. Rev. Lett.* *79*, page 4477, 1997.
- [8] J. Kondo. *J. Phys. Soc. Jpn.* *36*, page 1406, 1974.
- [9] S. Shindo and Y. H. Ohtsuki. *Phys. Rev. B* *14*, page 3929, 1976.
- [10] O. H. Crawford and R. H. Ritchie. *Phys. Rev. A* *20*, page 1848, 1979.
- [11] F. J. García de Abajo and P. M. Echenique. *Phys. Rev. Lett.* *76*, page 1856, 1996.
- [12] A. Salin, A. Arnau, and P. M. Echenique. *Phys. Rev. A* *57*, page 2772, 1998.
- [13] C. D. Moak, S. Datz, O. H. Crawford, H. F. Krause, P. F. Dittner, J. Gomez del Campo, J. A. Biggerstaff, P. D. Miller, P. Hvelplund, and K. Knudsen. *Phys. Rev. A* *19*, page 977, 1979.
- [14] S. Datz, C. D. Moak, O. H. Crawford, H. F. Krause, P. D. Miller, P. F. Dittner, J. Gomez del Campo, J. A. Biggerstaff, H. Knudsen, and P. Hvelplund. *Nucl. Instr. and Meth.* *170*, page 15, 1980.

- [15] P. D. Miller, H. F. Krause, J. A. Biggerstaff, O. H. Crawford, S. Datz, P. F. Dittner, J. Gomez del Campo, C. D. Moak, N. Neskovic, and P. L. Pepmiller. *Nucl. Instr. and Meth. B* 13, page 56, 1986.
- [16] Y. Iwata, K. Komaki, Y. Yamazaki, M. Sekiguchi, T. Hattori, T. Hasegawa, and F. Fujimoto. *Nucl. Instr. and Meth. B* 48, page 163, 1990.
- [17] S. Datz, P. F. Dittner, J. Gomez del Campo, K. Kimura, K. F. Krause, T. M. Rosseel, C. R. Vane, Y. Iwata, K. Komaki, Y. Yamazaki, F. Fujimoto, and Y. Honda. *Nucl. Instr. and Meth. B* 164-165, page 73, 1991.
- [18] H. F. Krause, S. Datz, P. F. Dittner, N. L. Jones, and C. R. Vane. *Phys. Rev. Lett.* 71, page 348, 1993.
- [19] S. Datz, P. F. Dittner, H. F. Krause, C. R. Vane, O. H. Crawford, J. S. Forster, G. S. Ball, W. G. Davies, and J. S. Geiger. *Nucl. Instr. and Meth. B* 100, page 272, 1995.
- [20] J. S. Forster, G. C. Ball, W. G. Davies, J. S. Geiger, J. U. Andersen, J. A. Davies, H. Geissel, and F. Nickel. *Nucl. Instr. and Meth. B* 107, page 27, 1996.
- [21] J. U. Andersen, G. C. Ball, J. Chevallier, J. A. Davies, W. G. Davies, J. S. Forster, J. S. Geiger, and H. Geissel. *Nucl. Instr. and Meth. B* 119, page 292, 1996.
- [22] K. Kimura and M. Mannami. *Phys. Rev. A* 57, page 1121, 1998.
- [23] T. Hecht and H. Winter. *Phys. Lett. A* 243, page 306, 1998.
- [24] C. Auth and H. Winter. *Phys. Rev. A* 62, page 012903, 2000.
- [25] N. Hatke, M. Dirska, M. Grether, E. Luderer, A. Robin, A. Nürmann, and W. Heiland. *Phys. Rev. Lett.* 79, page 3395, 1997.
- [26] T. Ito, T. Azuma, K. Komaki, Y. Yamazaki, T. Murakami, E. Takada, A. Kitagawa, M. Torikoshi, and M. Sano. *Phys. Scr. T73*, page 345, 1997.
- [27] T. Ito, T. Azuma, K. Komaki, Y. Yamazaki, M. Sano, M. Torikoshi, A. Kitagawa, E. Takada, and T. Murakami. *Nucl. Instr. and Meth. B* 135, page 132, 1998.
- [28] T. Azuma, T. Ito, K. Komaki, Y. Yamazaki, M. Sano, M. Torikoshi, A. Kitagawa, E. Takada, and T. Murakami. *Phys. Rev. Lett.* 83, page 528, 1999.
- [29] T. Ito. PhD thesis, University of Tokyo, 2000.
- [30] H. F. Beyer, R. D. Deslattes, F. Folkmann, and R. E. LaVilla. *J. Phys. B* 18, page 207, 1985.
- [31] K. Komaki, T. Azuma, T. Ito, Y. Takabayashi, Y. Yamazaki, M. Sano, M. Torikoshi, A. Kitagawa, E. Takada, and T. Murakami. *Nucl. Instr. and Meth. B* 146, page 19, 1998.

- [32] N. Stolterfoht, R. D. DuBois, and R. D. Rivarola. *Electron Emission in Heavy Ion-Atom Collisions*. Springer, 1997.
- [33] M. Breinig, S. B. Elston, S. Hultdt, L. Liljeby, C. R. Vane, S. D. Berry, G. A. Glass, M. Schauer, I. A. Sellin, G. D. Alton, S. Datz, S. Overbury, R. Laubert, and M. Suter. *Phys. Rev. A* *25*, page 3015, 1982.
- [34] J. Burgdörfer, M. Breinig, S. B. Elston, and I. A. Sellin. *Phys. Rev. A* *28*, page 3277, 1983.
- [35] H. F. Beyer, H. J. Kluge, and V. P. Shevelko. *X-ray Radiation of Highly Charged Ions*. Springer, 1997.
- [36] P. J. Mohr, G. Plunien, and G. Soff. *Phys. Rep.* *293*, page 227, 1998.
- [37] W. R. Johnson and G. Soff. *At. Data Nucl. Data Tables* *33*, page 405, 1985.
- [38] G. Soff. *unpublished*, 1993.
- [39] P. J. Mohr. *Nucl. Instr. and Meth. B* *87*, page 232, 1994.
- [40] H. Persson, S. Salomonson, P. Sunnergren, and I. Lindgren. *Phys. Rev. Lett.* *76*, page 204, 1996.
- [41] J. P. Briand, J. P. Mosse, P. Indelicato, P. Chevallier, D. Girard-Verhet, and A. Chetoui. *Phys. Rev. A* *28*, page 1413, 1983.
- [42] J. P. Briand, M. Tavernier, P. Indelicato, R. Marrus, and M. Gould. *Phys. Rev. Lett.* *50*, page 832, 1983.
- [43] J. D. Silver, A. F. McClelland, J. M. Laming, S. D. Rosner, G. C. Chandler, D. D. Dietrich, and P. O. Egan. *Phys. Rev. A* *36*, page 1515, 1987.
- [44] M. Tavernier, J. P. Briand, P. Indelicato, D. Liesen, and P. Richard. *J. Phys. B* *18*, page L327, 1985.
- [45] J. P. Briand, P. Indelicato, A. Simionovici, V. San Vicente, D. Liesen, and D. Dietrich. *Europhys. Lett.* *9*, page 225, 1989.
- [46] J. P. Briand, P. Chevallier, P. Indelicato, K. P. Ziock, and D. Dietrich. *Phys. Rev. Lett.* *65*, page 2761, 1990.
- [47] H. F. Beyer, G. Menzel, D. Liesen, A. Gallus, F. Bosch, R. D. Deslattes, P. Indelicato, Th. Stöhlker, O. Klepper, R. Moshhammer, F. Nolden, H. Eickhoff, B. Franzke, and M. Steck. *Z. Phys. D* *35*, page 169, 1995.
- [48] Th. Stöhlker, P. H. Mokler, K. Beckert, F. Bosch, H. Eickhoff, B. Franzke, M. Jung, T. Kandler, O. Kleppner, C. Kozhuharov, R. Moshhammer, F. Nolden, H. Reich, P. Rymuza, P. Spädtke, and M. Steck. *Phys. Rev. Lett.* *71*, page 2184, 1993.

- [49] J. H. Lupton, D. D. Dietrich, C. J. Hailey, R. E. Stewart, and K. P. Ziock. *Phys. Rev. A* *50*, page 2150, 1994.
- [50] M. H. Cheng, K. T. Chen, W. R. Johnson, and J. Sapirstein. *Phys. Rev. A* *50*, page 247, 1994.
- [51] G. W. Drake. *Can. J. Phys.* *66*, page 586, 1988.
- [52] D. R. Plante, W. R. Johnson, and J. Sapirstein. *unpublished*, 1994.
- [53] P. Indelicato, O. Gorceix, and J. P. Desclaux. *J. Phys. B* *20*, page 651, 1987.
- [54] R. D. Deslattes, H. F. Beyer, and F. Folkmann. *J. Phys. B* *17*, page L689, 1984.
- [55] P. Beiersdorfer, M. Bitter, S. von Goeler, and K. W. Hill. *Phys. Rev. A* *40*, page 150, 1989.
- [56] J. P. Briand, M. Tavernier, R. Marrus, and J. P. Desclaux. *Phys. Rev. A* *29*, page 3143, 1984.
- [57] P. Indelicato, J. P. Briand, M. Tavernier, and D. Liesen. *Z. Phys. D* *2*, page 249, 1986.
- [58] K. Widmann, P. Beiersdorfer, and V. Desclaux. *Nucl. Instr. and Meth. B* *98*, page 45, 1995.
- [59] P. H. Mokler, Th. Stöhlker, C. Kozhuharov, R. Moshhammer, P. Rymuza, F. Bosch, and T. Kandler. *Phys. Scr. T51*, page 28, 1994.
- [60] E. S. Marmor, J. E. Rice, K. Källne, J. Källne, and R. E. LaVilla. *Phys. Rev. A* *33*, page 774, 1986.
- [61] W. Lotz. *Z. Physik* *206*, page 205, 1967.
- [62] W. Lotz. *Z. Physik* *216*, page 241, 1968.
- [63] J. P. Rozet, C. Stéphan, and D. Vernhet. *Nucl. Instr. and Meth. B* *107*, page 67, 1996.
- [64] R. Shakeshaft and L. Spruch. *Rev. Mod. Phys.* *51*, page 369, 1979.
- [65] T. Ito, Y. Takabayashi, K. Komaki, T. Azuma, Y. Yamazaki, S. Datz, E. Takada, and T. Murakami. *Nucl. Instr. and Meth. B* *164-165*, page 68, 2000.
- [66] L. Pages, E. Bertel, H. Joffre, and L. Sklavenitis. *Atomic Data* *4*, page 1, 1972.
- [67] T. Azuma, T. Ito, Y. Takabayashi, K. Komaki, Y. Yamazaki, E. Takada, and T. Murakami. *Phys. Scr. T92*, page 61, 2001.

- [68] National Institute of Standards and Technology (NIST). *Atomic Spectra Database*.
- [69] H. A. Bethe and E. E. Salpeter. *Quantum Mechanics of One- and Two- Electron Atoms*. 1957.
- [70] G. Basile, A. Bergamin, G. Cavagnero, G. Mana, E. Vittone, and G. Zosi. *Phys. Rev. Lett.* *72*, page 3133, 1994.
- [71] P. Becker, K. Dorenwendt, G. Ebeling, R. Lauer, W. Lucas, R. Probst, H. J. Rademacher, G. Reim, P. Seyfried, and H. Siegert. *Phys. Rev. Lett.* *46*, page 1540, 1981.
- [72] Y. Yamazaki and N. Oda. *Phys. Rev. Lett.* *52*, page 29, 1984.
- [73] C. O. Reinhold, J. Burgdörfer, J. Kemmler, and P. Koschar. *Phys. Rev. A* *45*, page R2655, 1992.
- [74] S. D. Berry, G. A. Glass, I. A. Sellin, K. O. Groeneveld, D. Hofmann, L. H. Andersen, M. Breinig, S. B. Elston, P. Enger, M. M. Schauer, N. Stolterfoht, H. Schmidt-Böcking, G. Nolte, and G. Schiwietz. *Phys. Rev. A* *31*, page 1392, 1985.
- [75] S. B. Elston, S. D. Berry, J. Burgdörfer, I. A. Sellin, M. Breinig, R. DeSerio, C. E. Gonzalez-Lepera, L. Liljeby, K. O. Groeneveld, D. Hofmann, P. Koschar, and I. B. E. Nemirovsky. *Phys. Rev. Lett.* *55*, page 2281, 1985.
- [76] S. D. Berry, S. B. Elston, I. A. Sellin, M. Breinig, R. DeSerio, C. E. Gonzalez-Lepera, and L. Liljeby. *J. Phys. B* *19*, page L149, 1986.
- [77] J. P. Gibbons, S. B. Elston, K. Kimura, R. DeSerio, I. A. Sellin, J. Burgdörfer, J. P. Grandin, A. Cassimi, X. Husson, L. Liljeby, and M. Druetta. *Phys. Rev. Lett.* *67*, page 481, 1991.
- [78] Y. Takabayashi, T. Ito, T. Azuma, K. Komaki, Y. Yamazaki, H. Tawara, M. Torikoshi, A. Kitagawa, E. Takada, and T. Murakami. *Phys. Scr. T80*, page 249, 1999.
- [79] J. Burgdörfer. *Phys. Rev. Lett.* *51*, page 374, 1983.
- [80] J. Burgdörfer and J. Gibbons. *Phys. Rev. A* *42*, page 1206, 1990.
- [81] Y. Yamazaki, N. Stolterfoht, P. D. Miller, H. F. Krause, P. L. Pepmiller, S. Datz, I. A. Sellin, J. N. Scheurer, S. Andriamonje, D. Bertault, and J. F. Chemin. *Phys. Rev. Lett.* *61*, page 2913, 1988.
- [82] J. Burgdörfer and C. Bottcher. *Phys. Rev. Lett.* *61*, page 2917, 1988.
- [83] B. Gervais, C. O. Reinhold, and J. Burgdörfer. *Phys. Rev. A* *53*, page 3189, 1996.

- [84] M. Seliger, K. Tókési, C. O. Reinhold, J. Burgdörfer, Y. Takabayashi, T. Ito, K. Komaki, T. Azuma, and Y. Yamazaki. *Phys. Scr. T92*, page 211, 2001.
- [85] R. Moshhammer, P. D. Fainstein, M. Schulz, W. Schmitt, H. Kollmus, R. Mann, S. Hagmann, and J. Ullrich. *Phys. Rev. Lett. 83*, page 4721, 1999.